Alteration and carbonation of calcium and magnesium silicates: implications on capture, storage and use of CO_2

Doctoral Thesis

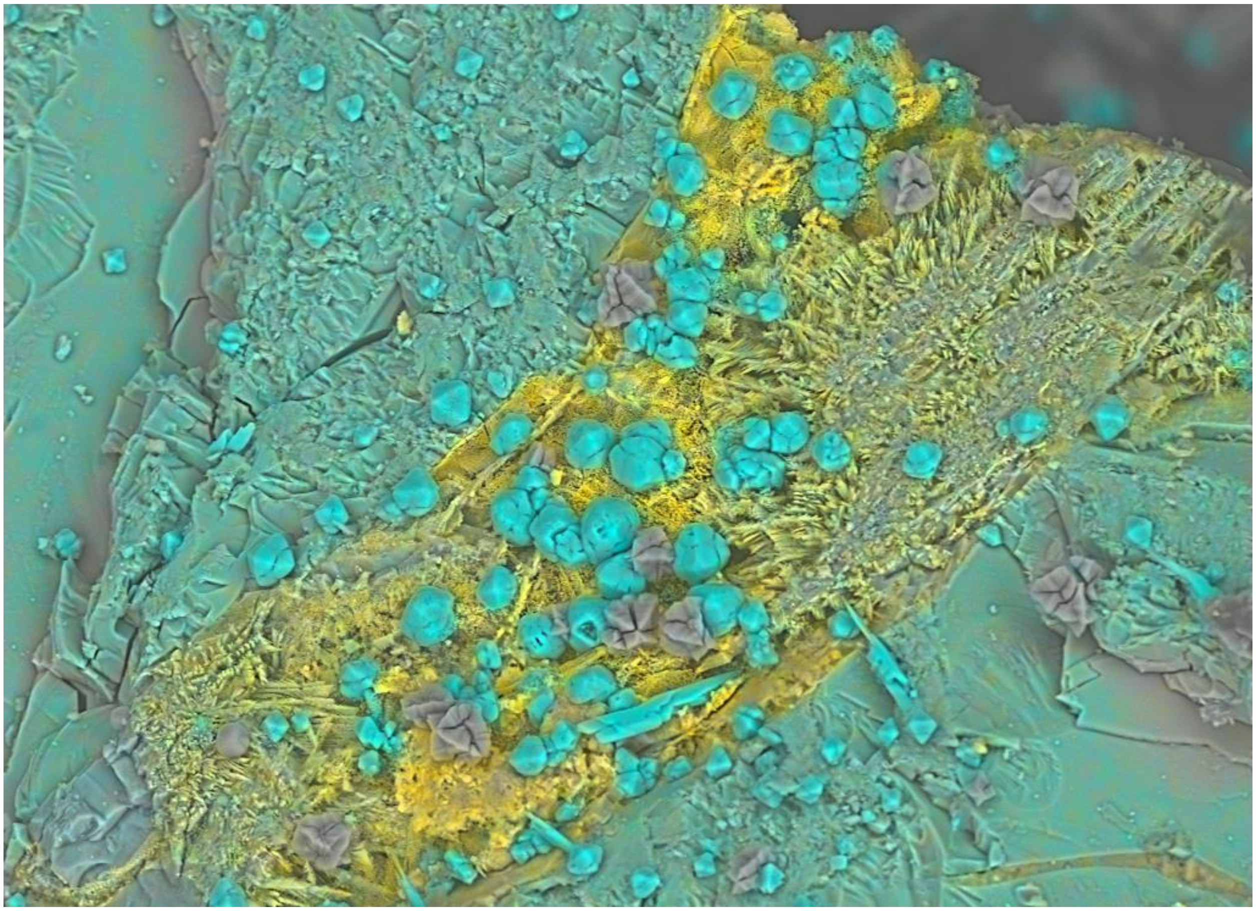

Luis Monasterio Guillot

UNIVERSIDAD
DE GRANADA

Supervisors: Carlos Rodríguez Navarro and Encarnación Ruiz Agudo

Programa Doctorado
Ciencias de la Tierra

Editor: Universidad de Granada. Tesis Doctorales
Autor: Luis Monasterio Guillot
ISBN: 978-84-1306-518-2
URI: http://hdl.handle.net/10481/62880

by Johanna Öst on Etsy

"None but those who have experienced them can conceive of the enticements of science. In other studies, you go as far as others have gone before you, and there is nothing more to know; but in a scientific pursuit there is continual food for discovery and wonder"

Frankenstein or the Modern Prometheus, by Mary Wollstonecraft Shelley

AGRADECIMIENTOS

Quisiera agradecer, en primer lugar, a mis directores de tesis, Encarni y Carlos, por haberme dado esta oportunidad profesional. Gracias por vuestra paciencia y dedicación, vuestro entusiasmo, vuestro ánimo y vuestro compromiso. Gracias a vosotros hoy comienza para mí, un nuevo camino como investigador. De vosotros he aprendido que la ciencia, más allá de cualquier esfuerzo, ha de nacer del corazón y merece toda nuestra entrega, coraje y pasión. Sois mi ejemplo a seguir en esta nueva etapa.

Gracias, también, a mi tutor Alejandro, por las horas dedicadas a mi preparación como docente, por los consejos acertados y las palabras de apoyo siempre disponibles para mí.

Agradecer a todo el personal del CIC por su amabilidad, ayuda y disponibilidad. Y al Departamento de Mineralogía y Petrología el haberme acogido como a uno más y haber sido hogar.

Fulvio, Alejandro, Estefanía, Nazaret, Cristina, Agustín, Laura, Christian… Vosotros habéis sido familia, bienvenida, risas en los buenos momentos y empujones de ánimo en los malos. Mucho más que Pendejolandia, vosotros sabéis que el lugar lo hace su gente.

Gracias a Aurelia, por haber sido en tantas ocasiones *mis pies y mis manos* y no haber pedido nunca nada a cambio.

Gracias también a Pedro, por haberme enseñado tanto y haber estado siempre disponible, hasta el punto de acogerme en su casa. Por personas como tú vale la pena el camino.

A Álex, por haberme aportado otros puntos de vista y haber sembrado en mí tantas preguntas necesarias.

Agradecer también a Mapi, Sara, Alba y Sander el haberme hecho sentir en casa en una ciudad tan nueva para mí. Mis estancias sin vosotros habrían sido mucho más duras.

Gracias a mis alumnos, al EIIG y al GIIM. Vosotros sois mi motor. Ojalá haber encendido en vuestros corazones la llama de esta pasión que me ha traído hasta aquí.

Je voudrais remercier a toute l'équipe de l'IS Terre, en particulier à Roland, Sarah, Silvain, Valérie et Germán. Merci de votre conseil, votre amabilité et votre aide toujours présente.

Gracias a mis padres, por haberme enseñado a levantarme después de cada caída y a seguir en la lucha aun cuando no quedan fuerzas. A Tis, por haberme enseñado a ofrecer siempre la mejor versión de mí mismo.

Gracias también a mis amigos, Jorge y Ras, por haber confiado siempre en mí y haber estado a mi lado desde el comienzo.

Y por último, gracias a Eli, por haber rescatado mi vocación en el momento en que creí haberla olvidado, haberme dado un porqué y haber estado a mi lado contra viento y marea.

Espero que me perdonen los que se me olvida nombrar. A todos los que os habéis cruzado en mi camino durante estos años os pertenece un poco de esta tesis. Gracias de todo corazón.

Abstract

According to the Intergovernmental Panel on Climate Change (IPCC), the current estimated global emission of anthropogenic carbon dioxide (CO_2), mostly from fossil fuel combustion and cement production, are the main cause of the warming of the climate system due to the unbalance of the inputs and outputs of CO_2 to the atmosphere and therefore, to the biogeochemical cycles that regulates Earth's climate. Furthermore, coal-fired power plants are main contributors to atmospheric CO_2 emissions, and also produce huge amounts of coal fly ash (CFA) waste. Despite the fact that chemical weathering reactions on the Earth's surface play a key role on the regulation of atmospheric carbon dioxide concentrations over geologic time-scales ($>10^5$ years) and thus, on the climate control, this unbalance is provoking a T increase of ~1.5 – 2 ºC (since the beginning of the industrial revolution back in the mid-XVII c.). CO_2 is considered the most important greenhouses gas (GHG), due to the dependence of world economies on fossil fuel combustion.

New environmental policies such as the Kyoto Protocol (2012) or the Paris Agreement (2016) are proposing the reduction of anthropogenic GHG emissions to the atmosphere, as well as the active capture of CO_2 and its safe storage, as an effective way to avoid/reduce the impact of global warming. Hence, the processes involving the capture, transport and storage of CO_2 are gaining attention on the socioeconomic and scientific community as a way to reduce the concentration of this gas in the atmosphere. These are the so-called Carbon Capture and Storage (CCS) strategies. CCS has been proposed as a potential mechanism to, on the one hand, allow the continued use of fossil fuels to avoid an economic slump, and on the other hand, to prevent the emissions of CO_2 to the atmosphere.

Among others, Geological Carbon Storage (GCS) strategies via aqueous carbonation of primary calcium and magnesium silicates are readily available technologies to reduce CO_2 emissions. They include ex situ and in situ strategies that have been developed during the last decades as permanent and safe mechanisms to capture and permanently store anthropogenic CO_2. However, the slow rates ascribed to these reactions, which typically take place in Nature at geological timescales, are a strong handicap for an effective GCS. This challenging issue has prompted the research of methods that can enhance mineral carbonation. At the same time, numerous efforts have been dedicated to better understand the kinetics and mechganisms of primari silicates carbonation, a process which is not yet fully understood. Despite these gaps in knowledge, successful examples of direct in situ mineral carbonation for CO_2 geological sequestration are for instance, the CarbFix pilot plant (Island) which have led to the trapping of 12 Gt y^{-1} of CO_2. This example strongly support mineral carbonation as an effective strategy for CCS.

Considering that the mechanisms and parameters that control mineral carbonation during CCS are still unclear, in the present thesis, a series of experimental studies have been conducted with the main aim of better understanding the kinetics and mechanisms of primary silicate mineral carbonation as a safe, permanent and economically feasible way for CCS. The gained knowledge is subsequently used here to explore the potential of ex situ carbonation of coal combustion wastes as a way to recycle such a waste material and as the same time effectively sequester CO_2.

In order to achieve these overall objectives, a series of experimental studies have been conducted, which are listed below:

Hydrothermal reaction of pseudowollastonite with carbonate-bearing fluids: Implications for CO_2 mineral sequestration

The kinetics of silicate carbonation in aqueous solutions are typically very slow, especially at neutral to alkaline conditions. This hampers the complete understanding of the mechanisms and parameters that control mineral carbonation during CCS.

Here the hydrothermal dissolution and carbonation of pseudowollastonite (psw; α-$CaSiO_3$), one of the most reactive silicates known, is studied under a range of geochemical conditions ranging from acidic to strongly alkaline pH, presence/absence of different background alkali metal ions and carbonate sources (K_2CO_3 and Na_2CO_3, pH ~13, or $NaHCO_3$ and $KHCO_3$, pH ~9).

It is shown that in addition to amorphous silica precipitation, the formation of secondary Na+Ca-, Ca-, or K+Ca-silicates, is critical for the progress of psw carbonation. The formation of pectolite and minor amounts of plombierite and/or tobermorite-11Å (calcium silicate hydrates, CSH, cement phases) in the presence of background Na^+ ions leads to full consumption of psw. Conversely, limited formation of a secondary K+Ca-silicate phase (shlykovite) in the presence of K^+ ions leads to incomplete psw conversion. The formation of Ca-containing secondary crystalline silicates and Ca-containing amorphous silica is shown to be a strong handicap for a fully effective carbonation, although it favors reactant conversion and cementation. In all cases a higher conversion into $CaCO_3$ (up to ~70 mol%) is achieved when using bicarbonate salts (i.e., lower initial pH).

By using a reactor with a pressurized CO_2-solution, with and without Na^+ or K^+ background ions, rapid and nearly complete conversion of psw with a $CaCO_3$ yield ~92 mol% is achieved because, in addition to the initial low pH (~3.7) that favored α-$CaSiO_3$ dissolution, abundant non-passivating amorphous silica formed along with calcite.

These results imply that the presence (e.g., use of sea water during CO_2 injection or mixing with saline formation solutions) and/or the release of different alkali metal ions (e.g., after feldspars and/or basaltic glass dissolution) in combination with a reaction-induced pH increase in GCS scenarios may strongly limit carbonation due to the capture of alkaline-earth metals in secondary silicates and a reduction in reaction rates.

In turn, these results show that the high conversion achieved in pure CO_2-aqueous systems, while relevant for *ex situ* CCS, may not reflect the actual conversion in multicomponent natural systems following reactive transport during *in situ* GCS.

It is also observed the solvent-mediated polymorphic transformation of psw (high-*T* polymorph) into parawollastonite (low-*T* polymorph) during carbonation under alkaline conditions in the presence of background Na^+ ions.

This is the first case ever reported for a non-solid-state polymorphic transformation of silicate minerals at mild *T*-conditions (150 °C).

Finally, the observed solvent-mediated silicate phase transformations plus the precipitation of secondary silicate and calcium carbonate phases have a direct cementing effect, which is relevant for the setting of novel $CaSiO_3$-based non-hydraulic cements with reduced CO_2 footprint.

Kinetics and mechanisms of the acidic weathering of pyroxenes

During dissolution of primary silicates, amorphous silica surface layers (ASSLs), also called Surface Altered Layers (SALs), coating the surface of the minerals, strongly influences the kinetics of these reactions, hampering the effective dissolution of the primary materials and therefore, inhibiting the release of alkaline-earth ions to the solution to complete the carbonation reactions. In the last decades, several studies have been performed to unravel the mechanisms that regulate the formation of ASSLs. This is due to the relevant effects affecting the effective implementation of GCS strategies. However, the mechanisms of ASSLs formation is a matter strong debate in the scientific community.

Here it is reported experimental results from the reaction of acidic solutions (pH 1.5) with fragments of the clinopyroxenes augite and diopside. Dissolution rates were measured at 80 °C using mixed-flow and batch reactors. Dissolution under far-from-equilibrium conditions such as those prevalent in our experiments results in the abundant formation of etch pits where crack can initiate and propagate by stress corrosion, particularly in the case of augite weathered in flow-through experiments. The high resolution X-ray Computed Tomography (Micro-CT) and electron microscopy (SEM-EDS and HRTEM-EDS) analyses showed a completely different behaviour, on the one hand, between the two different experimental procedures, and on the other hand, between the two primary silicates. The replacement of the starting material by amorphous silica was higher during flow-through experiments, and in turn, greater in augite than in diopside.

These results are not consistent with an interdiffusion-model for ASSLs formation, but are explained by an Interface-Coupled Dissolution-Precipitation (ICDP) mechanism, providing a clear experimental evidence of the formation mechanisms of the ASSLs.

These results also provide important information applicable to GCS strategies, particularly for predicting silicate weathering during *in-situ* CO2 mineral sequestration and affecting the calculations of CO_2 mineralization, depending on the mineralogy of the injection wells.

Physical-chemical control on carbonation of calcium-magnesium pyroxenes

Despite the several studies performed during the last decade, the mechanisms of aqueous carbonation of primary silicates are still unclear, especially at pH close to those prevailing in natural weathering systems. This is a handicap to apply effective CCS techniques.

Dissolution-carbonation reactions of single crystals of augite and diopside have been investigated in experiments conducted at hydrothermal conditions, in the presence/absence of different carbonate sources ($NaHCO_3$ and Na_2CO_3). We show that the main reaction products were low-magnesium calcite and amorphous silica.

In addition, Na-aluminosilicates (Na-phillipsite) were precipitated during augite reactions at moderately alkaline conditions, and Magnesium Silicate Hydrate (MSH) was precipitated under strongly alkaline conditions during diopside replacement, which fosters the progress of the reaction.

Furthermore, massive pervasive fracturing occurs during augite replacement in the presence of Na-phillipsite. In all cases, a higher conversion of augite (up to 38 wt%) as compared with diopside (~15 wt%) was achieved. These results imply that the presence of Fe, Al and Na in the composition of the pyroxenes strongly influences the release of cations to the solution (i.e. increase in the dissolution rates), and therefore, contributes to the formation of secondary crystalline silicates that exerted crystallization pressure that exceeds the tensile strength of the host rock, causing their fracturing, and the increase in exposed reactive surface area to the solution, that altogether contribute to the progress of the reaction in a “flow loop” mechanism.

Moreover, these results are relevant for CCS strategies, offering ways to enhance CO_2 mineralization (e.g., by promoting secondary phases formation via injection of CO_2 dissolved in Na-rich fluieds such as sea water) and, therefore, to a safe, effective and permanent carbon storage by the contribution of these newly-formed phases in the progress of the dissolution-carbonation reactions.

CO_2 sequestration with simultaneous zeolite production and toxic elements trapping by carbonation of Coal Fly Ash

Coal fly ash (CFA) waste are typically landfilled, posing significant environmental risks due to its high content of potentially toxic elements (PTE). However, CFA is an alkaline aluminosilicate-rich waste, which offers the possibility of CO_2 mineral capture and the production of economically-relevant mineral by-products such as zeolites.

Yet, the combined carbonation and zeolite production from CFA resulting in PTE trapping has never been explored. Here we show that under mild hydrothermal conditions (150 °C) and depending of process parameters such as pH and background alkali metal ion in alkaline (bi)carbonate solutions, a carbonation efficiency of up to 79%, with a net CO_2 mineral capture of 0.045 g/kg CFA can be achieved, even when using a low Ca and Mg (3.72 wt% CaO, 1.74 wt% MgO) Class F fly ash.

Moreover, amorphous zeolitic precursors and different crystalline zeolites (yield up to 60 wt%) are simultaneously obtained, and PTE in CFA are effectively trapped into the newly formed calcite, zeolitic precursors, and zeolite phases.

These results have important implications for carbon capture and storage, as well as for the safe reutilization and disposal of CFA waste.

The overall results of this experimental study for such different systems and process parameters (type of silicate phase(s), pH, T, pCO_2, background electrolyte, dissolved inorganic carbons, DIC, carbon source) show that both natural Ca-Mg-Fe primary silicates, and aluminosilicate-rich industrial wastes (coal fly ash), can be safely and effectively used for CCS. Moreover, key parameters that control de dissolution-carbonation process resulting in secondary silicate phases formation, along with carbonates are identified. It is observed that mineral passivation can have a direct impact on silicate dissolution, hampering carbonation. Conversely, reaction-driven fracturing due to crystallization pressure exerted by secondary silicate phases is key for the successful progress of the carbonation reaction. However, it is also shown that formation of secondary silicates including divalent metals is a strong handicap for an effective mineral carbonation. But such detrimental effects could be by passed by selecting appropriate mineral feed and reaction parameters during *ex situ* mineral carbonation. Conversely, these experimental results show that enhanced mineral carbonation can be achieved during in situ GCS if pore waters include alkali metal ions that can favour the precipitation of secondary Na or K silicates. Finally, it is shown that zeolites along with carbonates are formed under hydrothermal condition during coal fly ash carbonation. This process is not only effective for CO_2 mineral sequestration, but also results in the trapping and immobilization of potentially toxic elements such as heavy metals present in coal fly ash. Ultimately, these results show that mineral carbonation is not only and effective CCS strategy, but also have direct environmental applications for toxic element trapping, while at the same time resulting in the production of valuable minerals such as zeolites and calcite, with numerous industrial and technical uses. The latter ensures that recycling of alkaline industrial wastes is an economic and effective way to deal with the increasing problem associated with anthropogenic CO_2 emission to the atmosphere.

Resumen

De acuerdo con el Panel Intergubernamental del Cambio Climático (IPCC) la actual emisión de dióxido de carbono (CO_2) causada antropológicamente, mayormente por la combustión de combustibles fósiles y la producción de cementos, es la principal responsable del calentamiento global, provocado por un desequilibrio entre las emisiones de CO_2 a la atmósfera y su retirada de la misma (por distintos procesos) afectando, por lo tanto, a los ciclos biogeoquímicos que regulan el clima de la Tierra. En este sentido hay que destacar que las centrales termoeléctricas que usan carbón como combustble son uno de los mayores contribuyentes a las emisiones de CO_2 y también producen grandes cantidades de residuos tales como las cenizas volantes (CFA). A pesar del hecho de que la meteorización química en la superficie terrestre juega un papel clave en la regulación de la concentración de dióxido de carbono atmosférico a escalas de tiempo geológico ($>10^5$ años) y, por lo tanto, del control del clima, este desequilibrio está provocando un incremento de la temperatura media de la superficie terrestre de entre 1.5 – 2 ºC (desde el inicio de la era industrial, a mitad del siglo XVII) Asimismo, el CO_2 está considerado como el gas de de efecto invernadero (GEI o GHG) de mayor riesgo debido a la dependencia de las economías mundiales en la combustión de combustibles fósiles (petróleo y carbón).

Se han desarrollado nuevas políticas medioambientales, tales cómo el Protocolo de Kyoto (2012) o el Acuerdo de París (2016) que proponen una disminución de las emisiones antropogénicas de CO_2 a la atmósfera y que promueven su captura de una forma eficiente, segura y permanente para así evitar y/o reducir el impacto de este desequilibrio atmosférico en el cambio climático. Por lo tanto, los procesos que engloban la captura, transporte y almacenamiento de CO_2 están llamando la atención de la comunidad socioeconómica y científica. Se han realizado estudios

encaminados a reducir la concentración de este gas en la atmósfera mediante estrategias de captura y almacenamiento de carbono (CAC o CCS). La CCS ha sido propuesta como un mecanismo de gran potencial para, por un lado, permitir el uso continuado de combustibles fósiles y así evitar una crisis económica y, por otro lado, prevenir las emisiones de CO_2 a la atmósfera y regular el clima en la superficie terrestre.

Entre otras, las estrategias de Almacenamiento Geológico de Carbono (AGC o GCS) mediante la carbonatación en medio acuoso de silicatos primarios de calcio y magnesio son relativamente asequibles para la reducción de las emisiones de CO_2. Incluyen estrategias de tipo in situ y ex situ, las cuales han sido desarrolladas durante las últimas décadas como una vía para almacenar el CO_2 de una forma segura y permanente. Sin embargo, cabe destacar las lentas tasas de reacción en medios naturales. Este hándicap influye enormemente la captura efectiva mediante estrategias de CCS. Dicho problema ha sido investigado en mayor medida para evitar los problemas asociados a la carbonatación mineral y por lo tanto, mejorar y acelerar la disolución y carbonatación de silicatos. Para ello, se ha estudiado de forma pormenorizada la cinética y los mecanismos del proceso de carbonatación de silicatos primarios, aspectos poco comprendidos a pesar de la gran variedad de estudios realizados sobre este tema. Pese a estas lagunas en el conocimiento, existen ejemplos prometedores que han sido desarrollados para la carbonatación mineral *in situ*, como la planta piloto Carbfix, en Islandia, la cual está atrapando una media de 12 Gt año^{-1} Este ejemplo es un importante aval que otorga a la carbonatación mineral un papel importante como estrategia para la captura de CO_2 de forma eficiente y segura.

Por lo tanto, en esta tesis, se han desarrollado diversos estudios experimentales para comprender mejor la cinética y los mecanismos de carbonatación de silicatos y, a su vez, desarrollar una forma segura, permanente y económicamente viable de aplicar el conocimiento adquirido a la carbonatación *ex situ* de residuos de combustión del carbón.

Para alanzar estos objetivos se han desarrollado una serie de estudios experimentales que se señalan a continuación.

Reaccion hidrotermal de Pseudowollastonita con fluidos carbonáticos: Implicaciones en el secuestro mineral de CO2

La cinética de la carbonatación de los silicatos en medio acuoso es habitualmente muy lenta, especialmente en condiciones de pH neutro a alcalino. Esto dificulta la adecuada comprensión de los mecanismos y parámetros que gobiernan su carbonatación durante la CCS.

En este trabajo se ha estudiado la disolución y carbonatación en condiciones hidrotermales de la pseudowollastonita (psw; α-$CaSiO_3$), uno de los silicatos más reactivos, bajo un amplio rango de condiciones geoquímicas obtenidas variando el pH (desde condiciones ácidas a extremadamente alcalinas), en presencia o ausencia de diferentes metales alcalinos y fuentes de carbonato (K_2CO_3 y Na_2CO_3, pH ~13, o $NaHCO_3$ y $KHCO_3$, pH ~9).

Se demuestra que, además de la precipitación de sílice amorfa, la formación de silicatos secundarios de Na+Ca, Ca o K+Ca es clave para el progreso de la carbonatación de la psw. La formación de pectolita y pequeñas cantidades de plombierita o tobermorita-11Å (silicatos de calcio hidratados, CSH, fases de cemento) en presencia de Na^+, conlleva el consumo total de la psw. Por otro lado, la limitada formación del silicato de K+Ca (shlykovita) en presencia de K^+ conlleva la transformación incompleta de la psw. La formación de silicatos secundarios con calcio y de sílice amorfa que tambien incorpora calcio es un gran hándicap para la carbonatación efectiva, pero a su vez favorecen la conversión y la cementación de la psw. En todos los casos estudiados, la mayor conversión de psw en $CaCO_3$ (más de ~70 mol%) se consiguió usando sales de bicarbonato (pH inicial menor).

Usando un reactor con una solución presurizada de CO_2, en presencia o ausencia de Na^+ o K^+ cómo electrolitos de fondo, se consiguió una transformación más rápida y prácticamente completa de la psw con una producción de carbonato de calcio del ~92 mol% debida, además del bajo pH inicial (~3.7) que favorece la disolución de α-$CaSiO_3$, a la formación de abundante sílice amorfa pero no-pasivante junto con la calcita.

Estos resultados implican que la presencia (uso de agua marina durante la inyección de CO_2 o mezcla con formaciones salinas solubles) y/o la liberación de diferentes iones alcalinos (tras la disolución de feldespatos y/o vidrios basálticos) en conjunto con un aumento del pH inducido durante el proceso de GCS pueden limitar el grado de carbonatación debido a la captura de los iones alcalinotérreos en los silicatos secundarios y a la reduccción de las tasas de reacción.

A su vez, estos resultados demuestran que la alta conversión alcanzada en los sistemas ques solo incluyen CO_2, a pesar de ser relevantes para la captura y almacenamiento *ex situ* de CO_2, pueden no reflejar la transformación conseguida en este trabajo en sistemas naturales multicomponentes tras un proceso de transporte reactivo durante la GCS in situ.

Además, se observa la transformación polimórfica de la psw (polimorfo de alta temperatura) a parawollastonita (polimorfo de baja temperatura) durante la carbonatación bajo condiciones alcalinas en presecia de Na^+.

Este es el primer caso presentado para una transformación polimórfica de silicatos a temperaturas moderadas (150 ºC). Asimismo, las transformaciones observadas de silicatos en medio acuoso y la precipitación de silicatos secundarios y carbonatos de calcio tienen un efecto directo en la cementación, relevante para una novedosa gama de cementos no hidráulicos de $CaSiO_3$ que reducen la huella de CO_2.

Cinética y mecanismos de meteorización de piroxenos en condiciones ácidas.

Durante la disolución de los silicatos primarios, habitualmente se desarrollan capas superficiales de sílice amorfa, tambien llamadas capas superficiales de alteración (CSA ó SALs), cubriendo la superficie de los minerales, influyendo enormemente la cinética de las reacciones, dificultando la disolución efectiva de los materiales y, por lo tanto, inhibiendo la liberación de iones alcalinotérreos a la solución para completar la carbonatación. Durante las últimas décadas se han realizado bastantes estudios para discernir los mecanismos que regulan la formación de SALs debido a la relevancia de estas capas en la tasa de disolución y, por lo tanto, la dificultad para la implementación de las técnicas de almacenamiento geológico de carbono mediante estos procesos. Sin embargo, no se conocen bien los mecanismos de formación de estas capas.

En este trabajo, se estudian los estadíos iniciales de la formación de capas de alteración durante la disolución bajo condiciones extremas (pH 1.5) de dos piroxenos de Ca y Mg, augita y diópsido, dos de los minerales más representativos de la corteza terrestre. Las tasas de disolución se midieron a 80 ºC usando por un lado, reactores de flujo, y por otro lado, reactores cerrados. La disolución bajo estas condiciones dio lugar a la formación de abundantes pozos de disolución y a la formación de fracturas debidas a fenómenos de corrosión por estrés ("stress corrosion") en el caso concreto de la augita reaccionada en condiciones de flujo. Los resultado de Micro-tomografía y de microscopía electrónica muestraron un comportamiento completamente distinto entre ambos minerales, y también entre ambos procedimientos experimentales. El reemplazamiento del material de partida por sílice amorfa fue más extenso en condiciones de flujo, y a su vez, mayor en la augita que en el diópsido.

De acuerdo con estos resultados, la formación de las SALs no es congruente con un modelo de interdifusión, pero es perfectamente congruente con un mecanismo de Disolución-Precipitación acoplada (ICDP).

Los resultados obtenidos en este estudio revelan información de vital importancia para su aplicación en estrategias de GCS, en concreto, para la predicción de las tasas de meteorización química de silicatos primarios relevantes en procesos de inyección directa de CO_2, evidenciando la influencia clave que va a tener la mineralogía de la roca almacén.

Controles físico-químicos en la carbonatación de silicatos secundarios de calcio y magnesio.

Pese a los numerosos estudios realizados durante las últimas décadas, el conocimiento sobre los mecanismos de carbonatación en medio acuoso de silicatos primarios siguen siendo muy limitado, especialmente bajo condiciones similares a las que predominan durante las reacciones de meteorización en ambientes naturales (pH cercano a la neutralidad). Este es un enorme hándicap para la modelización y aplicación efectiva de técnicas de CCS.

En esta investigación se han estudiado las reacciones de disolución-carbonatación de cristales de augita y diopsido de 1x1x1 mm en condiciones hidrotermales y en presencia o ausencia de diferentes fuentes de carbonato ($NaHCO_3$ y Na_2CO_3). Se ha observado que los principales productos de reacción son calcita magnesiana y sílice amorfa.

Además, se ha comprobado que se promueve el avance de la reacción por la precipitación de silicatos de sodio (phillipsita-Na) en el caso de la augita alterada en condiciones moderadamente alcalinas y, de silicato de magnesio hidratado (MSH) en el del diopsido reaccionado en condiciones de alta alcalinidad.

Asimismo, se observó la formación de grandes fracturas penetrantes durante el remplazamiento de augita por phillipsita-Na. En todos los casos se consiguió una mayor conversión de la augita (hasta 38 wt%) respecto al diópsido (~15 wt%). Estos resultados implican que la presencia de hierro, aluminio y sodio en la estructura de los piroxenos influye enormemente la liberación de cationes a la solución (debido al aumento de las tasas de disolución) y, por lo tanto, contribuye a la formación de silicatos secundarios cristalinos que provocan una presión de cristalización mayor que la resistencia a la tracción del mineral (o la roca que lo contenga), provocando su fracturación, el incremento del área expuesta a la solución y contribuyendo al progreso de la reacción mediante un mecanismo de retroalimentación

Además, estos resultados son relevantes para el procese de CCS, contribuyendo al diseño de estrategias de mejora de la mineralización de CO_2 y, por lo tanto, a la captura de forma permanente y segura de carbono mediante la precipitación de nuevas fases durante los procesos de disolución-carbonatación de silicatos primarios.

Secuestro de CO_2 simultáneo a la producción de zeolitas y al atrapamiento de elementos tóxicos mediante carbonatación de Cenizas Volantes.

Las cenizas volantes (CFA) son residuos que típicamente se almacenan en vertederos, conllevando importantes riesgos para el medio ambiente debido a su alto contenido en elementos potencialmente tóxicos (PTE). Sin embargo, las CFA son residuos alcalinos alumino-silicatados que ofrecen la posibilidad de la captura mineral de CO_2 y la producción de subproductos económicamente rentables, cómo son las zeolitas.

Hasta la fecha no se ha explorado la posibilidad de combinar de carbonatación y la formación de zeolitas a partir de las CFA, dando lugar al atrapamiento de los PTE presentes en en dicho residuo. En este estudio se muestra que bajo condiciones hidrotermales (150 ºC) y dependiendo de los parámetros seleccionados, tales como cómo pH e iones alcalinos de fondo en soluciones de (bi)carbonatos, se puede conseguir una eficiencia de carbonatación del 79% con una captura neta de CO_2 de 0.045g/kg de CFA, incluso utilizando cenizas de bajo contenido en Ca y Mg (3.72 wt% CaO, 1.74 wt% MgO) de tipo F.

Asimismo, simultáneamente se han obtenido precursores zeolíticos y zeolitas cristalinas (~60 wt%) además del atrapamiento efectivo de los PTE contenidos en las CFA.

Estos resultados tienen importantes aplicaciones para la captura y almacenamiento de carbono, así como para la reutilización y almacenamiento seguro de las cenizas volantes.

Por último y a modo de síntesis, hay que destacar que los los resultados obtenidos en todos los sistemas estudiados y frente a los diferentes parametros explorados (tipo de silicatos, pH, T, pCO_2, electrolitos de fondo, fuentes de carbono inorgánico) muestran que tanto los silicatos de Ca-Mg-Fe naturales cómo los residuos industriales aluminosilicatados (CFA) pueden ser utilizados para la captura efectiva de CO_2. Además, se han sido identificados parámetros clave en el control de la disolución-precipitación que da lugar a silicatos secundarios, junto con carbonatos. Se ha observado que la pasivación de la reacción tiene un impacto directo en las tasas de disolución mineral, impidiendo la carbonatación. Sin embargo, la fracturación mediante presión de cristalización de silicatos secundarios es un efeto clave en la inhibición de la pasivación. Por otro lado, estos efectos pueden verse afectados según los parámetros de reacción en la carbonatación mineral *ex situ*. Asimismo, estos resultados experimentales muestran que la mejora del grado de carbonatación mineral puede alcanzarse durante la GCS en los poros de la roca original si hay elementos alcalinos que favorezcan la precipitación de (alumino)silicatos secundarios de sodio o potasio. Finalmente, se demuestra que la formación de zeolitas durante la carbonatación de cenizas volantes es posible llevala a cabo bajo condiciones hidrotermales. Este proceso no es solo efectivo por la captura de CO_2 sino que además atrapa elementos tóxicos como metales pesados, inmovilizándolos y por lo tanto, impidiendo su liberación y la consiguente contaminación de acuíferos y suelos. Estos resultados muestran que la carbonatación mineral no solo afecta a las estrategias de CCS sino que tiene un impacto directo con el medio ambiente, además de producir fases como las zeolitas y la calcita con numerosas aplicaciones industriales. Esto último refleja que el reciclaje de residuos industriales alcalinos es una forma económica y efectiva de solventar en gran medida el problema asociado a las emisiones antropológicas de CO_2.

Chapter I. Introduction

I.1 Geochemical Carbon Cycle

Natural climate evolution is driven by the concentration of CO_2 in the atmosphere. Periods of elevated CO_2 emissions due to inputs from volcanic activity and decarbonation via subduction of rocks with high carbon content (following eq. I.1) are associated to higher temperatures, and, on the other side, periods of reduced CO_2 emissions are linked to lower temperatures (Shackleton, 2000; Archer, 2008; Zeebe and Caldeira, 2008).

$$CaCO_3 \rightarrow CaO + CO_2 \qquad \text{(I.1)}$$

Walker et al. (1981) was the first to postulate the existence of a negative feedback mechanism including the greenhouse effect of CO_2 and the T dependence of silicate weathering for the long-term stabilization of Earth's surface temperature. According to the IPCC report of 2014, the Carbon Cycle is *the term used to describe the flow of carbon (as carbon dioxide) through the atmosphere, ocean, terrestrial and marine biosphere and lithosphere*. The global carbon cycle plays a regulator role on the Earth's climate over millions of years (Walker et al., 1981; Crowley and Berner, 2001; Prentice et al., 2001; Berner, 2003; Archer, 2008; Hilley and Porder, 2008;

Gislason et al., 2009). This long-term cycle (Figure I.1) includes the exchange of carbon between the rocks and all the systems present in the Earth (atmosphere, biosphere and soils), which contribute to stabilize the climate (Walker et al., 1981; Berner, 1992; Crowley and Berner, 2001; Berner, 2003; Archer, 2008; Matter and Kelemen, 2009).

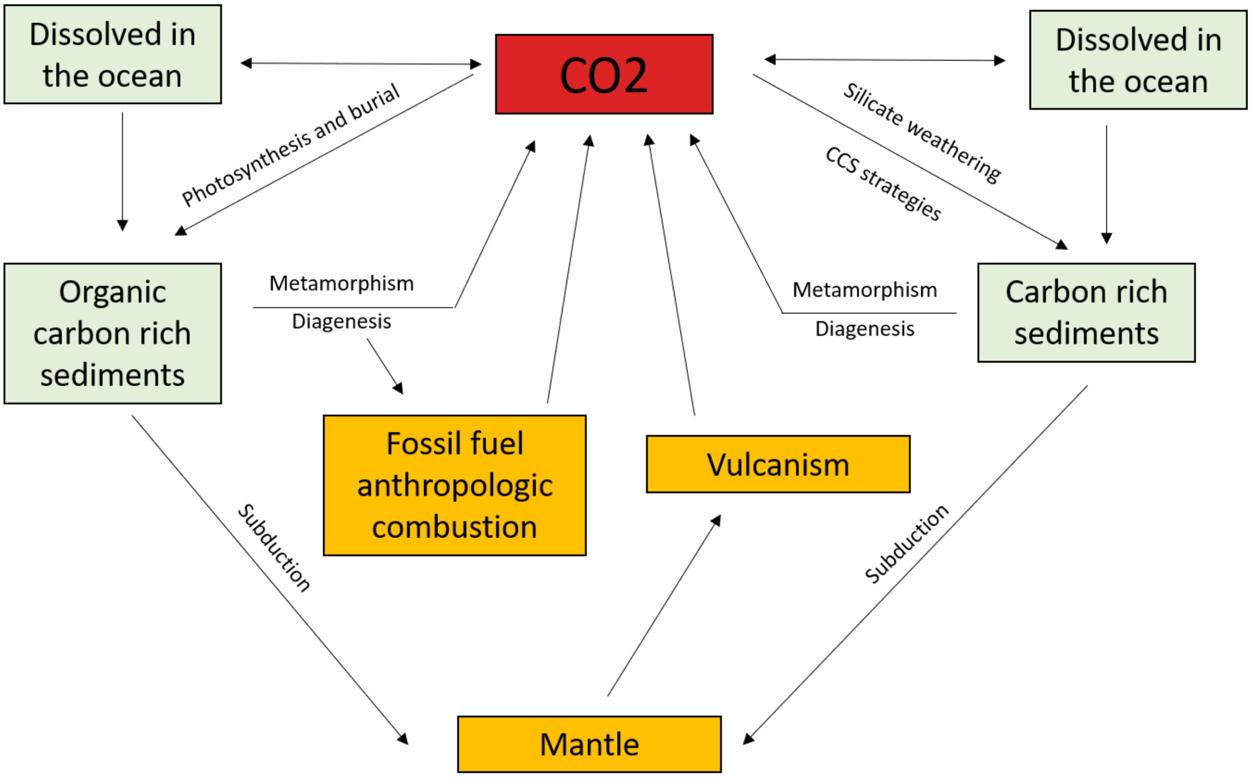

Figure I.1. Simplified model of the carbon cycle.

The carbon cycle consists of two main parts: the organic and the inorganic carbon cycle. Photosynthesis processes, the respiration of animals and bacteria and the burial of organic matter are included in the organic carbon cycle. However, the concentration of atmospheric CO_2 is primarily controlled by the inorganic carbon cycle, also called the *carbonate-silicate cycle*. No oxygen or organic matter is formed during this process (Walker et al., 1981; Kasting, 2019).

The main CO_2 inputs to the atmosphere are (i) the diagenesis of carbon-rich rocks, (ii) volcanism generating a continuous input of 10^{13} mol y^{-1} of C and, during the last two centuries, (iii) the anthropogenic emissions to the atmosphere, mostly caused by fossil fuel combustion and cement production (Walker et al., 1981; Crowley and Berner, 2001; Berner, 2003; Archer, 2008; IPCC, 2014). On the other hand, the uptake for atmospheric CO2 is mainly constituted by the dissolution in the oceans (eq. I.2), plant photosynthesis (eq. I.3) and primary calcium and magnesium silicate weathering (eq.4 detailed in the next section).

$$H_2O + CO_2 \leftrightarrow H_2CO_3 \qquad \text{(I.2)}$$

$$H_2O + CO_2 \leftrightarrow CH_2O + O_2 \qquad \text{(I.3)}$$

The fluxes of CO_2 into the atmosphere emitted by natural processes such as volcano eruptions or diagenesis (“Earth degassing”), have varied over the Earth’s history. This triggers a negative feedback mechanism between the atmospheric CO_2 and primary silicate weathering, whereby an increase in the atmospheric CO_2 causes an increase in temperature and rainfall that in turn accelerates silicate weathering trapping more carbon as stable phases and thus decreasing the concentration of atmospheric CO_2 (Frings, 2019). However, other factors can affect this cycle. Elevated rates of tectonic activity cause a fast physical erosion, while slow uplift rates lead the formation of isolated bedrocks that lower silicate weathering rates (Frings, 2019). Therefore, is a complicate task to disclose how silicate weathering rates have controlled the atmospheric carbon content over geological timescales. Several models have been proposed (e.g. (Berner and Caldeira, 1997; Crowley and Berner, 2001; Berner, 2003; Berner, 2006; Foster et al., 2017; Frings, 2019; Frings and Buss, 2019). Nevertheless, it is widely accepted that silicate mineral weathering plays a critical role on climate control and the habitability of the Earth’s Surface.

I.1.1 Silicate weathering and CO_2 mineralization

Mineral weathering is an irreversible thermodynamic process that causes the alteration of the mineral phases on the Earth's surface (Frings and Buss, 2019 and references therein). This process is responsible for the release of solutes to ecosystems representing the first step of the biogeochemical cycles of most elements, including the C cycle. Furthermore, primary silicates are the major components of the Earth's crust and, silicate weathering, one of the most important processes that regulates atmospheric CO_2 concentrations over millions of years (Casey et al., 1988; Banfield et al., 1995; Hilley and Porder, 2008). As mentioned above, high levels of atmospheric CO_2 cause the development of vegetation, accelerating silicate weathering and therefore, decreasing CO_2 concentration in the atmosphere (Walker et al., 1981; Crowley and Berner, 2001). The mineralization of CO_2 via carbonation of primary silicates is a natural process that actively contributes to the geochemical carbon cycle and the regulation of the Earth's climate over geologic timescales (Walker et al., 1981). It can be summarized using the Urey reaction (Urey, 1952):

$$MSiO_3 + CO_2 \leftrightarrow CaCO_3 + SiO_2 \qquad \text{(I.4)}$$

where M is an alkaline earth metal (i.e., Ca^{2+}, Mg^{2+}) or a divalent transition metal (i.e., Fe^{2+}). This reaction has been extended to ultramafic rocks and pyroxenes in the form of the more specific equation (Damien Daval et al., 2009a):

$$M_xSi_yO_{x+2y-t}(OH)_{2t} + xCO_2 = xMCO_3 + ySiO_2 + tH_2O \quad (I.5)$$

This, added to the huge representation of mafic and ultramafic rocks (i.e. with high olivine and pyroxene content), highlights the key role of calcium and magnesium-rich basic and ultrabasic rocks in the climate control (Schott et al., 1981; Knauss et al., 1993; Berner and Caldeira, 1997; Berner, 2003; Daval et al., 2009b; Schott et al., 2012).

Urey's reaction is composed by some parallel reactions that can be simplified as:

1. Carbon dioxyde dissolution :

   $$CO_2 + H_2O \rightarrow H_2CO_3 \quad (I.6)$$

2. Carbonic acid dissociation:

   $$H_2CO_3 \rightarrow HCO_3^- + H^+ \quad (I.7)$$

   $$HCO_3^- \rightarrow CO_3^{2} + H^+ \quad (I.8)$$

3. Silicate dissolution:

   $$MSiO_3 + 2H_2O \rightarrow M^{2+} + H_4SiO_4 + ½O_2 \quad (I.9)$$

4. Precipitation of secondary silicates (silica):

   $$H_4SiO_4 \rightarrow SiO_2 + 2H_2O \quad (I.10)$$

5. Precipitation of carbonates:

   $$M^{2+} + CO_3^{2-} \rightarrow MCO_3 \quad (I.11)$$

High CO_2 atmospheric concentration periods causes a greenhouse effect in the surface of the Earth, rising the global *T* and therefore, increasing the rates of silicate weathering and carbonation, resulting in the decrease of atmospheric CO_2 and the global *T* in the surface. In turn, glacial periods entail a decrease in the silicate weathering, causing an increase in the CO_2 concentration due to vulcanism and decomposition of carbon rich sediments and therefore, a gradual increase in the surface *T* (Walker et al., 1981; Brady and Carroll, 1994; Crowley and Berner, 2001). However, as mentioned above, silicate weathering, despite of the high CO_2 uptake capacity (~8 x 10^{18} mol of carbon per million years) is not the only mechanism that regulates Green House Gases (GHGs) emissions to the atmosphere from natural sources as volcanism or metamorphism. Other processes such as CO_2 dissolution in the oceans (eq. 2), organic matter burial in sediments as a hydrocarbon source, and plant photosynthesis (eq. 3), contribute to the regulation of atmospheric carbon concentration are displayed in Figure 1 (Berner, 1992; Crowley and Berner, 2001; Berner, 2003). Thus, the geochemical carbon cycle is able to control the natural emissions of GHGs to the atmosphere. However, the rates of anthropogenic emissions of CO_2 to the atmosphere are hundreds of times higher than those of natural emissions, and for this reason, new techniques must be employed to mitigate their huge environmental impact.

I.1.3 Anthropogenic GHG emissions

To determine the effect of anthropogenic CO_2 emissions to the atmosphere it is important to understand the role of natural silicate weathering at regulating the CO_2 concentration in the atmosphere over geological timescales. It is crucial to shed light on the actual climate behavior and also, to develop geomimetic initiatives to regulate the current imbalance of carbon in the atmosphere caused by anthropic activities.

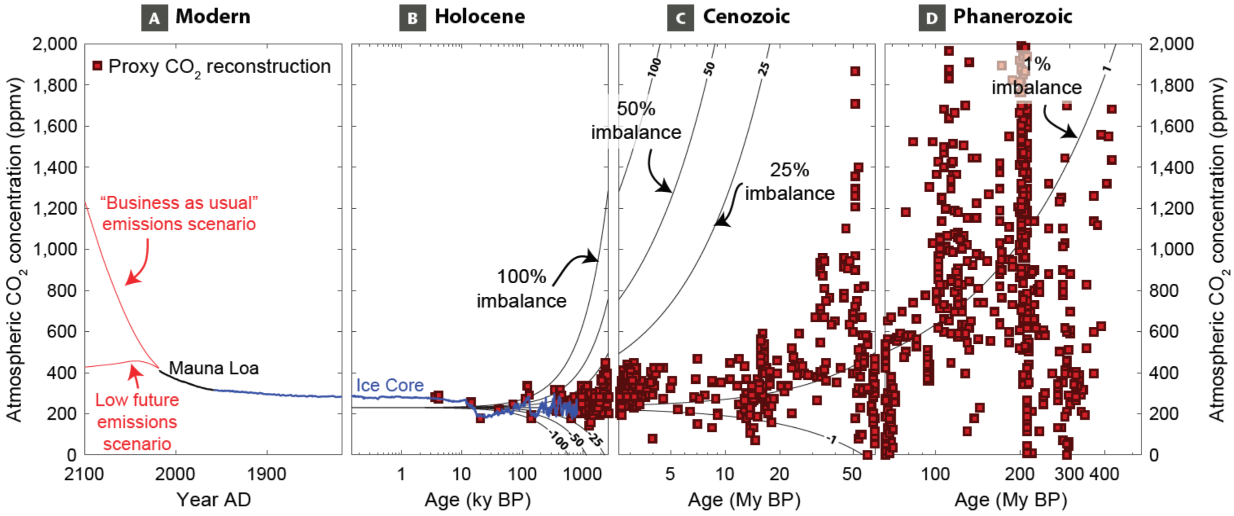

Figure I.2. Reconstructed atmospheric CO_2 from the Phanerozoic and deviation of this value from an average late-Quaternary value expected for ±1%, 25%, 50% and 100% imbalances between silicate weathering and Earth carbon emissions. ppmv = parts per million by volume. Taken from (Frings, 2019) based on the work performed by (Foster et al., 2017).

Figure I.2 represents the theoretical evolution of atmospheric CO_2 if the rates of carbon sequestration through primary silicate weathering and carbon inputs to the atmosphere differ. It can be observed that an imbalance of even 100% between CO_2 inputs and silicate weathering would have small an effect on atmospheric CO_2 concentration in the short term (10 to 100 years). However, an imbalance of 1% between both mechanisms on million-year timescales would be totally devastating and lead to a greenhouse or icehouse periods (Berner and Caldeira, 1997; Foster et al., 2017; Frings, 2019; Frings and Buss, 2019).

Berner and Caldeira (1997) also showed the effects of imbalances between CO_2 inputs and outputs into the atmosphere. If, for example, a 25% imbalance is established, after millions of years the excess or fault of CO_2 would inhibit the presence of life on Earth as it is known (Berner and Caldeira, 1997). In this framework, inputs of CO_2 before the industrial revolution (ca. 1750) were related mainly to volcanic activity and weathering of carbon rich sediments, both organic and inorganic sediments, resulting in a CO_2 concentration of 280±10ppm (Prentice et al., 2001; Berner, 2003; Archer, 2008). However, after the industrial revolution, levels of greenhouse gases (GHG), and in particular of carbon dioxide, suffered an exponential increase due to anthropogenic emissions worldwide. Between 1750 and 2011, the anthropogenic cumulative CO_2 emissions to the atmosphere reached 2040±310 Gt CO_2-eq. In 1970 levels of GHG emissions to the atmosphere were ~27 Gt CO_2-eq according to the IPCC report of 2014. Nowadays, an input of ~49GtCO_2-eq/yr is released to the atmosphere by industrial processes. In this context, coal combustion is the second energy source most used worldwide, with a consumption of 1.4 billion tons in 2018, 4% higher than the previous year (IPCC, 2014). It accounts for more than 30% of the global yearly anthropogenic CO_2 emissions, being a key contributor to climate warming and the associated changes in the oceans and atmosphere equilibrium. Here, it is currently experiencing an imbalance of two orders of magnitude between the primary silicate weathering rates and the CO_2 inputs to the atmosphere. This means that about the 50% of the GHGs emissions to the atmosphere have occurred in the last 40 years (Figure I.3).

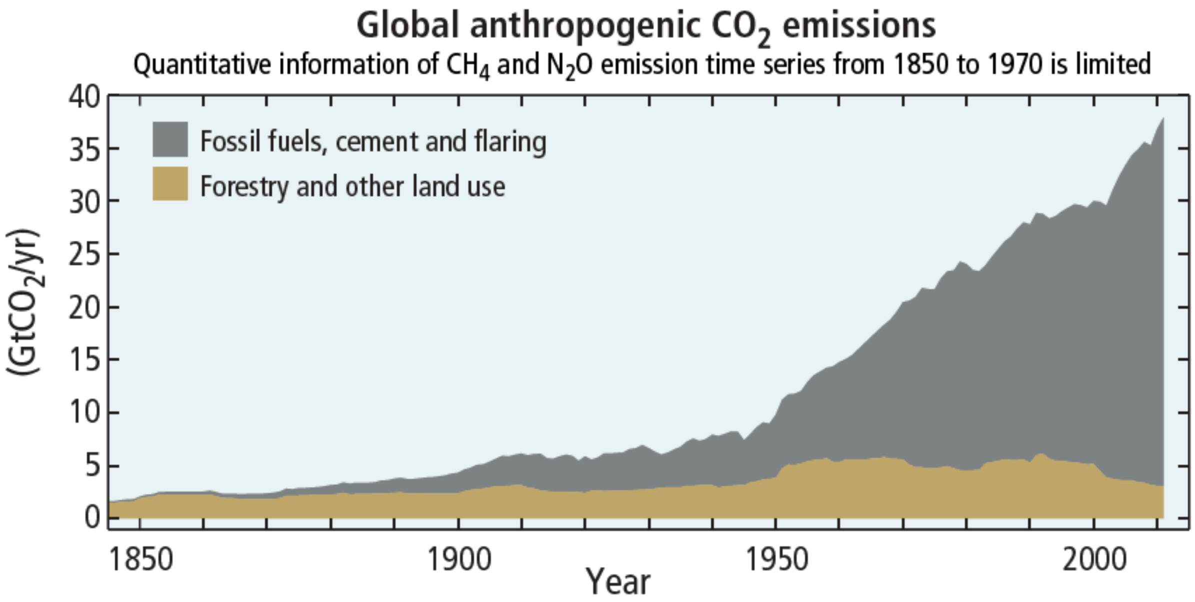

Figure I.3. Global anthropogenic emissions from fossil fuel combustion, cement production and flaring, forestry and other land use. Taken from IPCC 2014.

As mentioned above, high concentrations of CO_2 in the atmosphere entail an increase in global *T* and therefore, an increase in the rate of silicate weathering to balance the output of this GHG (Walker et al., 1981; Crowley and Berner, 2001). However, the geochemical carbon cycle cannot cope with the anthropologic imbalance of CO_2 inputs and thus, a progressive increase in the global *T* is expected with a decrease in the average precipitation (IPCC, 2014) (Figure I.4). The predictions of *T* and precipitations for the next 80 years foresee a warm and dry age due to the anthropogenic emissions of GHGs, causing an environmental disaster.

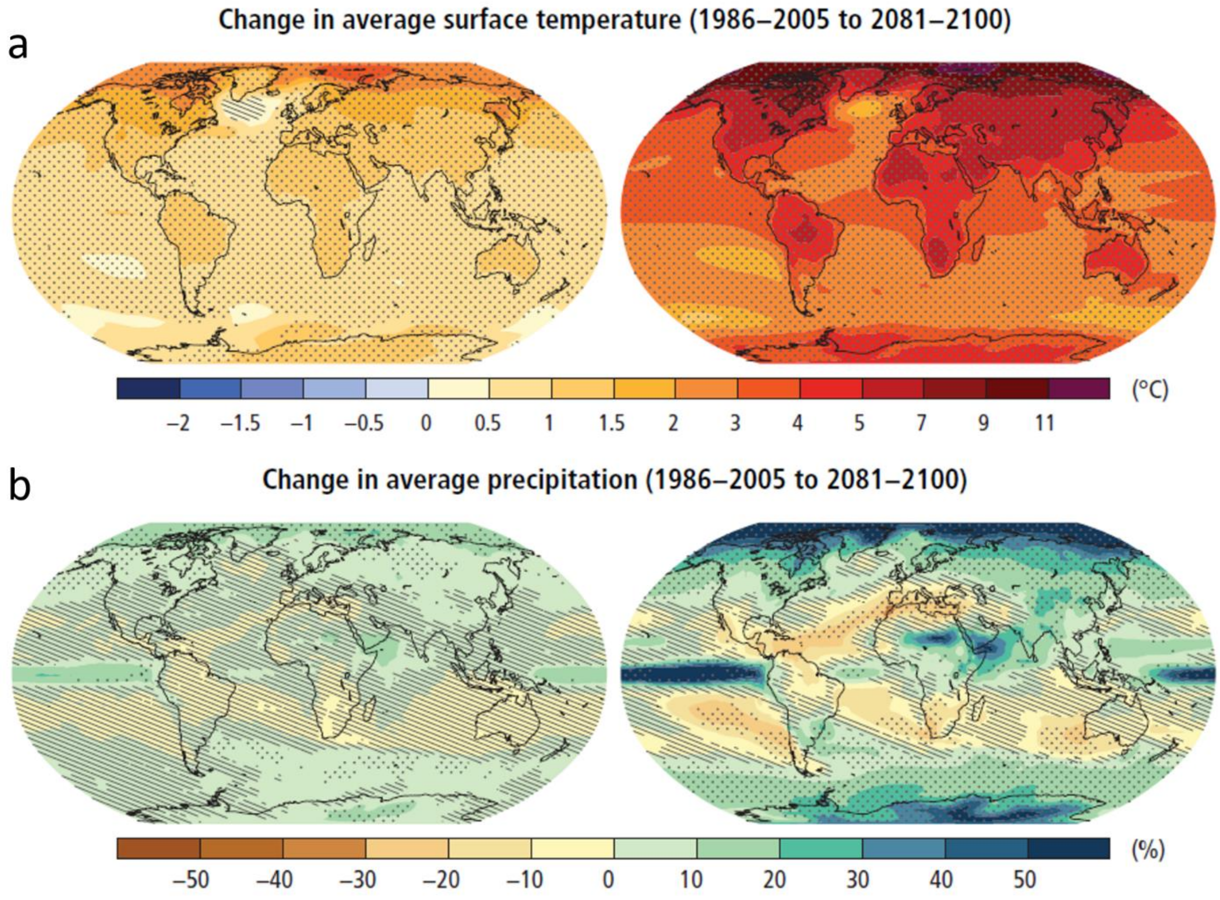

Figure I.4. Change in the average surface temperature (a) and precipitation (b) of the Earth (taken from IPCC 2014).

One way to prevent this negative impact is to minimize the use of traditional energy sources, such as fossil fuels, thus reducing CO_2 anthropogenic emissions. A significant reduction in the current anthropogenic CO_2 emissions is, however, highly unlikely, as the actual socio-economic context relies on the use of fossil fuels as primary energy source and many key industrial processes such as cement production deliver huge amounts of CO_2 into the atmosphere (IPCC, 2014). A strategy to decrease the emissions of this greenhouse gas should involve capturing of CO_2 emitted from stationary sources. Collecting CO_2 from emitting sources is still easier and cheaper than its direct capture from the atmosphere (Lackner, 2009), despite recent progress on functionalized membrane filters and metal organic frameworks (MOFs) that can absorb CO_2 directly from the air (Sumida et al., 2011; Boyd et al., 2019). In any case, CO_2 capture is still challenging because separation of gas mixtures (required for collection from both stationary sources and directly from the atmosphere) using existing technology is very expensive (Sumida et al., 2011). Several authors have prompted initiatives for carbon capture and storage (e.g.Berner, 1992; Pacala and Socolow, 2004; Marini, 2006; Cole and Oelkers, 2008; Oelkers et al., 2008; Gislason et al., 2009; IPCC, 2014; Leung et al., 2014; Zhang and Depaolo, 2017)

I.2 Carbon Capture and Storage (CCS)

Carbon Capture and Storage (CCS) strategies comprise a whole range of processes for CO_2 capture (post-combustion, pre-combustion and oxyfuel combustion), separation, transport, storage and monitoring of this GHG (Cole and Oelkers, 2008; Boot-Handford et al., 2014; Leung et al., 2014; Snæbjörnsdóttir et al., 2020). In addition, CCS strategies have an important role in achieving the objectives of the Paris Agreement of 2015 to reduce the anthropogenic warming to 1.5-2 ºC (United Nations Framework Convention on Climate Change, 2015).

Although there is no insurmountable technological barrier, the huge amounts of CO_2 that should be stored once captured either during *in situ* (i.e., at point emission sources) or *ex situ* (i.e., within geological formations) CCS represent another significant challenge. Several initiatives had been proposed that would allow maintaining the actual use of fossil-fuel sources whilst avoiding the CO_2 emissions to the atmosphere, including the use of ionic liquids as alternative solvents for CO2 capture at point sources, calcium looping, or the use of low temperature adsorbents (i.e. zeolites, MOFs) (Boot-Handford et al., 2014). But the problem exist regarding what to do with captures CO_2. In this respect, several possibilities have been explored. Currently, enhanced oil recovery projects are the largest number of operational large-scale CCS projects, where CO_2 is used to retrieve the remaining oil (Global CCS Institute, 2018). According to the Kyoto Protocol of 1997, *geological sequestration is the capture of* CO_2 *directly from anthropogenic sources and disposing of it deep into the ground for geologically significant periods of time* (Bachu, 2002). This approach, also called Geological Carbon Storage (GCS) into deep porous rocks (Boot-Handford et al., 2014), consists on the injection of gaseous, liquid or supercritical CO_2 into deep underground reservoirs (e.g. sedimentary porous rocks as saline aquifers, depleted oil and gas fields), where CO_2 can be physically trapped below an impermeable cap rock (structural trap), dissolved in groundwater, trapped in pores and bubbles (capillary trap) or reacted with the host rock to form stable carbonate minerals (mineral trapping) (Oelkers et al., 2008; Boot-Handford et al., 2014; Snæbjörnsdóttir et al., 2020). However, the limitations of this technique are manifold. First, the efficacy of the cap rock could be modified by several factors (i.e. tectonic processes) causing the migration of the gas to the surface. Secondly, seismicity can be induced due to the pressure increase of the reservoir (e.g., Castor Project, Castellón, Spain). Finally, mineral trapping could be limited by the absence of divalent metal-bearing silicates (i.e. Ca/Mg bearing silicates), necessary for the carbonation reactions.

Alternative GCS methods to overcome the above-described limitations of the geological storage of CO_2 into deep porous rocks have been developed. A promising large scale solution to this problem is the GCS via mineralization of CO_2 (Seifritz, 1990b; Pacala and Socolow, 2004; Oelkers et al., 2008; Daval et al., 2009a; Kelemen, P. B., Matter, J., Streit, E. E., Rudge, J. F., Curry, W. B., & Blusztajn, 2011; Boot-Handford et al., 2014; Leung et al., 2014). Among the different CCS strategies, CO_2 mineralization through the replacement of silicate minerals by carbonates, the so-called **mineral carbonation** (Seifritz, 1990a; Oelkers et al., 2008), seems to offer the best perspectives from the point of view of: (i) safety, as the interaction between silicate minerals and aqueous inorganic carbon does not involve the leaking of a buoyant phase as may occur, for instance, following injection of supercritical CO_2 into depleted oil and gas reservoirs, (ii) long term stability, as the relatively low solubility of carbonate minerals formed during silicate carbonation ensures a durable disposal, and (iii) substrate availability, as silicate minerals are the most abundant constituents of the Earth upper crust (Lackner, 2002; Cole and Oelkers, 2008; Oelkers et al., 2008; Lackner, 2011; Sanna et al., 2014; Di Lorenzo et al., 2018).

I.2.1 GCS via Mineral Carbonation

Geological Carbon Storage strategies based on mineralization of CO_2 via dissolution-carbonation primary silicates and following the Equations I.4 and I.5 can be divided in two categories: in situ and ex situ strategies.

I.2.1.1 In situ Strategies

In situ GCS strategies involve the deep injection of CO_2 in gaseous, liquid or supercritical state into mafic or ultramafic silicate rocks (e.g. basalts and peridotites). In contrast to GCS via injection of CO_2 in porous sedimentary rocks, the captured CO_2 is stored in reactive rocks composed principally of divalent metal-bearing silicates (Ca^{2+}, Mg^{2+} or Fe^{2+}) such as olivine, augite, diopside or wollastonite, for its mineralization into calcite ($CaCO_3$), magnesite ($MgCO_3$) or dolomite ($CaMg(CO_3)_2$) (Tai et al., 2006; Daval et al., 2009c; Sanna et al., 2014; Zhang and Depaolo, 2017; Di Lorenzo et al., 2018; Snæbjörnsdóttir et al., 2020). The reactive solution, with a very low pH (3-5), promotes the dissolution of the silicate minerals with a subsequent pH increase and the release to solution of divalent cations, which react with the dissolved CO_2 to form stable carbonates phases following reactions 16 to 18 (Seifritz, 1990a; Lackner et al., 1995; O'Connor et al., 2005; Huijgen et al., 2006; Oelkers et al., 2008; Di Lorenzo and Prieto, 2017; Di Lorenzo et al., 2018; Snæbjörnsdóttir et al., 2020). Previous reports have estimated the time to fully convert CO_2 to carbonate minerals during primary silicate carbonation in ~2 years (i.e. average of different primary silicate minerals reaction rate) (Matter et al., 2016). Temperature range of these reactions is between 65 ºC and 300 ºC (Park and Fan, 2004; Daval et al., 2009b; Daval et al., 2009c; Kelemen, P. B., Savage, H., & Hirth, 2013; Di Lorenzo and Prieto, 2017; Di Lorenzo et al., 2018; Monasterio-Guillot et al., 2019; Snæbjörnsdóttir et al., 2020). Successful examples of *in situ* mineral carbonation are the cases of CarbFix (Island) and Wallula (USA) projects. Currently, these two plants are the only field-scale projects of mineral carbonation. In the CarbFix project the CO_2 produced on the geothermal power plant of Hellisheidi is injected into basic and ultrabasic basalt rocks (45-49% SiO_2) and hyaloclastites of olivine-tholeiite composition. The current CO_2 trapping rate is 12 Gton y^{-1} with the aim to capture 33 Gton y^{-1} of CO_2 in 2030.

I.2.1.2 Ex situ Strategies

Among the *ex situ* strategies to capture and mineralize the CO_2, aqueous mineral carbonation is a more promising approach than gas-solid or liquid-gas carbonation methods (Sanna et al., 2014; Di Lorenzo et al., 2018). In the aqueous mineral carbonation processes, silicate dissolution has been generally considered to be the rate-limiting step (Park and Fan, 2004; Hellmann et al., 2012; Ruiz-Agudo et al., 2012; Sanna et al., 2014; Ruiz-Agudo et al., 2016; Snæbjörnsdóttir et al., 2020). A reduction in the grain size (< 300 µm) results in an increase in the surface area and consequently, an increase in the dissolution rate of the mineral (Sanna et al., 2014). Regarding the temperature conditions to enhance mineral dissolution-carbonation reactions, several studies revealed an optimum temperature range of 150-200 ºC independently of the stirring rate, while the CO_2 pressure (P_{CO_2}) has been directly correlated with the yield of carbonation reactions (Huijgen et al., 2006; Marini, 2006; Cole and Oelkers, 2008; Oelkers et al., 2008; Sanna et al., 2014; Peuble et al., 2015; Zhang and Depaolo, 2017).

The use of organic acids in direct processes has been explored to enhance the dissolution of the primary silicates by the decrease in pH or the formation of complexes with cations at the mineral surface. The use of acetic, oxalic, citric, EDTA (ethylenediaminetetraacetic acid) and aspartic acids have been evaluated in previous works (Drever and Stillings, 1997; Yanagisawa, 2001; Pokrovsky et al., 2009; Sun et al., 2012; Sanna et al., 2014). Despite the low effect on dissolution-carbonation rates of primary silicates during the attack with strongly acid pHs, the effect on moderately-acid to neutral pH was higher as compared to the low pH conditions. However, their implementation at a large scale is difficult due to their cost and the complicated recycling.

Most *ex situ* strategies include the pre-treatment of the mineral prior to the carbonation reaction. This pre-treatment can be mechanical (grinding of the starting material), chemical (activation by additives) or thermal (heating) (Sanna et al., 2014). Despite the fact that intense grinding and/or heat activation of the silicate materials enhance the carbonation reaction, also entails a high energy cost (Lackner et al., 1995; Huijgen and Comans, 2005; Oelkers et al., 2008; Sanna et al., 2014), so chemical activation is preferred.

Furthermore, during the dissolution-carbonation of natural calcium and magnesium silicates, the formation of amorphous silica-rich surface layers has been described as a handicap of the effective carbonation of primary silicate minerals due to the passivation of the unreacted silicate surface

(Schott et al., 1981; Casey et al., 1988; Schott and Oelkers, 1995; Ruiz-Agudo et al., 2012; Hellmann et al., 2013; Encarnación Ruiz-Agudo et al., 2016; Daval et al., 2017; Wild et al., 2019).

Ex situ mineralization processes have been applied to alkaline waste materials from the coal, metallurgic and mining industries and municipal wastes (Querol et al., 1997b; Siriwardane et al., 2005; Jones et al., 2006; Montes-Hernandez et al., 2009; Wee, 2013; Jha and Singh, 2016; Tamilselvi Dananjayan et al., 2016). In particular, coal combustion produces huge amounts of waste products (coal combustion products, CCP), which include coal fly ash, CFA (representing ca. 70 % of the total CCP) (Bhatt et al., 2019), bottom ash, boiler slag, and fluidized bed combustion wastes (Blissett and Rowson, 2012; Wee, 2013). The global production of CFA during 2012 was over 700 million tons (Mt) (Blissett and Rowson, 2012; Wee, 2013), and this figure kept growing in recent years (Ji et al., 2017).

A promising two step mineral-carbonation method was proposed by Park and Fan, (2004), which consists first on an acid-promoted dissolution step where Ca^{2+} and Mg^{2+} are released to the solution, and subsequently an increase in pH to precipitate Fe oxides which are removed by filtration and finally, the bubbling of CO_2 into the alkali-earth metal-rich solution to obtain stable carbonate phases (Park and Fan, 2004). The final solution is normally able to be recycled.

.

I.3 Management of Coal Combustion Wastes

Management of the huge amounts of CFA wastes produced globally is a significant problem, with important economic, health, and environmental implications (Blissett and Rowson, 2012). Worldwide, ca. 70% of CFA wastes are disposed of in ash ponds or landfills, the rest being recycled for several applications (Wee, 2013). Only in the U.S., 34 Mt of CFAs were generated in

2016 (Anon, n.d.; IPCC, 2014), of which 20 Mt were used mainly as a construction material (e.g., concrete products, blended cements, road base) due to its puzzolanic activity or in mining applications; still, 14 Mt of CFAs were discarded and disposed in ponds or used in landfilling (Anon, n.d.). In addition to the huge area needed to store or dispose of CFA (Dwivedi and Jain, 2014), this waste contains significant amounts of potentially toxic trace elements (PTE)(Querol et al., 1997b; Álvarez-Ayuso et al., 2003; Moreno et al., 2005) which may limit its recyclability and make CFA spilling or leaching a hazard which may lead to contamination of soils, water bodies and groundwater (Ruhl et al., 2010; Catalano et al., 2012; Yang et al., 2015; Harkness et al., 2016; Brandt et al., 2019).

In addition to its use in construction, other reutilization processes for CFA waste include (i) synthesis of zeolites (Höller and Wirsching, 1985; Lin and Hsi, 1995; Querol et al., 2002) and (ii) to a lesser extent, carbon capture and storage (CCS) via accelerated mineral carbonation (Thomas and Matthews, 1992; Ecke, 2003; Back et al., 2008; Montes-Hernandez et al., 2009; Wang et al., 2010; Chang et al., 2011; Tamilselvi Dananjayan et al., 2016). Zeolites are microporous crystalline aluminosilicates formed by corner-sharing tetrahedral groups conforming voids and channels that allow the adsorption of gases, metal ions and organic molecules (Lin and Hsi, 1995; Querol et al., 1997b; Querol et al., 1997a; Steenbruggen and Hollman, 1998; Murayama et al., 2002). Due to their pore characteristics and high ion exchange capacity (Inglezakis and Grigoropoulou, 2001), CFA-derived zeolites are employed for CO_2 and other pollutant gases capture, removal of toxic metals, water decontamination, and soil improvement (Lin and Hsi, 1995; Singer and Berkgaut, 1995; Moreno et al., 2001; Querol et al., 2002; Lee and Jo, 2010). The synthesis of zeolites from CFAs has focused on the use of NaOH (and KOH) in hydrothermal, alkali fusion, or microwave-assisted processes (Querol et al., 2002). A few works have evaluated the use of alkali carbonate activators for zeolite hydrothermal synthesis (120 °C), reporting a limited zeolite yield but, interestingly, resulting in calcium carbonate precipitation (Murayama et al., 2002). The latter suggests that the combined carbonation and zeolite synthesis using CFA is feasible. Although several works have shown that zeolites formed after CFA can be used to capture PTE (Lin and Hsi, 1995; Querol et al., 2002), no study has evaluated the actual trapping of PTE present in the CFA used for zeolite synthesis.

Despite the limited foreseen contribution of CFA to mineral carbon sequestration (~7.6 Mt/CO_2/y) (Georgakodopoulos et al., 2016) its use for CCS must be considered as it could contribute to the reduction in the C footprint of coal-fired power plants (Anon, n.d.; Montes-Hernandez et al., 2009; IPCC, 2014), it would result in the production of an economically-valuable by-products such as carbonates and zeolites, and in a reduction of the potential leaching of PTE during CFA disposal (Montes-Hernandez et al., 2009). Previous works have evaluated the carbonation efficiency and net CO_2 capture capacity of CFAs from different sources and with different compositions under a range of conditions (e.g., direct and indirect carbonation, dry vs. wet processes, pH, *T*, solid/solution ratios, aqueous solution composition, pCO_2) (Pan et al., 2012; Wee, 2013). These studies show that carbonation efficiency values are typically <<80% (Bauer et al., 2011; Ji et al., 2017), and the net CO_2 capture can be as low as ~8 kg per ton of CFA. With a few exceptions (CFAs with CaO + MgO > 20 wt%, Moreno et al., 2005; Back et al., 2008; Bhatt et al., 2019), the average CaO content in CFA is 7±3 wt% (Pan et al., 2012), resulting in relatively low values of effective CO_2 mineral capture. The limited carbonation efficiency and relatively low net CO_2 capture capacity have been strong handicaps for the widespread implementation of CCS strategies for CFA. Several recent studies have focused on ways to improve carbonation efficiency values (Ji et al., 2017; Ji et al., 2018). However, progress in this direction has been limited, mostly because the mechanisms of CFA carbonation are not fully understood. For instance, it has been assumed that only the easily leached crystalline phases containing calcium (e.g., CaO and $Ca(OH)_2$) were able to feed the solution for CFA carbonation (Back et al., 2008; Montes-Hernandez et al., 2009). However, a significant fraction (≥50%) of CaO (and MgO, which can also contribute to CO_2 mineralization) in CFA is present in the not-so-easily leachable amorphous aluminosilicate phase, which typically accounts for ≥70 wt% of CFA (Moreno et al., 2005). It is thus necessary to better understand the carbonation mechanisms of CFA and to explore means to effectively leach the Ca and Mg present in such amorphous phase in order to achieve the highest possible carbonation efficiency. Moreover, no work has evaluated the potential of CFA carbonation as a means to achieving an effective CCUS by the simultaneous production of valuable zeolite by-products, while trapping PTE.

All the above mentioned processes are regulated by thermodynamic and kinetic factors that controls the feasibility and the

I.4 Reactions between minerals and aqueous solutions

The thermodynamic driving force that controls the dissolution and the precipitation of any mineral phase is the saturation index (SI) or supersaturation (Ω) that can be calculated as:

$$SI = log\frac{IAP}{K_{sp}} = \log \mathbf{\Omega}$$

$$\ln \mathbf{\Omega} = \frac{\Delta G}{\mathrm{R}T}$$

(I.12)

where ΔG is the free energy difference of the reaction, R is the molar gas constant, T is the temperature (Kelvin), IAP is the Ion Activity Product of the species and K_{sp} is the solubility product of a particular solid specie. Dissolution is expected when $SI<0$, while precipitation can occur if $SI>0$. The solution is at the equilibrium when $IAP = K_{sp}$ and then SI=0.

I.4.1 Kinetics and Thermodynamics of mineral dissolution-precipitation

The dissolution of a mineral A_aB_b can be described by the equation:

$$A_aB_b \leftrightarrow aA^{c+}_{(aq)} + bB^{d-}_{(aq)} \tag{I.13}$$

The change in free energy of the process is given by:

$$\Delta G = \Delta G_0 + \mathrm{R}T\left(\frac{\{A^{c+}\}^a_{aq}\{B^{d-}\}^b_{aq}}{\{A_aB_b\}_s}\right) \tag{I.14}$$

where ΔG_0 is the change in free energy of the process at standard state conditions. For a solid, $\{A_aB_b\}_s = 1$. At the equilibrium, $\Delta G = 0$ and the equation can be written as:

$$\Delta G_0 = -RT\ln\left(\{A^{c+}\}^a_{aq}\{B^{d-}\}^b_{aq}\right)_{eq} \tag{I.15}$$

$\{A^{c+}\}^a_{aq}\{B^{d-}\}^b_{aq}$ is the solubility product (K_{sp}) of the mineral A_aB_b.

However, reactions in the field are slower than predicted due to several factors such as (i) the effect of aging of the mineral surfaces, caused by the fast disappearance of the high energy lattice defects of the crystals, or from the passivation of secondary phases coating (Daval et al., 2010; Hellmann et al., 2012; Ruiz-Agudo et al., 2012; Encarnación Ruiz-Agudo et al., 2016; Ruiz-Agudo et al., 2017), (ii) the presence of solutes with inhibiting effect (Schott and Oelkers, 1995) or (iii) the proximity of the saturation index to the equilibrium during mineral-fluid reactions (Daval et al., 2010).

A general formula derived from the Transition State Theory (TST) and the Principle of Detailed Balancing (PDB) has been postulated to link the thermodynamics to the kinetics that regulate the dissolution-precipitation mechanism during mineral reactions (Lasaga, 1995; Dove and Han, 2007):

$$r = k \cdot \left\{1 - exp\left(\frac{\Delta G}{\mathrm{R}T}\right)\right\}^n = k \cdot \left\{1 - exp\left(\frac{IAP}{\mathrm{K}_{sp}}\right)\right\}^n = k \cdot \{1 - exp(\Omega)\}^n \tag{I.16}$$

where r is the rate of the reaction (mol.m^{-2}s^{-1}), k is the dissolution rate constant and the exponent n is the order of the reaction, which does not need to be an integer, and n values typically > 1 have been related to the control of surface defects on dissolution (Dove and Han, 2007; Ruiz-Agudo et al., 2017). This equation has some shortcomings when describing dissolution kinetics. For instance, it does not consider the different reactivity of different (*hkl*) crystal faces. Several studies have demonstrated that the reactivity changes between the different faces of a crystal (e.g. Lüttge et al., 2013; King et al., 2014). Another key factor affecting dissolution kinetics is the formation of Si-rich surface altered layers covering the minerals. This results in an apparent incongruent behaviour during dissolution, where the relations between the fluxes of the elements in the mineral are different to those in the solid. The mechanism of formation of these Si-rich layers is still under debate (see section I.3.1).

I.4.2 Surface Altered Layers (SALs) or Amorphous Silica Surface Layers (ASSLs).

Surface altered layers (SALs) are amorphous silica-rich layers formed at the solid-liquid interface during the interaction of alumino-silicate materials (e.g. wollastonite, forsterite, labradorite, diopside, glass) and aqueous solutions (Hellmann et al., 2013; Wild et al., 2019). The development of SALs have been reported since decades during silicate dissolution processes (e.g. Casey et al., 1988; Casey, 1990; Schott and Oelkers, 1995; Cole and Oelkers, 2008; Ruiz-Agudo et al., 2012; Schott et al., 2012; Hellmann et al., 2013; Ruiz-Agudo et al., 2016; Daval et al., 2017). It is generally considered that these layers significantly reduce the dissolution rate of primary silicates, hampering the contact between the solution and the unreacted mineral surface and thus decreasing the effective release of alkali-earth metals to the solution. As a consequence carbonation of silicates according to eq. (5) is inhibited (Oelkers et al., 2008; Daval et al., 2011; Ruiz-Agudo et al., 2012; Hellmann et al., 2013; Encarnación Ruiz-Agudo et al., 2016; Wild et al., 2019).

Factors governing the formation of SALs are still unknown. Two main mechanisms have been suggested for the formation of SALs. A first set of studies claims that SALs form upon the incongruent or non-stoichiometric dissolution of silicate minerals, related to the preferential release of calcium and/or magnesium compared to silicon, which creates an alkali-earth metal depleted layer (Schott et al., 1981; Casey et al., 1988; Casey et al., 1989; Casey, 1990; Knauss et al., 1993; Schott et al., 2012). However multiple experimental observations reported during the last decade have questioned the validity of this model, suggesting that SALs form by precipitation from a fluid layer at the mineral-solution interface where strong compositional gradients develop at the interface between the substrate and the solution upon the congruent or stoichiometric dissolution of the mineral (Putnis, 2009; Ruiz-Agudo et al., 2012; Putnis, 2014; Ruiz-Agudo et al., 2014; Ruiz-Agudo et al., 2016).

I.4.2.1 Models of SALs formation

I.4.2.1.1 Solid-state interdiffusion mechanism

A widely accepted model for the formation of the amorphous silica-rich layers suggests that SALs form by a solid-state interdiffusion mechanism of protons and cations. According to this model, it is a pH-independent reaction that leads to a preferential release of divalent cations (Ca, Mg or Fe) in the mineral structure to the solution (incongruent or non-stoichiometric dissolution), resulting in the formation a cation depleted and silicon enriched layer at the mineral-fluid interface (Schott et al., 1981; Schott and Berner, 1985; Casey et al., 1988; Casey et al., 1989; Casey, 1990; Knauss et al., 1993; Banfield et al., 1995; Schott and Oelkers, 1995; Schott et al., 2012). This preferential “leaching” of alkaline earth metals to the solution causes the formation of a proton-enriched leached layer that polymerizes, increasing the connectivity of the silica layer and reducing leaching rate (Casey, 1990; Schott et al., 2012).

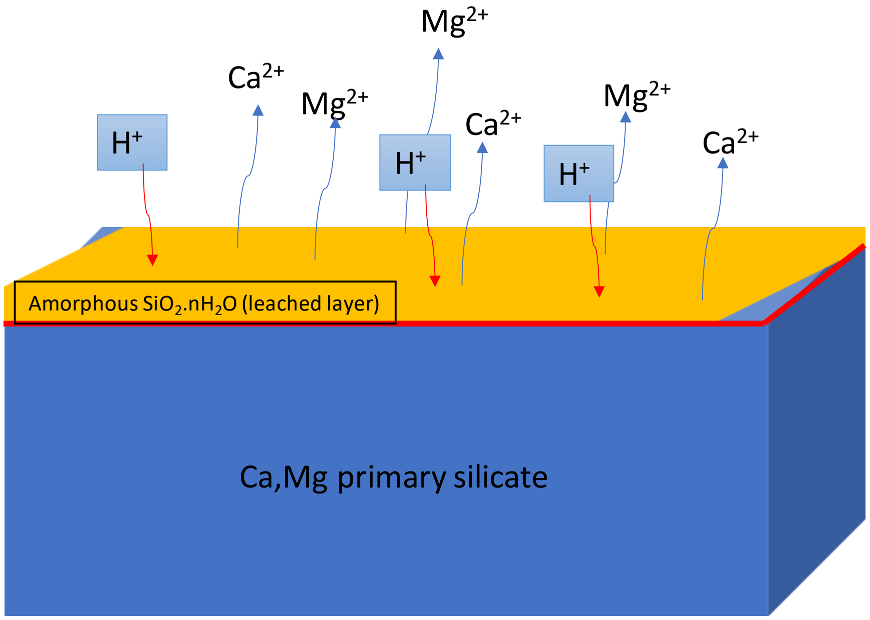

Figure I.5. Schematic representation of cation depletion and hydroxylation of a mineral surface during mineral dissolution

This model is mostly based on the observation that the elemental molar ratios measured in the bulk solution during laboratory-scale dissolution experiments are different to those in the solids, and the (apparently) diffusional elemental profiles measured in the solid surface after the reaction. In this model, the main factor that controls the non-stoichiometric release of cations has been reported to be the difference on the bond strengths of different cations exposed to hydrolysis in acid solution during far-from-equilibrium conditions (Pokrovsky and Schott, 2000). This may help to explain the observation that chain silicates (e.g. wollastonite) have more tendency to form leached layer than, for instance, nesosilicates (e.g. forsterite) (Casey, 1990; Schott et al., 2012).

I.4.2.1.2 Dissolution-Precipitation process

More recent experimental evidence supports a model whereby SALs form by an interface-coupled, dissolution-precipitation process. This evidence arises from Atomic Force Microscopy (AFM), Transmission Electron Microscopy (TEM) and X-Ray Reflectivity (XRR) analyses (Hellmann et al., 2013; Ruiz-Agudo et al., 2016; Wild et al., 2019). In this model the release of cations is congruent, but coupled to the precipitation of amorphous silica from a fluid layer at the mineral-solution interface where strong concentration gradients develop so that supersaturation with respect to amorphous silica is reach. This occurs despite the fact that the bulk solution remains undersaturated with respect to amorphous silica (Hellmann et al., 2003; Ruiz-Agudo et al., 2012; Ruiz-Agudo et al., 2014; Ruiz-Agudo et al., 2016; Di Lorenzo et al., 2018; Monasterio-Guillot et al., 2019). This model explains the fast kinetics of this process, not achievable by a (interdiffusion) solid-state mechanism, and has been experimentally proved by tracing with Raman the distribution in SALs of oxygen isotopes added in the reaction solution.. Thus, these authors propose an interface-coupled dissolution-precipitation mechanism (ICDP) (Putnis, 2009) for the formation of silica coatings during silicate dissolution.

I.4.2.1.3 Mineral replacement by an interface-coupled dissolution-precipitation mechanism

Mineral replacement reactions in the Earth’s crust and mantle are commonly considered to take place by solid-state mechanisms (e.g. Abart et al., 2009; Petrischeva and Avart, 2016). Pseudomorphic mineral replacements characterized by structural similarities, interfacial strength and elastic anisotropy have been explained by a solid state mechanism (Abart et al., 2009). However, the slow rates ascribed to these reactions suggests geological timescales to complete the replacements. The ubiquitous presence of fluids during mineral-replacement reactions and the faster reaction rates observed in laboratory and in the field, have questioned a solid-state transformation mechanism and makes necessary to consider another replacement mechanism. It is also known that even a few ppm of water in the system increases substantially the reaction rates (Putnis, 2014). Experimental observations have demonstrated that the mechanisms of mineral reequilibration processes in aqueous solution are described by a two-step process in which (i) the mineral surface began to dissolve, releasing ions to the solution, and (ii) the increase in the concentration of ions in the fluid in the vicinity of the mineral surface results in such fluid to become supersaturated with respect to a secondary phase, allowing its precipitation. These two processes are coupled at the mineral-fluid interface and when the coupling occurs at the nano- or microscale, a pseudomorphic process takes place (Figure I.6).

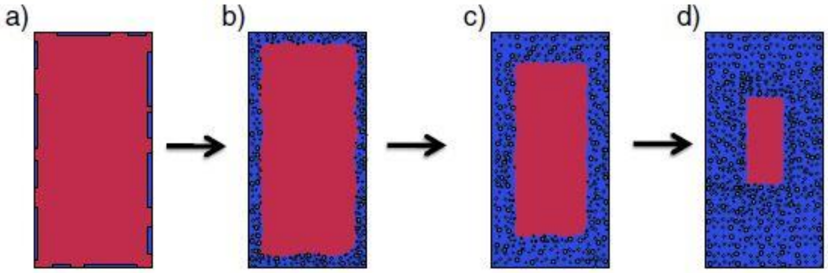

Figure I.6. Conceptual representation of an ICPD reaction (taken from Ruiz-Agudo et al. 2014)

The kinetics of these coupled reactions depend on pH, temperature, ionic strength or activity products. During mineral replacement processes, strong compositional gradients at the mineral-fluid interface are developed (Putnis, 2009; Ruiz-Agudo et al., 2017), which allow supersaturation with respect to the product phase to be reached within the boundary layer, while the bulk solution remains undersaturated (Ruiz-Agudo et al., 2012; Putnis, 2014; Ruiz-Agudo et al., 2016; Ruiz-Agudo et al., 2017). Also, in an ICDP mechanism, the crystallographic information can be transferred from the substrate to the product via epitaxial growth, provided that a structural matching between parent and precipitated phase exists (Putnis, 2009; Putnis, 2014; Ruiz-Agudo et al., 2016).

For an ICDP mineral replacement reaction to progress, it is necessary that new phase presents porosity, and hence permeability, which allows the continuous access of the fluid to the parent phase. The generation of this porosity depends on the differences between the relative molar volume and the relatively solubility of parent and product phases. If more volume is precipitated than dissolved, a non-porous layer will take place that would passivate the surface reaction (Hellmann et al., 2012; Ruiz-Agudo et al., 2012; Hellmann et al., 2013; Ruiz-Agudo et al., 2016; Wild et al., 2019). However, replacement processes can involve a volume increase during the precipitation of the secondary phase in a confined volume. This effect, in many cases could be the precursor of a huge stress in the pores and fractures where the newly-formed phase is precipitating, also called as "crystallization pressure" than , if it exceed the tensile strength of the host material provoke the fracture of the parent phase, which in turn, increases permeability and exposes fresh reactive surface area (Scherer, 1999; Putnis and Putnis, 2007; Emmanuel and Ague, 2011; Kelemen, P. B., Savage, H., & Hirth, 2013). Fracture generation via crystallization pressure generation has been reported during hydration (serpentinization) of olivine (Müntener, 2010; Kelemen and Hirth, 2012; Lafay et al., 2018), carbonation processes (Matter and Kelemen, 2009; Kelemen, P. B., Matter, J., Streit, E. E., Rudge, J. F., Curry, W. B., & Blusztajn, 2011; Kelemen et al., 2011). Moreover, reaction-driven fracturing has also been associated with weathering-realted mineral dissolution resulting in volume decrease and collapse (Jamtveit et al., 2000).

Altogether, these replacement processes are key factors during primary silicate minerals weatering, acting as passivators and/or catalysts of the dissolution-carbonation reaction and therefore, controlling the safe, effective and permanent capture of CO_2 during mineral carbonation.

As in the case of SALs, carbonation studies of primary silicates have reported passivation due to the formation of a carbonate mineral coating on the primary mineral surface, decreasing the porosity and the permeability of the starting material and limiting the progress of reaction (O'Connor et al., 2005; Kelemen and Hirth, 2012, Ruiz-Agudo et al. ongoing) (O'Connor et al., 2005; Stockmann et al., 2008; Kelemen et al., 2011; Kelemen and Hirth, 2012). This effect plays a critical role in GCS processes, controlling the dissolution rate of silicate materials and acting as a handicap to the effective CO_2 mineralization of primary silicate minerals (McGrail et al., 2006; Stockmann et al., 2008; Daval et al., 2009b; Daval et al., 2009c; Daval et al., 2010; Kelemen et al., 2011; Ruiz-Agudo et al., 2012; Encarnación Ruiz-Agudo et al., 2016; Daval et al., 2017; Wild et al., 2019).

I.4.3 Fracture formation during mineral-replacement reactions

Two mechanisms had been proposed to explain fracture generation during mineral replacement reactions. On the one hand, the precipitating mineral can exert stress on the pore walls leading to fracture of the host rock which in turn, increases the permeability and reactive surface area (Scherer, 1999; Emmanuel and Ague, 2011; Kelemen et al., 2011; Schiro et al., 2012; Kelemen and Hirth, 2012; Kelemen, P. B., Savage, H., & Hirth, 2013). On the other hand, Jamtveit et al. (2000) explored the idea that fracture generation was caused by the solid volume decrease taking place during mineral weathering.

It is widely accepted that porosity and permeability are key parameter in the progress of replacement reactions (Putnis and Putnis, 2007; Cole and Oelkers, 2008; Oelkers et al., 2008; Putnis, 2009; Emmanuel and Ague, 2011; Ruiz-Agudo et al., 2017). Even nanometre-size pores in a host material can strongly influence mineralization by increasing the specific surface area (Simon Emmanuel, 2009; Emmanuel and Ague, 2011). A critical parameter affecting the pore-scale reactions during dissolution-carbonation processes is the pore size-controlled solubility (PCS) of a mineral phase. A dissolution process that starts in the pores of a host rock will eventually reach the equilibrium with respect to the dissolving phase in these pores, and if a microfracture lead to the transport of this solution to larger pores, this fluid phase will be supersaturated with respect to the dissolving phase and therefore, will precipitate (Simon Emmanuel, 2009; Emmanuel and Ague, 2011). The opposite case is also possible, where a fluid goes from large pores to small pores, the solution will become undersaturated and will dissolved the host material. So it can be infer that pore size is one of the key parameters that influence crystallization in pores and the pore dimensions limit the maximum value of the supersaturation with respect to a specific phase (Simon Emmanuel, 2009). Rijniers at al., (2005) also demonstrated that pressure is a relevant factor in the saturation index of a given phase, changing totally in confined spaces such as pores, as compared to the bulk solution.

The crystallization pressure (Δp) exerted by a given phase during nucleation and growth in a porous material can be expressed using poroelasticity theory as:

$$\Delta p = \frac{3K\varepsilon_f}{b\phi_e} \tag{I.17}$$

where *K* is the bulk modulus of the host material, ε_f is the linear strain, $b = (1\text{-}K/K_m)$ is the *biot* coefficient, *Km* is the bulk modulus of the matrix and ϕ_e is the local volume fraction of the material. Therefore, the local crystallization pressure related to the effective stress can be written as:

$$P \cong b\phi_e \, \Delta p = 3K_{\varepsilon f} \tag{I.18}$$

According to Scherer (1999), when a crystal grows within a pore, it causes fractures on the host material when the crystallization pressure excerted by the newly-formed phases is higher than the tensile strength of the porous material; i.e. $P>\sigma_T$. . The nucleation and growth of newly-formed phases in the pores continues despite the first fracture formation due to a liquid film, or a mineral-fluid interface sustained between the crystal and the pore-wall or crack-wall which allows the growth of the newly formed phase and the stablishment of a disjoining pressure that enables the transmission of stress to the pore wall, further opening the cracks. The presence of such a fluid film (a few nm thick) can in theory also enable the progress of dissolution via an ICDP mechanism (Putnis, 2009) after new cracks open and propagate.

However, more processes have been proposed that result in crack generation. Fracture formation by a decrease in volume as a consequence of a replacement reaction has been studied by Jamtveit et al. (2000). Also, the idea that the stress associated with the volume expansion occurring during a replacement reaction in a confined area increases the permeability of a host rock has been studied for the case of olivine hydration and carbonation, and also for chemical weathering reactions (Jamtveit et al., 2000; Jamtveit Bjørn, Putnis Christine V., 2008; Iyer et al., 2008; Jamtveit et al., 2008; Røyne et al., 2008; Müntener, 2010; Kelemen, P. B., Matter, J., Streit, E. E., Rudge, J. F., Curry, W. B., & Blusztajn, 2011; Kelemen et al., 2011; Kelemen and Hirth, 2012; Gadikota et al., 2014). All these works were motivated by the ubiquitous presence of serpentine or magnesite in the micro- and macro-scale veins observed both in the field and in the laboratory experiments, such as brecciated textures in outcrops filled by secondary materials. Calculated values for the crystallization pressure exerted by the newly formed phases during olivine hydration and carbonation exceeds 300 MPa), enough to exceed the tensile strength of the host rock and generate fractures, even under lithostatic pressures corresponding a few km deep into the earth crust (Kelemen and Hirch, 2012). Thus, it is possible that, during the course of a dissolution-carbonation reaction, fractures generate in the substrate as a result of the differences in the precipitated and dissolved volumes and as a result of crystallization pressure. This would on the one hand, counteract the passivating effected exerted by SALs and/or carbonate layers and on the other hand, increase the the reactive surface area to enhance the carbonation reaction.

Altogether, these factors controls carbonation of primary silicates and industrial wastes.

I.5 Research goal

The ultimate goal of this Thesis is to unravel the mechanisms of dissolution and carbonation of Ca and Mg silicates to obtain a way to mineralize CO_2 in an effective, safe and permanent mode and apply all the gained knowledge to sequester CO_2 using industrial wastes, while at the same time reutilizing them, giving an added value to these materials. For this reason, it is critical to obtain an in-depth understanding of the factors that govern silicate dissolution and the mechanism of silicate carbonation, as well as the effect that reaction-driven fracturing might play on these processes.

This main goal is developed in five specific objectives, which are outlined in the following section.

I.6 Main and Specific objectives

There are five main objectives in this Thesis that are developed according to the dissolution and carbonation mechanisms that take place during Carbon Capture and Storage strategies via Geological Carbon Storage mechanisms.

I.6.1 Effect of pH and specific background electrolytes in the progress of the carbonation reaction of primary silicates for ex situ carbonation

The current knowledge regarding the effects of key variables such as pH, carbonate speciation and background electrolytes on the progress of dissolution-carbonations reactions of primary calcium and magnesium silicates is still incomplete. For instance, many silicate carbonation experiments are performed using Na or K (bi)carbonate salts (O'Connor et al., 2004; Béarat et al., 2006; Tai et al., 2006; Gerdemann et al., 2007; Chizmeshya et al., 2008; Daval et al., 2009a,b; King et al., 2010; Stockmann et al., 2013; Zhao et al., 2013; Gadikota et al., 2014; Di Lorenzo et al., 2018), but the role of the alkali metal ions on the progress of the carbonation reaction is not well-known (Gadikota et al., 2014; Wang and Giammar, 2012; Eikeland et al., 2015). Similarly, when CO_2-aqueous solutions react with silicate minerals during *in situ* GCS, no background alkali metal ions might be first present in the (initially) low pH (e.g., pH 3.8-4.0) injection fluid (Matter et al., 2016). Upon mixing of the CO_2-aqueous solution with (typically) alkaline and often saline pore waters, as well as upon reaction with the host rock, release of a range of metal cations, including alkali metal ions (e.g., K^+ and Na^+) and a pH rise occur (Matter et al., 2016). The presence of background ions (not directly involved in carbonate precipitation) on the progress of the carbonation reaction of primary silicate minerals are, however, not well known.

In relation to that, a **first specific objective (developed in Chapter III)** of this Thesis is improving our understanding of **the effect of background electrolytes** during CCS via silicate mineral carbonation. With this purpose, it has been studied the role of Na^+ and K^+ by the presence/absence of ion-bearing carbonates (Na (bi) carbonates and K (bi) carbonates, and ion-bearing hydroxides KOH and NaOH) in the dissolution-carbonatoion of a highly reactive silicate, pseudowollastonite (CaSiO3), under hydrothermal experiments (150 ºC). Additionally, CO_2 direct injection experiments using the same calcium silicate were performed using KCl and NaCl as background electrolytes sources to gain knowledge on the different effects of these ions depending on the carbon source.

The **second specific objective (Chapter III and V**) of this Thesis is to evaluate **the effect of the pH during carbonation reactions of primary silicates**. For this purpose, and as mentioned above, different hydrothermal reactions were carried out under near-neutral to moderately-alkaline pH using carbonates and bicarbonates (i.e. lower initial pH) sources, on the one hand, using pseudowollastonite (Chapter III), and on the other hand, using less reactive primary silicates (diopside ($CaMgSi_2O_6$) and augite ($(Ca, Mg, Fe^{2+})_2Si_2O_6$), Chapter V), two calcium and magnesium primary silicates of the group of pyroxenes, one of the most abundant group of rock-forming minerals in the Earth's crust (Deer et al., 1966; Schott et al., 1981; Knauss et al., 1993). Many of the studies aimed at unravelling the mechanisms of dissolution-carbonation reactions have used wollastonite ($CaSiO_3$) as a model system due to its fast dissolution rate, relatively simple structure and chemical composition (Banfield et al., 1995; Weissbart and Rimstidt, 2000; Green and Luttge, 2006; Daval et al., 2009a; Ruiz-Agudo et al., 2012; Schott et al., 2012; Daval et al., 2013; Ruiz-Agudo et al., 2016). Comparatively, minerals with lower reactivity and more abundant on the Earth's crust such as those clinopyroxenes investigated here, have been poorly studied

(Morimoto, n.d.; Schott and Berner, 1985; Knauss et al., 1993; Brady and Carroll, 1994; P Richet et al., 1998; McGrail et al., 2006; Dixit and Carroll, 2007; Stockmann et al., 2008; Zakaznova-Herzog et al., 2008; Daval et al., 2010). Consequently, mineralogical and compositional analyses of reacted samples and the changes in the replacement reactions were evaluated.

Finally, the **third specific objective** (Chapter III and V) of this Thesis is to determine **the effect of secondary phases formation during carbonation reactions of primary silicates.** To fill the current gap in knowledge, X-ray (X-ray diffraction and micro-Computed Tomography) in addition to Infrared spectroscopy and electron microscopy analyses were carried out in the reaction products to explore the consequences of secondary phases formation not contemplated in the Urey's reaction model (Eq. 4).

I.6.2 Mechanism of the acidic weathering of silicate materials and the formation of passivation layers.

The dissolution of primary silicates reportedly results in the development of amorphous silica layers coating the surface of the minerals. Although early studies suggest that these layers form by a mechanism in which alkali-earth metals are preferentially released to the solution and exchanged for H^+ by a diffusion-reaction forming a cation-depleted surface layer (Casey et al., 1988; Casey et al., 1989; Banfield et al., 1995; Schott and Oelkers, 1995; Weissbart and Rimstidt, 2000; Schott et al., 2012), an increasing number of studies are reporting experimental evidence showing that SALs formed by an interface-coupled dissolution–precipitation mechanism (Daval et al., 2009b; Zhang and Lüttge, 2009; Daval et al., 2010; Hellmann et al., 2012; Ruiz-Agudo et al., 2012; Daval et al., 2013; Wild et al., 2016; Wild et al., 2019).

Therefore, the **fourth specific objective** of this Thesis is to gain some insights on **the actual mechanisms of pyroxene dissolution and SALs formation at low pH and the effect of the hydrodynamic conditions**. To achieve this objective, it has been further evaluated the mechanism of SALs formation performing acidic weathering experiments in laboratory by submerging single crystals of diopside and augite in stagnant and flowing acidic solutions ($pH = 1.5$) for 10 h, and comparing their IR spectral characteristics and their microscopic physical and chemical properties using scanning and transmission electron microscopy and micro-tomography.

I.6.3 Coal Fly Ash (CFA) carbonation and zeolite formation

The recycling of waste materials produced from coal combustion, CFA in particular, has received an increased interest for zeolitic transformation and carbonation strategies. However, strong handicaps have been found for the implementation as an effective CCS strategy using CFA, due to the assumption that only the Ca-crystalline containing phases (e.g. $Ca(OH)_2$) were able to feed the solution with alkaline-earth metals, causing a highly limited carbonation yield. Therefore, the **fifth specific objective (Chapter VI)** of this investigation is to **disclose the key features of CFA carbonation under mild hydrothermal conditions using alkaline (bi)carbonate solutions, combined with the formation of zeolites and the effective capture of PTE present in CFA**. Here, it has been applied and evaluated the effectiveness of the GCS treatments developed in the previous sections of this Thesis to the case of aluminosilicate-rich CFA waste to enhance its recycling.

Chapter II. Materials and methods

While materials and experiments performed in each chapter of this PhD thesis are different and therefore, described in detail in each corresponding chapter, most of the analytical techniques used in the whole research are basically the same. For this reason, detailed explanation of the techniques used in all chapters are described here.

II.1 Starting materials

II.1.1 Pseudowollastonite powder (Chapter III)

Pseudowollastonite (psw) has monoclinic structure ($C2/c$) and is formed by alternate stacking of ternary [Si_3O_9] tetrahedral rings and distorted-bicapped Ca octahedra along [001] (Yang and Prewitt, 1999). It presents several polytypes (Yamanaka and Mori, 1981), being the 4-layer the most common one (Ingrin, 1993). The other polymorphs of $CaSiO_3$ are wollastonite-1T, which has a triclinic structure ($P\bar{1}$) formed by [SiO_4] tetrahedral chains running along [010], cross-linked by apical tetrahedral oxygen to octahedrally-coordinated Ca (Seryotkin et al., 2012), and is a common mineral in the upper crust (Deer et al., 1997); and wollastonite-2M (or parawollastonite, (Seryotkin et al., 2012)), which has a monoclinic structure ($P2_1/a$) formed by two layers of [SiO_4] tetrahedral chains combined with two Ca layers (Seryotkin et al., 2012). Despite being a very rare mineral in natural environments (i.e., it forms in paralavas during pyrometamorphism triggered by hydrocarbon combustion) (Seryotkin et al., 2012), psw was used in this study as a model $MSiO_3$ silicate due to several reasons. First, it is a commercial synthetic phase, which can be obtained in high purity (>99%, the main impurities being Al and Mg). Second, it is one of the most soluble silicate minerals in neutral to alkaline solutions, as shown in Figure 1, where the moles of silicate mineral dissolved at equilibrium (calculated using PHREEQC computer model, see Methods section) are plotted as a function of solution pH (maintained constant by the addition of the proper amount of HCl or NaOH). Additionally, the dissolution of psw is kinetically favored: at pH 2 and 25 °C, its dissolution rate is $10^{-8.1}$ $mol \cdot cm^{-2} \cdot s^{-1}$, while that of wollastonite-1*T* is $10^{-11.5}$ $mol \cdot cm^{-2} \cdot s^{-1}$ (Bailey, A., & Reesman, 1971; Banfield et al., 1995 and references therein; Schott et al., 2012). The purity of synthetic psw in combination with its high reactivity and facility towards dissolution-precipitation have enabled its successful use as a bioactive material for bone implants (Aza and Aza, 2000).

Sieved crystals (ø < 74 µm) of synthetic pseudowollastonite were obtained from Sigma-Aldrich with a chemical purity higher than 99 %. The mineralogical characterization of the starting material was carried out by X-ray diffraction (XRD) and the obtained pattern was compared with the pattern calculated by HighScore Xpert Plus computer code (PANalytical) from the psw crystallographic information file (.cif) (Yang & Prewitt, 1999). All the observed reflections could be attributed to the monoclinic structure of α-CaSiO3. Nevertheless, the presence of trace amounts of rankinite (~ 1 wt%) was detected.

II.1.2 Pyroxene single crystals (Chapter IV and V)

The primary silicate materials used in this work are diopside ($Ca_{0.97}Mg_{0.84}Fe_{0.17}Si_2O_6$), with monoclinic structure (C2/c) and augite $Na_{0.05}Ca_{0.86}Mg_{0.76}Fe_{0.23}Ti_{0.07}Al_{0.3}Si_{1.7}O_6$, with monoclinic structure (C2/c) (Figure II.1). These two pyroxenes were cleaved in fragments (1 x 1 x 1mm in size, ~0.005g weight), polished with diamond paste and cleaned in ethanol.

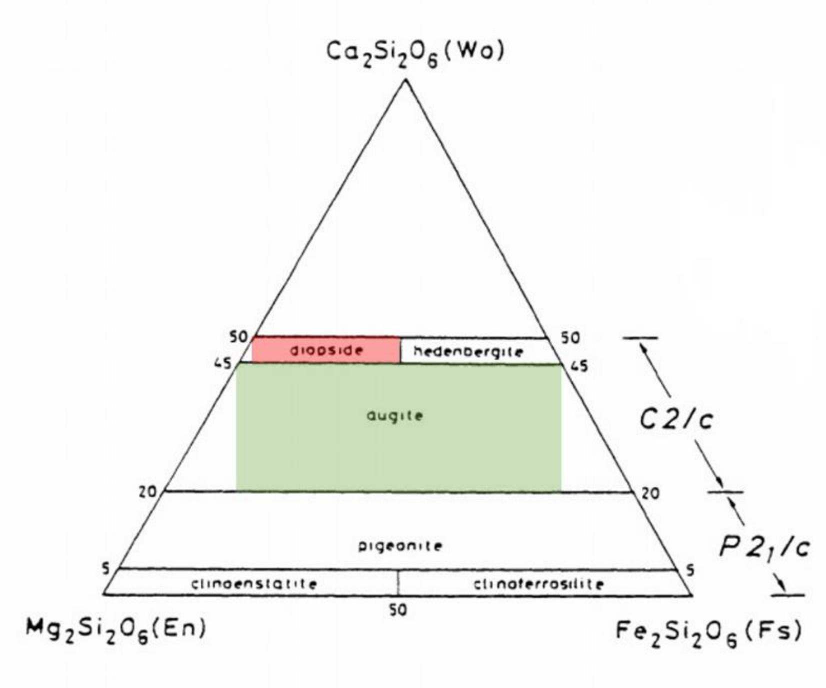

Figure II.1. Ternary diagram showing compositional range of diopside (red) and augite (green) and its relation to other pyroxenes (modified from Morimoto, et al. 1989)

The mineralogical characterization of the starting materials was carried out by X-ray diffraction (XRD) and the obtained pattern was compared with the pattern included in the Joint Committee for Powder Diffraction Standards (JCPDS) PDF-2 database by HighScore Xpert Plus diffraction software (PANalytical). All the observed reflexions were attributed to the pure minerals phase. Furthermore, chemical composition of each mineral was revealed by ICP-OES (see below for specific characteristics).

These two minerals were chosen due to their abundance in mafic and ultramafic rocks and their relatively lower dissolution rate as compared with other Ca/Mg silicates commonly used for the investigation of dissolution kinetics under far-from-equilibrium conditions and subsequent carbonation for GCS strategies (Figure II.2).

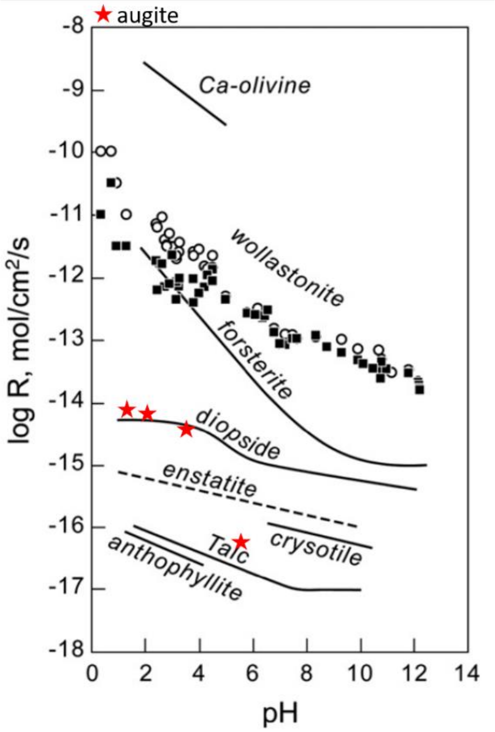

Figure II.2. Comparison of dissolution rates of Ca/Mg silicates vs. pH (room T). Red stars corresponds to augite dissolution rate data from (McAdam et al., 2008). Scheme modified from (Schott et al., 2012).

II.1.3 Coal Fly Ash powders (Chapter VI)

The coal fly ash used in this report was provided by Compostilla thermal power plant, in León, Spain. It is a fine powder composed principally by spherical particles. Detailed characterization is presented in Chapter VI.

II.1.2 Experimental methods for the study of dissolution and carbonation reactions

II.1.2.1 Hydrothermal batch reactors

In this work, two types of hydrothermal reactors were used to compare and evaluate the role of initial pH on silicate carbonation: (i) stain steel reactors (V_{max} = 3mL) with PTFE (polytetrafluoroethylene) capsules inside, used for silicate dissolution-carbonation batch experiments, adding or not a source of Dissolved Inorganic Carbon (DIC), and (ii) titanium reactors for the direct injection of CO_2, used to study carbonation processes (described below).

Batch hydrothermal reactors. In the case of the study reported in Chapter 3 (dissolution and carbonation of pseudowollastonite), experiments involved the addition of 1 mL of the different solutions described below to PTFE vessels containing 0.5 g of psw (0.0043 mol) and different solutions depending on the aim of the experiments, dissolution (D) or carbonation (C). The former involved the aqueous dissolution of psw in the absence of any dissolved inorganic carbon (DIC), whereas the latter involved dissolution and subsequent carbonation of psw (i.e., precipitation of calcium carbonate phases) in the presence of DIC. For the hydrothermal dissolution and carbonation experiments, different experimental solutions were prepared: (D1) 1 mL of Mili-Q water (resistivity 18.2 MΩ·cm, Millipore) adjusted to pH 12 using NaOH (Sical); (D2) 1 mL of Mili-Q adjusted to pH 12 using KOH (Sigma-Aldrich); (D3) 1 mL of water and 0.251 g of sodium chloride (NaCl, Sigma-Aldrich), pH = 7; (C1) 1 mL of H_2O and 0.361 g of sodium bicarbonate ($NaHCO_3$, Sigma-Aldrich), with a pH = 9; (C2) 1 mL of Mili-Q water and 0.456 g of sodium carbonate (Na_2CO_3, Panreac), with a pH of 12.8 calculated using PHREEQC; (C3) 1 mL of H_2O and 0.2623 g of potassium bicarbonate ($KHCO_3$, Sigma-Aldrich), with a pH of 9.4; and (C4) 1 mL of H2O and 0.594 g of potassium carbonate (K_2CO_3, Sigma-Aldrich), with a calculated pH of 12.7. Calculated pH values were in good agreement with experimental pH values (despite the uncertainty of experimental pH measurements for such highly alkaline solutions; see below). Note that sodium chloride and sodium or potassium (bi)carbonate reactants were dosed at a concentration of 0.0043 mol/ml, to match the molar concentration of dosed pseudowollastonite. Molar concentration used in this work was 0.0043 $mol.mL^{-1}$ to match the molar concentration of dosed psw.

In the case of the studies reported in chapters IV and V (dissolution and carbonation of pyroxenes), fragments of augite or diopside were introduced in the PTFE vessels with 1mL of Milli-Q water adjusted to different pHs depending on the purpose of the experiments. In the case of chapter IV, water was adjusted to pH 1.5 using HCl, and for the chapter V, Milli-Q water was adjusted to pH 7.5 adjusted with NaOH (Sigma-Aldrich) for the hydrothermal dissolution experiments, and to pH 7.5 using 0.025 g of $NaHCO_3$ (Sigma-Aldrich) or pH 11.5 using 0.031 g of Na_2CO_3 (Sigma-Aldrich) for carbonation experiments.

Finally, in chapter VI (dissolution and carbonation of CFAs), 0.5g of CFA were introduced in 1mL of Na_2CO_3, $NaHCO_3$, K_2CO_3 and $KHCO_3$ solutions prepared using ultrapure water and 97%-grade solid reactants from Sigma-Aldrich.

In all cases, the absence of calcium, magnesium and silicon in the input solutions ensured a far-from-equilibrium conditions with respect to the original materials at the beginning of the experiments. Note also that all the experiments were performed with a constant mole ratio between total inorganic carbon and reactant materials.

After sealing the reactors, they were heated up to 80 ºC or 150 °C for different periods of time, ranging from 10 h to 40 days. Each experiment was repeated two or three times to ensure reproducibility. At each preset elapsed time, the reactors were cooled down to room T and opened; the solid products and liquid supernatant were subsequently collected. The content of the vessels was immediately filtered using a 0.2 µm filter. The filtered liquid phase was acidified with HCl (pH<2) and stored for further chemical analysis, whereas the solids were dried in an oven (12-24 h) at 60 °C and, in the case of psw and CFA materials, were subsequently grinded with an agate mortar for further analysis. Crystals of diopside and augite were separated and introduced in absolute ethanol (99.8%, Sigma Aldrich) to avoid affecting the structural features of silica-rich precipitates. Pseudowollastonite powders after carbonation experiments (i.e., C1-C4) were cemented into tabs with the shape of the reaction vessel that were very strong and hard to break apart during extraction using a steel spatula.

Batch hydrothermal reactors with CO_2 injection. Carbonation experiments were performed using gaseous CO_2 in a stainless steel, high-pressure Berghof (BR-300) reactor lined with PTFE autoclave system and equipped with gas inlet and outlet. The experiments with gaseous CO_2 were performed adding psw or CFA (5 g) to the PTFE vessel (volume of 300 mL) and half filling it with MilliQ water (150 mL) without, and in the case of psw, with 37.65 g of NaCl (Sigma-Aldrich) or 48.02 g of KCl (Sigma-Aldrich). The tests involving the use of Na and K salts dosed in the same molar concentration (0.0043 mol/mL) as in dissolution experiments at neutral pH were intended to disclose the role of these two alkali metal ions on the carbonation of psw at high pCO_2 (i.e., most typical experimental conditions for ex situ silicate carbonation) (O'Connor et al., 2001; Bearat et al., 2006; Daval et al., 2009a,b; King et al., 2010; Sissmann et al., 2014; Svensson et al., 2018). During 2 h before heating, the gas was continuously supplied to the reactor to achieve saturation of the solution with respect to the gas. Then, the gas supply was stopped and the heating cycle started (T = 100 °C in the case of psw 150ºC in the case of CFA, 2-7 days; calculated pCO_2 = 13.6 bar at 100 °C at the start of the experiment). Elapsed the specific time, the reactors were cooled to room T and opened. Upon filtering (Pall Corporation, ø = 0.45 μm), the solids were dried (60 °C, 12-24 h) before analysis.

II.1.2.2 Flow-through reactors.

For the study of pyroxene dissolution under acidic conditions, a dilute HCl solution (pH= 1.5) at T= 80ºC was pumped using a peristaltic device into PTFE (polytetrafluoroethylene, Vtot = 30 mL) reactors containing single crystals of each pyroxene, at a flow rate of 2mL/min (Figure II.3) and under continuous stirring. 10 mL aliquots of effluent solution were continuously collected at 5 min intervals.

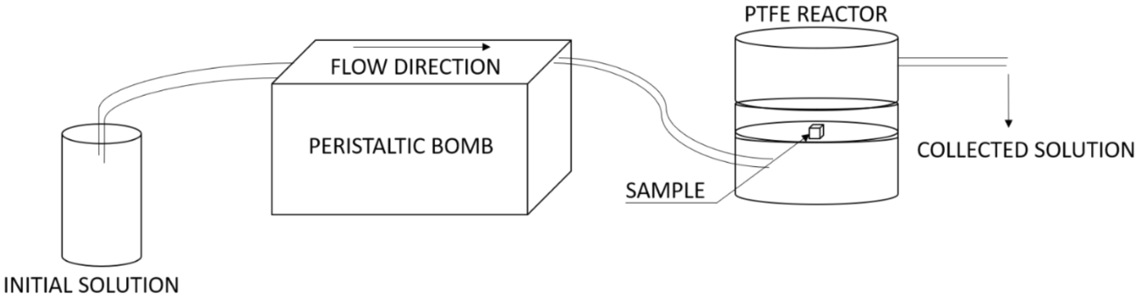

Figure II.3. Experimental flow through setup used in this Thesis.

For the analysis of the release of potentially toxic elements, PTE, from CFAs 1 g of solids (powder) was placed in each reactor and solutions were introduced in the reactors at a rate of 2 mL min^{-1}. In order to evaluate the effect of pH on this process, experiments were performed at a near-neutral pH 6 and at an alkaline pH 10 (adjusted using 1M NaOH), the latter corresponding to the natural pH of the studied CFA. Aliquots of the effluent solution were collected at predefined time intervals for ICP-MS analysis of PTE (see below).

II.1.3 Analysis of the solids

II.1.3.1 X-ray Diffraction Analysis

All solid products were analyzed by powder X-ray diffraction (XRD) using a X'Pert PRO diffractometer (PANalytical) with the following instrumental parameters: Cu Kα-radiation (λ= 1.5405 Å) and current = 40 mA, tension = 45 kV, measurement range = 3-70 °2θ, time per step = 4 s, and step size = 0.04 °2θ. To minimize orientation effects, powder samples were back loaded into the sample holders and diffraction patterns were collected under constant sample rotation. Diffraction patterns were analyzed using the computer code HighScore Plus 2.2.4 (PANalytical). Phase identification was performed by matching the experimental diffraction peaks with those included in the Joint Committee for Powder Diffraction Standards (JCPDS) PDF-2 database. For the quantification of the crystalline products it has been used Rietveld analysis (Rietveld, 1969) (routine included in the HighScore Plus 2.2.4. computer code) and the crystalline structures provided by the American Mineralogist Crystal Structure Database. Reported structure and PDF-2 codes used in this Thesis are reported in Table II.1.

The content of amorphous phase (e.g., amorphous SiO_2) was determined by the Rietveld method using a crystalline internal standard. Metallic Si powder was thoroughly mixed in a 5 wt% concentration with the starting powder (as well as pure calcite as a reference) and with the solids collected at the end of each run. In this case, best fittings and lowest residuals following Rietveld analysis were achieved using TOPAS 6.0 computer program (Bruker). For the case of psw it has been used a pattern calculated by HighScore Plus from the crystal structure reported by Yang and Prewitt (1999).

Table II.1. Unit formula, XRD pattern codes (JCPDS PDF-2 database) and structure codes (American Mineralogist Crystal Structure Database) of crystalline phases.

Mineral	Unit formula	JCPDS Code	Structure code
Graphite	C	41-1487	13980
Quartz	SiO_2	46-1045	n.a.
Mullite	$Al_6Si_2O_{13}$	15-0776	1059
Calcite	$CaCO_3$	05-0586	98
Hematite	Fe_2O_3	33-0664	143
Na-Chabazite	$NaAlSi_2O_6 \cdot 3H_2O$	88-1262	14781
NaP1	$Na_6Al_6Si_{10}O_{32} \cdot 12H_2O$	39-0219	n.a.
Hydroxysodalite	$(Na,Ca,K)_8Al_6Si_6O_{24}\ (OH)_2 \cdot 2H_2O$	76-1639	7133
Analcime	$NaAlSi_2O_6 \cdot H_2O$	41-1478	4133
K-zeolite	$K_2NaAl_3Si_9O_{24} \cdot 7H_2O$	22-0773	n.a.
aragonite	$CaCO_3$	41-1475	236
shortite	$Na_2Ca_2(CO_3)_3$	21-1348	13288
kalicinite	$KHCO_3$	12-0292	18502
parawollastonite	$CaSiO_3$	43-1460	7360
pectolite	$Ca_2NaSi_3O_8(OH)$	33-1223	10648
plombierite	$Ca_{2.5}Si_3O_8(OH)_{0.5} \cdot 6H_2O$	29-0331	14073
pseudowollastonite (psw)	$CaSiO_3$	n.a.	2247
rankinite	$Ca_3Si_2O_7$	22-0539	14417
tobermorite-11Å	$Ca_2Si_3O_9(OH) \cdot H_2O$	45-1480	6884
shlykovite	$KCaSi_4O_9(OH) \cdot 3H_2O$	n.a.	17556
Augite	$Ca(Ti,Mg,Al)(Si,Al)_2O_6$	25-0306	1000035
Diopside	$CaMgSi_2O_6$	41-1370	5235
Phillipsite-Na	$(Na,Mg)_2(Si,Al)_8O_{16}\ .\ 6(H_2O)$	73-1419	9270
Magnesian calcite	$(Ca,Mg)CO_3$	43-0697	n.a.

n.a. Not available. Structure created during this Thesis

II.1.3.2 Fourier Transform Infrared Spectroscopy analysis

Solids were analyzed by Fourier transform infrared spectroscopy using an attenuated total reflectance sample holder (ATR-FTIR, Jasco) in the frequency range 4000 – 400 cm-1 with a step size of 0.48 cm-1. Reported spectra correspond to the average of 36 accumulations in the case of the analysis of solids after pyroxene dissolution and pseudowollastonite dissolution and carbonation (chapter III and IV), and 126 accumulations in the case of of the analysis of solids after pyroxene carbonation and CFA dissolution and carbonation (chapter V and VI).

II.1.3.3 Thermogravimetric analysis (TGA) and differential scanning calorimetry (DSC) analysis.

Thermogravimetry coupled with differential scanning calorimetry (TG/DSC, Mettler Toledo) was used to quantify the total amount of $CaCO_3$ formed after completion of carbonation experiments. For this task ~40 mg of solids were placed on Al crucibles and heated in flowing air (100 mL min^{-1}) from 25 to 950 °C at a heating rate of 20 °C min^{-1}.

II.1.3.4 Scanning Electron Microscopy (SEM)

Reacted and unreacted solids (pseudowollastonite, wollastonite, pyroxenes and CFA) were deposited on Al-stubs covered with sticky carbon tape and, in the case of powder samples, carbon-coated. All samples were characterized by scanning electron microscopy (SEM, FEI Quanta 400 or Auriga, Carl Zeiss) working at an acceleration voltage of 20 kV and coupled to a X-Ray energy dispersive spectrometer (EDS, xFlash Bruker, or Oxford Instruments detectors) for microanalysis.

II.1.3.5 Transmission Electron Microscopy (TEM)

A detailed characterization of reacted and unreacted solids was performed by means of transmission electron microscopy (TEM) using either a Philips CM-20 operating at 200 kV or High Resolution TEM-FEI TITAN with 300 kV acceleration voltage, and equipped with a high angle annular dark field detector (HAADF) for Z-contrast imaging. Selected area electron diffraction (SAED) patterns and EDS analyses were used to determine the crystalline structure and the chemical composition, respectively. Samples for TEM were prepared as follows: 100 mg of the powdered solids were first suspended in 5 mL of absolute ethanol (99.8%, Sigma Aldrich), dispersed in an ultrasound bath for 2 minutes, and then collected directly from the beaker using Formvar film-coated copper grids.

. Analytical electron microscopy (AEM) was performed by EDS microanalysis (under scanning-TEM operation mode) using the thin-foil method (Cliff and Lorimer, 1980) and *k*-factors determined using standard minerals of known composition.

II.1.3.6 X-ray Microtomography

Reacted samples of pyroxenes (Chapter IV and V) were analyzed by high resolution X-ray computed tomography (Micro-CT) for the secondary phases spatial variability and quantification by high-resolution contrast images using a Xradia 510 equipment (VERSA ZEISS). Scans were performed using the following instrumental settings: tension=40 kV, energy=3.00W. Data were acquired with a 4x magnification optical objective for a total scan time of 15 h including the collection of reference images. The voxel size achieved under these conditions was 3µm. It should be noted that analyses of Micro-CT were performed on the same crystals first analyzed by SEM-EDX to avoid any potential error on the selection of the threshold to quantify the selected phases. The image analysis was treated using the ImageJ software (Schneider et al., 2012) and Dragonfly Software (Version 4.1, Object Research Systems).

II.1.3.7 X-ray fluorescence

In the chapter VI, the concentrations of major/minor and trace elements in unreacted CFA were determined on a Bruker AXS S4 Pioneer X-ray fluorescence (XRF) equipment.

II.1.3.8 N_2 adsorption

The surface area (BET method) of reacted and unreacted solids was determined by means of N_2 adsorption at 77 K using a Micrometrics Tristar 3000 following degassing for 12 hours at 120ºC under vacuum on a Micrometrics FlowPrep device.

II.1.3.9 Calculation of carbonation efficiency (CE) (carbonation of CFA).

It can be considered that all amorphous and crystalline Ca- and Mg-containing phases (excluding already formed $CaCO_3$) in unreacted CFA can contribute to the release of Ca and Mg in solution and therefore, to the effective carbonation of CFA.(Thiery et al., 2007; Pan et al., 2012) Multiple equations have been proposed to calculate the carbonation efficiency CE for CO_2 sequestration.(Nyambura et al., n.d.; Fernández Bertos et al., 2004; Montes-Hernandez et al., 2009; Tamilselvi Dananjayan et al., 2016; Ji et al., 2017; Ji et al., 2018) In this chapter, it has been calculated the CaO contained in the calcite present in unreacted CFA using:

$$iCaO = wt_{CaCO3}\, x\, \frac{M_{CaO}}{M_{CaCO3}} = 0.56\, wt\% \qquad \text{(II.1)}$$

where wt_{CaCO3} is the wt% of $CaCO_3$ determined by the XRD analysis of the unreacted material using the Rietveld method, M_{CaCO3} is the molar mass of $CaCO_3$ (100 g mol^{-1}) and M_{CaO} is the molar mass of CaO (56 g mol^{-1}). $iCaO$ is subtracted from the total CaO + MgO content of the unreacted material, to determine the theoretical sequestration capacity of these CFA using the Stenoir formula,(Nyambura et al., n.d.; Fernández Bertos et al., 2004; Tamilselvi Dananjayan et al., 2016)

$$Th_{Cc} = (wt_{Cao} - iCaO) + wt_{Mgo} = 4.87\, wt\% \qquad \text{(II.2)}$$

where wt_{CaO} and wt_{MgO} are the content of CaO and MgO, respectively, in unreacted material measured by XRF. Finally, it has been adapted the equation used by Dananjayan et al.(Tamilselvi Dananjayan et al., 2016) to calculate CE (%) as follows:

$$CE = \frac{[(\Delta wt\%\ 590°C - 800°C\ ) \times (M_{(Ca,Mg)CO3}/M_{CO2})] - 1}{Th\ Cc}\ x\ 100 \qquad \text{(II.3)}$$

where $(\Delta wt\%\ 590°C - 800°C\ )$ was calculated from TGA analyses, and $M_{(Ca,Mg)CO3}$ is the molar mass of calcite in the products, which can include a fraction of Mg replacing Ca (i.e., Mg-calcite)

II.1.4 Analysis of the solutions

The pH of the solutions was measured using a glass electrode by Metrohm calibrated with three standard solutions (pH= 4.01, 7.01 and 10.01 at 25 °C) with ±0.01 of uncertainty. Due to the high alkalinity of most of the experimental solutions, experimental pH values cannot be considered fully accurate because they are out of the calibration range.

The concentration of Ca, Si, Na and K in the reacted fluid was determined by ICP-OES at Centro de Instrumentación Científica (CIC-UGR, Perkin Elmer, Optima 8300) or at Institut de Sciences de la Terre (ISTerre, Varian 720ES). Furthermore, solutions collected on the flow-through experiments performed in Chapter VI were analyzed by ICP-MS on a NexION 300D equipment.

Calcium, magnesium and silicon-based dissolution rates in pyroxene dissolution experiments were calculated using the equation II.4. for flow through experiments (Daval et al. 2010):

$$r_i = \frac{\mathrm{v}\ [i]}{\eta_i\ SSA\ m_o} \tag{II.4}$$

where v is the flow rate of the solution (m^3 s^{-1}), $[i]$ is the concentration of the selected ion in the effluent solution (mol m^{-3}), η_i is the stoichiometric coefficient of element *i* in the mineral, SSA is the surface area determined by BET-N$_2$ method and m_o is the initial mass of the mineral.

Dissolution rates in batch experiments were determined using the following equation:

$$r_i = \frac{V\ [i]}{\eta_i\ SSA\, t\, m_o} \tag{II.5}$$

where V is the volume of the reactor (m^3), $[i]$ is the concentration of the selected ion in the effluent solution (mol m^{-3}), η_i is the stoichiometric coefficient of element i in the mineral, SSA is the surface area exposed to the solution (m^2), t is the duration of the experiments (s) and m_o is the initial mass of the mineral.

II.1.5 Geochemical calculations

Geochemical calculations and solution speciation under the experimental conditions for primary silicates reactions were carried out using PHREEQC geochemical code (version 3.3.12, USGS, Reston, VA, USA) and the minteq.dat or lnll.dat databases (Parkhurst and Appelo, 2018).

Furthermore, in Chapter IV the distribution of monomers, oligomers, and polymers were calculated using FITYK software for data processing and non-linear curve fitting (Wojdyr, 2010). Gaussian adjust was performed following the equation:

$$y = a_0 \exp\left[-\ln(2)\left(\frac{x - a_1}{a_2}\right)^2\right] \tag{II.6}$$

where a_0 is the height of the peak, a_1 is the full width at half maximum (FWHM) and a_2 is the standard deviation: $a_2 = \sqrt{2 \ln 2\sigma}$. Subsequently, areas of the different species were summed and normalized to the total area to calculate the contribution percent to the solid members in the surface of the crystals.

Chapter III. Hydrothermal reaction of pseudowollastonite with carbonate-bearing fluids: Implications for CO2 mineral sequestration

III.1 The dissolution of Pseudowollastonite

In all dissolution experiments performed, both under alkaline (NaOH, KOH) and neutral (NaCl) pH conditions, no significant changes in the starting material were observed by XRD, other than an increase in the amount of amorphous phase (Table III.2) and the appearance at the very early stages of reaction of a very weak reflection attributed to tobermorite-11Å (7.75 °2θ Cu-Kα) (Figure III.1), a member of the tobermorite supergroup (Biagioni et al., 2015). The presence of trace amounts (2-3 wt%) of such a crystalline calcium silicate hydrate (CSH) phase, which typically forms during cement hydration (Hewlett, 2003), was confirmed by SEM-EDS (Figure III.2a and b) and TEM (Figure III.2c). TEM-AEM and SEAD analyses showed the presence of aggregates of amorphous Ca-rich silicate particles interspersed with a few tobermorite crystals (Figure III.2c). The amorphous nature of the precipitate was demonstrated by the diffuse haloes in the SAED pattern, which also showed a few spots corresponding to tobermorite crystals (Figure III.2c). Such features correspond to a CSH gel phase (Hewlett, 2003). In some cases, the amorphous nanoparticles were Si-rich (EDS analysis), i.e., amorphous SiO2 (Figure III.2b).

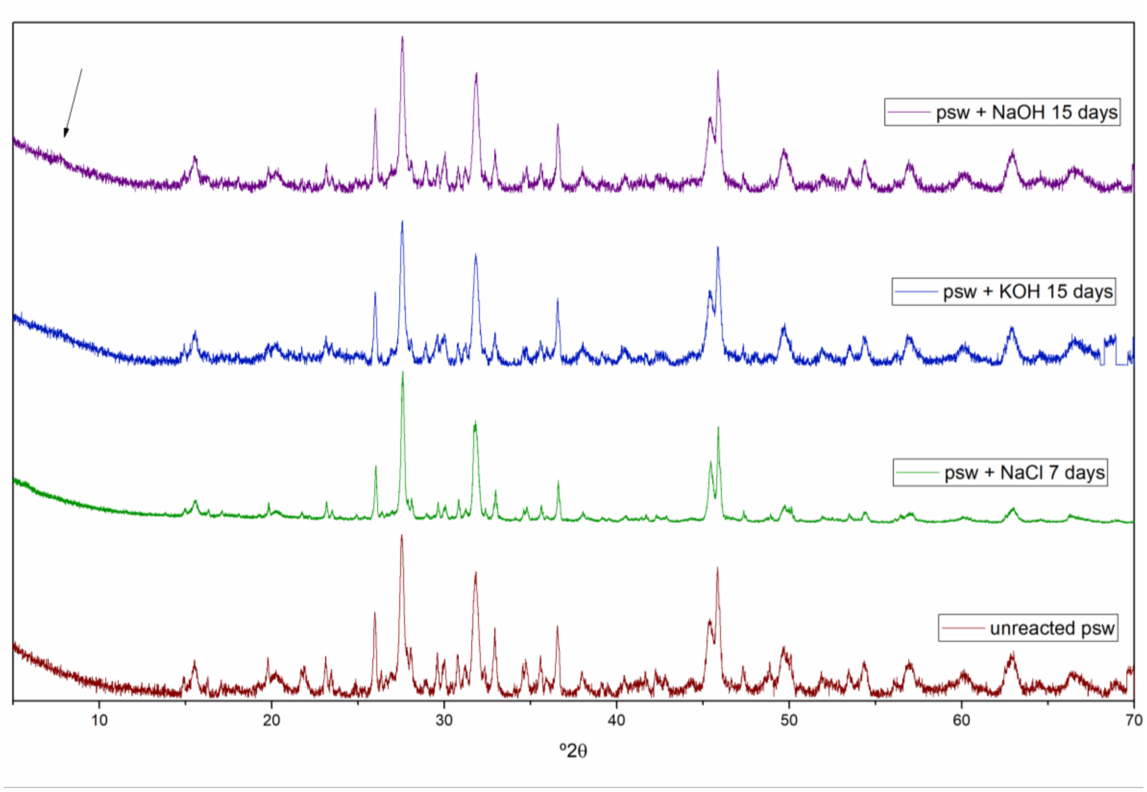

Figure III.1. XRD patterns of unreacted and psw reacted in the different solutions. Black arrow in upper patter shows the 11Å Bragg peak of tobermorite

TG-DSC analyses (Figure III.2d) showed that the starting psw experienced no marked weight loss or α- to β-CaSiO3 phase transition, which should be evident by an exothermic event during heating up to 950 °C. Nonetheless, both unreacted and reacted psw showed very small weight losses at 100-150 °C (~0.5 wt%), due to vaporization of adsorbed water, and at 550-800 °C (~0.5 wt%), indicative of (~1 wt%) calcium carbonate decomposition via the reaction CaCO3 = CaO + CO2 (Rodriguez-Navarro et al., 2009). This is likely due to limited carbonation of psw in contact with atmospheric CO2 and humidity during sample handling. Regardless solution composition, powders recovered after reaction showed an additional weight loss of ~0.5 wt% at 150-550 °C, corresponding to the dehydration/dehydroxylation of tobermorite and/or CSH gel, which convert into β-CaSiO3 at T > 700 °C (Taylor, 1959; Yu and Kirkpatrick, 1999; Hewlett, 2003). Such a conversion is consistent with the very small exothermal peak at 840 °C in the DSC trace.

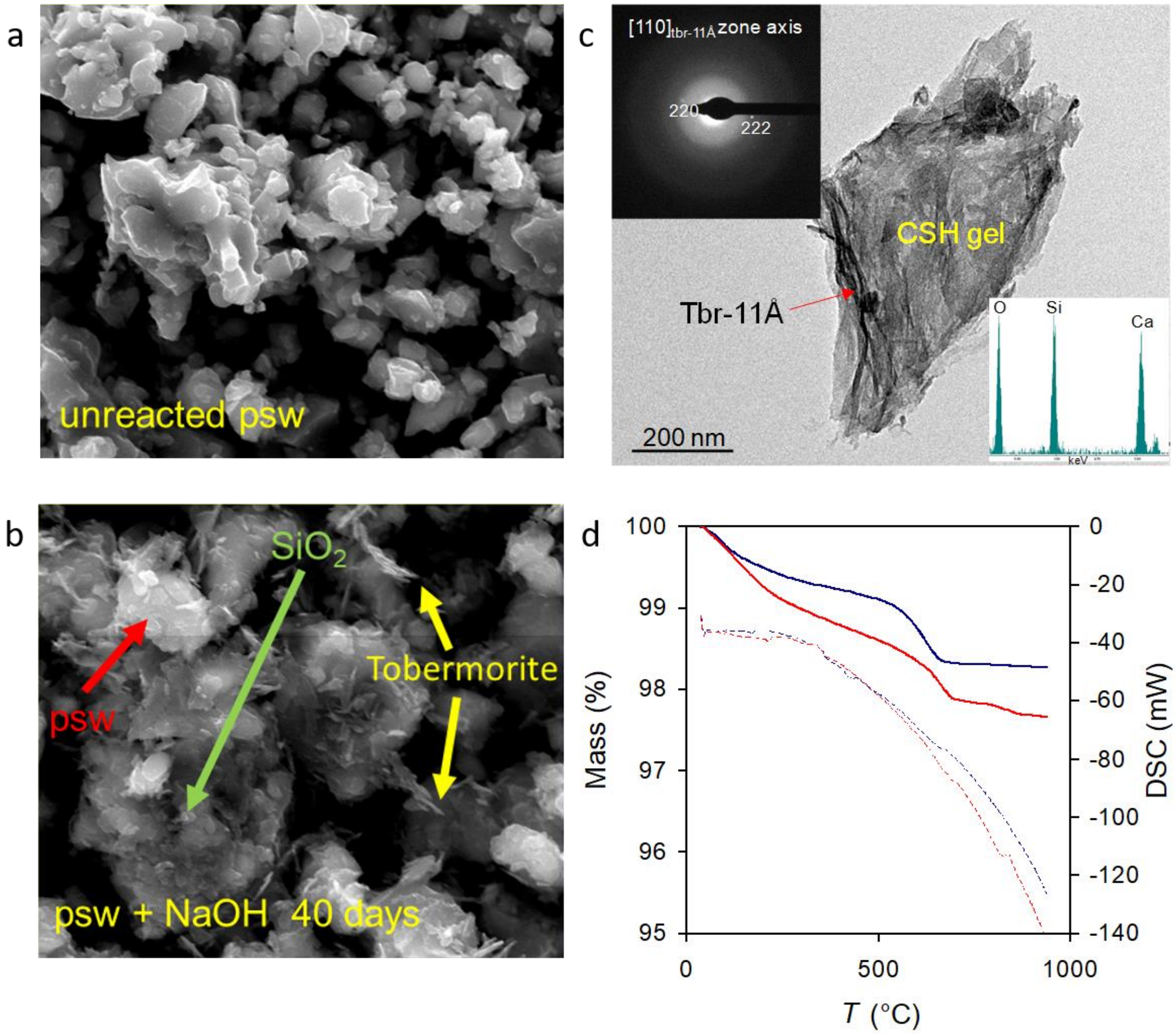

Figure III.2. SEM photomicrographs of unreacted (b) and (c) reacted psw; (d) TEM photomicrograph of psw reacted for 7 days in a NaCl neutral solution showing amorphous CSH gel phase (EDS spectrum in inset). The red arrow points to an edge-on plate of tobermorite attached to the gel phase (identified by SAED, inset). (e) TG-DSC traces for unreacted psw (blue trace) and psw reacted for 40 days in a NaOH solution (pH 12) at 150 °C (red trace) (see main text for details).

ATR-FTIR spectra showed no significant changes in reacted psw (Figure III.3), other than a slight increase in the intensity of the broad δ-OH stretching centered around 3400 cm^{-1} and δ-OH bending at 1632 cm^{-1} of water and the υ3 in-plane asymmetric stretching of CO3 groups at ~1400 cm^{-1} of calcium carbonate, as well as a slight broadening of the band with a maxima at 1067 cm^{-1}, corresponding to the Si-O stretching of amorphous silica.

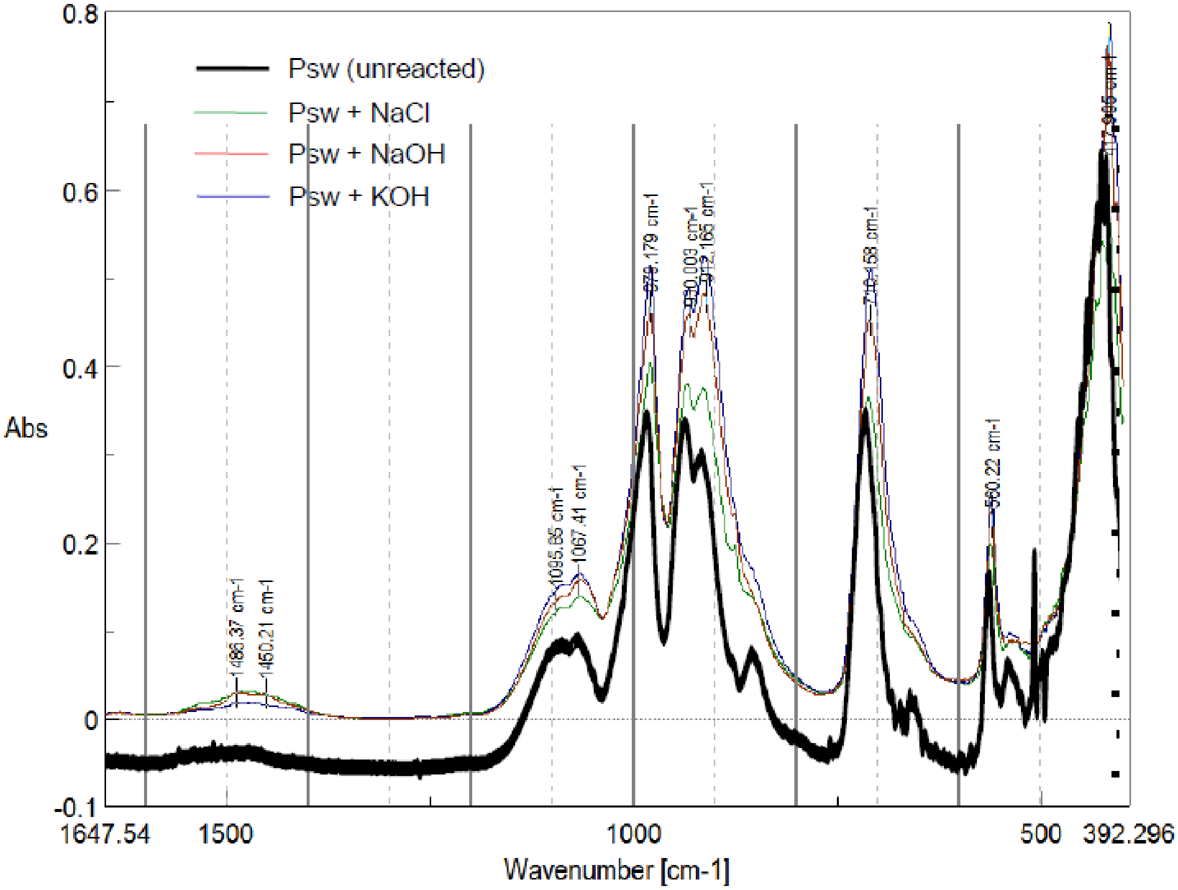

Figure III.3. ATR-FTIR spectra of unreacted psw and psw subjected to dissolution in NaCl, NaOH, and KOH solutions

It is important to note that despite the metastability of psw, not polymorphic transformation were observe into a β-CaCO3 phase (wollastonite 1T or 2M) under the P-T conditions of these dissolution experiments (150 °C, reaction time up to 40 days).

It is interesting to stress that nearly all previous studies on CaSiO3 dissolution and/or carbonation have been performed using natural wollastonite (i.e., β-CaSiO3) (Bailey and Reesman, 1971; Murphy and Helgesson, 1987; Casey et al., 1993; Xie and Walther, 1994; Rimstidt and Dove, 1996; Weissbart and Rimstidt, 2000; Wu et al., 2001; Golubev et al., 2005; Green and Lutge, 2006; Huiggen et al., 2006; Tai et al., 2006; Daval et al., 2009a,b; Ruiz-Agudo et al. 2012; Schott et al., 2012; Miller et al., 2013; Zhao et al., 2013; Ding et al., 2014; Ghoorah et al., 2014; Xiao et al., 2015; Ruiz-Agudo et al., 2016; Daval et al., 2017; Min et al, 2017; Min and Jun, 2018; Ashraf et al., 2016, 2017; Ashraf and Olek, 2018; Di Lorenzo et al., 2018; Svensson et al., 2018). In contrast, only a few studies on psw dissolution have been published (Banfield et al., 1995; Ohlin et al., 2010, Plattenberger et al. 2018, Plattenberger et al. 2019). These studies showed that psw was significantly more reactive than wollastonite due to its structural characteristics: i.e., the presence of [Si_3O_9] tetrahedral rings, instead of the infinite [SiO_4] tetrahedral chain of pyroxenes and pyroxenoids. In the former case, no SALs formed, while in the latter case SALs typically developed, specially under acidic conditions (Ruiz-Agudo et al., 2012, 2016; Ohlin et al., 2010; Schott et al., 2012). SALs can hamper the progress of dissolution and carbonation via the formation of passivating amorphous silica alone or in combination with calcium carbonate (Daval et al., 2009a,b; Di Lorenzo et al., 2018). Recent interest in psw dissolution is related to its use as a biomaterial, showing a rapid resorption in contact with body fluids (De Aza et al., 2000). Moreover, psw and CaSiO3 glass dissolution has been studied in relation to the formation of crystalline and amorphous CSH with relevance in cement setting (Paradiso et al., 2018).

Conversely, to my knowledge, only a few studies have been published on psw carbonation, and those were either focused on its carbonation as part of a complex mixture in an industrial waste (Sheng et al., 2015), or on its role during low Ca/Si cement setting/hardening (Bukowski & Berger, 1979; Qian et al., 2016). These studies, however, offered limited insights on the phase evolution during psw carbonation.

These results show that the dissolution of psw led to the formation of crystalline CSH and increased the amorphous content (via silica gel plus amorphous CSH gel formation) regardless the pH (neutral to alkaline) and the background alkali metal (Na or K). As expected (Figure III.4), the amount of amorphous product phase was negatively correlated with pH in the case of Na+ as background ion (i.e., a higher amount at neutral than alkaline pH), but not in the case of K^+ (alkaline conditions).

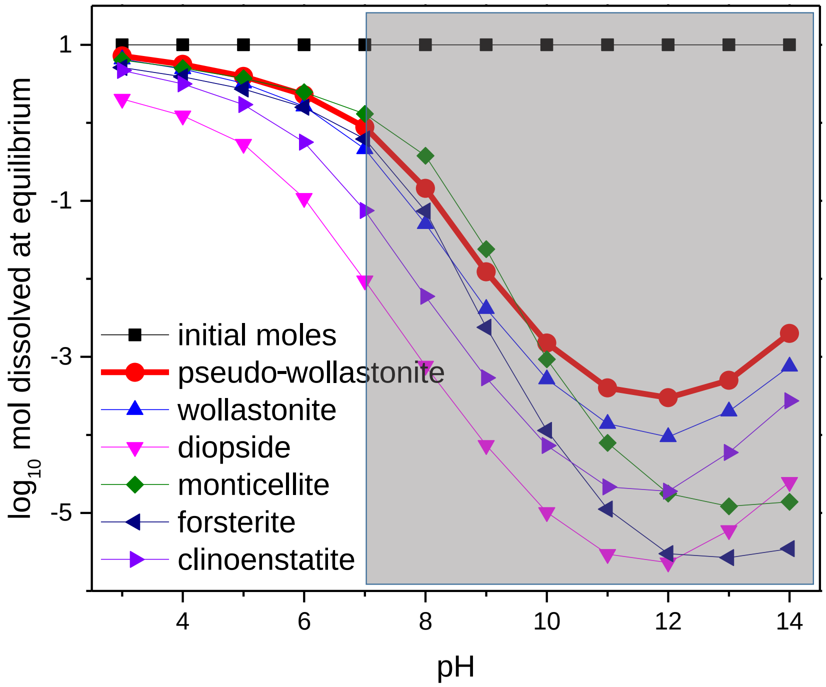

Figure III.4. Dissolved moles of selected silicate minerals at equilibrium (STP conditions) under constant pH determined by PHREEQC simulations using the Minteq.dat database. Note the general decrease in solubility at alkaline pH conditions (shaded area).

Apparently, K^+ ions favored the dissolution of psw and the formation of an amorphous product phase. This could be related to the fact that K+ can be preferentially bound into amorphous products as compared with Na+ (Leemann et al., 2011). Regarding a plausible mechanism for the formation of crystalline and amorphous CSH phases, it has been reported that chemisorption of Ca ions (i.e., released after psw dissolution) by acidic SiOH groups of silica gel (i.e., a byproduct of psw dissolution) under alkaline conditions results in CSH formation (Greenberg, 1956). Alkaline conditions in these experiments were achieved by the addition of NaOH and KOH, thereby ensuring the possibility of CSH phases formation upon Ca^{2+} release after (limited) psw dissolution. In the case of the NaCl solution, the starting pH was neutral, which favored psw dissolution as compared with alkaline conditions. However, $CaSiO_3$ dissolution consumes protons (Daval et al., 2009), thereby resulting in a continuous pH increase (Ruiz-Agudo et al., 2012, 2016; Di Lorenzo et al., 2018) which would limit further dissolution. Nonetheless, such an alkalization would also favor CSH precipitation in the NaCl system, in agreement with these experimental results.

It should be noted that the original psw included 10 wt% amorphous CaSiO3, which likely was the first phase to react (i.e., most soluble and reactive phase) (Richet et al., 1991; Paradiso et al., 2018). Note, however, that these XRD analysis using a crystalline internal standard could not distinguish between this reactant amorphous phase and that formed upon reaction (i.e., silica gel and CSH gel). Therefore, in this study, no attempt to quantify the time evolution of the amorphous product phase using XRD was done for the dissolution (and carbonation) tests. Note however that based on these independent TEM-AEM and SAED analyses, the amorphous phases present after completion of the dissolution (and carbonation) runs corresponded to product phases.

In contrast to previous assumptions regarding the non-hydraulic character of psw, as well as wollastonite (Qian et al., 2016; Ashraf et al., 2017), these results show that psw is slightly hydraulic under these experimental conditions as demonstrated by the formation of tobermorite and CSH gel. This is in agreement with recent results reported by Paradiso et al. (2018) who also found an amorphous solid phase in reactant psw, which likely was the first phase to react (i.e., most soluble and reactive phase) (Richet et al., 1991; Paradiso et al., 2018). These results also show that despite its known high reactivity (Banfield et al., 1995; Ohlin et al., 2010), the limited conversion of psw under these experimental dissolution conditions demonstrates that DIC is necessary for the complete transformation of psw (see below).

III.2 Pseudowollastonite reaction in carbonate solution

III.2.1 Evolution of the solution composition during carbonation experiments

In all runs, the total Ca concentration was ~1 to 3 orders of magnitude lower than that of Si (compare Figure III.5a and b). This evidences a significant removal of calcium ions from solution due to the formation of Ca-bearing phases. The relatively high Si concentration measured in the experiments with NaHCO3 and KHCO3 as compared with those with Na2CO3 and K2CO3 is possibly related to: (i) enhanced psw dissolution at the lower initial pH of bicarbonate solutions, consistent with the reduced solubility of psw with increasing pH (Figure III.4), and (ii) the subsequent significant increase in pH with the progress of the dissolution experiments (Figure III.5c). Note that silica solubility increases with increasing pH and T (Figure III.5d) (Fleming and Crerar, 1982). This explains why these alkaline solutions maintained a relatively high aqueous Si concentration throughout the time spam of the experiments, despite the precipitation of silica and secondary silicates (see below). Interestingly, very high Si concentrations (> 1000 mM) were observed during the early stages of psw carbonation in KHCO3 solution, an effect that was not observed in the NaHCO3 run, despite their similar starting pH. This suggests that K+ ions exerted an inhibitory role for the early precipitation of secondary silicates and amorphous silica, as compared with Na+. While the concentration of Si was higher in the case of KHCO3 than in NaHCO3, the situation was reversed for the case of Ca, possibly due to enhanced CaCO3 precipitation (see above). Finally, the concentrations of Si and Ca were always higher in the experiments with K2CO3 than in those with Na2CO3, despite their almost identical initial pH.

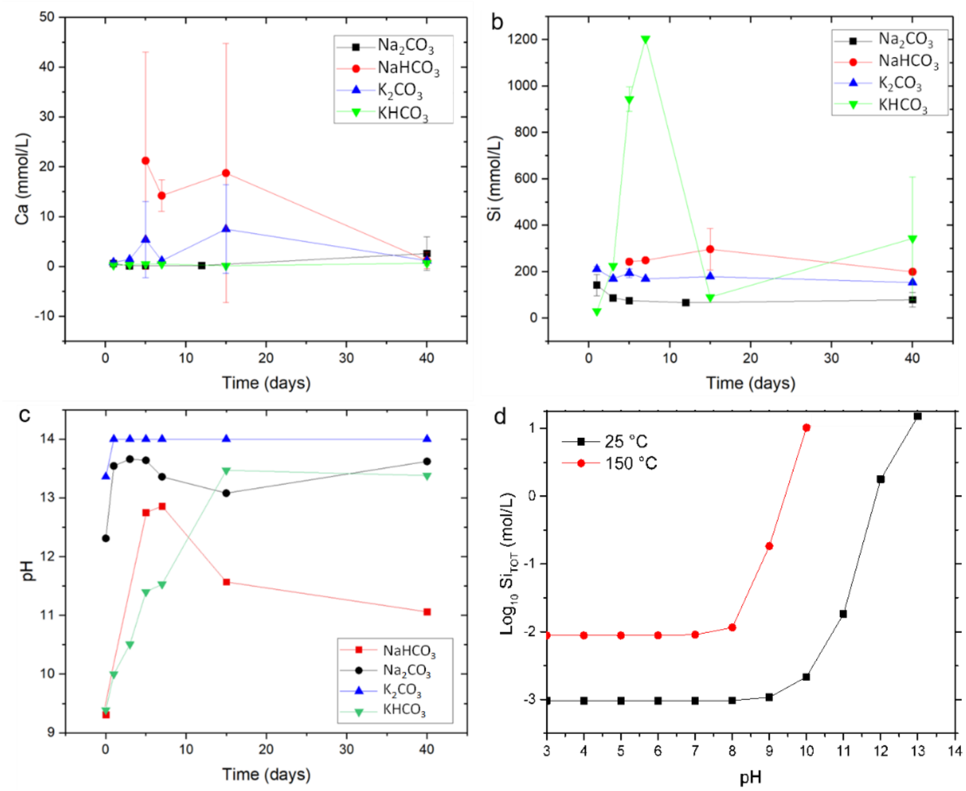

Figure III.5. Chemistry evolution during pseudowollastonite carbonation: (a) total calcium concentration; (b) total concentration of aqueous silicon; (c) pH evolution. Error bars refer to the standard deviation of three independent experiments; (d) variation of amorphous SiO2 solubility vs. pH at STP conditions (25 °C) and at hydrothermal conditions (150 °C) modeled using PHREEQC (minteq.dat database; excess SiO2(aq) in 1 L H2O, pH fixed with HCl or NaOH).

III.2.2 Reaction in sodium bicarbonate solution

XRD results show that pseudowollastonite was almost completely replaced by aragonite, calcite, parawollastonite, pectolite and plombierite after 15 days of reaction (Figure III.6a). Pectolite is a Na-substituted CSH, which typically forms after a CSH gel phase upon hydrothermal cement hydration (T ≥ 150 °C) in the presence of Na+ ions (Hewlett, 2003).

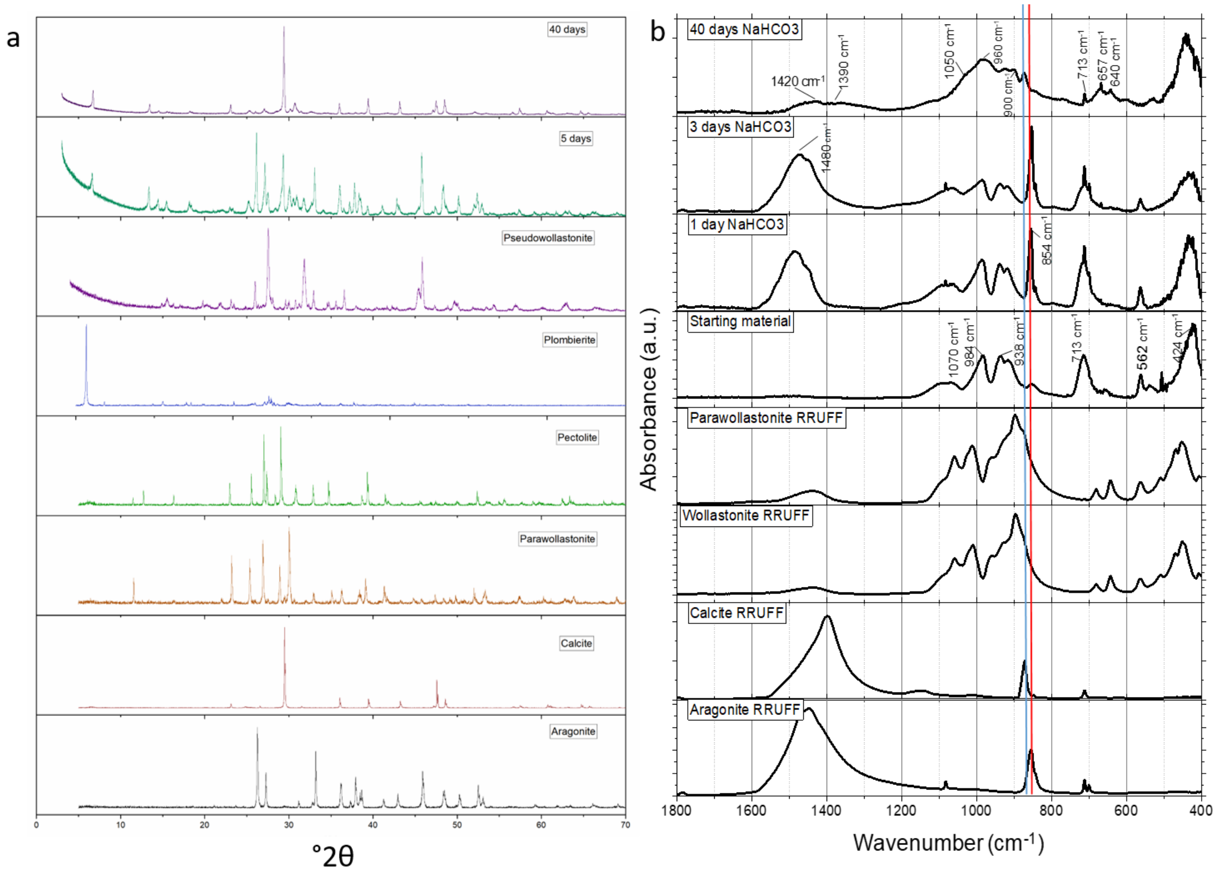

Figure III.6. Products of the reaction between psw and NaHCO3 solutions: (a) XRD patterns of reference phases (aragonite, calcite, plombierite, pectolite and parawollastonite) and, unreacted and reacted psw. The vertical blue line marks the position of the calcite 104 Bragg peak; (b) FTIR spectra of unreacted and reacted psw (RUFF reference spectra are included for comparison). The vertical blue and red lines mark the position of the σ3 band of calcite and aragonite, respectively.

Plombierite, another member of the tobermorite supergruop (Biagioni et al., 2015), is a common CSH phase formed during cement hydration and also appears in a few natural settings (McConnell, 1954). It has a composition and structure very similar to that of tobermorite-11Å, but its characteristic 002 Bragg peak appears at 14 Å (this is why it is also known as tobermorite-14 Å) and has a higher degree of hydration (Table III.1) (Bonnaccorsi et al., 2005). Weak diffraction peaks located at 29.98°, 26.84°, 25.29° 2θ attributed to parawollastonite (β-CaSiO3) were observed.

Aragonite was the first carbonate phase to form, but after two weeks it was no longer detected and only calcite remained. ATR-FTIR spectroscopy confirmed the formation of these two CaCO3 polymorphs (Figure III.6b). With the progress of the reaction, the ν3 in-plane asymmetric stretching of CO3 groups shifted from ~1480 cm-1 (aragonite) to ~1420 cm-1 (calcite), while the ν2 out-of-plane bending shifted from 853 cm-1 (aragonite) to 870 cm-1 (calcite). Moreover, the ν4 in-plane bending at 712 cm-1 of calcite was clearly observed after 40 days reaction. ATR-FTIR spectra confirmed the disappearance of psw with the progress of the carbonation reaction, and the newformation of secondary Ca and Ca-Na silicates such as parawollastonite, plombierite and pectolite, as well as amorphous SiO2. The strong bands at 800–1200 cm-1 correspond to the ν1 and ν3 symmetric and asymmetric stretching modes of Si–O within SiO4 tetrahedra, respectively, in pyroxenes and pyroxenoids (Mills et al., 2005), while the mid-frequency ones at 600–800 cm-1 correspond to the υ4 out-of-plane and the υ2 in-plane bending vibrations of Si–O bonds, and those in the low frequency range (400–600 cm-1) originate from the O–Si–O bending and Ca–O stretching modes in these phases (Richet et al., 1998; Mills et al., 2005; Makreski et al., 2006; Ashraf & Olek, 2016). Interestingly, the intense ν3 asymmetric stretching of Si–O bonds in Q2 tetrahedra of psw at 984 cm-1, got broader upon carbonation, shifting to lower wavenumbers, whereas the υ2 in-plane vibration of Si–O bonds at 713 cm-1 decreased its intensity until nearly zero. After 40 days almost all the absorbance of this band was due to the contribution of the ν4 in-plane bending of carbonate groups in calcite. This is consistent with psw transformation into the abovementioned secondary silicates. In parallel, a broad band centered at ~960 cm-1 with a broad shoulder at ~1050 cm-1 appeared and its absorbance increased with the progress of the reaction.

These bands correspond to the υ3 vibration of Si–O bonds in CSH and amorphous SiO2 phases, respectively (Ashraf & Olek, 2016). The bands at 640-680 cm-1 and at ~900 cm-1 that were present after 40 days reaction time correspond to the ν2– ν4 and υ3 vibrations, respectively, of both pectolite and parawollastonite. Finally, the band at 1396 cm-1 corresponds to the bending mode of the strongly hydrogen-bonded OH groups in pectolite (Hammer et al., 1998).

Figure III.7 shows the time evolution of crystalline phases content obtained from the Rietveld analysis. Error bars in this plot correspond to the standard deviation of three independent replicas. For this reason, in some cases they are significantly larger than the uncertainty of a typical Rietveld analysis (~1-5 wt%). Psw was continuously consumed during the reaction and its diffraction peaks could no longer be detected after 15 days. In parallel, the content of pectolite, parawollastonite and plombierite increased. Pectolite was very abundant (> 15 wt%) since the early stages of carbonation (≥ 5 days). Formation of pectolite resulted in Na consumption, thereby explaining why nahcolite originally present in the reactant solution was eventually fully consumed. The initially formed aragonite was progressively consumed and calcite was the only carbonate-bearing phase found in the longest experiments (15 and 40 days) with a final concentration of 45 wt% of all crystalline phases. Finally, the wt% of newly-formed secondary silicate minerals (plombierite, parawollastonite and pectolite) remained approximately constant after the initial increase experienced during the first two weeks of the experiment. Table III.2 shows the phase content, including amorphous (i.e., Rietveld analysis using an internal crystalline standard), present at the end of the experiment. The content of amorphous phase was 14 wt%. It corresponded to amorphous silica, although the contribution of a small amount of amorphous calcium carbonate (ACC) cannot be ruled out (see TG-DSC results below).

Table III.2. Results of the semiquantitative Rietveld analysis using an internal crystalline standard of reactant and product phases collected after completion of the carbonation experiments (wt%)

Reagent	psw	para-wo	cal	ara	shrt	pct	tob-11Å	plomb	kal	shly	rank	amorphous
psw $_{\text{solid}}$	88										1	11
NaCl $_{\text{solution}}$	71						2					27
KOH $_{\text{solution}}$	62						3					35
NaOH $_{\text{solution}}$	78						2					20
$NaHCO_3$ $_{\text{solution}}$		14	39			29		4				14
Na_2CO_3 $_{\text{solution}}$		2	1		47	34	1					15
$KHCO_3$ $_{\text{solution}}$	16		36	4						15		29
K_2CO_3 $_{\text{solution}}$	43		22						4			31
CO_2 $_{\text{dissolved}}$[1]	4		70									26

Mineral abbreviations: psw, pseudowallastonite; para-wo, parawollastonite; cal, calcite; ara, aragonite; shrt, shortite; pct, pectolite; tob, tobermorite; plomb, plombierite; kal, kalicinite; K-sil, potassium silicate; rank, rankinite; shly, shlykovite.

[1] Reported data correspond to the salt-free run. Note that in runs containing NaCl and KCl, these salts represented 4 and 5 wt % of the whole sample, respectively, but the relative amounts of calcite, psw and amorphous (silica) were similar to the salt-free run.

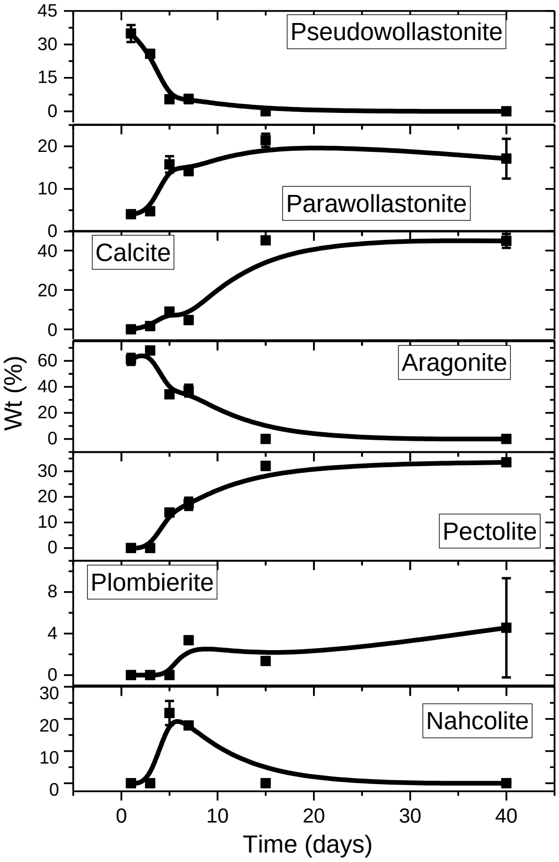

Figure III.7. Time evolution of crystalline phases content determined from XRD (Rietveld analysis). Error bars in this plot correspond to the standard deviation of three independent replicas.

TEM-AEM (along with SAED) and SEM-EDS analyses confirmed the formation of abundant pectolite (Figure III.8a and b), along with fibrous (needle-like) crystals of parawollastonite (see inset in Fig. Gb). TEM-AEM analyses also showed the presence of amorphous SiO2 (Figure III.8c). The amorphous nature of this phase was confirmed by the diffuse haloes in the SAED pattern (see inset in Figure III.8c). However, TEM-AEM and SEM-EDS analyses did not show the presence of amorphous silica surface altered layers, also known as SALs (Ruiz-Agudo et al., 2016; Di Lorenzo et al., 2018), on the reactant and/or product phases. Note that amorphous silica layers formed on β-CaSiO3 are easily identified by means of SEM-EDS due to their smooth, cracked, wax-like appearance and high Si-content (Ruiz-Agudo et al., 2012, 2016; Di Lorenzo et al., 2018). Moreover, SEM-EDS analyses showed abundant aggregates of micrometer-sized calcite crystals.

TG-DSC results (Figure III.8d) showed that the total amount of CaCO3 formed after 40 days reaction was 39 wt%, a value which matches the calcite content determined by XRD using an internal metallic Si standard for amorphous phase quantification (Table 2). Remarkably, recalculating the XRD semiquantitative values for crystalline phases (i.e., Rietveld analysis performed using no internal crystalline standard) after 40 days reaction time using the TG-derived CaCO3 content as the fixed value of calcite, yielded a total amount of crystalline secondary silicates (parawollastonite + plombierite + pectolite) of 47 wt%, being the remaining 14 wt% amorphous silica, values in perfect agreement with those calculated by XRD using an internal crystalline standard.

It should be noted that the full conversion of psw into calcite and amorphous silica according to reaction (1) should lead to a CaCO3/SiO2-amorphous mass ratio of 1.66. However, the actual mass ratio in these experiments was 2.78. This disparity can be explained by considering that a significant amount of Si released after the dissolution of psw was incorporated into the secondary Ca and Ca+Na silicates. Moreover, and regarding the actual yield of CaCO3 during psw carbonation, it should be noted that a fraction of Ca can also be incorporated into the silica gel, forming what is called a "Ca-modified silica gel" (Ashraf & Olek, 2016, Ashraf et al., 2016, 2017). These effects help to explain why only a conversion of 62.4 mol% of psw into CaCO3 was achieved despite the full consumption of psw.

TG analyses also showed that H2O lost in the T-interval 100-150 °C accounted for 7 wt% of the total mass of carbonated psw. Although a fraction of H2O lost in this T-interval corresponds to pectolite and CSH phases (and possibly, amorphous calcium carbonate, see below), it is very likely that a fraction of H2O was lost from amorphous silica. Note that the typical content of bond H2O in silica gel is ~7 wt% (Brunauer et al., 1956). This means that the actual mass of dry silica gel in these samples was slightly lower than 14 wt%.

Interestingly, the DSC trace of reacted psw showed a small exothermic peak at 340 °C. This is characteristic of amorphous calcium carbonate (ACC), and corresponds to its transformation into calcite (Rodriguez-Navarro et al., 2016). Note that formation of ACC following carbonation of CaSiO3 has been previously reported (Miller et al., 2013) and this phase appears to concentrate in the silica gel phase (Ashraf et al., 2017; Ashraf & Olek, 2018). Nonetheless, the amount ACC should be very minor, in agreement with the fact that the exothermic peak at 340 °C was very small, and the amorphous phase content determined by XRD and TG were similar (within experimental error).

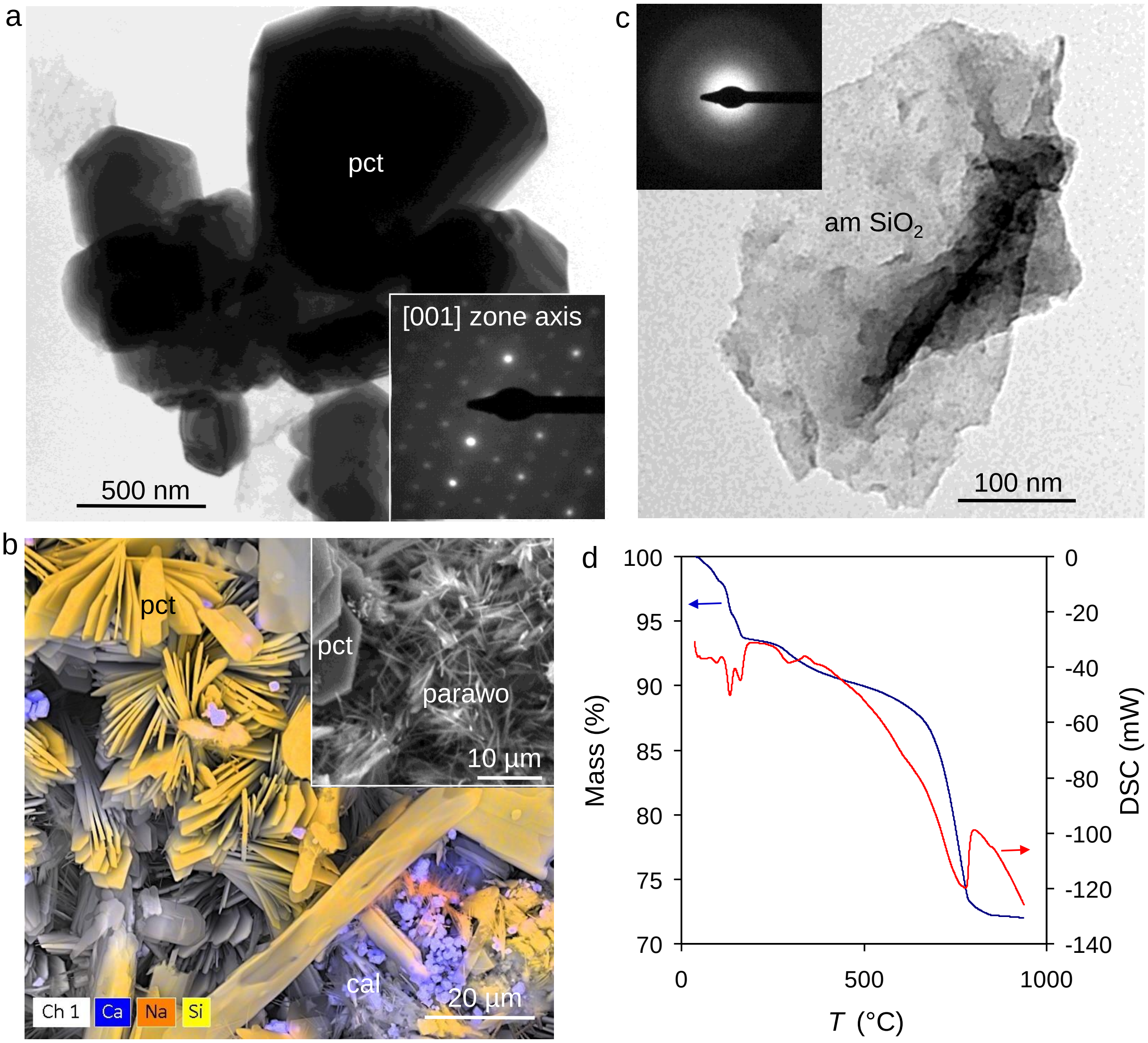

Figure III.8. Electron microscopy and TG-DSC analysis of reaction products of psw and NaHCO3 solutions: (a) TEM image of pectolite (pct) crystals (SAED pattern in inset); (b) SEM image overlaid with EDS compositional map showing aggregates of well-formed plate-like pectolite crystals (orange-yellow) along with abundant calcite (cal) aggregates (violet). Fibrous aggregates of parawollastonite (parawo) are shown in inset; (c) TEM image of amorphous silica (amSiO2). The inset shows the SAED pattern (diffuse haloes) of this amorphous phase; (d) TGDSC traces of reacted psw.

Finally, TEM-HAADF imaging (Z-contrast) (Figure III.9a) and AEM analyses (Figure III.9b) showed that aragonite formed during the early stages of carbonation (< 15 days) was systematically associated with amorphous silica (Figure III.9c and d). This latter phase covered aragonite and, apparently, played a role in its formation and/or partial stabilization.

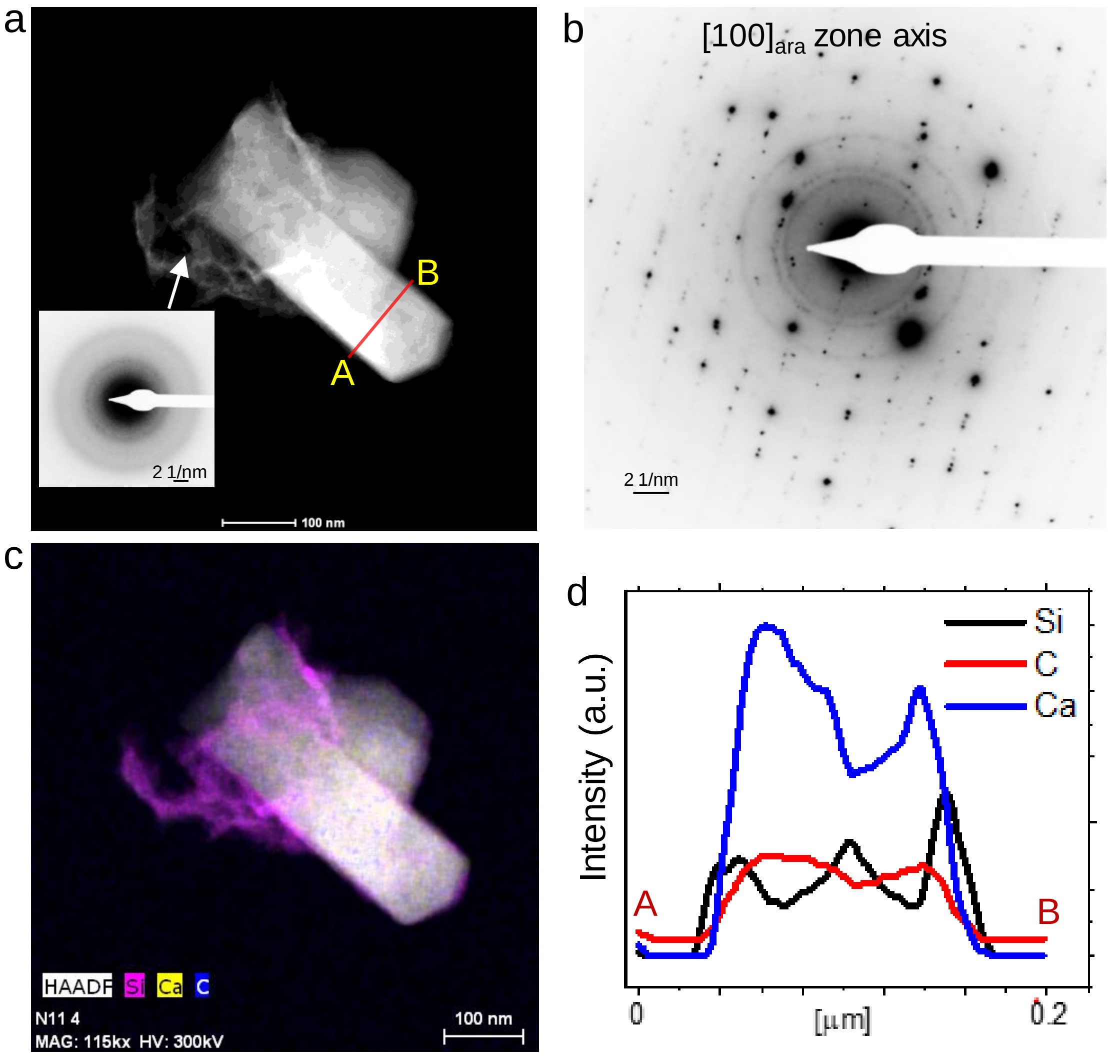

Figure III.9. TEM-HAADF analysis of an aragonite crystal formed during reaction of psw in NaHCO3 solution for 1 day. a) HAADF image of the crystal. The SAED (diffuse haloes) of the amorphous silica veil is shown in inset; b) [100] zone axis SAED pattern of the prismatic aragonite crystal in (a); c) HAADF-EDS mapping of the crystal, the two different phases, amorphous silica and aragonite, are easily distinguishable by the color combination of the elements silicon (pink), calcium (yellow) and carbon (blue). Note that the thin veil of silica covers the upper left part of the aragonite crystal, as well as its edges; d) Chemical profile of the aragonite crystal (AB line in (a)). It is observed how silica was deposited on the crystal edges and in the middle of the aragonite crystal.

III.2.3 Reaction in sodium carbonate solution

XRD results show that the reaction of psw in Na2CO3 solutions (C2) led to the formation of five crystalline phases: calcite, pectolite, parawollastonite, tobermorite-11Å and shortite. Despite the complexity of the phase identification and the resulting uncertainty in the semiquantitative Rietveld analysis (Figure III.10), it is clear that the starting material was completely consumed after 12-15 days.

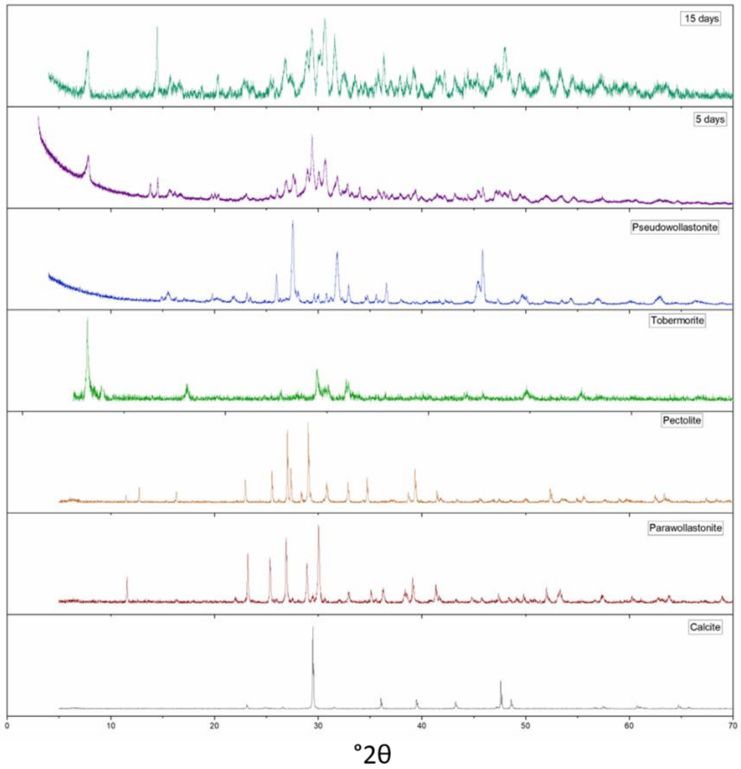

Figure III.10 XRD patterns of reference phases (calcite, tobermorite, pectolite and parawollastonite), as well as of unreacted psw and the products of the reaction between psw and Na2CO3 solutions (after different periods of time).

TEM analysis of samples reacted for 40 days confirmed the presence of abundant shortite (Figure III.11b and c) and pectolite (Figure III.11d and e), along with minor amounts of parawollastonite (Fig. III.11b). Despite the textural similarity between psw and pectolite, the latter phase could be easily distinguished by HRTEM (see lattice fringes in inset of Figure III.11e) and by the fact that this hydrated phase is highly sensitive to electron irradiation, rapidly undergoing amorphization (after dehydration) during HRTEM observations (see inset in Figure III.11e). Moreover, TEM-SAED in combination with HAADF imaging and elemental mapping confirmed the presence of the Ca-Na rich phases pectolite and shortite, along with small amounts of calcite and amorphous silica (Figure III.11f-g). AEM analysis of the amorphous phase showed that it was not pure amorphous SiO2, but a solid solution with relatively high Ca/Si and Na/Si molar ratios of 0.66 and 0.29, respectively. These results are consistent with the reported "Ca-modified silica gel phase" observed after carbonation of psw-based cements (Ahsraf and Olek, 2016), and demonstrate that this amorphous phase is compositionally very close to low-Ca CSH gel phases in OPC. Note, however, that the standard Ca/Si in the CSH gel phase of OPC is ~1.7 (Hawlett, 2003). As in the case of run C1, no SALs formed on the observed crystalline silicate phases at any stage of the carbonation run. Overall, these results confirm that at a very high pH, psw can be fully replaced by other silicate and carbonate phases (within these experimental time-scale). It is important to remark that under these conditions, the amount of secondary silicate minerals is significant (about half the mass of the product phases), being pectolite the most abundant secondary silicate. Note also that calcite was not the only carbonate phase detected by XRD: a more soluble Na-Ca carbonate, shortite, was detected after 15 days reaction time, and was the most abundant carbonate at the end of the experiment (40 days). Shortite reportedly forms under hydrothermal conditions (T >125 °C) upon reaction of CaCO3 (calcite) with Na2CO3 (Bradley and Eugster, 1969). This explains why after 15 days reaction time the amount of calcite was reduced while the amount of shortite increased (Figure III.11a). Interestingly, the amounts of both tobermorite 11Å and pectolite were significantly reduced after 15 days reaction time, when the amount of shortite continuously increased. This is likely due to carbonation of these secondary silicates. Carbonation of CSH phases is a well known phenomenon during setting and/or degradation of OPC (Hewlett, 2003). Similarly, pectolite has been reported to carbonate under hydrothermal conditions when in contact with Na2CO3 solutions (Suzuki et al., 2013).

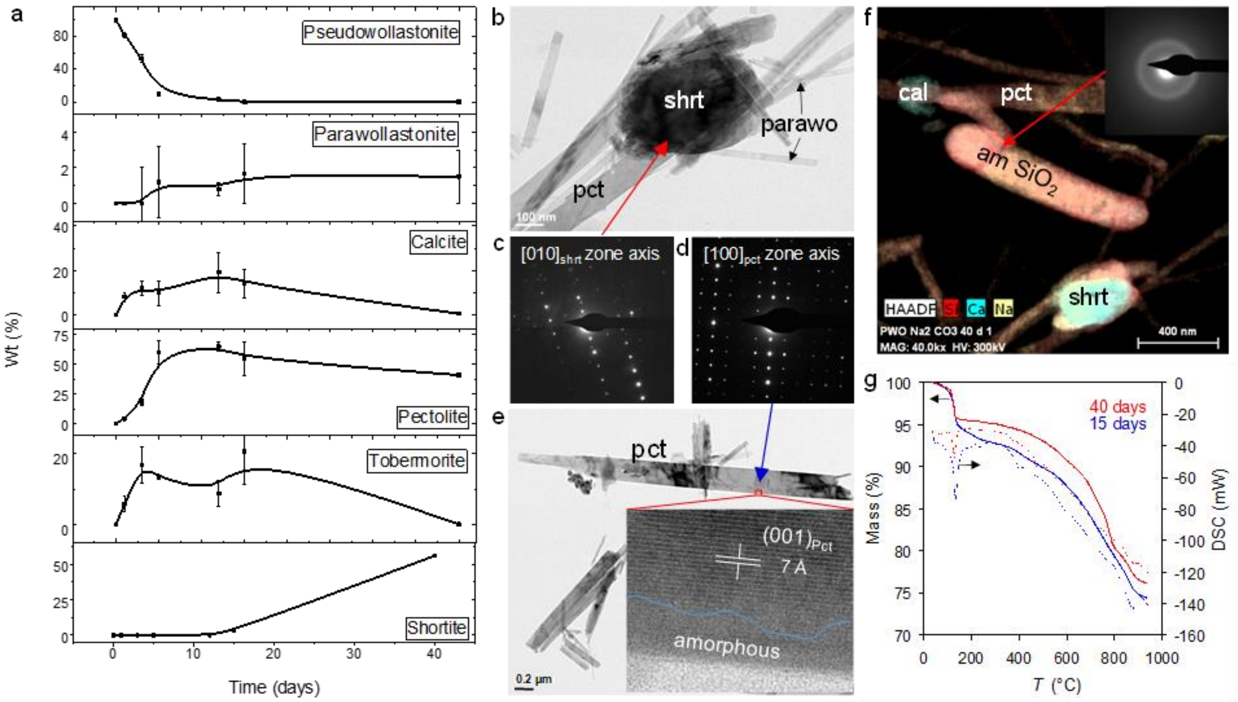

Figure III.11. Products of the reaction between psw and Na2CO3 solutions: (a) Time evolution of the crystalline phases content determined by XRD Rietveld analysis; b) TEM bright field image of an aggregate of pectolite (pct), shortite (shrt) and parawollastonite (parawoll); c) SAED pattern of shortite in (b); d) SAED pattern of pectolite in (e); e) TEM image of pectolite crystals. The inset shows a HRTEM image of pectolite. Note the discontinuity on the (001) lattice fringes of pectolite at the bottom edge of the crystal (marked by the blue trace) due to e-beam amorphization. Despite the textural similarity between psw and pectolite, the latter phase could be easily distinguished not only by the distinctive lattice fringes (inset) but also by the fact that this hydrated phase is highly e-beam sensitive, rapidly undergoing amorphization (after dehydration); f) HAADF image overlaid with EDS compositional maps showing the presence of calcite (cal), pectolite, amorphous silica (amSiO2) and shortite. The inset shows the SAED patter of the amorphous silica particle in the center of the image; g) TG/DSC traces of psw reacted for 15 and 40 days (blue and red traces, respectively).

Semiquantitative Rietveld analysis using an internal crystalline standard of products collected after 40 days reaction time showed that the amount of amorphous phase was 15 wt%, whereas the amount of carbonates (shortite plus calcite) was 48 wt%, being the amount of secondary silicates 37 wt% (Table 2).

TG-DSC analysis (Figure III.11g) showed that the amounts of CaCO3 after 15 days reaction time and after completion of the reaction (40 days) based on CO2 release (weight loss) at T > 600 °C were 32 wt% and 35 wt%, respectively. As stated above, at 15 days the main carbonate phase was calcite, but at 40 days it was shortite. Therefore, in the latter case, the released CO2 corresponded to the thermal decomposition of shortite via the reaction $Na_2Ca_2(CO_3)_3 = Na_2CO_{3(melt)} + 2CaCO_3$, followed by $2CaCO_3 = 2CaO + 2CO_2$ (Johnson and Robb, 1973). Considering that XRD results of crystalline phases showed an amount of 1 wt% untransformed calcite and also considering the molecular weight of shortite (306 g/mol) and calcite (100 g/mol), the observed weight loss due to thermal decarbonation corresponded to a total amount of 52 wt% shortite in this sample. However, the semiquantitative Rietveld analysis of crystalline phases (Figure III.11a) showed that the amount of shortite in the 40 days reacted sample was 57 wt % with a residual amount of non-transformed calcite of 1 wt%, which makes the total amount of carbonates equal to 58 wt%. This latter value is higher than the total amount of carbonates determined by TG (53 wt%). If it is recalculated the crystalline phases content determined by XRD considering the content of carbonate phases determined by TG, it is obtained that the amorphous phase (unaccounted for by standard Rietveld analysis) amounts to 9 wt%. This value is lower than that (15 wt%) determined by Rietveld analysis using an internal crystalline standard (see above). Although amorphous silica was detected by TEM-AEM and SAED, the small exothermal peak in the DSC trace at 330 °C confirms that a fraction of the amorphous phases in the sample was ACC. The presence of ACC which is accounted for as CaCO3 in the TG analysis but contributes to the amorphous phase in the XRD analysis, can help to explain why the amount of amorphous phase determined using TG results is lower than that determined using the Rietveld method with an internal crystalline standard. It cannot rule out, however, the possibility that the above-mentioned disagreement could be related to the errors associated with the semiquantitative Rietveld analysis (both with and without a crystalline internal standard).

Overall, these TG results show that only a conversion of 56 mol% of psw into CaCO3 was achieved after 40 days reaction time. Note that this value includes both the CaCO3 in calcite (plus ACC) and shortite.

ATR-FTIR spectra of samples reacted in Na2CO3 solutions showed very similar features as those corresponding to samples reacted in NaHCO3 solutions (Figure III.12). A continuous decrease in the intensity of the Si-O stretching bands of psw at 917-981 cm-1 with the progress of the reaction was observed. In parallel, the intensity of the broad band of amorphous silica at 1028 cm-1, increased. Additionally, it is observed a splitting of the broad υ3 stretching band of CO3 groups corresponding to calcite (1410 cm-1) into two bands at 1400 and 1450 cm-1 after 15-40 days reaction time due to the presence of a mixed Na-Ca carbonate (shortite).

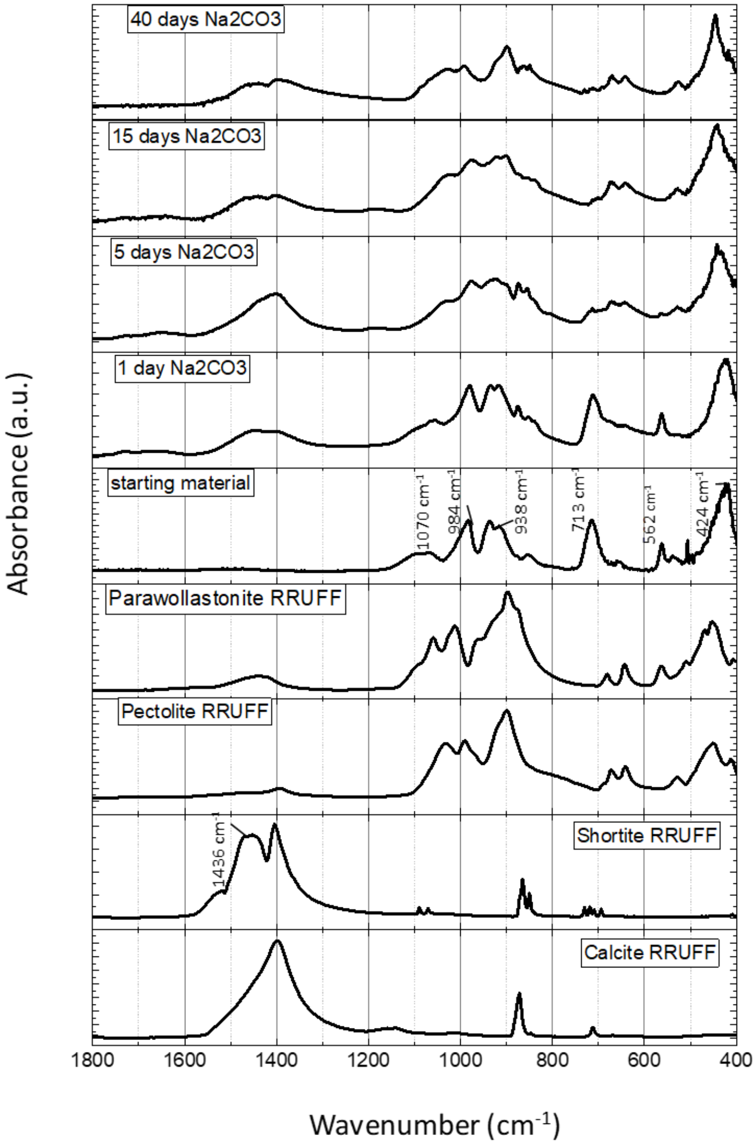

Figure III.12. ATR-FTIR spectra of unreacted psw and psw subjected to carbonation in Na2CO3 solution. The reference spectra of the relevant phases are included (RRUFF data).

III.2.4 Reaction in potassium bicarbonate solutions

XRD analysis showed the presence of psw, calcite, aragonite, and a crystalline potassium-calcium silicate phase, the mineral shlykovite (Table III.1), after 40 days reaction time (Figure III.13). Shlykovite is a phyllosilicate reportedly formed during hydrothermal alteration of peralkaline pegmatites (Pekov et al., 2010). In contrast to the Na-containing runs (C1 and C2), full psw conversion was not achieved in this run (C3). Interestingly, shlykovite was not detected until 15 days reaction time. This helps to explain the very high Si concentrations detected in solution at 5 and 7 days reaction time (Figure III.6b). Apparently, the delayed (and limited) formation of secondary crystalline silicates prevented the full conversion of psw. A reduction in the aragonite content and a parallel increase in the content of calcite as the run progressed was also observed. The formation of aragonite at the initial pH ~9 is in agreement with the formation of this carbonate phase in C1 run.

Rietveld analysis using an internal crystalline standard of products collected after 40 days reaction time showed that the amount of amorphous phase was 29 wt%, whereas the amount of carbonates (calcite plus aragonite) was 40 wt% (Table III.2).

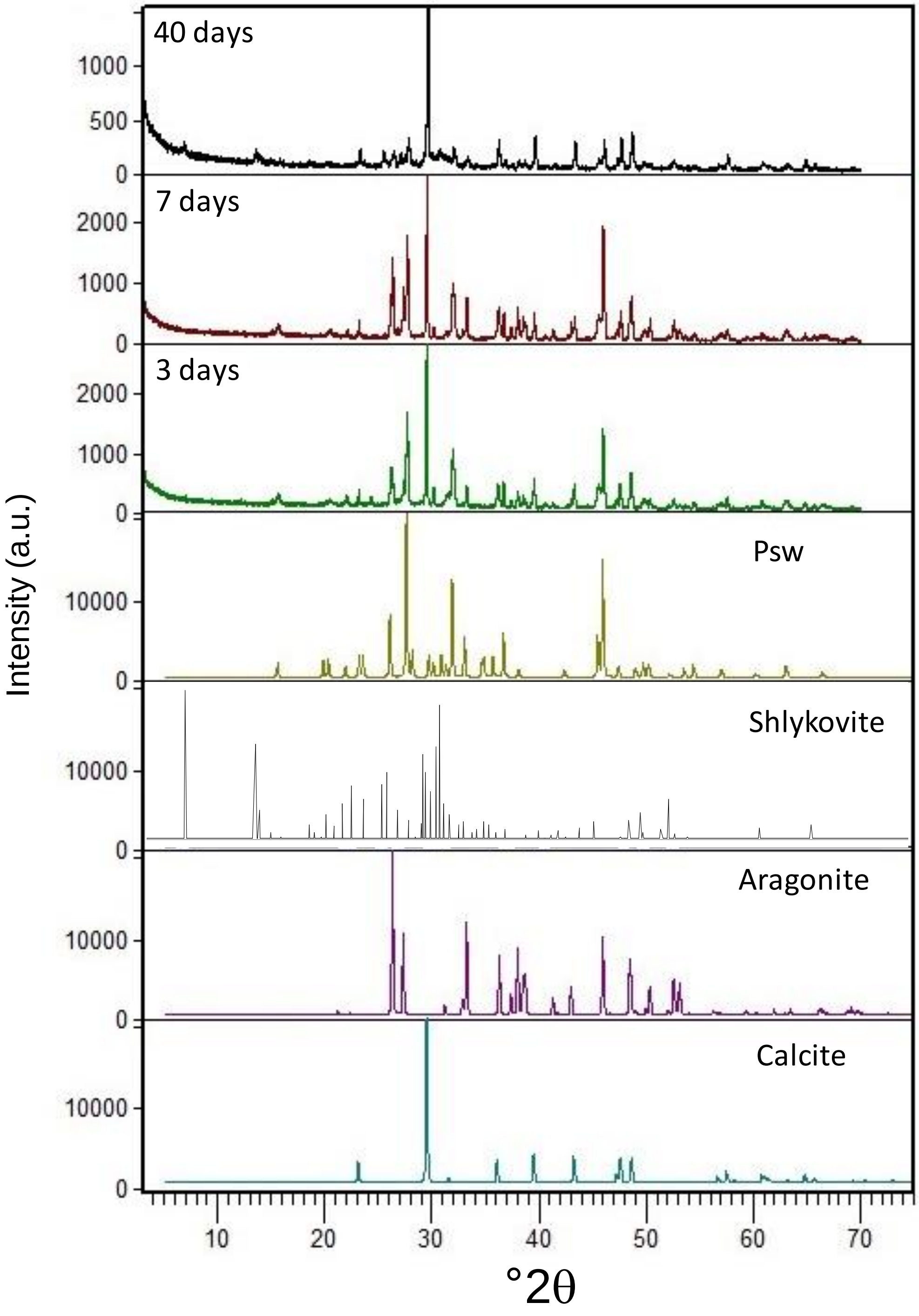

Figure III.13. XRD patterns of reference phases, as well as of unreacted psw and the products of the reaction between psw and $KHCO_3$ solutions.

SEM-EDS elemental maps showed that in addition to abundant rhombohedral calcite crystals, and nanogranular aggregates of amorphous silica, scattered palm-like aggregates of blade-shaped crystals, 20–50 μm long and containing K, Ca, Si and O were present (Figure III.14a). These aggregates correspond to shlykovite. TEM-SAED (Figure III.14b) and HAADF-EDS compositional maps (Figure III.14c) confirmed its presence, along with calcite and amorphous silica. AEM analyses of shlykovite crystals yielded the following structural formula: K1.15Ca0.85Si4O9(OH)·3H2O (based on the idealized structural formula KCaSi4O9(OH)·3H2O reported by Zubkova et al. (2010)). AEM analysis of amorphous silica showed that the Ca/Si mole ratio was 0.07, whereas no K was detected in this phase.

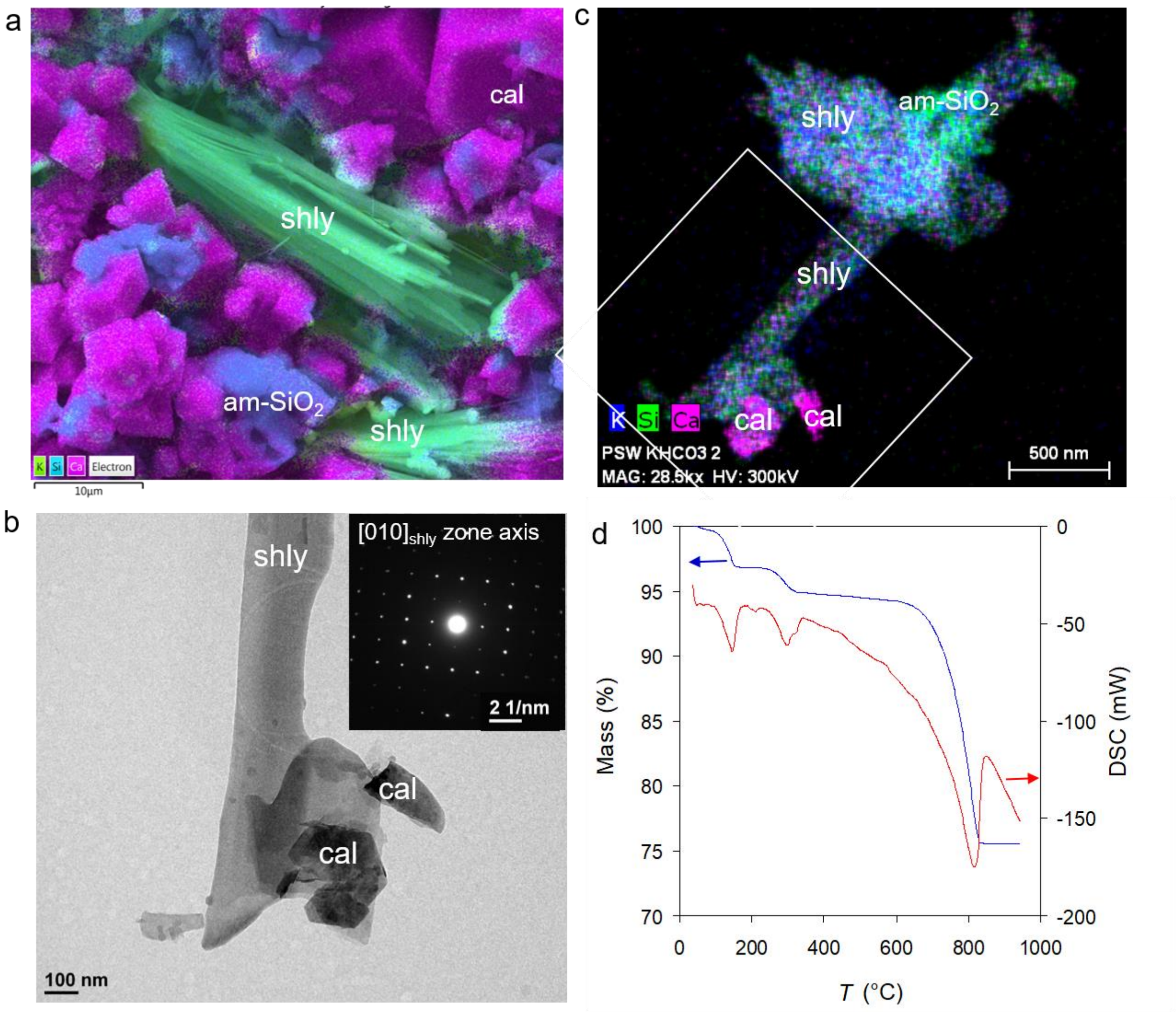

Figure III.14. Products of the reaction between psw and KHCO3 solutions. a) SEM of product phases after 40 days reaction time overlaid with EDS compositional maps: b) TEM image of product phases. The inset shows the [010] zone axis SAED pattern of the shlykovite crystal in the center of the TEM bright field image; c) HAADF image overlaid with EDS elemental maps of product phases after 40 days reaction time. The squared area corresponds to the area depicted in figure part (b); d) TG-DSC traces of product collected after 40 days reaction time. Red trace: DSC; blue trace: TG. Legend: cal, calcite; amSiO2, amorphous silica; shly, shlykovite.

TG/DSC traces of samples collected after 40 days reaction (Figure III.14d) showed the same features observed in the case of C1 and C2 runs, although the loss of both adsorbed and structural water in amorphous silica and in shlykovite occurred in two distinctive steps at 100-165 °C and 250-350 °C, respectively. The weight loss was 2.27 wt%. Considering that the amount of structural water in shlykovite is 14.73 wt% (Zubkova et al., 2010), then the total amount of shlykovite in the solid product is calculated to be 15.4 wt%, a value in excellent agreement with that calculated by Rietveld. The amount of CaCO3 determined from TG was 44 wt%, a value slightly higher than that determined from XRD using a crystalline internal standard (40 wt%). As in runs C1 and C3, this discrepancy is likely due to the presence of small amounts of ACC (consistent with the small exothermic peak at ~340 °C in the DSC trace, Fig. Md). Overall, and based on TG results, the CaCO3 yield after 40 days reaction time was 70.4 mol%.

ATR-FTIR analysis results showed the characteristic bands of the above mentioned carbonates and silicates, disclosing an increase with reaction time in the intensity and broadness of the Si-O stretching band/shoulder at 998/1050 cm-1 corresponding to amorphous silica (Figure III.15).

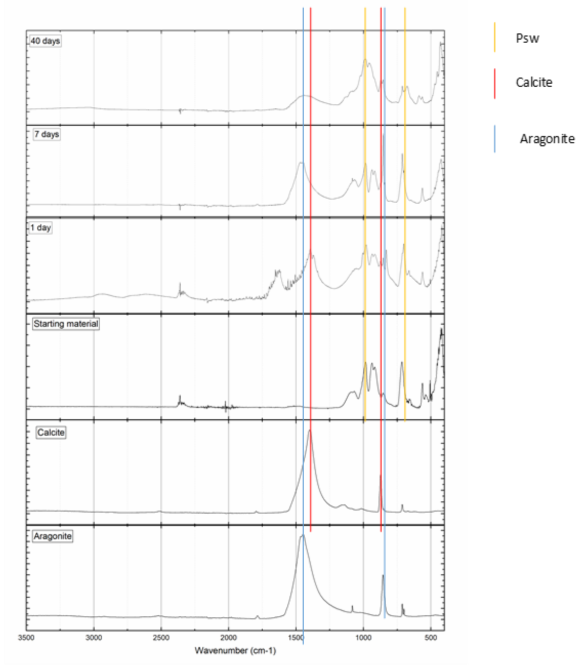

Figure III.15. ATR-FTIR spectra of unreacted psw and psw subjected to carbonation in KHCO3 solution. The reference spectra of calcite and aragonite are included. The vertical colored lines mark the main bands of each relevant phase

III.2.5 Reaction in potassium carbonate solutions

Figure III.16 shows the time evolution of crystalline phases content (XRD results) in experiments performed using K2CO3 solutions (C4). The most striking result was the abundant presence of unreacted psw (60 wt%) after 40 days of reaction, along 35 wt% calcite and 5 wt% kalicinite. The kalicinite content estimated by Rietveld analyses (considering crystalline phases only) was always low (0-10 wt%) and it did not follow any tendency with reaction time. In contrast, the calcite content continuously increased as a function of reaction time, but even in the longest experiments (40 days), its amount was lower than that of residual psw (Figure III.17a)

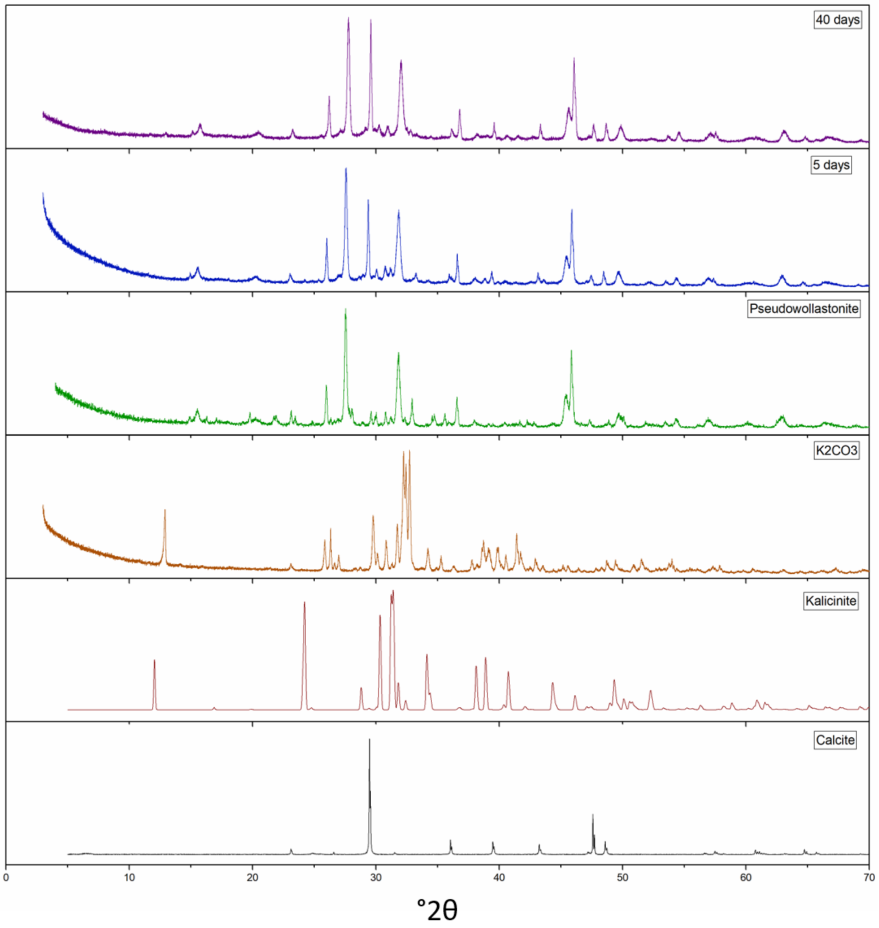

Figure III.16. XRD patterns of reference phases, as well as of unreacted psw and the products of the reaction between psw and K2CO3 solutions (after 5 and 40 days reaction time).

SEM-EDX analyses showed the presence of well-developed rhombohedral calcite crystals (Figure III.17b) as well as wire-like crystals of kalicinite (Figure III.17c). TEM-SAED confirmed the presence of abundant unreacted psw (Figure III.17d), whereas HAADF imaging and elemental mapping showed the close association of psw, amorphous silica, calcite and kalicinite (Figure III.17e). AEM analysis showed that the amorphous silica product included significant amounts of Ca and K, with Ca/Si and K/Si mol ratios of 0.46 and 0.30, respectively. As in the case of runs C1 and C2, the amorphous silica did not form SALs on the reactant phase.

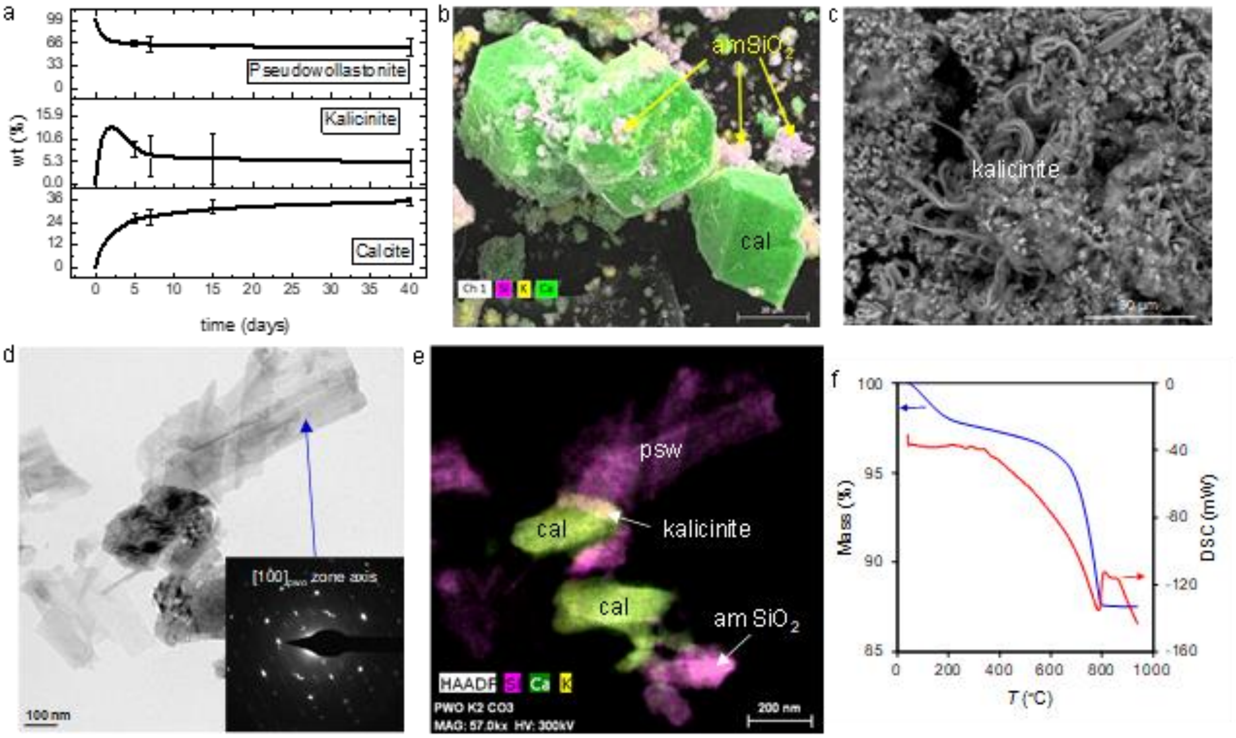

Figure III.17. Products of the reaction between psw and K2CO3 solutions. a) Time evolution of the crystalline phases content determined by XRD Rietveld analysis; b) SEM image of product phases after 40 days reaction time overlaid with EDS compositional maps. Legend: cal, calcite; amSiO2, amorphous silica; c) SEM image of kalicinite; d) TEM image of untransformed pseudowollastonite (psw) after 40 days reaction time (SAED pattern in inset); e) HAADF image of the same area depicted in (d), overlaid with EDS compositional maps; f) TG/DSC traces of solids reacted for 40 days.

TG/DSC traces (Figure III.17f) showed a small but well-defined weight loss in the T interval 100-200 °C (~2 wt%) corresponding to the thermal decomposition of kalicinite according to the reaction $2KHCO_3 = K_2CO_3 + CO_2 + H_2O$, and a small but continuous weight loss at 200-550 °C (~1 wt%) corresponding to water in amorphous silica. Subsequently, the thermal decomposition of calcium carbonate (calcite) took place (T >600 °C). Note that K_2CO_3, as well as Na_2CO_3, undergo melting at 900 °C (see endothermic band in the DSC trace of Fig. III.17f) and 850 °C, respectively, thereby not affecting the weight loss associated with $CaCO_3$ thermal decomposition. From this last weight loss the amount of calcite was determined to be 21 wt%. This value is significantly smaller than the calcite content determined by semiquantitative XRD analysis of crystalline phases (36 wt%), but in very good agreement with the calcite content of 22 wt% determined by Rietveld analysis using an internal crystalline standard (Table III.2). If it is recalculated the phase content determined by the standard Rietveld method (no internal crystalline standard) using the calcite content determined by TG, the total amount of crystalline phases in this sample amounts to 58 wt%, being the amorphous content 42 wt %. This amorphous content is, however, higher than the value of 31 wt% determined by Rietveld analysis using an internal crystalline standard (Table III.2). Based on TEM-SAED and HAADF-AEM analyses, the amorphous phase is basically amorphous silica with a small fraction of ACC, consistent with the exothermic peak at 330 °C in the DSC trace. Overall, the $CaCO_3$ yield after 40 days reaction time was only 33.6 mol% of the theoretical amount established by reaction (1).

ATR-FTIR analysis of samples reacted for different periods of time showed the strong bands corresponding to psw and the appearance and growth of those corresponding to calcite (Figure III.18). Additionally, it was observed the presence of bands at 1620 cm^{-1} and 1395 cm^{-1} assigned to the carbonate stretch mode and the in-plane bending of the OH…O mode of kalicinite, respectively (Kagi et al., 2003).

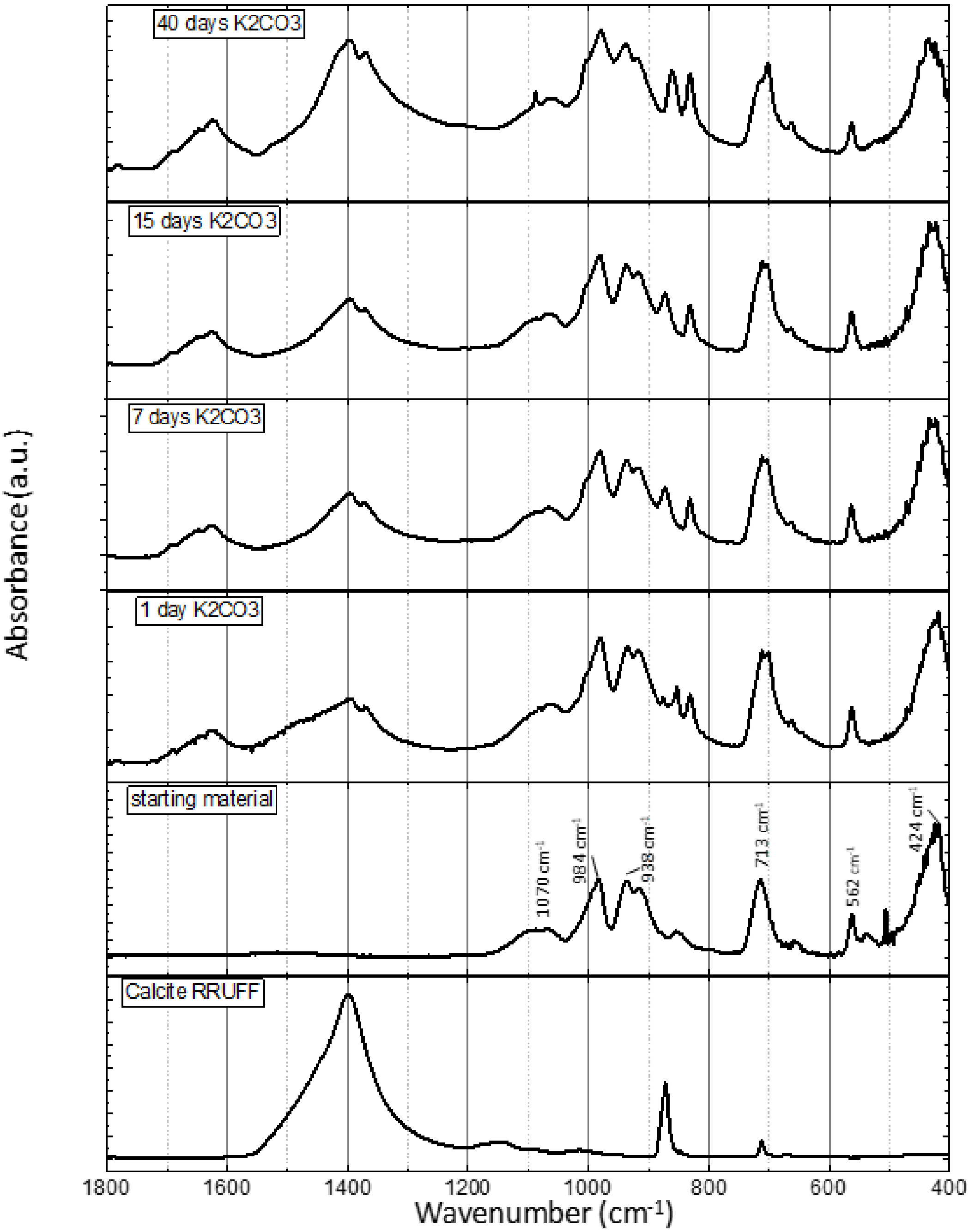

Figure III.18. ATR-FTIR spectra of unreacted psw and psw subjected to carbonation in K2CO3 solution.

III.2.6 Carbonation in CO_2-aqueous solution

XRD analyses showed that after 7 days of reaction, almost all psw was converted into calcite (Figure III.19a). Halite (~4 wt%) and sylvite (~5 wt %) were detected in the runs including these salts in the starting solution. Likely these salts precipitated out of the residual solution in the product phase during the drying of the recovered reacted samples. The presence of abundant calcite and amorphous silica, along with trace amounts of unreacted psw was confirmed by SEM-EDS (Figure III.19b and c) and TEM-SAED (Figure III.19d) analyses. In no case was passivation of residual psw by amorphous silica detected. However, it was observed that deposits of amorphous silica typically decorated the surface of calcite rhombohedra (Figure III.19c). Moreover, the amorphous silica displayed negligible incorporation of Ca (inset in Fig. 6d), Na or K, as demonstrated by AEM analyses showing that the maximum Ca/Si, K/Si, and Na/Si molar ratios were 0.007, 0.015, and 0.039, respectively. Interestingly, HRTEM analyses showed the presence of a few psw pseudomorphs fully transformed into highly porous amorphous silica structures (Figure III.20a) confirmed by a HAADF-EDS maps showing the distribution of Si an Na (Fig.III.20b) and therefore, by EDS spectrum (Figure III.20c).

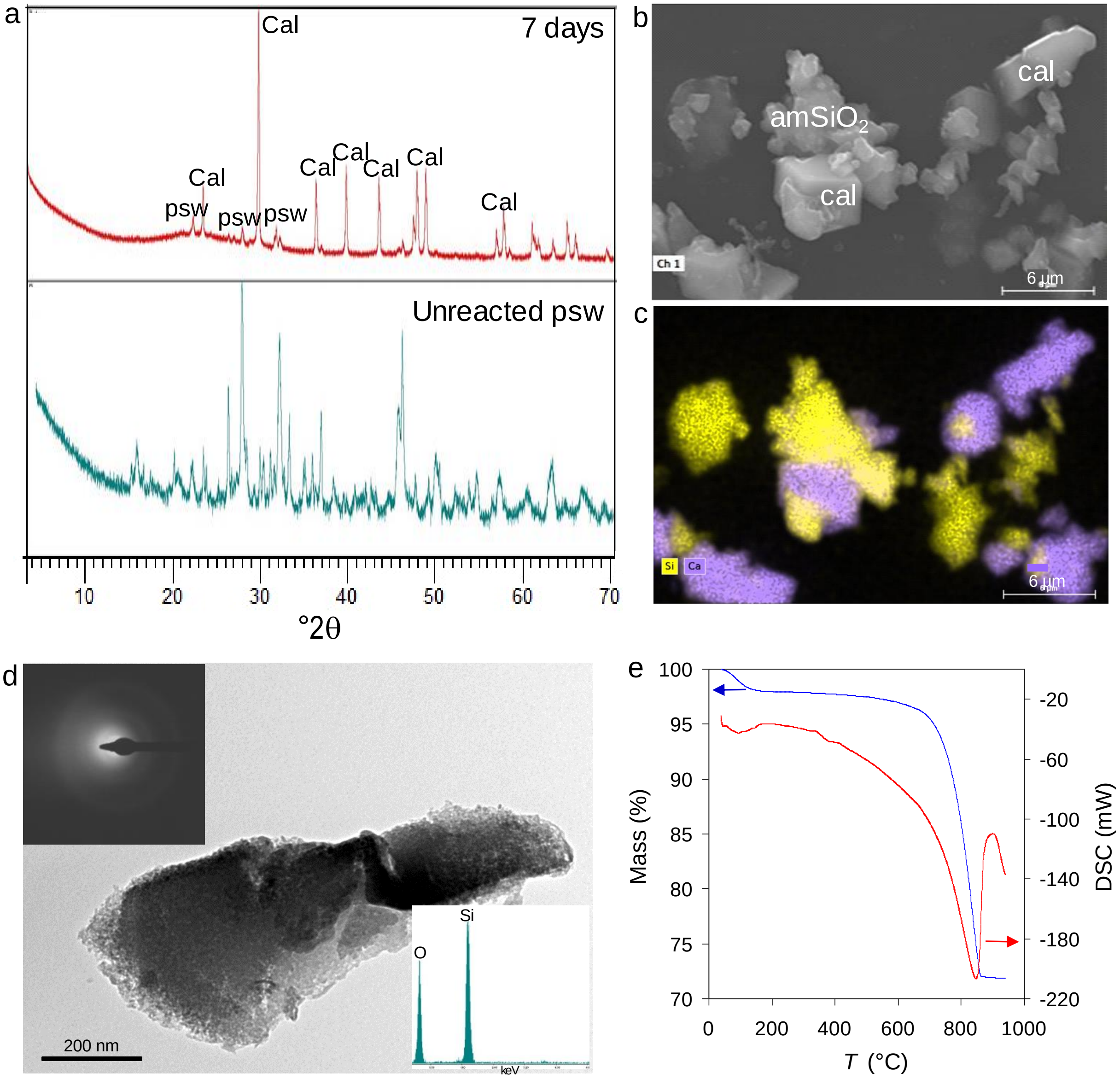

Figure III.19. Products of the reaction between psw and gaseous CO2 solutions. a) XRD patterns of unreacted and reacted (7 days) pseudowollastonite (psw). The main Bragg peak of psw and calcite (cal) are indicated; b) SEM image and c) corresponding EDS map of product phases; c) TEM image of amorphous silica (EDS spectrum and SAED pattern in insets); d) TG/DSC traces of solids reacted for 40 days.

In all cases, TG-DSC analysis of the reacted solids showed two endothermic bands corresponding to an initial small weight loss (2 wt%) at 100-150 °C due to water desorption from silica gel, followed by a marked weight loss at 600-900 °C, associated with CaCO3 decomposition (Fig III.20e). From the second weight loss, the amount of CaCO3 was determined to be 57.9 wt%, 56.4 wt% and 56.5 wt% for the case of pure water, NaCl and KCl solutions, respectively. Note that the wt% of solid NaCl and KCl determined measuring the mass change in reacted solids upon lixiviation of the soluble halide salts un DI water was detracted from the total sample mass during calculation of the weight loss associated to calcite thermal decomposition. This implies that in all cases the amount of amorphous silica was 43.3-46.2 wt%, values that slightly exceed the maximum theoretical yield of amorphous silica following reaction (1), which is 37.5 wt%. This discrepancy is due to the fact that amorphous silica included adsorbed/bound H2O and that a small fraction of psw was not transformed (see Table 2), both contributing to the total mass of the samples analyzed using TG. Overall, these results show that the CaCO3 yield was 90.2-92.6 mol%.

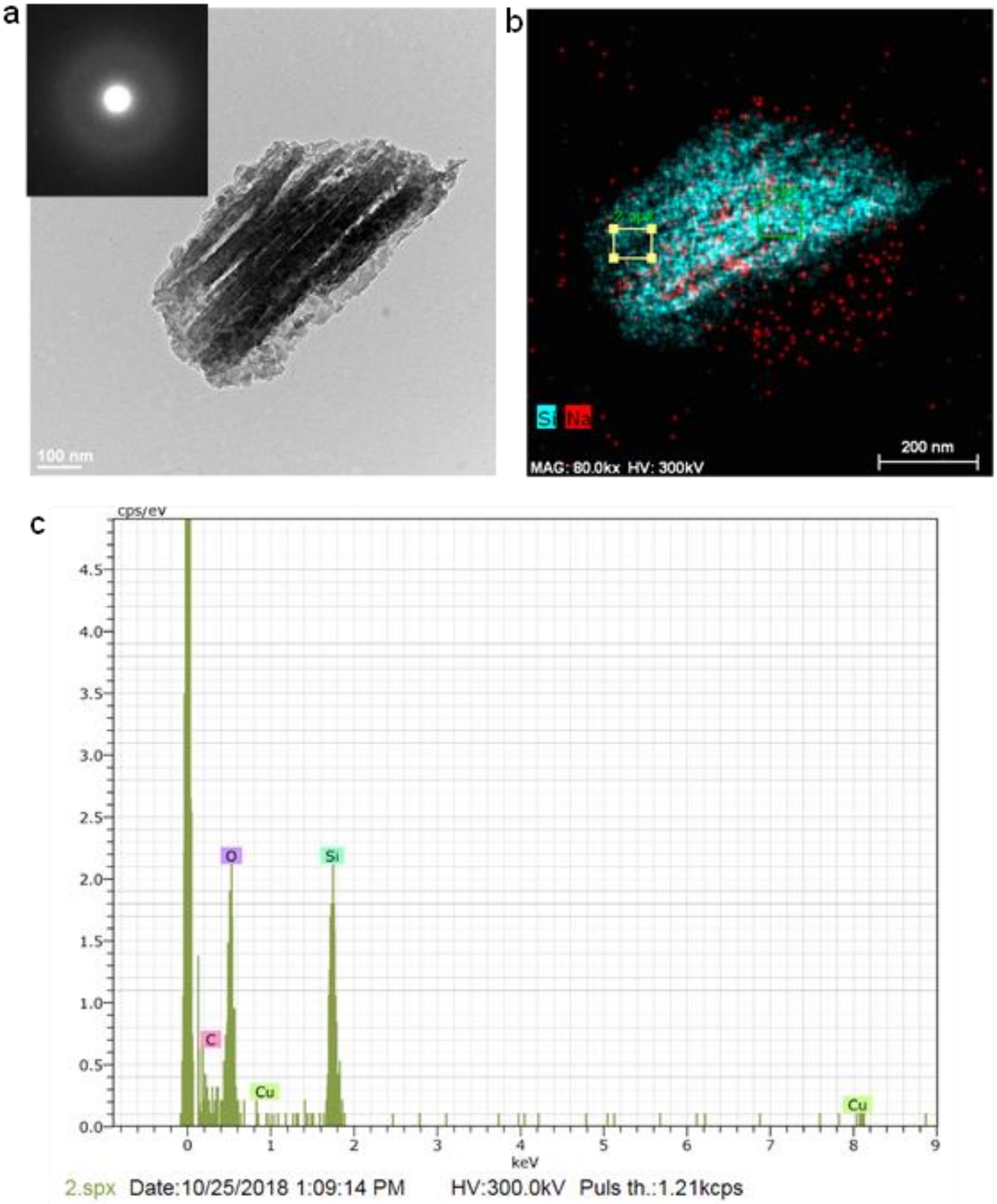

Figure III.20 a) TEM image of a psw pseudomorph fully transformed into highly porous amorphous silica (SAED pattern in inset) following carbonation in the presence of gaseous CO2 in NaCl solution; b) HAADF-EDS map of Si and Na distribution of the pseudomorphs in (a); c) EDS spectrum of analysis point #2 in (b) (yellow square).

In contrast, the Rietveld analysis using an internal crystalline standard showed that the amount of amorphous phase was only 26 wt%, whereas that of calcite and psw were 70 wt% and 4 wt%, respectively (Table III.2). This yields a CaCO3/SiO2 mass ratio of 2.69, which is significantly higher than the theoretical ratio of 1.66 in reaction (1), and therefore it is not consistent with the stoichiometry of psw carbonation via such a reaction. It is likely that the presence of a large amount of amorphous phase in this sample led the Rietveld method to underestimate its content and to overestimate the content of calcite.

ATR-FTIR analyses confirmed that all reacted samples included calcite (prominent carbonate bands at 1400, 868, and 714 cm-1) and hydrated amorphous silica (broad bands at 3400, 1064, 940, 798, and 458 cm-1) (Figure III.21).

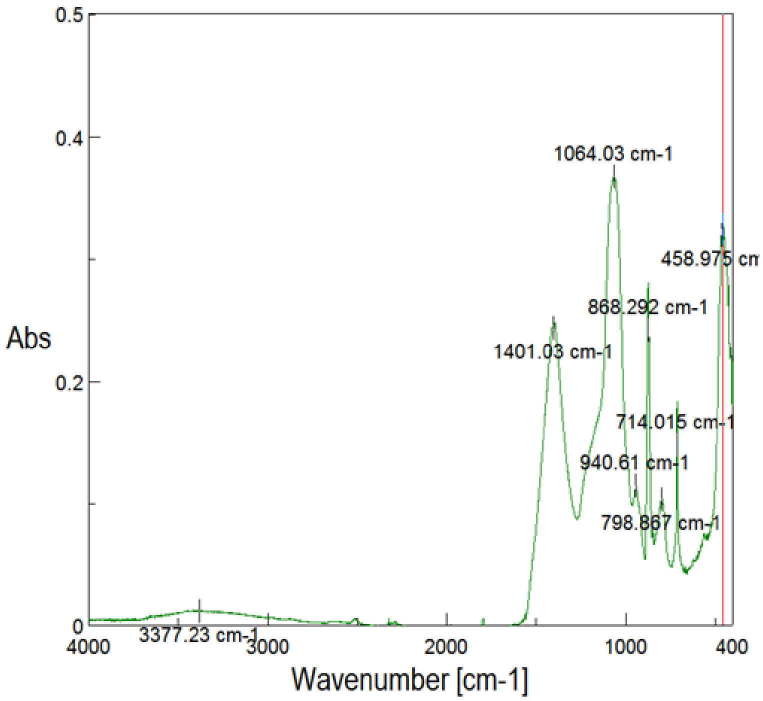

Figure III.21 ATR-FTIR spectrum of psw subjected to carbonation in gaseous CO2 aqueous solution for 7 days (note that similar spectra are obtained in DI water, NaCl and KCl solutions).

It should be noted that the pH of the solutions in contact with the reacted solids (i.e., after completion of the carbonation run) ranged from 9.08 (KCl solution) up to 9.34 (NaCl solution). Those values were substantially lower than those reached at the end of the carbonation runs under alkaline conditions (see Figure III.6c).

III.3 The effect of monovalent cations during psw carbonation

Simple chemical reactions are often described in terms of the transition state theory (TST) (Lasaga 1998; Putnis 1992) and mineral replacement reactions could be included in the range of validity of this theory, with some restrictions. The main one is that the physical meaning of the activation energy cannot be directly attributed to a particular spatial configuration between substrate and reactant, because it corresponds to a combination of many factors (related to dissolution, mass transfer, precipitation and growth processes). In the framework of this theory, for a simple reaction such as A + B = C, the Gibbs free energy difference between reactant and product phases represents the thermodynamic driving force of the process, and the activation energy corresponds to a kinetic barrier that should be overcome to reach equilibrium. Applying TST to describe the equilibrium in this system, it could be described the process of psw carbonation as a combination of the reactions for dissolution of psw and precipitation of calcite (according to the solution species and solubility products definition of llnl.dat database included in PHREEQC software):

$HCO_3^- + Ca_2^+ = CaCO_3 + H^+$ at equilibrium: $1/K_{s,cal}$ (III.1)

$CaSiO_3 + 2H^+ = Ca_2^+ + SiO_2 + H_2O$ at equilibrium: $K_{s,psw}$ (III.2)

$CaSiO_3 + HCO_3^- + H^+ = CaCO_3 + SiO_2 + H_2O$ at equilibrium: $K_r =:K_{s,psw} \cdot \frac{1}{K_{s,cal}}$ (III.3)

where $K_{s,cal}$ and $K_{s,psw}$ are the solubility product of calcite and psw, respectively, and K_r is the overall reaction constant. These equations can be solved using PHREEQC and, adjusting solution pH by adding an acid (e.g., HCl) or a base (e.g., NaOH), the moles of calcite and pseudowollastonite at equilibrium can be determined as a function of pH. Figure III.22 shows the mol% of psw and calcite at equilibrium calculated in this way. It can be seen that, for a final pH > 11, psw is more abundant than calcite at thermodynamic equilibrium. Even in the presence of enough inorganic carbon to completely replace the initial amount of psw, the low solubility of the pristine mineral under these conditions, does not (in theory) allow carbonation to proceed significantly. This is consistent with the results of these dissolution experiments showing very limited phase transformation.

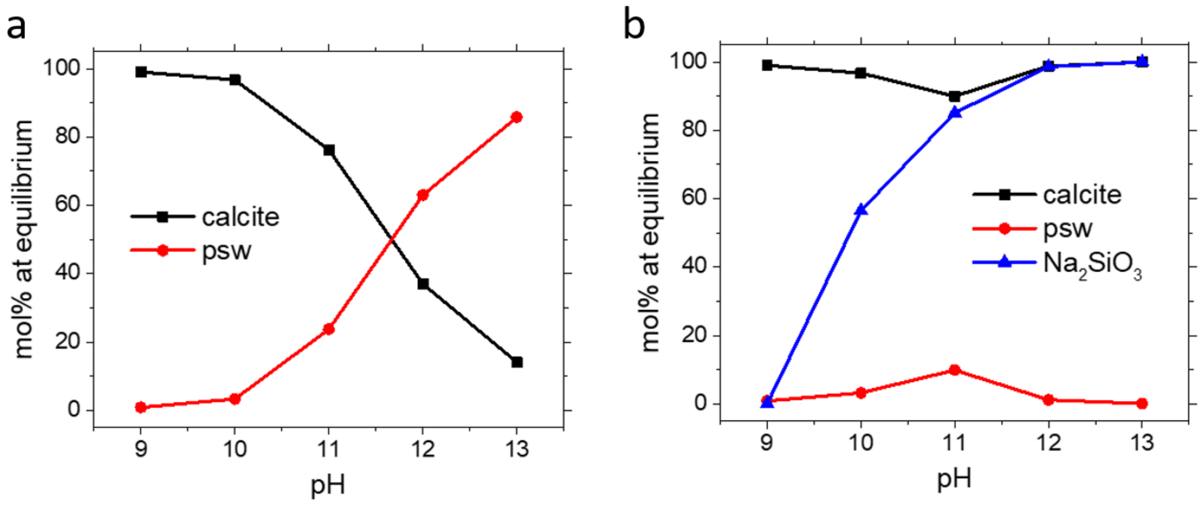

Figure III.22. PHREEQC simulation of phase evolution with pH: a) calculated mol% of psw and calcite at equilibrium; and b) mol% of psw, calcite and sodium silicate phase at equilibrium. Simulations performed at 150 °C, 1 mL of H2O, 0.0043 mol of initial psw (LLNL.dat database). Note that in (b) it has been simulated an increase in total moles with pH (up to 0.0086; i.e., double the amount of moles of psw at the start of the simulation) because a new silicate phase incorporating Na formed.

To my knowledge, no solubility data are available for pectolite, so it could not include this phase in equilibrium calculations. To overcome this limitation, it has been used here a Na-bearing silicate phase such as Na2SiO3 as an approximation to simulate qualitatively the effect exerted by precipitation of pectolite as a sink for sodium and silicate ions released to the aqueous solution after psw dissolution. Figure III.22b shows the same equilibrium calculation described above, but now including the possibility for Na_2SiO_3 to form in the system. In this latter case, the thermodynamic driving force to replace psw by calcite is higher under highly alkaline pH conditions. The final assemblage is mainly constituted by calcite and secondary silicates over the whole pH range considered, whereas psw is almost fully consumed. Thus, these experimental results demonstrate the crucial influence exerted by side reactions (e.g., precipitation of secondary silicates) on the control of the overall carbonation process which leads to psw replacement by calcite. The same rationale is applicable for the case of K-bearing carbonate solutions, although in this case and according to these experimental results the formation of secondary K-containing crystalline silicates is limited (only form in run C3). The alkali metal ion-containing amorphous silica phase can also be considered as a side-reaction product that would favor psw conversion in both the Na-and K-containing systems. Similarly, the precipitation of secondary (crystalline) Ca-silicates under alkaline conditions would also favor the conversion of psw, but this phenomenon will result in a less efficient carbon sequestration due to the reduction in the amount of divalent cations able to form sparingly soluble carbonate minerals in this closed system. The alkali metal ion containing amorphous silica phase can also be considered as a side reaction product that would favor psw conversion in both the Na- and K-containing systems, although its effect should be less marked due to its higher solubility at the alkaline pH of these runs.

It should be noted that previous studies reported that addition of a mixture of NaCl and NaHCO3 (or KHCO3), or NaHCO3 alone, during ex situ aqueous silicate mineral carbonation at high pCO2 (up to 200 bar) and T (up to ~180 °C) substantially increased the extent of carbonation by acting as a sort of catalyst (O'Connor et al., 2004; Tai et al., 2006; Chizmeshya et al. 2007; Eikeland et al., 2015). However, Gadikota et al (2014) demonstrated that while NaCl had a very minor effect of carbonation extent (of olivine), NaHCO3 had a major effect, which according to the authors was not due to a catalytic effect but to its capacity to buffer the pH. These results show that in addition to a possible buffering effect, the formation of secondary (crystalline) silicate phases is a major player favoring carbonation of silicates (with some restrictions associated with the formation of secondary Ca-silicate phases: see below). Note that in the gaseous CO_2 experiments, the presence of NaCl or KCl, which resulted in the formation of no secondary crystalline silicates, did not increased the conversion of psw into calcite. Rather, a slight decrease in the conversion was observed as compared with the salt-free run. This might be due to the decrease in water activity of the solutions associated with the high ionic strength conditions. Nonetheless, it has been reported that in the case of olivine carbonation, the presence of NaCl increased the dissolution rate of this magnesium silicate because this salt might hamper the formation of passivating SALs (Wang and Giammar, 2012). It also must be due to the reported reduction in CO2 solubility with increasing ionic strength (Duan and Sun, 2003).

The nature of the “background” monovalent cation significantly influences the progress of the progress of psw carbonation. Comparing the advancement of the carbonation reaction, given by the time evolution of the total wt% of psw and carbonates in the solid assemblage after reaction for the different experimental conditions used in this study (Rietveld XRD results), different features of the psw-solution interaction can be described. In the experiments conducted using a

Na-bearing carbonate sources (C1 and C2), complete psw transformation is achieved in less than 2 weeks and the amount of CaCO3 formed is 39 wt% and 35 wt%, respectively (TG results). Note that parawollastonite, plombierite and tobermorite do not include Na ions in their structures, so it could be argued that their formation would not contribute to scavenge Na from the solution, so that their precipitation would not strongly affect the progress of the carbonation reaction. However, in these two systems (C1 and C2), the formation of abundant pectolite (and shortite in C2) helped to bypass this possible handicap. Note also that the newly formed amorphous silica included a fraction of Na (up to a Na/Si mol ratio of 0.29 in C2 run) which could also favor this process. Moreover, precipitation of secondary crystalline Ca-silicates, also contributes to shift the equilibrium in reaction (1) to the right. All these combined effects explain why full consumption of psw takes place in runs C1 and C2. In contrast, in the case of experiments with a K-bearing carbonate sources (C3 and C4) full transformation of the initial psw was not reached even after 40 days. A passivation mechanism due to SALs formation could explain the lack of full psw conversion. However, this is ruled out, because no SALs were observed developing on psw, neither in C3 and C4 runs, nor in C1 and C2 runs. The incomplete conversion of psw in runs C3 and C4 appears to be related to the fact that a limited amount (C3) or no (C4) secondary K-bearing (and Ca-bearing) crystalline silicate phases formed under these experimental conditions. In the case of run C3, however, the amount of calcium carbonate formed at the end of the experiment was higher (44 wt%) than in runs C1 and C2. In addition to the relatively low alkaline pH at the start of the experiment, which favored psw dissolution, the relatively high carbonate yield in experiment C3 appears to be due to the fact that the delayed formation of crystalline K+Ca-silicate (shlykovite) favored the, yet incomplete, conversion of psw. Although this secondary silicate phase included Ca, its amount was relatively minor and, in addition, the amorphous silica product phase had a negligible amount of Ca (i.e., Ca/Si mole ration of 0.07), which limited the amount of Ca that was not incorporated into the structure of carbonates. In the case of run C4, the absence of an effective sink for both silicate and K+ ions other than amorphous silica, hampered the progress of the overall carbonation reaction, yielding only 21 wt% CaCO3 (TG results) along with residual kalicinite. If it is compared the amount of total Ca and Si in solution between the two high pH runs (C2 and C4), it is observed that both ions accumulated to a larger extent in the K-containing runs compared with Na-bearing runs (Figure III.6a and b). As a result, the dissolution of psw was hampered due to the continuous decrease in the driving force for dissolution (i.e., the undersaturation of the solution with respect to psw) and, consequently, the overall rate of psw carbonation. This suggests that Na+ ions accelerate the precipitation of insoluble secondary crystalline phases incorporating Ca and Si, thus depleting their concentration in solution faster and more efficiently than through the sole precipitation of more soluble calcite and amorphous silica, as occurs in the K_2CO_3 system. These results for the highest pH runs (C2 and C4) thus demonstrate that the enhancement of psw dissolution and subsequent carbonation is cation-specific. However, enhanced psw dissolution at a lower initial pH as that induced by KHCO3 or NaHCO3 somehow masked the role of the background alkali metal ion in the progress of psw carbonation. Still, it was clearly observed that the extremely high Si concentrations in KHCO3 solutions at the early stages of reaction (< 7 days) were associated with the lack of precipitation of secondary silicate phases. These results show that in the case of the mildly alkaline runs, K+ ions hampered the precipitation of secondary silicates thereby delaying/limiting psw conversion. Why Na+ ions do foster the formation of secondary crystalline silicate phases (i.e., more insoluble than amorphous silica, specially at the highly alkaline pH reached during the final stages of the experiments), whereas K+ ions are less effective in this respect? Likely this is due to thermodynamic and/or kinetic constraints that hamper the precipitation of K-containing silicates (other than K-containing amorphous silica) under these experimental conditions. Interestingly, it has been shown that during zeolite and geopolymer synthesis using highly alkaline NaOH and KOH solutions, NaOH demonstrates a greater capacity to liberate silicate (and aluminate) monomers from reactant (alumino)silicates, Na+ ions also demonstrating a greater capacity to act as "structure builders" favoring the formation of insoluble crystalline product phases (e.g., zeolites) (Duxson et al., 2007). Conversely, K+ ions are shown to hamper the formation of crystalline phases and to favor the polymerization of silica, thereby contributing to the precipitation of amorphous silica incorporating this cation (Duxson et al., 2007). It is very likely that ion size and ionic potential differences are at the root of the contrasting effects of these two alkali metal ions (see Duxson et al, 2007, and references there in). These observations are in full agreement with these experimental results showing a contrasting behavior between Na- and K-containing (bi)carbonate solutions.

The presence of kalicinite (KHCO3) in the final mixture of run C4 confirmed that potassium was not easily hosted in secondary silicate phases and, consequently, it was available for re-precipitation as a secondary soluble carbonate (i.e., not efficient for the safe long-term storage of CO2). Further studies will explore the effect of introducing other multivalent ions (in particular Al3+) in the reaction solution, as they could favor K-bearing aluminum silicates to form thus enhancing psw carbonation in the presence of potassium at alkaline pH.

III.4 Effect of secondary phases on carbonate yield under alkaline conditions

Five secondary crystalline silicate phases formed in runs C1, C2 and C3 include Ca in their structure (i.e., parawollastonite, pectolite, plombierite, tobermorite and shlykovite), in addition to Ca-containing amorphous silica (formed in all alkaline runs). This represents a handicap for an effective capture of CO_2, because incorporation of alkaline earth metals in secondary silicates, both crystalline and amorphous, reduces carbonation yield (Hellmann et al., 2013; Sissmann et al., 2013, Plattenberter et al. 2018, 2019). In this respect, however, there are two important aspects to consider. First, as discussed above, the formation of secondary crystalline silicate phases favors the dissolution of psw and the amount of these newly formed phases is in general minor, with the exception of pectolite, especially in the Na2CO3 system. The latter helps to explain why the amount of CaCO3 (calcite plus CaCO3 in shortite) formed in the Na2CO3 systems was smaller than in the NaHCO3 system, despite the full consumption of psw in both runs. And, second, because the Ca/Si mol ratio is higher in psw (1/1) than in plombierite (2.5/3), pectolite (2/3), tobermorite (2/3) and shlykovite (1/4), upon dissolution of the former there is still a significant amount of Ca that does not get trapped in the crystal structure of the secondary Ca-, Ca+Na- and K+Ca-silicates and which can be incorporated into CaCO3. Similarly, in the case of Ca-containing amorphous silica the Ca/Si mol ratio was lower (up to 2/3) than in psw.

These considerations not only explain why the carbonate yield in systems C1–C3 was relatively high (> 56 mol%), but also help to explain why in run C3 the highest conversion (70 mol%) of all alkaline carbonation runs was achieved (despite the incomplete conversion of psw). This is so because: (i) shlykovite has the lowest Ca/Si molar ratio of all secondary crystalline silicates; (ii) amorphous silica in this run includes the smallest amount of Ca of all alkaline runs; and (iii) the observed delayed precipitation of secondary K+Ca-silicates enabled the early incorporation of all released Ca into the carbonates (i.e., calcite plus aragonite), consistent with the very low total Ca in solution detected by ICP-OES analysis and the abundant CaCO3 (calcite plus aragonite) detected by XRD during the first two weeks of the run. Overall, and despite the fact that the formation of secondary crystalline K+Ca-silicates in run C3 was more limited than the formation of Ca and Na+Ca-silicates in run C1 or C2, it was still sufficient to achieve a significant degree of psw conversion as to result in the highest carbonate yield of all alkaline runs. Finally, it is obvious that the formation of parawollastonite after psw does not contribute to the mineral capture of CO2. However, the amount of parawollastonite formed in these experiments (C1 and C2) is relatively minor (≤14 wt%).

In the case of the Na2CO3 system, the amount of Na is double than that present in the NaHCO3 system. The most direct effect of such a higher Na concentration in the former system is the increase in the amount of newly-formed Na-containing secondary silicates such as pectolite, and the formation of abundant shortite instead of calcite. It could be argued that being shortite a relatively soluble double carbonate (Fahey, 1962), CO_2 would not be stored in a safe and/or permanent way in this carbonate. However, it is known that shortite dissolves incongruently (Fahey, 1962), one mole of shortite yielding one mole of (soluble) Na2CO3 and two moles of (sparingly soluble) CaCO3 (calcite). There is laboratory and field evidence showing that shortite can be pseudomorphically replaced by calcite (Fahey, 1962; Jagniecki et al., 2013), this latter phase representing a net, stable carbon sink. In any case, these results show that the lower initial pH of the NaHCO3 system as compared with the Na2CO3 enabled a more efficient CO2 capture.

Finally, in the KHCO3 and K2CO3 systems, in addition to the above indicated limited transformation of psw, the carbonation yield is also limited by the incorporation of Ca into the shlykovite, minor plombierite and the abundant silica gel phase, whose formation was not sufficiently efficient as to enable the full conversion of psw. Nonetheless, the observed delayed incorporation of K into K-silicate crystalline phase and amorphous silica, helps to explain why the carbonate yield in run C3 was higher than in C1 run (for an equal starting pH of ~9). First, such a delayed precipitation of secondary silicates enabled the early incorporation of all released Ca into the carbonates (i.e., calcite plus aragonite). Second, despite the fact that the formation of shlykovite was more limited that the formation of Na/Ca-silicates in run C1, it was still sufficient to achieve a significant degree of psw conversion. Finally, in run C3, the amount of secondary Ca-silicates (plombierite) was relatively minor (15 wt%), thus a large fraction of Ca released after psw dissolution was incorporated into CaCO3.

In addition, the precipitation of secondary silicates in CCS systems have an important impact on the permeability reduction (Plattenberger et al. 2019), favoring the formation of a barrier to prevent the migration of the injection fluids used in CCS. Furthermore, this study also aims in K+ effect on mineral carbonation systems so it can be assumed a reduction of porosity in this system. This effect is orders of magnitude lesser in CO2 systems, where no Ca or K silicates are precipitated so it can be infered that the precipitation of secondary silicates is an advantage on porosity control.

III.5 The effect of pH and silica precipitation

Silicate dissolution (and thus the release of cations to the solution from the silicate substrate) is a process that strongly depends on pH (Figure III.4). The concentration in solution of silicate-derived divalent cations available for carbonate precipitation is expected to be considerably higher at moderately alkaline pH than in highly alkaline conditions. However, these results show that while the Ca] in solution was higher in the NaHCO3 solutions than in the Na2CO3 or K2CO3 solution, it was the lowest in the case of KHCO3. Moreover, the carbonation experiments carried out in Na2CO3 and NaHCO3 solutions did not show significant variations in terms of psw reaction rate, despite the different initial pH of these two carbonate solutions. Probably, the effect of pH in this case was masked by the influence exerted by other parameters, such as the pH-dependent species distribution and secondary phase formation. In contrast, the carbonation rate of solutions containing KHCO3 (pH ~ 9) was significantly higher than those containing K2CO3 (pH ~ 13), in full agreement with the pH-dependency of CaSiO3 dissolution rates (Schott et al., 2012). In this case, the most likely explanation for the very low Ca concentration in solution measured all along the carbonation experiment is the rapid incorporation of this divalent metal ion into calcium carbonates.

The experiments performed at high pCO2 demonstrated that the conversion of psw into calcite was very fast as compared to the experiments performed using an aqueous carbonate source. The pH of an aqueous solution in equilibrium with pCO2 = 12.6 bar at 373 K (i.e., the initial conditions in the hydrothermal reactor) was calculated to be 3.7 (Peng et al., 2013). Such an acidic solution favored the massive dissolution of psw, which consumed protons (two moles of H+ per mole of dissolved psw; see Di Lorenzo et al., 2018), thereby increasing the pH and resulting in the precipitation of calcite along with amorphous silica. Indeed, after 7 days the reaction was almost complete. Apparently, the very low pH of the initial solution led to extremely high reaction rates that enabled to bypass the thermodynamic constrains existing at higher pH (see Figure III.4). As a result, the precipitation of secondary alkali metal-, Ca- or Ca+alkali metal-silicates was not required to enable the (nearly) full conversion of psw. According to these results for runs C1, C2 and C3, Na- or K-containing silicate phases such as pectolite or shlykovite could form in NaCl- and KCl-containing runs. However, note that precipitation of pectolite reportedly occurs at the highly alkaline conditions achieved during hydrothermal cement setting/curing and shlykovite only precipitate under highly alkaline conditions (Vail, 1952).

Although a direct comparison with the experiments at alkaline pH cannot be performed due to the different experimental conditions, experiments with gaseous CO2 provide interesting information regarding the influence of silica formation on the progress of the carbonation reaction. In particular, it is remarkable that the extensive formation of silica did not prevent psw from being almost completely carbonated. This points to an uncoupled dissolution-precipitation mechanism for psw-silica conversion. Previous studies have systematically reported the formation of passivating amorphous silica or SALs during the dissolution and carbonation of primary silicate minerals (e.g., Bailey and Reesman 1971; Bearat et al., 2006; Huijgen et al. 2006; King et al., 2010; Schott et al. 2012, Ruiz-Agudo et al. 2012, 2016, Power et al., 2013; Di Lorenzo et al. 2018, Plattenberger et al. 2018). Two different mechanisms for SALs formation have been proposed: (i) interface-coupled dissolution-precipitation, by which the dissolution of the silicate mineral in an undersaturated solution induces the formation of a boundary layer rich in Si ions and, as a consequence, supersaturation with respect to amorphous silica is locally achieved, leading to amorphous silica precipitation (Putnis 2009, Ruiz Agudo et al. 2012, 2016); and (ii) ion-exchange, by which exchange between H+ from solution and divalent cations in the silicate structure leads to the formation of a relict layer of silica (the so-called "leached layer") at the solution-mineral interface (Casey et al. 1993, Schott et al. 2009, 2012). Both mechanisms result in the formation of SALs, but they present a substantial difference. If the process is an interface-coupled dissolution-precipitation, the relative rate of the reactions could be potentially tuned geochemically (catalysts or inhibitors) to uncouple the individual reactions and to achieve a complete mineral replacement despite the potential passivation exerted by silica (Di Lorenzo et al., 2018). In contrast, the possibility to control ion exchange phenomena at the solution-mineral interface is limited to the control of the pH during the process.

The very fast dissolution of psw, and the increase in silica solubility with increasing pH would facilitate such an uncoupling. However, TEM observation of a few, relatively large (≥300 nm thick) psw pseudomorphs fully transformed into porous aggregates of amorphous silica nanoparticles suggests that a tight interface-coupled dissolution-precipitation mechanism was also at work here (Ruiz-Agudo et al., 2012, 2016). Likely, pseudomorphic replacement of psw by amorphous silica took place at the very early stages of reaction, when the pH was relatively low and silica solubility was at a minimum value. Such a process did not lead to passivation due to the high porosity of the silica pseudomorph.

Interestingly, SEM and TEM analyses revealed that amorphous silica in products recovered after gaseous CO2 runs partially covered calcite crystals. This means that a fraction of amorphous silica precipitated after calcite precipitation. This implies that a significant amount of the released silica remained in solution at the alkaline conditions reached after psw dissolution (see above) and only precipitated after the pH decreased following calcium carbonate precipitation (a reaction that releases protons). Indeed, PHREEQC simulation shows that while at pH≤5.5, saturation with respect to amorphous silica was achieved earlier than saturation with respect to calcite, which helps to explain why amorphous silica psw pseudomorphs formed (during the earlier stage of carbonation), at pH≥6 the situation reverted in gaseous CO2 experiments, thereby enabling the precipitation of calcite before amorphous silica (Figure III.23). Note that a pH of 6 was reached after dissolution of just 2.3 mol% psw (Fig. 8), which shows that most calcite formed before amorphous silica at pH≥6. In contrast, silica formed in all alkaline experiments included Ca, which suggests that in such experiments amorphous silica formation took place not only after CaCO3 precipitation (e.g., veil of amorphous silica around aragonite crystals formed during the early stage of carbonation) but also concomitantly to CaCO3 precipitation.

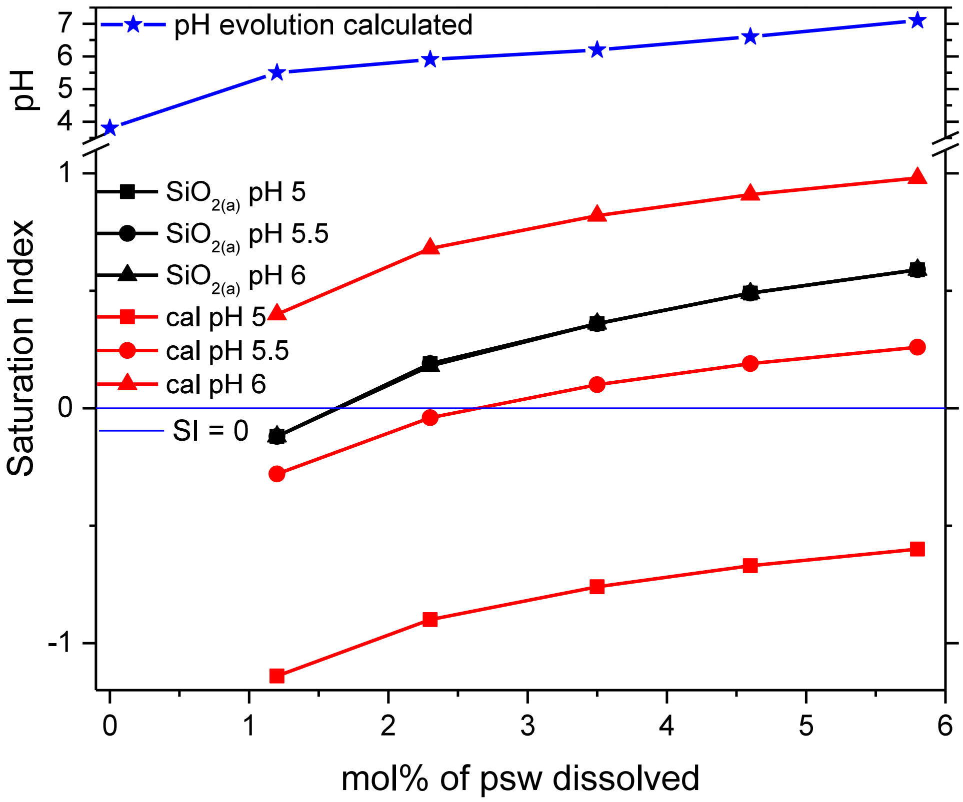

Figure III.23. PHREEQC modeling of the evolution of calcite and amorphous silica saturation index (SI=log(IAP/Ksp), where IAP is the ion activity product and Ksp is the solubility product of a relevant phase) as well as pH during gaseous CO2 hydrothermal carbonation of psw ([psw]=0.043 mol; VH2O=0.15 L; pCO2=10 bar; Vgas=0.15 L; T=150 °C). The modeling shows that calcite precipitation can precede amorphous silica precipitation at pH≥6. Note also the significant pH increase achieved with just a few mol% conversion of psw.

The absence of passivating SALs formation under these conditions, however, could only partially be extrapolated to other silicate minerals because psw has a very high solubility and very fast dissolution kinetics compared to most natural silicates (Schott et al., 2012). It is likely that for other less reactive silicates such as feldspars, serpentine, olivine and pyroxenes, passivation via SALs formation would be the rule, not the exception, due to the coupling of the dissolution-precipitation reactions. This is consistent with the results of several carbonation studies (Béarat et a., 2006; King et al., 2010; Daval et al., 2011; 2012; Wang and Giammar, 2012; Sissmann et al., 2014). It should be noted, however, that because silicate dissolution consumes protons, the alkalinization taking place as carbonation progresses would affect the formation of passivating SALs under real-case CCS scenarios, with lower reaction rates than those typical for laboratory conditions, relevant for ex situ mineral carbonation (Gadikota et al., 2014). It is very likely that following alkalinization and the decrease in reaction rates, SAL formation would be promoted in the case of primary silicates with lower reaction rates than psw (Ruiz-Agudo et al., 2016).

It should be noted that previous studies on the carbonation of both wollastonite (Whitfield and Mitchell, 2009; Huigens et al., 2006) and psw (Bukowski and Berger, 1979) concluded that Ca leaching leading to a passivating Ca-depleted amorphous silica layer was the dominant process during the dissolution of these two calcium silicate minerals prior to carbonate precipitation. In the case of wollastonite, growing evidence shows, however, that this is not the case, being the stoichiometric, congruent dissolution of wollastonite and the subsequent precipitation of a SAL on the dissolving silicate surface the main dissolution mechanism preceding carbonate precipitation over a range of initial pH conditions and carbonate sources (Daval et al. 2009; Di Lorenzo et al. 2018). These results show that the latter mechanism also applies for the dissolution and subsequent carbonation of psw both at acid and alkaline pH.

III.6 Polymorphic transformations during pseudowollastonite carbonation.

Because pseudowollastonite is the high-T polymorph (α) of $CaSiO_3$, under these experimental T/P conditions it should undergo a polymorphic transformation into the more stable low-T (β) polymorph. If such a transformation were to occur via a solid state mechanism, as it is commonly assumed for nearly all polymorphic transitions in silicates (Putnis, 1992), it would be very slow under these relatively low T experimental conditions. Indeed, these experiments in NaOH and KOH solutions demonstrated that such a transformation did not take place during the time scale of these experiments. Remarkably, it has been identified the formation of parawollastonite (β-$CaSiO_3$) during the carbonation experiments using Na-containing solutions, but not in K-containing solutions. The formation of this polymorph only in these experiments seems to be related to the high reactivity showed by psw under these conditions (i.e., fastest psw consumption rate). The crucial influence exerted by the chemical composition of the aqueous phase (i.e., presence vs. absence of carbonate ions at a similar pH) on the α- to β-$CaSiO_3$ polymorphic transformation could be difficult to explain by assuming a solid-state mechanism. On the contrary, a dissolution-precipitation mechanism could readily explain the formation of the β-$CaSiO_3$ polymorph by considering the high supersaturation with respect to this phase that could be achieved in the presence of carbonates due to the massive psw dissolution. Moreover, the formation of needle-shaped $CaSiO_3$ crystals (detected by SEM-EDX) in the systems where parawollastonite formation was identified by XRD, a morphology not present in the unreacted psw, strongly supports the notion that the polymorphic transformation in this silicate system takes place via a dissolution-reprecipitation mechanism under these experimental conditions. Previous studies (Platenberger et al. 2018 and 2019) did not achieved to explain this polymorphic transformation between both minerals and interpreted as a secondary CCSH. To the best of these knowledge, this is the first time that such a dissolution-precipitation mechanism has been reported for the polymorphic transformation of a silicate mineral at mild T-conditions (150 °C).

Another polymorphic transformation also took place in the system but in this case between two calcium carbonate polymorphs, calcite and aragonite. Aragonite, the orthorhombic polymorph of CaCO3, only formed in the carbonation experiments using NaHCO3 and KHCO3 solutions, which corresponded to the highest Si concentrations measured in solution. Aragonite has also been reported to precipitate along with pectolite following dissolution of Na-Ca-silicate glass in sodium carbonate solutions at 150 °C (Chen et al., 2005). Kellermeier et al. (2013) reported aragonite stabilization induced by high silica concentration in the crystallization medium. Similarly, Kellermaier et al. (2015) reported that another calcium carbonate phase, ACC, can also be stabilized by silica forming a protective layer around the precipitated nanoparticles. On the one hand this stabilization effect may help to explain why a metastable (highly unstable) amorphous phase such as ACC was still present in these samples after collection, storage and analysis. On the other hand, HAADF-EDS analysis in STEM mode showing the presence of a thin layer of silica covering the aragonite surface provides textural evidence for the possible role of silica in favoring the formation and (partial) stabilization of aragonite. It seems reasonable, however, that the low crystallinity and the small size of aragonite crystals made a fundamental contribution at determining the polymorphic transformation that undergoes aragonite in these experiments, leading to the formation via a dissolution-precipitation of the calcite rhombohedral crystals observed at latter stages of the experiments. To this silica-effect inducing the formation of aragonite, one must add the possible effect that the initial pH of the solution could play on the initial precipitation of aragonite. Tai and Chen (1998) report that at T > 50 °C and pH ≤ 10 aragonite formation is favored, whereas at pH > 10 calcite is formed. This helps to explain why only calcite formed in the Na2CO3 and K2CO3 runs, whereas aragonite and subsequently calcite formed in the NaHCO3 and KHCO3 runs. The final formation of calcite at the expenses of aragonite dissolution in the NaHCO3 and KHCO3 runs is fully consistent with the observed increase in the pH from ~9 to > 11 as the reaction progressed. Due to experimental constraints, it could not follows the time-evolution of calcium carbonate product phases during the gaseous CO2 runs, although it could be hypothesized that the high silica content in solution and the initial low pH could also favor the initial formation of aragonite followed by its transformation into calcite, which was the only carbonate present at the end of the runs.

III.7 Implications of psw carbonation

Interestingly, the very limited conversion of psw under these DIC-free experimental dissolution conditions, and its complete conversion in (some of) the DIC-inclusive experiments, demonstrate that DIC is necessary for the transformation of this calcium silicate. The implications of these results are manifold. For instance, they may have direct implications in the dissolution of psw bone implants in contact with carbonate-bearing body fluids (De Aza et al., 2000). They also have direct implications in CCS, showing that conversion of primary Ca- (and likely Mg-) silicates into carbonates requires the enhanced dissolution of the parent phase via a dissolution-precipitation process that shifts the equilibrium towards the carbonate and secondary silicate product phases.

Most importantly, these results show that the presence of alkali metal ions such as Na+, and to a lesser extent K+, as "background electrolytes" are critical for the effective transformation of reactant calcium silicate under alkaline conditions as they enable the crystallization of secondary alkali metal-bearing silicates, which shift the equilibrium towards the product phases. Nonetheless, the final carbonate yield may strongly depend on the formation of secondary Ca-silicates. The implications of these results on CCS are very important: (i) they show that the presence of Na+ (and K+) ions in injection fluids, as could be the case of the use of sea water (Wolff-Boenisch, 2011), mixing with saline formation solutions (Jun et al., 2012), or their release upon dissolution of primary silicates (e.g., feldspars and/or basaltic glass) (Matter et al., 2016), can have a profound effect on the carbonation of primary silicates: both on the formation of secondary phases as well as on the carbonate yield; and (ii) the simple case scenario typically studied for silicate carbonation using pure CO2-water solutions (King et al., 2010; Daval et al., 2009; 2012), or water-bearing supercritical CO2 (Daval et al., 2009), which might be directly applicable for ex situ mineral carbonation, is shown here to be an oversimplification for cases involving in situ CCS. This is due to the fact that such experiments can yield very high conversions (i.e., high carbonate yield) that may not be representative of real case scenarios during in situ CCS where both pure CO2-water solutions and supercritical CO2 will eventually mix with formation fluids and undergo reactive transport, altering the composition of the injected fluid. Indeed, after CO2 injection at the Carbfix site in Iceland, the solution mixed with the formation fluids, and its reaction with the host rock released different ions (e.g., K+ and Na+) and its pH rose as this reacting plume advected (Matter et al., 2016). Eventually, conditions likely similar to those of alkaline carbonation experiments could be reached, and in such a scenario, precipitation of multicomponent secondary silicates will play the above described role, favoring phase transformation. Formation of secondary silicates, such as clay minerals, in multicomponent silicate rocks enables a higher carbonation yield than experiments using a single silicate phase as reported by Sissmann et al. (2014) for the case of olivine carbonation within basalts as compared with single-phase carbonation of olivine. However, the formation of secondary silicate phases incorporating divalent metal ions would limit the maximum carbonation yield as it is observed here and in the field (Oelkers et al., 2019).

Interestingly, weathering of psw-containing paralavas in natural settings results in a mixture of tobermorite phases along with aggregates of calcite and calcium silicate hydrates (Seryotkin et al., 2012). This shows that natural weathering and carbonation of psw closely follows the trend observed here for the alkaline carbonation experiments, particularly those including Na as a background electrolyte. Remarkably, a strong cementation of the initial psw powder occurred upon its transformation into the product phases during carbonation experiments. The harder products, which were more difficult to extract from the reactors and to grind, were those carbonated at alkaline conditions, especially when Na was present in the reactant solution. Apparently, such a strong cementing capacity was not just due to the formation of calcite and amorphous silica, but also to the formation of secondary Ca-, Na+Ca- and K+Ca-silicates. The observed cementation may have a negative impact during in situ CCS as it would likely reduce host rock permeability. However, it might be highly positive in the case of novel cements with reduced CO2 footprint. Previous studies on the setting and hardening of the novel class of low Ca/Si cements based on wollastonite and/or psw have reported that their setting and hardening following carbonation result in a matrix composed by calcite (about 30 wt%) and a Ca-modified silica gel (Ashraf et al., 2017). The Ca-containing gel phase is similar to that observed here upon carbonation of psw in alkaline conditions. Interestingly, as pointed above, the formation of crystalline tobermorite-group phases as well as secondary Na+Ca- and K+Ca-silicates in these experiments led to harder products. Although the actual mechanical properties of the products obtained here were not quantitatively determined, the qualitative observations suggest that carbonation of low Ca/Si cements in the presence of sodium and/or potassium carbonate or bicarbonate solutions would be beneficial for the setting and hardening of such novel cements. It is expected that such crystalline secondary silicates would also form and contribute to strength development following carbonation of CaSiO3-based cements proposed to seal injection wells in deep geologic formations after geological carbon storage (Svensson et al., 2018), under conditions likely involving the presence of saline solutions (Matter et al., 2016). By being already carbonated, such cements with higher durability and weathering resistance than OPC (Farnam et al., 2016) will not necessarily have the problems of OPC, which degrades upon carbonation, a process that can result in CO2 leaking (Matteo and Scherer, 2012) leading to significant environmental risks (Jun et al., 2013).

Chapter IV. Kinetics and mechanisms of the acidic weathering of pyroxenes

IV.1 ATR-FTIR analysis and silicate species distribution in unreacted and reacted pyroxenes.

Pyroxenes in space group C2/c such as diopside or augite have three different oxygen positions in their structure: the apical non-bridging oxygen O1; the side non-bridging oxygens (nbr) O2 and the bridging oxygen (br) O3, affecting the position of the FTIR bands (Omori, 1971). ATR-FTIR spectra of unreacted materials (Figure IV.1a) shows two invariant bands at ca. 630 and 670 cm^{-1}, corresponding to $O_{(nbr)}$-Si-$O_{(nbr)}$ bending and a mixed stretching-bending mode of Si-O-Si bridging bond (Richet et al., 1998 and references therein). It can be also observed a broad band spanning from ~929-760 cm^{-1} in augite and 892-705 cm^{-1} in diopside that corresponds to the v_3 asymmetric stretching of Si-O (Figure IV.1a). Finally, two bands located at 1052-1066 cm^{-1} and 958-959 cm^{-1} corresponding to the Si-O-Si stretching vibration and the v_3 vibration of Si-O bond in crystalline silicates, respectively, are also observed.

After augite batch dissolution experiments, the bands located at 632 and 670 cm^{-1} remain basically unaltered, although they appear less defined and with lower intensity. However, the v_3 Si-O asymmetric stretching band suffers a broadening as compared with the v_3 band of the unreacted material, changing from ~929-776 cm^{-1} to ~893-682 cm^{-1} and a reduction in intensity. This suggests an increase in the amorphous content in the reacted crystal, probably related to the presence of SiO_2(am) or CSH (Sáez Del Bosque et al., 2014; Ashraf and Olek, 2016). Furthermore, the 958cm^{-1} band shifts to higher wavenumbers in the weathered material. This would suggest an increase in the contribution of the Si – (OH) vibration from $Si(OH)_4$ monomers (Yang et al., 2008), in agreement with the formation of amorphous silica (Richet; Ashraf). Finally, the band at 1052cm^{-1} shifts to 1061cm^{-1}, which indicates again an increase in the degree of polymerization. All in all, these results support the formation of SiO_2(am) in the system (Richet et al., 1998; Mozgawa et al., 2004; Saez del Bosque et al., 2014; Ashraf and Olek, 2016). In the case of diopside, after batch dissolution experiments (Figure IV.1b) the bending and stretching bands of Si-O-Si bonds (630 and 670 cm^{-1}) appear invariant. These results are in full agreement with the bands reported in amorphous silica and CSH in previous works (e.g. Omori, 1971; P. Richet et al., 1998; Sáez del Bosque et al., 2014). As in the case of augite, the v_3 asymmetric stretching of Si-O bond (~892 - 705 cm^{-1} in unreacted diopside) suffers a shift and broadening to ~858-683 cm^{-1} suggesting the presence of amorphous silica (Vicente-Rodríguez et al., 1996; Sáez Del Bosque et al., 2014; Ashraf and Olek, 2016). In contrast with augite, the Si-O (bridging oxygens) stretching band located at 959 cm^{-1} in unreacted diopside shifts to lower wavenumbers in the reacted mineral (943 cm^{-1}) suggesting silicate depolymerization of (Omori, 1971; Sáez Del Bosque et al., 2014). The same behavior was observed in the v3 Si-O (br) stretching band of diopside (1066 cm^{-1}), shifting to 1044 cm^{-1}.

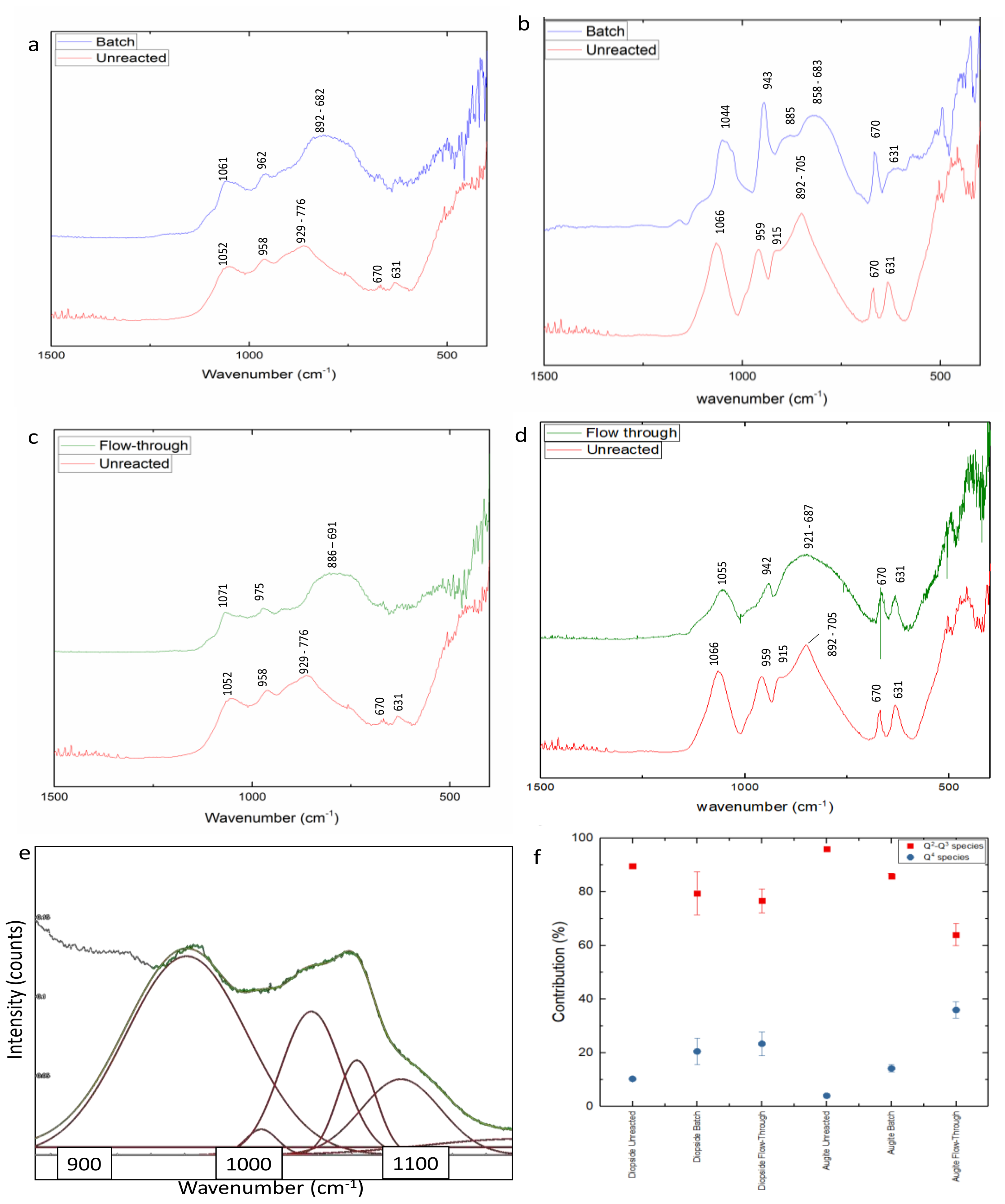

Figure IV.1. FTIR analyses of unreacted and reacted samples (a) FTIR spectra of unreacted and reacted augite under batch experiments. (b)) FTIR spectra of unreacted and reacted diopside under batch experiments. (c) FTIR spectra of unreacted and reacted augite under flow-through experiments. (d) FTIR spectra of unreacted and reacted diopside under flow-through experiments. (e) example of fitted FTIR spectra analyses (augite under flow-through experiments). (f) Q1 -Q3 and Q4 species contribution to the reacted and unreacted crystals adding the total area of the integrated peaks of ATR-FTIR spectra regarding to the different species with FYTYK peak fitting software. Q1 -Q3 species(900 – 1050 cm-1), Q4 species (> 1050 cm-1).

ATR-FTIR spectra of augite after flow-through experiments (Figure IV.1c) also show a shift and broadening of the v_3 asymmetric stretching of Si-O bond to lower wavenumbers, from ~929-760 cm^{-1} in unreacted mineral to ~866-691 cm^{-1}. Furthermore, the band at 958cm^{-1} is shifted to 975 cm^{-1} and the band corresponding to Si-O-Si stretching is shifted to 1071 cm^{-1}. These observations, as mentioned above, indicate an increase in the amorphous content and in the degree of polymerization of silica units and thus, are in agreement with the formation of amorphous silica, to a higher extent than in the batch experiments, as determined by micro-CT analysis (Ashraf and Olek, 2016; Mozgawa et al., 2004; Yang et al., 2008; Yang et al., 2009; Sáez Del Bosque et al., 2014). In the case of diopside (Figure IV.1c), the behaviour is very similar to that described above for the batch experiments. However, the v_3 Si-O (br) stretching band of diopside (1066 cm^{-1}), shifts to a higher wavenumber than in the batch run (1055 cm^{-1}), while the band at 915 cm^{-1} in the unreacted mineral is not observed due to the broadening of the 921 – 687 cm^{-1} band, corresponding to the v_3 asymmetric stretching of Si-O bond (Omori, 1971). Overall, these observations are in agreement with a higher extent of silica formation during diopside flow-through experiments as compared to batch experiments, as in the case of augite (Ashraf and Olek, 2016.; Yang et al., 2008; Yang et al., 2009; Sáez Del Bosque et al., 2014).

The Q^n notation (n = 0, 1, 2, 3 or 4) represents the number of bridging oxygens per Si tetrahedron in silicates (Karlsson et al., 2005; Yang et al., 2009). The vibration bands located between 950 and 1050 cm^{-1} in ATR-FTIR spectra of silicate minerals correspond to Q^1-Q^3 units, while vibration bands corresponding to Q^4 units (amorphous silica) are located above 1051 cm^{-1} (Zholobenko et al., 1997; Yang et al., 2008; Simonsen et al., 2009; Yang et al., 2009). The contribution of Q^1-Q^3 and Q^4 units in FTIR spectra of augite and diopside samples, before and after dissolution experiments, can be estimated by peak area measurements using the software FYTIK (Wojdyr,

2010) (Figure IV.1e and f). Peak contribution data from the analyses are reported in (Table IV.1). Gaussian profiles were used due to the multiple contribution profiles needed to fit the asymmetry of almost all the bands. Only the region of the spectra > 900 cm^{-1} was taken into account to avoid possible artifacts related to the contribution of Q^1 dimeric species. Here, it can be observed that Q^1-Q^3 units are dominant in all samples. This is consistent with the pyroxene structure, based on chains of tetrahedra (type T-O) linked by two corners (Q^2 units), except the terminal tetrahedra of the chain (Q^1) and one Ca-Mg octahedral strip unit (Hamilton, 2000). On the other hand, amorphous SiO_2 is composed of tetrahedra connected via four corner-sharing bridging oxygens constituting Q^4 species forming a homogeneous random network. It can also include Q^3 species due to unsatisfied bridging between surface tetrahedra (Dove et al., 2008). Figure IV.1f shows that the unreacted diopside and augite presents a higher contribution of Q^1-Q^3 units as compared to the weathered material. An increase in the contribution of Q^4 species present in the surface of the mineral was observed after batch and flow-through acid dissolution experiments. Interestingly, it can be observed that the contribution of Q^4 is higher in flow-through experiments than in batch experiments, particularly in the case of augite, suggesting a higher degree of silica polymerization related to the higher presence of amorphous silica in the materials weathered in flow through experiments (Karlsson et al., 2005; Simonsen et al., 2009; Yang et al., 2009). Although this ATR-FTIR analysis was performed on the surface of the crystals and thus it can only be considered as a semi-quantitative and not absolute analysis, FTIR data and the Q^n contribution analysis presented here corroborate the results obtained by other techniques, described below.

Table IV.1 Detailed values Q1-3 and Q4 units contribution in the FTIR spectral data measured by Fityk analyses

	Experiment	**$Q_{1\text{-}3}$ units** %	**Error** %	**Q_4 units** %	**Error** %
Diopside	Unreacted	89.7		10.26	
	Batch experiments	79.5	7.99764	20.49911	4.99764
	Flow-Through experiments	76.65293	4.40214	23.34707	4.40214
Augite	Unreacted	96.04296		3.95704	
	Batch experiments	85.83977	1.10709	14.16023	1.3669
	Flow-Through experiments	64.05694	4.0839	35.94306	3.0839

IV.2 SEM, TEM and Micro-CT study of acid-weathered pyroxenes.

SEM-EDX analysis (Figure IV.2a) confirmed the presence of abundant Si-rich patches on augite reacted at 80ºC for 10 h (batch experiments), without any detected incorporation of other cations (i.e. Ca, Mg, Fe, Al). These patches show a “mud crack”-like structure due to the dehydration of amorphous silica gel. Dendritic iron-rich precipitates, most likely iron oxy-hydroxides, formed after augite dissolution, but also possibly associated woth dissolution of iron-rich crystals with iron-titanium composition observed in the unreacted augite crystals. This type of precipitates are commonly associated with silica precipitation following augite dissolution in an oxidizing environment (Siever and Woodford, 1979; Hoch et al., 1996). In the case of diopside reacted under the same conditions, abundant etch pits were observed on the surface of the mineral (Figure IV.2b). This is an evidence that suggests that the rate-controlling step of the process is the surface-reaction (i.e. dissolution of diopside, (Berner et al., 1980). However, no surficial Si-rich layers were evident on reacted diopside. Very similar textures were observed in augite treated in flow-through experiments (Figure IV.2c), and in the case of diopside, the presence of Si-rich phases is limited to the interior of dissolution features (Figure IV.2d).

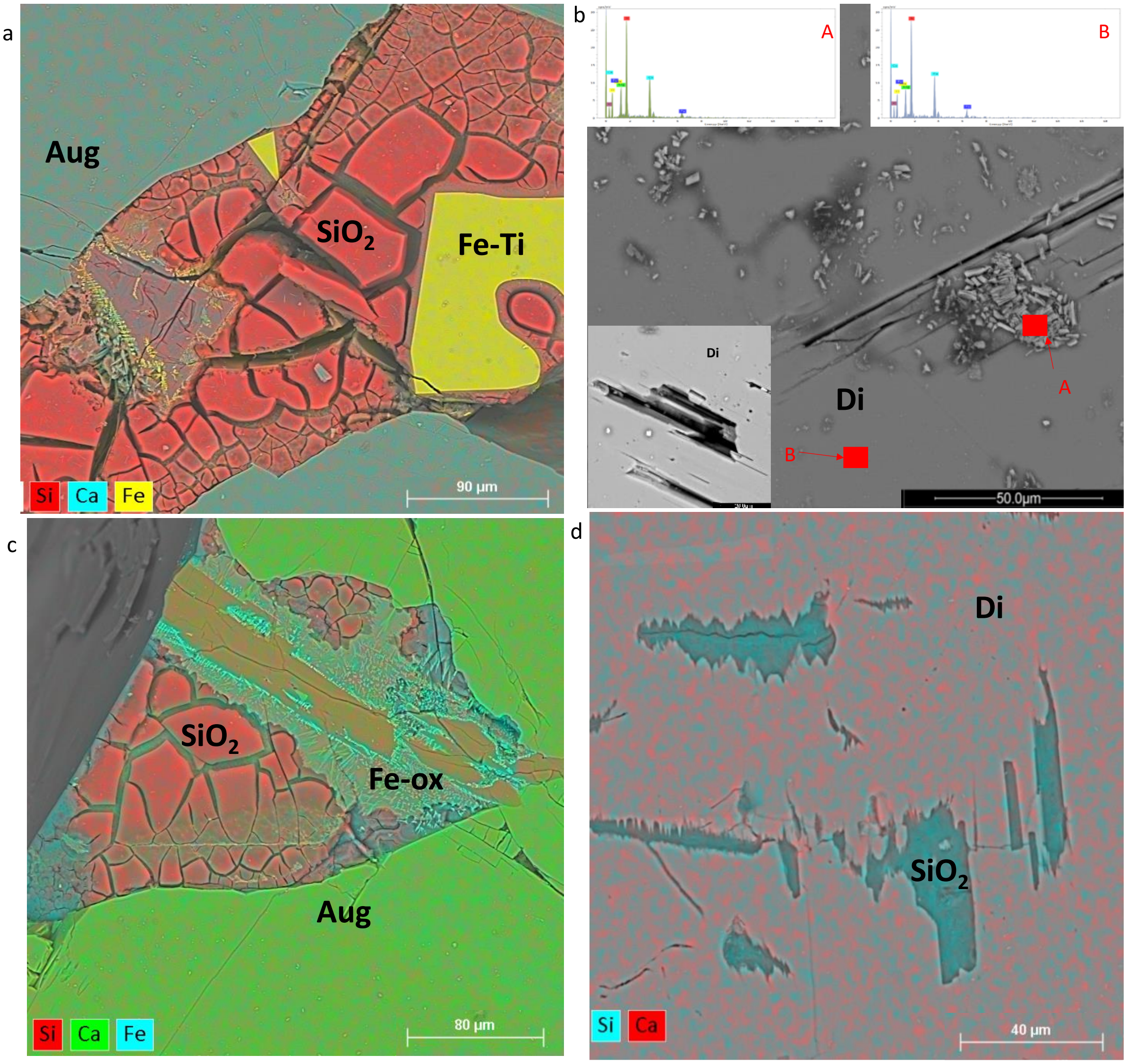

Figure IV.2. SEM-EDS analyses of reacted samples (a) SEM-EDS elemental map of reacted augite under batch experiments showing the augite (aug), amorphous silica (SiO_2) and iron-titanium particles (Fe-Ti). (b SEM-EDS spectrums of Diopside run in batch experiment. (A). Spectra of surface precipitate showing Ca, Mg, Si and Fe (detailed spectra in Figure S4). (B) Spectra of mineral substrate showing Ca, Mg, Si and Fe (detailed spectra in Figure S4). Inset SEM image of etch pits in the surface of the reacted diopside (Di) (c) SEM-EDS elemental map of reacted augite under flow-through experiments showing the augite (aug), amorphous silica (SiO_2) and oxides precipitate (Fe-ox). (d) SEM-EDS elemental map of reacted diopside showing the diopside (Di) and the amorphous silica (SiO_2).

TEM-SAED and HAADF-EDS compositional analyses of crushed weathered samples confirmed the presence of amorphous silica in contact with weathered augite and diopside crystals (Figure IV.3). Interestingly, AEM point analyses showed the incorporation of variable amounts of Mg, Fe and Ca in the amorphous SiO_2 (Daval et al., 2011), not detected by SEM-EDX, as it has been also reported by Daval et al., (2011). Elemental mole ratios of the alteration products in augite determined by AEM are very close to those of pure amorphous silica (O/Si ≈ 2, see Table IV.2 and Figure IV.4). Despite the similar Mg/Si ratios in both unaltered minerals, significantly higher amounts of Mg and Fe were detected in the amorphous, silica-rich phase formed during diopside dissolution (Mg/Si =0.28-0.36 and Fe/Si= 0.10-0.21). Note, however, that Fe is not included homogenously within the matrix of this phase, but it is present in the form of scattered nanoparticles.

Micro-CT analyses allow the direct visualization and quantification of the volume of amorphous silica formed in the weathering experiments (Figure IV.5 and IV.2). Volume calculations show that augite presents the higher SiO_2(am) content after weathering experiments, particularly after flow-through runs (9.55 vol. % in batch reactions vs. 25.63 vol. % in flow-through experiments). Diopside, on the contrary, shows much smaller silica contents in the reacted samples after both types of dissolution experiments (< 1 vol % vs. 2.76 vol. %, for batch and flow-through runs, respectively). Micro-CT analysis showed a wide spatial distribution of the amorphous silica all through the whole volume of the crystals of augite. It can be observed that most of the pores and dissolution features of the crystal are filled with amorphous silica, particularly in the case of flow-through experiments (Figure IV.5 and 6). Amorphous silica on the augite surface is only visible using this technique in the areas where cracks, which further propagate towards the interior of the crystal, initiate at or intersect with the mineral surface.

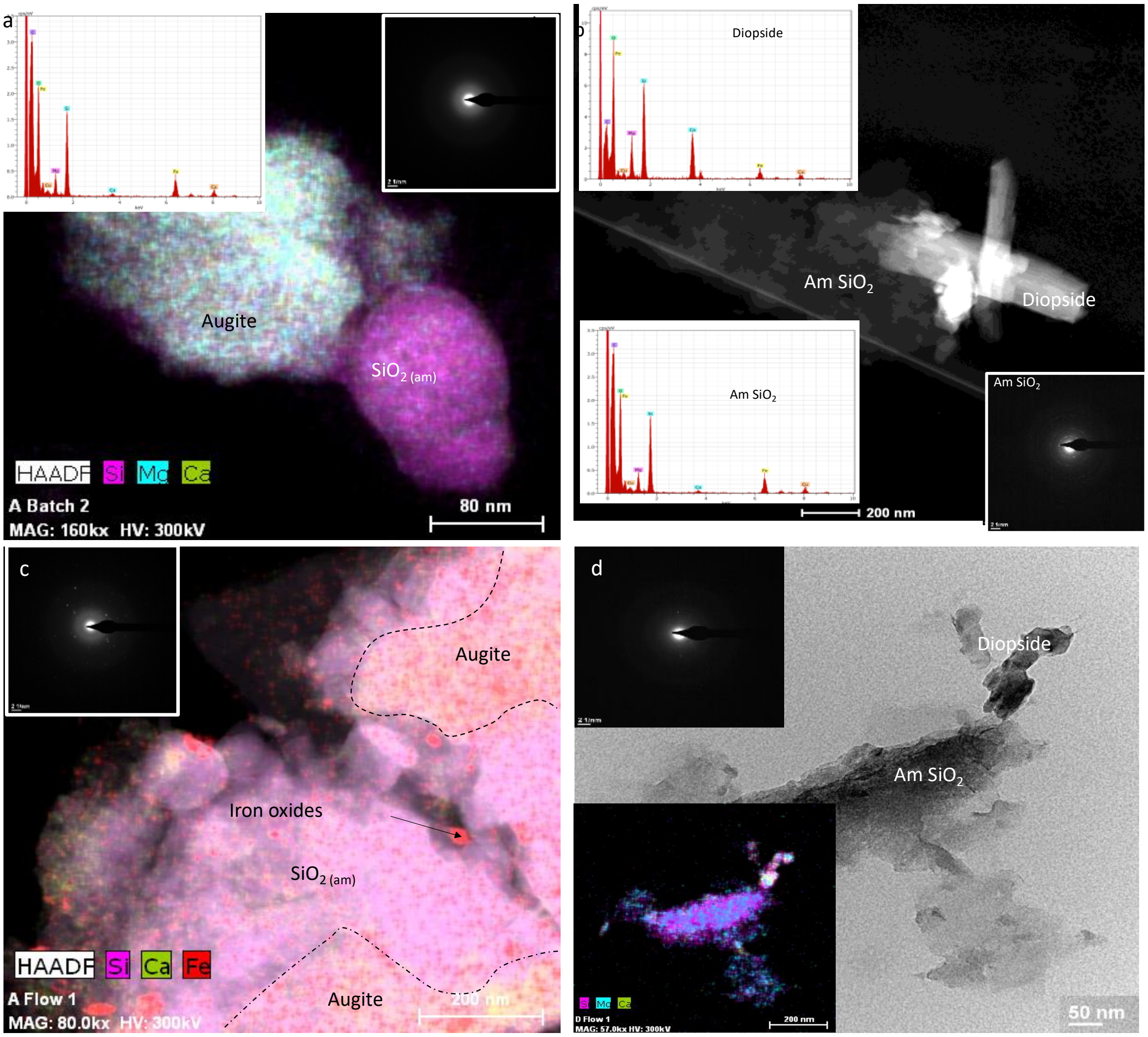

Figure IV.3. HRTEM-EDS analyses of reacted samples (a) HAADF image overlaid with EDS elemental map of products phases after batch reaction. Inset in the left correspond to EDS analysis of the amorphous silica zone and the right inset to SAED analysis of the Si rich zone.. (b) HAADF image of product phases after batch reaction in diopside. SAED and EDS analyses of MSH in inset. (c) HAADF image overlaid with EDS elemental map of products phases after flow-through reaction distinguishing the primary silicate, the amorphous SiO2 phase and the iron oxydes on the surface of silica. The upper inset shows SAED pattern of the Si rich zone (d) HRTEM image The upper inset corresponds to the SAED pattern of the amorphous SiO2. with minor amounts of Ca and Mg.with EDS elemental map of products phases in lower inset after flow-through reaction.

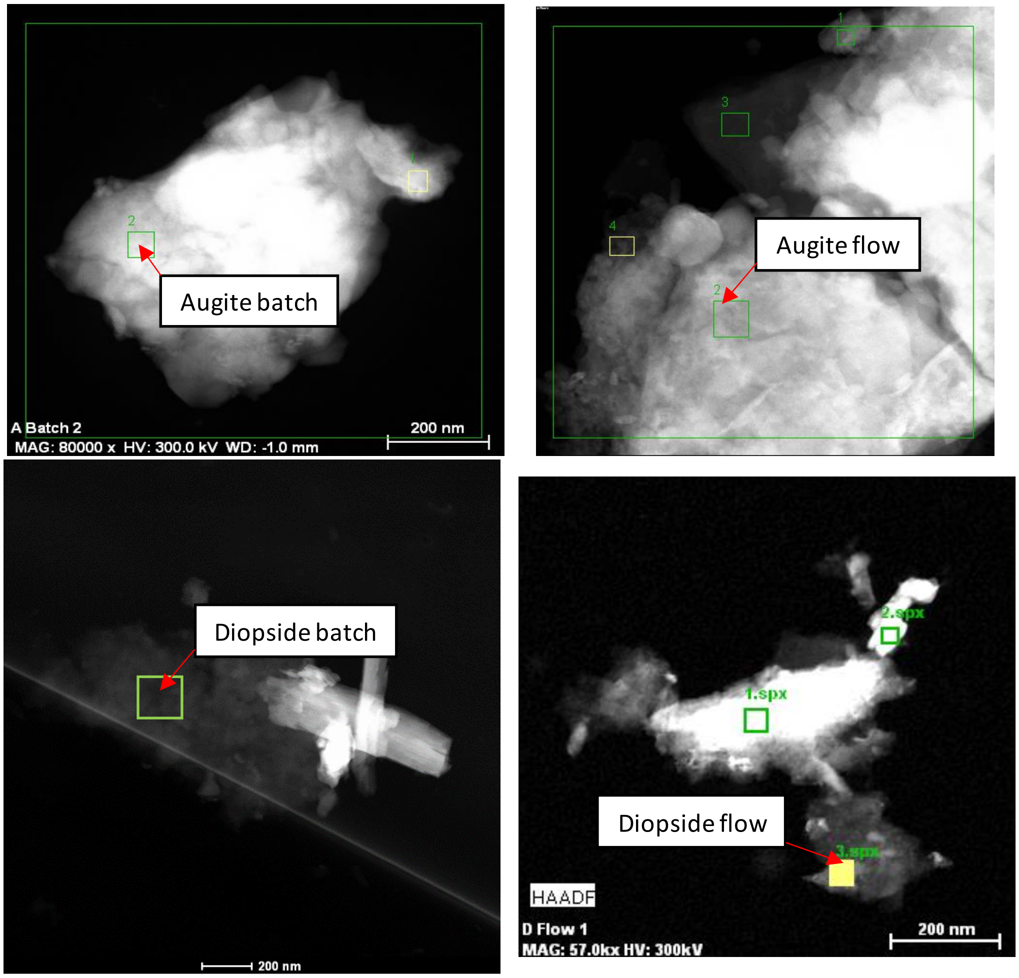

Figure IV.4. HAADF image of amorphous silica observed in (a) augite after batch experiment, (b) augite after flow-through experiment, (c) diopside after batch experiments, (d) diopside after flow-through experiment. Green squared areas correspond to AEM analyses reported in Table IV.2.

Table IV.2 AEM elemental composition (at %) of amorphous silica analyzed with TEM-AEM. Analysis refer to named spots in the HAADF image in Figure IV.4

Experiment	Si	Al	Mg	Ca	Fe	O	Al/Si	Mg/Si	Ca/Si	Fe/Si	O/Si
Augite Batch	32.42	0.62	0.16	0.34	0.089	66.37	0.02	0.01	0.01	0.003	2.05
Augite flow	29.72	2.55	0.93	0.98	0.045	65.24	0.09	0.03	0.03	0.002	2.20
Diopside batch	24.57	0.49	6.84	0.63	5.06	62.41	0.02	0.28	0.03	0.21	2.54
Diopside flow	23.82	0	8.65	3.27	2.34	61.91	0	0.36	0.14	0.09	2.60

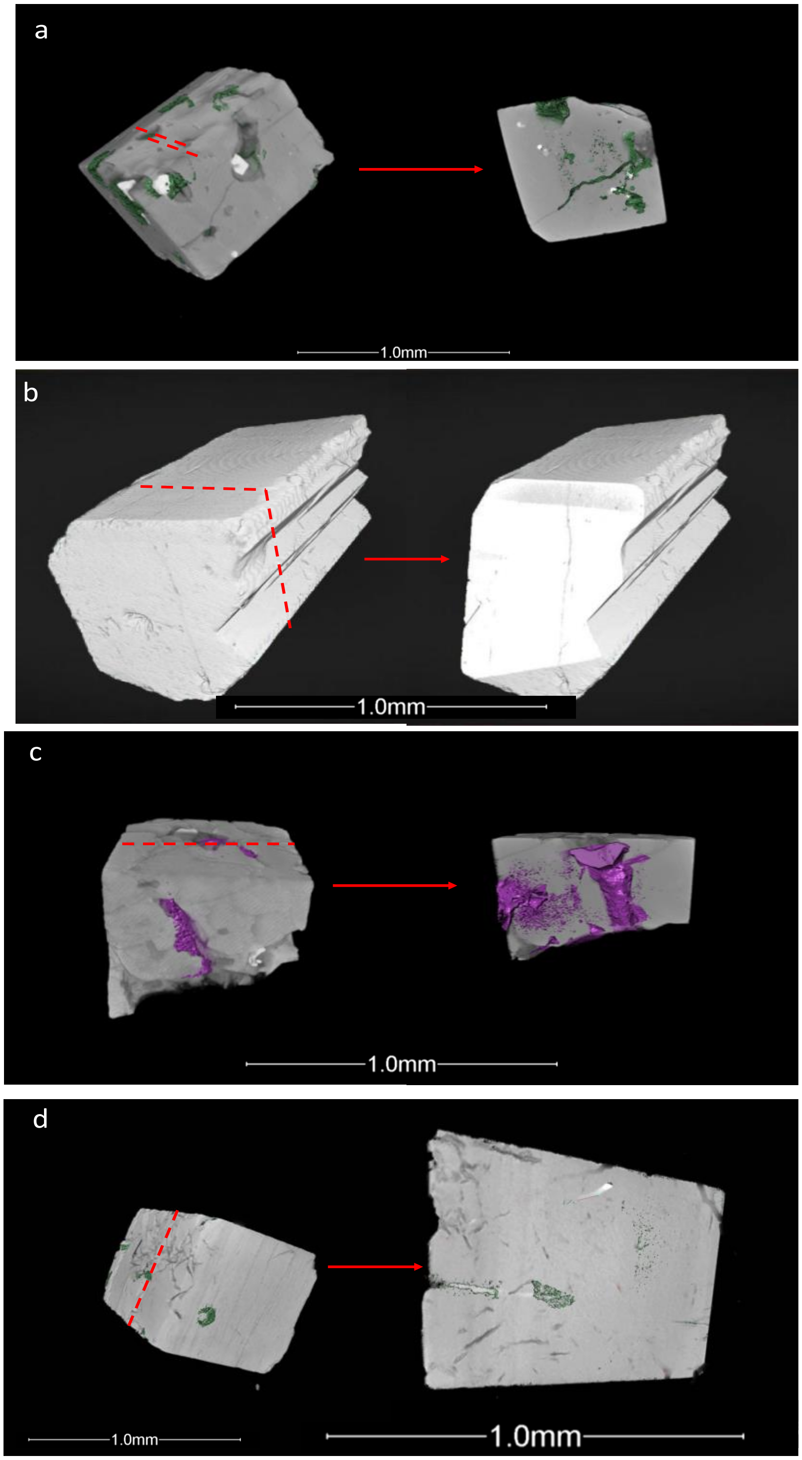

Figure IV.5. Micro-CT images of reacted crystal with SiO_2 precipitate in color. Red dotted line in the left images represent the virtual cut made by Dragonfly software to observe the inside zone of the reacted crystals of the right images. (a) Augite after batch experiments. (b) diopside after batch experiments. (c) augite after flow-through experiments. (d) diopside after flow-through experiments

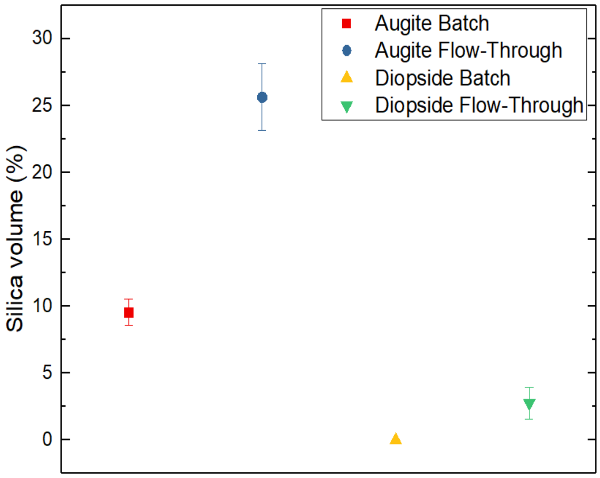

Figure IV.6. Micro-CT volume calculations of SiO_2 secondary precipitate for each experiment

IV.3 Kinetics of element release to the solution.

Ca, Mg and Si fluxes during augite and diopside flow-through experiments show the typical evolution as a function of time reported during silicate dissolution processes (e.g. Daval et al., 2010; Ruiz-Agudo et al., 2012; Di Lorenzo et al., 2018), with a steep monotonic decrease in the ion concentration during the first steps of the dissolution process, subsequently reaching a steady-state (Daval et al., 2010) for both pyroxenes after ca. 200 min (Figure IV.7). Although stoichiometric steady state has been reported to be reached at much longer reaction times (e.g. diopside ~2700 h at 25°C or ~100 h at 90°C for flow rates between 0.38 – 1.92 mL h^{-1}; Chen and Brantley, 1995), the significantly faster flow rate in these experiments (2 mL min^{-1}) speeds the rate of attainment of a steady state. Ca/Mg and Ca/Si elemental mole ratios in the outflow solutions are different both for augite and diopside (augite: 1.13 and 0.50, respectively; diopside: 1.15 and 0.48, respectively) (Figure IV.7 and Table IV.3). This apparent non-stoichiometric behavior can be explained by the formation of amorphous silica detected in Micro-CT and TEM, and inferred from ATR-FTIR analysis, as described above. At the same time, these elemental ratios are lower in batch dissolution experiments than in flow-through runs, which is consistent with the higher amount of $SiO_{2(am)}$ found in flow-through experiments. This non-stoichiometric behaviour implies that dissolution rates, calculated from Si release rates (r_{Si}), represent minimum values (Table IV.4). r_{Si} determined in batch experiments are lower than those measured in flow-through experiments (0.90 and 1.49 log units for augite and diopside, respectively) (Table IV.5). These differences arise from the fact that in batch experiments, the driving force for dissolution decreases as the system approaches equilibrium, and so do the dissolution rates. In batch experiments, the dissolution rate determined for augite is faster than for diopside (log r_{Si} (mol cm^{-2} s^{-1}) = -10.79 ±0.04 and -11.20 ± 0.07 for augite and diopside, respectively), In flow-through experiments the rates are higher and the trend is reversed (log r_{Si} (mol cm^{-2} s^{-1}) = -9.88 ± 0.02 and 9.71 ± 0.04 for augite and diopside, respectively) (Table IV.3 to IV.5). This is related to the massive formation of amorphous silica in both augite and diopside, and the fact that a larger amount of amorphous silica was observed to form in the case of augite as compared with diopside after flow.through experiments which significantly decreases the measured Si flux.

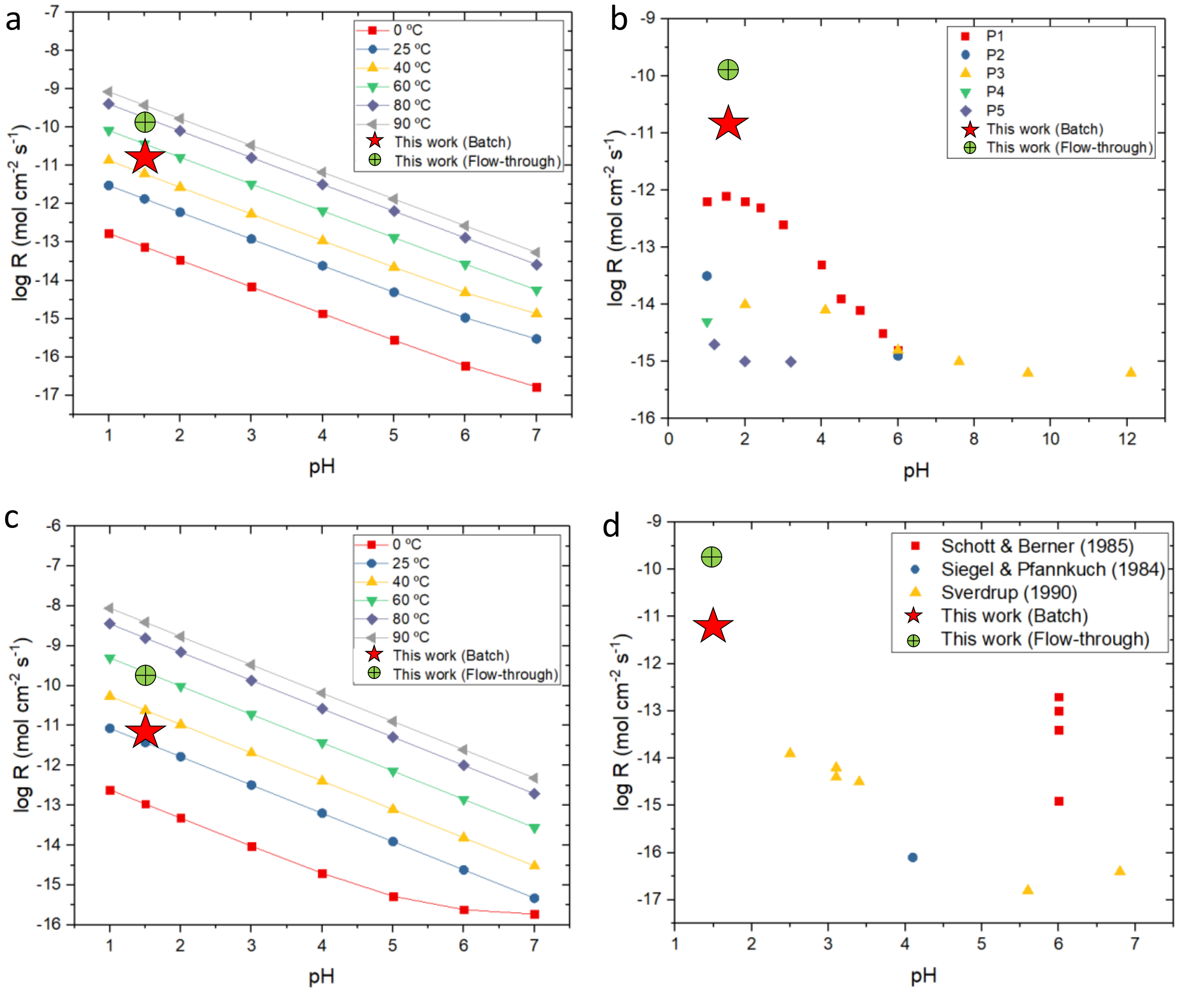

Figure IV.7. Comparison of dissolution rates vs. pH (a) augite experimental data compared to dissolution rate modelling of augite at different temperatures. (b) augite experimental data compared to dissolution rate reported in previous works (reported data were taken at 25ºC). (c) diopside experimental data compared to dissolution rate modelling of diopside at different temperatures. (b) diopside experimental data compared to dissolution rate reported in previous works (reported data were taken at 25ºC).

Table IV.3 Detailed values of chemistry composition of flow-through experiments. First row represent the reacted mineral, second row represent the selected time to measure, following sixth rows represent the chemical composition of the solution for the different elements and their standard deviation error and following rows represent the Ca/Si and Ca/Mg ratios.

Mineral	Time min	Ca (µmol/L)	error StdDev	Mg (µmol/L)	error StdDev	Si (µmol/L)	error StdDev	Ca/Mg	Ca/Si			
Augite	5	63.62	0.13	9.05	0.01	4.98	0.06	7.03	12.76		Ca/Mg	Ca/Si
	35	31.19	0.12	4.94	0.02	3.56	0.12	6.32	8.76	Average	6.45	7.61
	65	23.70	0.09	4.52	0.01	3.92	0.10	5.24	6.05	Error (StdDev)	0.52	0.99
	95	29.69	0.12	4.52	0.00	3.56	0.09	6.56	8.34			
	155	20.46	0.06	3.29	0.02	2.85	0.18	6.22	7.18			
	215	19.46	0.04	3.29	0.01	2.85	0.00	5.91	6.83			
	335	23.95	0.14	3.29	0.02	2.85	0.05	7.28	8.41			
	455	22.95	0.02	3.70	0.01	2.63	0.06	6.20	8.73			
	600	18.46	0.04	2.88	0.01	2.85	0.24	6.41	6.48			
Diopside	5	429.39	0.86	13.99	0.03	24.57	0.54	30.70	17.48		Ca/Mg	Ca/Si
	35	57.88	0.17	5.76	0.02	6.77	0.10	10.05	8.56	Average	6.01	5.23
	65	28.19	0.14	3.70	0.01	5.70	0.17	7.62	4.95	Error (StdDev)	0.25	0.71
	125	33.93	0.20	4.94	0.02	5.34	0.18	6.87	6.35			
	185	25.45	0.10	4.11	0.02	4.27	0.38	6.19	5.96			
	245	28.19	0.06	4.52	0.01	4.98	0.18	6.23	5.66			
	365	23.20	0.02	4.11	0.01	5.34	0.08	5.64	4.34			
	485	22.95	0.02	3.70	0.01	4.63	0.11	6.20	4.96			
	600	31.94	0.06	5.35	0.00	5.34	0.01	5.97	5.98			

Table IV.4 Detailed values of dissolution rates during flow-through experiments First row represent the reacted mineral, second row represent the selected time to measure, following seventh rows represent the dissolution rate for the different elements and their standard deviation error and following rows represent the Ca/Si and Ca/Mg ratios.

Mineral	Time (min)	Ca	Error (StdDev)	Mg	Error (StdDev)	Si	log R (mol cm^{-2} s^{-1})	Error (StdDev)	Ca/Si	Ca/Mg			
Augite	**5**	5.9E-09	1.7E-13	8.4E-10	1.3E-14	2.3E-10	-9.6E+00	5.5E-12	25.23	7.03		**Ca/Mg**	**Ca/Si**
	35	2.9E-09	1.6E-13	4.6E-10	2.9E-14	1.7E-10	-9.8E+00	1.1E-11	17.31	6.32	**Average**	15.05	6.45
	65	2.2E-09	1.2E-13	4.2E-10	2.0E-14	1.8E-10	-9.7E+00	9.0E-12	11.96	5.24	**error**	1.96	0.52
	95	2.7E-09	1.6E-13	4.2E-10	6.7E-15	1.7E-10	-9.8E+00	8.2E-12	16.48	6.56			
	155	1.9E-09	8.1E-14	3.0E-10	2.5E-14	1.3E-10	-9.9E+00	1.6E-11	14.20	6.22			
	215	1.8E-09	5.1E-14	3.0E-10	1.5E-14	1.3E-10	-9.9E+00	0.0E+00	13.51	5.91			
	335	2.2E-09	1.9E-13	3.0E-10	2.5E-14	1.3E-10	-9.9E+00	4.2E-12	16.62	7.28			
	455	2.1E-09	3.0E-14	3.4E-10	1.1E-14	1.2E-10	-9.9E+00	9.8E-12	17.26	6.20			
	600	1.7E-09	4.9E-14	2.7E-10	1.3E-14	1.3E-10	-9.9E+00	2.2E-11	12.81	6.41			
log R$_{Augite}$ (mol cm^{-2} s^{-1})		-8.67		-9.58		1.31E-10	-9.88						
error		1.01E-12		1.58E-13		4.59E-12	0.02						
Diopside	**5**	4E-08	1E-12	1E-09	4E-14	1E-09	-9E+00	4E-11	36.04	30.70		**Ca/Mg**	**Ca/Si**
	35	5E-09	2E-13	5E-10	2E-14	3E-10	-1E+01	8E-12	17.64	10.05	**Average**	10.79	6.01
	65	2E-09	2E-13	3E-10	2E-14	2E-10	-1E+01	1E-11	10.20	7.62	**error**	1.46	0.25
	125	3E-09	2E-13	4E-10	3E-14	2E-10	-1E+01	1E-11	13.10	6.87			
	185	2E-09	1E-13	3E-10	2E-14	2E-10	-1E+01	3E-11	12.28	6.19			
	245	2E-09	7E-14	4E-10	1E-14	2E-10	-1E+01	2E-11	11.66	6.23			
	365	2E-09	3E-14	3E-10	1E-14	2E-10	-1E+01	7E-12	8.96	5.64			
	485	2E-09	3E-14	3E-10	1E-14	2E-10	-1E+01	9E-12	10.22	6.20			
	600	3E-09	7E-14	4E-10	2E-15	2E-10	-1E+01	4E-13	12.33	5.97			
log R$_{Diopside}$ (mol cm^{-2} s^{-1})		-8.73		-9.52		1.95E-10	-9.71						
error		1.92E-12		1.65E-13		1.84E-11	0.04						

Table IV.5 Detailed values of solution chemistry and dissolution rates of batch experiments.

Mineral	Ca (µmol/L)	error	Mg (µmol/L)	error	Si (µmol/L)	error	Ca/Mg	Ca/Si
Diopside	304.62	2.44	100.45	0.50	94.85	4.36	3.03	3.21
Augite	351.79	1.41	98.15	0.29	247.16	1.73	3.58	1.42
Rate diopside (mol cm^{-2} s^{-1})	-10.70	0.95	-11.18	1.00	-11.20	0.4	0.96	0.95
Rate augite (mol cm-2 s-1)	-10.63	0.99	-11.19	1.04	-10.79	0.2	0.95	0.99

IV.4. General Discussion

Based on the measured pattern of element release to the bulk aqueous solutions during both flow-through and batch acid dissolution experiments, apparent incongruent dissolution was observed in all experiments (i.e., the elemental ratios measured in the solution differ from those measured in the solid, especially at the initial stages of dissolution; e.g., see Casey, 1990; Pokrovsky and Schott, 2000; Hellmann et al., 2003; Brantley, 2008; Tisserand and Hellmann, 2008; Daval et al., 2011). This apparent incongruent behaviour arises from the formation of Si-rich SALs, which are chemically and structurally altered zones at the fluid-solid interface which are depleted in some elements relative to the bulk mineral composition (Casey et al., 1989; Brantley, 2008; Hellmann et al., 2012). In this case, SALs form not only on the outer mineral surfaces, but also further into the crystal, within cracks formed during dissolution. The formation mechanism of these layers has been the subject of much research and debate. As explained above in the Introduction chapter (Chapter I), most recent experimental studies suggest a mechanism whereby SALs form by interfacial dissolution–precipitation (e.g. Teng et al., 2001; Hellmann et al., 2003; Daval et al., 2009b; Putnis, 2009; Zhang and Lüttge, 2009; King et al., 2010; Hellmann et al., 2012; Ruiz-Agudo et al., 2012; Ruiz-Agudo et al., 2016), initially controlled by the establishment of a steep compositional gradient at the mineral fluid-interface, as the most plausible mechanism for SAL formation.

Thermodynamic calculations performed using PHREEQC (lnll database.) show that bulk solutions in batch and flow-through experiments remain highly undersaturated with respect to both augite and diopside at the end of the experiments (Table IV.6). As expected, solutions are more undersaturated in flow through runs than at the end of batch experiments for the same period of time (10 h). Additionally, batch and flow-through bulk solutions are undersaturated with respect to amorphous silica in all experiments performed, for both total Si and the stoichiometric amount of Si and Mg, as well as for the measured Si and Mg concentrations. The saturation index with respect to amorphous silica varied from −0.45 to −2.53 for diopside between augite (Table IV.6). Therefore, bulk precipitation of amorphous silica is unlikely. Nevertheless, it has been previously shown that steep concentration gradients develop at the mineral-fluid interface upon contact with the solution, and that supersaturation with respect to amorphous silica can be reached in this interfacial fluid resulting in amorphous silica precipitation (Ruiz-Agudo et al., 2016). This ultimately depends on the relative rates of mass transport and surface reaction in the system, and strong compositional gradients are expected in those systems in which the kinetics of the surface reaction is fast relative to diffusion of dissolved species into the bulk solution.

Table IV.6 Detailed values of saturation index of augite measured and calculated values

Sat.Ind.	**Augite**	**SiO_2(am)**
measured		
Flow-trough	-35.61	-2.53
Batch	-26.26	-1.28
stoichiometric		
Flow-trough	-32.41	-1.43
Batch	-24.19	-0.45

In chain silicates, reactivities are related to their chemical composition; typically, Ca-rich minerals are more reactive than Mg-rich phases (e.g. they decrease in the order wollastonite > augite > diopside > enstatite) (Marini, 2006), and previous works reported higher dissolution rates in iron-bearing pyroxenes as compared to non-iron-bearing pyroxenes (Siever and Woodford, 1979; Hoch et al., 1996). A comparison of the published far-from-equilibrium dissolution rates of the clinopyroxenes diopside and augite is shown as a function of pH at 25 °C in Fig. IV.6. Experimental data included there were obtained by Siegel and Pfannkuch, (1984), Schott and Berner, (1985) and Sverdrup, (1990). Also, values calculated using the dissolution rate law and rate parameters given by Palandri and Kharaka (2004), considering both acidic and neutral dissolution mechanisms, are plotted. The experimental dissolution rates determined in this work are significantly higher than those determined experimentally in previous works, as most of them were collected at room *T* while ours were determined for dissolution at 80 °C (Figure IV.6). Despite the extensive formation of Si-rich secondary phases in augite during flow through experiments (25.6 vol% determined by Micro-CT), dissolution rates are in remarkably good agreement with those predicted from equations compiled in Palandri and Kharaka (2004). Flow-through determined rates for diopside differ though by 0.82 log units. As stated above, r_{Si} determined in batch experiments are lower than those measured in flow-through experiments, as in batch experiments the system is closer to equilibrium and therefore, the driving force decreases. As shown in batch experiments, augite dissolves faster than diopside due to its higher iron content. Oxidation of Fe^{2+} at the mineral surface in contact with the aqueous solution is accompanied by the release of electrons to acceptors in the solution. To maintain charge balance in the structure of the mineral, cations must also be released from the mineral in a coupled electron-cation transfer reaction, this enhancing the dissolution of the parent mineral, particularly at low pH (White and Yee, 1985; Hoch et al., 1996). However, this behaviour is masked by the extensive formation of Si-rich precipitates in the case of augite weathered under continuous solution flow. In this sense, Ca-based rates reflect better the actual kinetics of the congruent dissolution. Both in batch and flow through experiments, Ca-based rates are higher for augite than diopside (see table IV.4 and IV.5).

The observed linear rate of silica release to solution with time has been reported as an indication of surface-limited dissolution in pyroxenes (Schott et al., 1981; Stumm, 1987). This behaviour contrasts with these observations for wollastonite, in which the much faster dissolution rate of this pyroxenoid as compared to pyroxenes (~3 orders of magnitude) may result in the kinetics of the process being controlled by diffusion of dissolved species into the bulk solution (Ruiz-Agudo et al., 2016). In augite and diopside, compositional gradients between the mineral surface and the fluid would be thus flatter, and thus the precipitation of amorphous silica will be more limited. Although the formation of an homogeneous, thin SAL all over the mineral surface (with thickness in or below the nm range) cannot be discarded, it is clear from SEM observations or X-Ray Micro-CT study of the samples after the reactions that the thick Si-rich coatings found in wollastonite, that fully covered the unreacted wollastonite surfaces, are not observed here. Interestingly, SiO_2 formation seems to be limited to specific areas of the crystal surface and, more importantly, to the interior of cracks and other features most likely formed upon dissolution of the substrate. Singh and Gilkes (1993) reported similar observations on weathered samples of the pyroxene spodumene, which shows randomly oriented smectite in etch pits and cleavage cracks after the formation of an amorphous material. Based on these observations, these authors concluded that the dissolution of spodumene takes place through the complete breakdown of the structure involving a solution phase and the subsequent precipitation of an amorphous phase. Cracks can initiate at surface features (etch pits and coalesced etch pits) formed upon dissolution where stress will be concentrated within high-curvature regions (e.g. pit corners), (Plümper et al., 2012), and their propagation might be triggered by stress release. At etch pit corners and crack tips, strained Si-O bonds can react more readily with water compared to other areas with unstrained bonds (Atkinson, 1984). The presence of water in the liquid or vapor states in these environments can trigger crack propagation by promoting weakening reactions. This mechanism is commonly known as stress corrosion (Atkinson, 1982). Stress corrosion is regarded as the preeminent mechanism explaining subcritical crack propagation in rocks under shallow crustal conditions (Atkinson, 1984). Ultimately, this mechanism leads to intensive fracturing that generates fluid pathways to facilitate dissolution along the fracture surfaces, coupled with amorphous silica precipitation. Furthermore, although the precipitation of an amorphous material is not expected to exert much stress via crystallization pressure generation due to the low critical supersaturation reached in the system and thus the low crystallization pressure (Schiro et al., 2012), it may contribute to fracture propagation, as it has been suggested for the case of amorphous proto-serpentine phase formed during serpentinization of olivine (Plümper et al., 2012). Formation of SiO_2 at specific, limited areas of the mineral surface can be linked to highly defective areas or regions with a high step density, where the Si flux to the solution may be locally high. In the second scenario (i.e. within cracks and narrow dissolution features), ion diffusivities are expected to be significantly reduced with respect to the bulk solution. In both cases the build-up of high Si concentrations may be possible locally, which would allow supersaturation with respect to amorphous silica to be reached and its subsequent precipitation.

The higher extent of secondary, Si-rich phase formation in weathered augite may be related with its faster dissolution as compared with diopside, linked to its higher iron content as discussed above. Additionally, a continuous fast flow of fresh solution over the mineral surface will maintain the solution in contact with the mineral highly undersaturated with respect to augite or diopside, so that the driving force for dissolution in flow-through experiments remains higher than in batch experiments during the course of these experiments. Far-from-equilibrium conditions, such as those in flow-through experiments, result in an increase in etch pit abundance which are the seed for crack nucleation and its subsequent propagation by stress corrosion. Fast enough flow rates ensure a high degree of undersaturation and allow the progress of the dissolution reaction and the formation of Si-rich phases within cracks of the crystal.

Interesting conclusions can be drawn from the results of the characterization of the secondary phases formed during the acidic dissolution of augite and diopside. First, the observation of the presence of Fe in the form of nanoparticles within the matrix of the amorphous silica phase provides direct evidence supporting an interface-coupled dissolution precipitation process as a mechanism for the formation of amorphous Si-rich phases during pyroxene weathering. By a solid-state, interdifusional process is not possible to explain such a non-homogeneous distribution of iron in the SALs. Also, the Si-rich, Mg-bearing amorphous phase detected mainly in weathered diopside samples is most likely an amorphous magnesium silicate hydrate (M-S-H) precursor. M-S-H phases are nano-crystallite hydrated phases displaying a phyllosilicate-like structure with relatively short coherence length (~1.2 nm) and small particle size (Bernard et al., 2019). Formation of M-S-H phases has been reported in numerous scenarios (Roosz et al., 2015 and refs therein), including some related to the alteration of silicate materials, such as at the interface of cement-based materials with aqueous solutions (De Weerdt and Justnes, 2015; Dauzeres et al., 2016), during borosilicate glass dissolution (Fleury et al., 2013) or as a natural cement in tillites, formed upon quartz alteration by Mg-rich alkaline fluids (de Ruiter and Austrheim, 2017). These phases show a wide compositional variation with Mg/Si ratios ranging from 0.2-0.4 in the case of borosilicate glass dissolution, 0.5 for the interface between high-pH cement and clay rocks (Dauzeres et al., 2016), 0.86 to 1.21 in MSH cement in tillites, and up to 2 for M-S-H formed at the interaction zone of cement with seawater (De Weerdt and Justnes, 2015). This wide range of compositions has been attributed to variations in the crystal structure of M-S-H phases. The ratios of the Si-rich, Mg-bearing phases formed in these experiments are in the lower limit of the values found in the literature, and within the range reported for borosilicate glass dissolution. Considering that the formation of these phases is strongly favored at pH values above 8, it can be assumed that such pH conditions are prevailing close to the mineral surface mostly during diopside dissolution, in agreement with the expected higher silica concentration in solution in this case compared to augite (since the amount of Si removed from solution by amorphous silica precipitation is lower). This is an indirect indication of the high pH conditions prevailing at the diopside-solution interface, in contrast with those measured in the bulk. Nevertheless, note that bulk pH values (pH ~ 2) are higher for diopside than augite as well, although much more acidic than those needed for M-S-H precipitation (pH ~7). Finally, it should be considered that the formation of this M-S-H precursor may reduce the yield of carbonation in diopside-bearing rocks used for CO_2 storage, due to the incorporation of Mg in the silica matrix, which is therefore not available for the precipitation of carbonates.

Chapter V. Physical-chemical control on carbonation of calcium-magnesium pyroxenes: Effect of reaction-driven fracturing

V.1. Evolution of solution chemistry during dissolution-carbonation experiments

In all systems studied here, augite runs systematically presented a higher release of Ca, Mg and Si to the solution as compared to diopside runs (Figure V.1). In water (initial pH 7.5) a significant amount of alkaline-earth metals were released from both pyroxenes and remained in solution after 28 days of reaction (Figure V.1a-d), an effect that can be related to the relatively large extent of dissolution of the starting material and the very limited dissolved inorganic carbon source (i.e., CO_2 present in the head space of the reactor). A decrease in the total concentration of Ca and Mg up to 14 days, followed by a further increase was observed, while the pH suffered an increase up to 14 days and a subsequent decrease (pH 8.6 in augite and pH 9 in diopside runs). These results suggest that after an initial period of pyroxene dissolution, Ca-Mg bearing carbonates formed after 14 days (corroborated by the analysis of reacted solids, see section 3.2). Precipitation of carbonates releases protons (O'Connor et al., 2005; Rodriguez-Navarro et al., 2015), causing a decrease in pH and, therefore, a renewed dissolution of the primary silicate to feed cations to the solution. If only Mg-Ca carbonate were precipitated, Si in solution should display a constant increase due to the two dissolution steps.

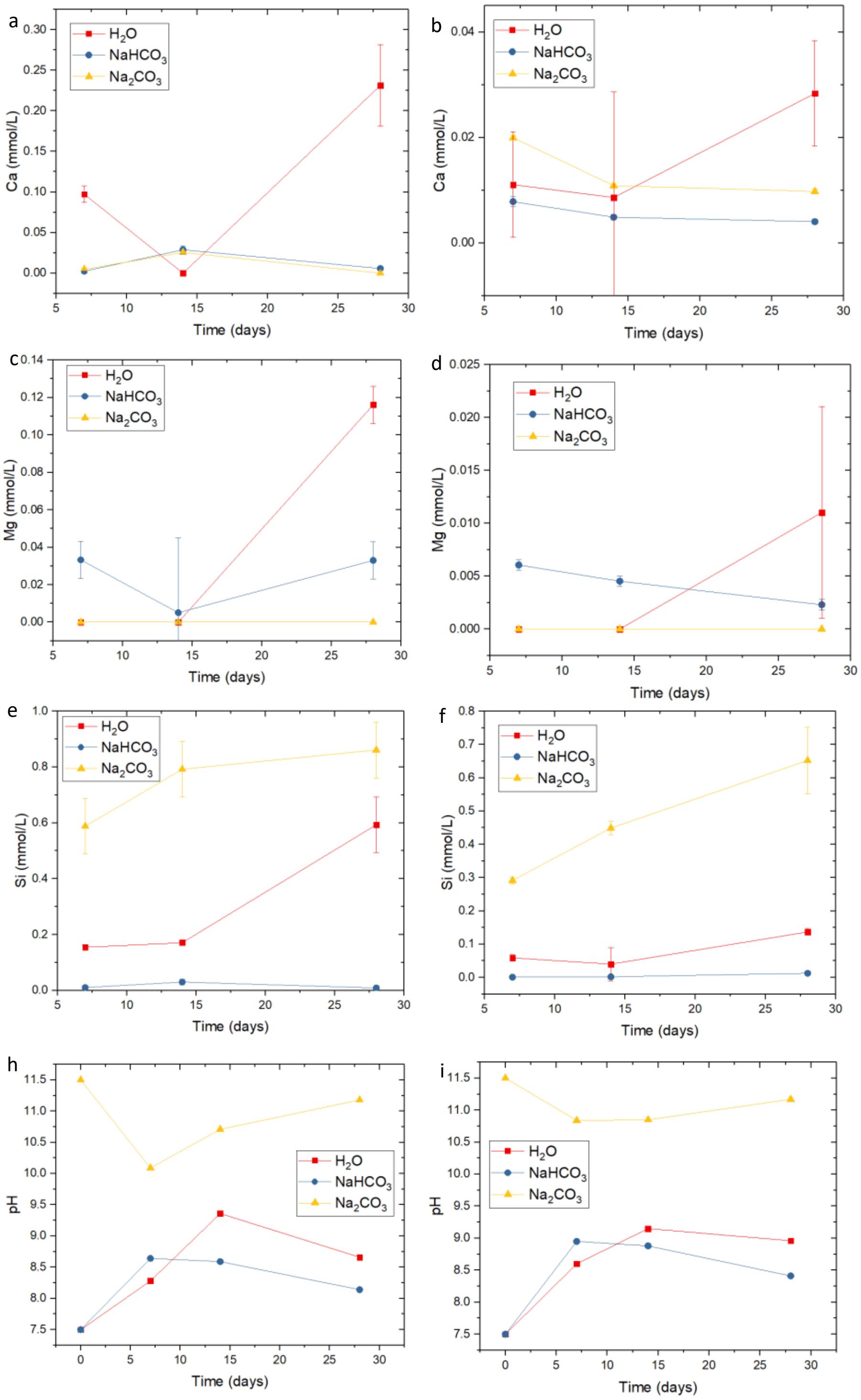

Figure V1. Chemistry evolution during augite and diopside dissolution and carbonation: (a) total concentration of aqueous calcium in augite experiments. (b) total concentration of aqueous calcium in diopside experiments. (c) total concentration of aqueous magnesium in augite experiments (d) total concentration of aqueous magnesium in diopside experiments (e) total concentration of aqueous silicon in augite experiments. (f) total concentration of aqueous silicon in diopside experiments. (h) pH evolution augite experiments. (i) pH evolution diopside experiments.

However, Figures V.1e and f show that in the case of diopside runs, Si in solution showed a constant concentration during the whole experimental runs, whereas in augite systems, the concentration of Si presented an initial plateau between 7 and 14 days, matching the pH rise, and a later increase with a pH decrease. It is suggested that in both runs formation of amorphous silica (SiO_{2am}) took place, which is consistent with previous works on pyroxene dissolution (Schott et al., 1981; Dixit and Carroll, 2007; McAdam et al., 2008; Zakaznova-Herzog et al., 2008; Daval et al., 2010). Time-course variations in Si concentration during augite dissolution should be explained by the precipitation of an additional Si-bearing phase (Na-Phillipsite, see below) that fostered further release of Si from the parent phase.

Ca release to the dissolution from both pyroxenes in $NaHCO_3$ runs presented a first increase until 14 days, less pronounced in diopside runs, and a subsequent decrease caused by the precipitation of secondary Ca-bearing phases, as corroborated by XRD (see V.3 section). Mg release in augite runs showed a slight increase after 14 days of reaction. However, due to measurement error, it cannot be infered a real decrease or a more stable behavior. For this reason, it must be assumed, in agreement with XRD results (V.3 section), a constant release of Mg from augite and the subsequent formation of a Ca-Mg secondary phase. In the case of diopside, the release of Mg showed a similar trend as that of Ca, but resulting in a higher concentration in solution due to the lower formation of Mg-Ca carbonate as compared to the augite runs. The Si concentration in solution in $NaHCO_3$ systems was the lowest measured in this work, suggesting an important precipitation of Si-bearing secondary phases. It must be noted that the starting pH was the same in water and $NaHCO_3$ solutions, however, water systems suffered a higher pH increase over the first 14 days of reaction. It is suggested that a higher level of carbonate precipitation in $NaHCO_3$ runs produced this inequality due to a higher proton release during the carbonation process (Seifritz, 1990; Lackner et al., 1995; Gadikota and Alissa Park, 2015).

In Na_2CO_3 runs, the concentration of Si in solution was up to two orders of magnitude higher than in the other systems. This result is consistent with the pH-dependent solubility of silica, which increases significantly at highly alkaline pHs (Fleming and Crerar, 1982; Luis Monasterio-Guillot et al., 2019). Interestingly, the Si concentration in augite runs was higher than in diopside runs. On the one hand, this suggests that the dissolution rate of augite is higher than that of diopside, and on the other hand, that a secondary Si-bearing phases formed in diopside runs. It must be noted that the extremely high Si concentration in the augite solution prompted us to reevaluate the amount of dissolved pyroxene using Micro-CT, Rietveld, and mass balance results. This reevaluation showed an imbalance between the total amount of augite reacted as determined from µ-CT and XRD results, and that dissolved as determined from ICP-OES results. This inconsistency likely originated from a technical artifact while performing the latter analyses. In any case, these results suggest that augite has a higher dissolution rate than diopside, as it is detailed in the discussion section.

V.2 Characterization of solids reacted in water

XRD results showed small changes after 28 days augite reaction in water (Figure V.2a). Rietveld analyses (Figure V.2b and Table V.1) showed that after 28 days of reaction less than 15 wt% of augite was replaced by crystalline phases: Low Mg-calcite (2.61 wt%), Na-phillipsite (~11 wt%) and iron oxides (hematite, 2.16 wt%). Na-phillipsite is a zeolite composed by Na, Al and Si, with the possibility of Mg, Ca and K incorporation (theoretical formula: $(Na,K,Ca)_{1-2}(Si,Al)_8O_{16}\cdot 6H_2O$). Phillipsite has been frequently associated with pelagic deposits formed by low-*T* hydrothermal alteration of mafic and ultramafic rocks, and in turn is associated with amorphous Si-rich glass (Glaccum and Boström, 1976; Iijima, 1988; Iyer et al., 2007; Etame et al., 2012).

Hematite was also present from the early stages of reaction, showing a continuous but minor increase in concentration over time due to Fe release from the parent phases and the decrease in the solubility of iron oxides and hydroxides with increasing pH (Schwertmann, 1991) causing fast precipitation.

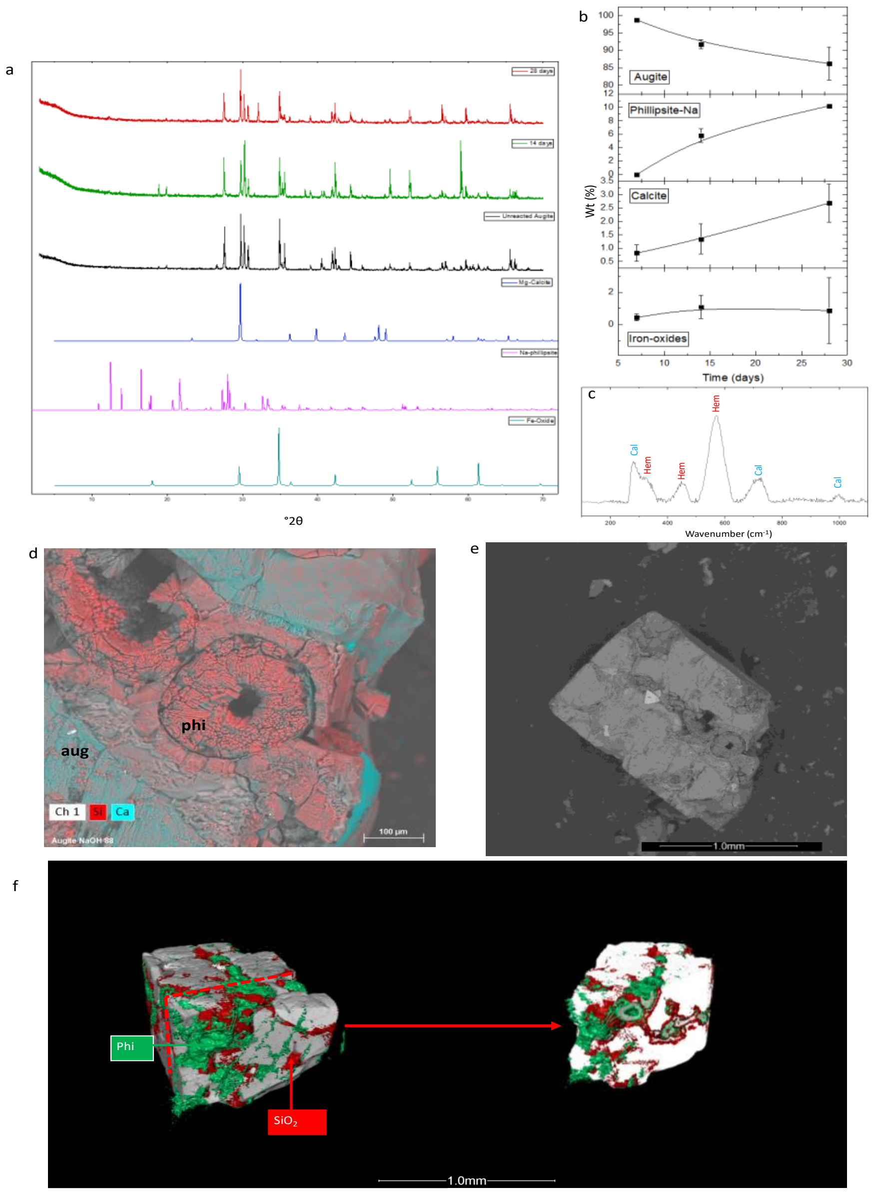

Figure V.2. Products of reaction between augite and NaOH solution: (a) XRD patterns of reacted augite, unreacted augite and reference phases (Mg-calcite, Phillipsite and Iron Oxide). (b) Time evolution of the crystalline phases determined by XRD Rietveld analyses. (c) µ-Raman spectra of calcite crystal (cal, blue) and hematite precipitated (hem, red). (d) SEM image overlaid with EDS compositional map showing the augite (aug) crystal fractured after 28 days of reaction, and, inside the fractures, phillipsite (phi). (e) SEM image of augite crystal after 28 days in water (f) Micro-CT image showing in red the 3D distribution of amorphous silica (SiO2) and in green the phillipsite (phi) in augite crystal after 28 days of reaction. Red dotted line of left image represents the virtual cut performed to observe the inside of the newly-formed filled fracture

SEM-EDS analysis of augite crystals reacted for 28 days showed fractures filled by a secondary Na-rich silicate, Na-phillipsite as shown by XRD analysis (Figure V.3 and V.1d). EDS point analyses (Figure S10 and Table S3) confirmed the presence of this phase with formula $Na_{1.95}Mg_{0.05}Al_{3.21}Si_{4.79}O_{16}\cdot 6H_2O$. Despite the lack of intentionally added DIC, a small amount of calcite was observed (Figure V.4). The presence of calcite suggests that the CO_2 present in the head space of the reactor, dissolved in the solution forming HCO_3^-, which upon dissociation, supplied CO_3^{2-} ions that, in the presence of Ca^{2+} ions, caused the precipitation of calcite and the release of H^+. This is consistent with the pH and Ca^{+2} concentration evolution in solution analyses (Figure V.1a and d). SEM-EDS analysis of calcite showed that this phase included Mg. To unravel the actual content of Mg in calcite, the lattice parameters of calcite were calculated by Rietveld refinement and the Mg content was determined according to Goldsmith et al. (1958) (Table V.2). The calculated Mg amount in calcite was 8 mol%.

Table V.1. Results of the semiquantitative Rietveld analysis after normalization to amorphous phases content mass balance analyses. Data for samples after 28 days of reaction. The last two columns report the extent of carbonation calculated using Rietveld refinement (ξnRR) and mass balance (ξnMB).

Reactant	Augite	Diopside	Phillipsite-Na	Hematite	Calcite	SiO2	MSH	ξ_n^{RR}	ξ_n^{MB}
NaOH	83.97		9.86	0.85	2.61	2.16		0.0016	0.0018
NaHCO3	61.93		12.39	2.01	21.71	2.09		0.1669	0.1842
Na2CO3	96.34		0	1.05	2.65			0.0131	0.0147
NaOH		96.73		0.37	1.23	1.62		0.0004	0.0004
NaHCO3		86.32		0.81	11.5	1.27		0.0328	0.0379
Na2CO3		93.09			2.13		5.01	0.0011	0.0012

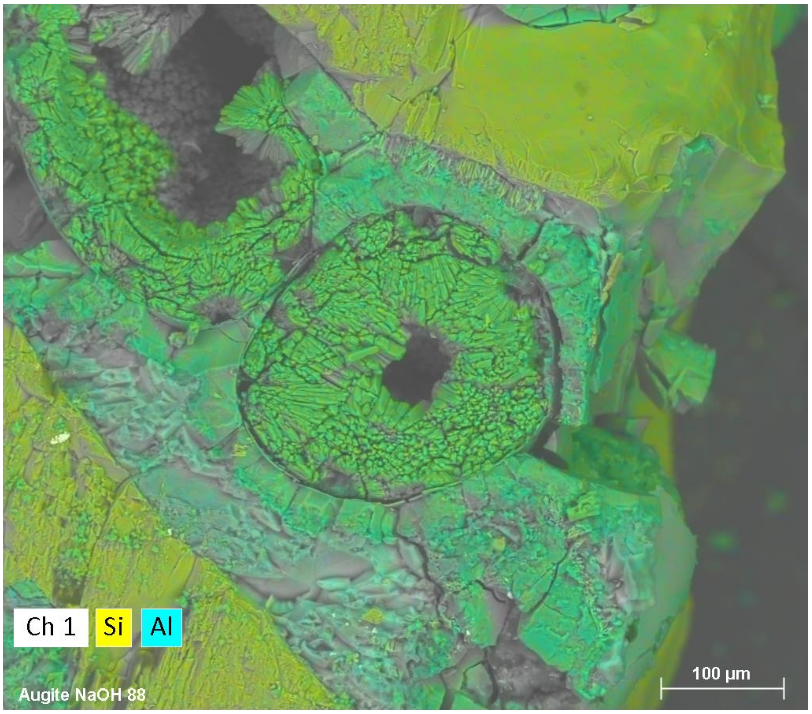

Figure V.3. SEM-EDS compositional map of Figure 2d showing Si (yellow) and Al (Blue). It can be observed that the augite (aug) crystal is fractured after 28 days of reaction and inside the fractures, phillipsite (phi) was precipitated

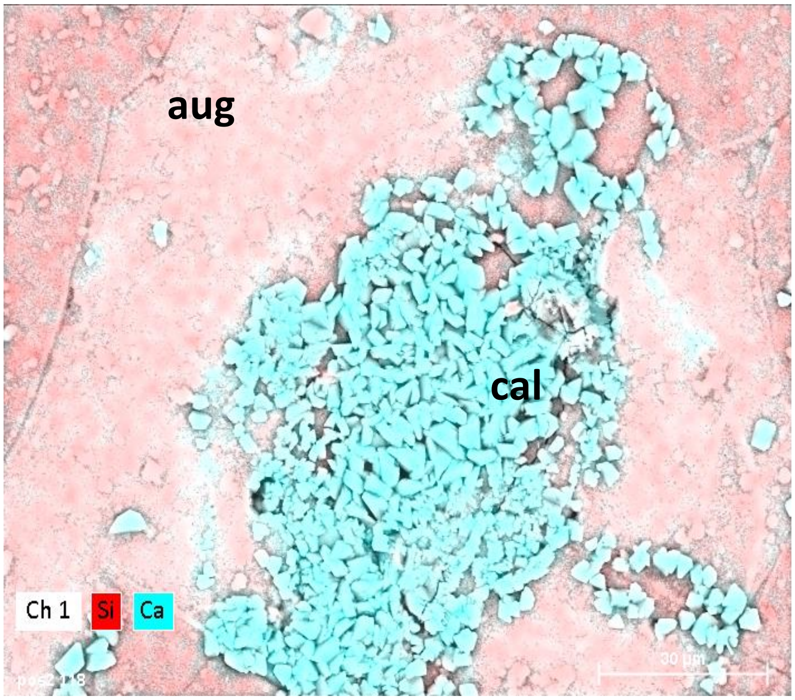

Figure V.4. SEM-EDS compositional map showing calcite crystals (cal) and augite (aug) after 28 days in water μ-Raman analyses confirmed the precipitation of calcite (Figure V.2c) showing the translational lattice mode (T) of (Ca, CO_3) at 286 cm^{-1}, the v_4-symmetric CO_3 deformation at 717 cm^{-1} and the v_1-symmetric CO_3 stretching band at 1085 cm^{-1} (Gunasekaran et al., 2006). Hematite was also identified by μ-Raman showing bands at 326 cm^{-1}, 449 cm^{-1} and 570 cm^{-1} corresponding to hematite E_g, E_u, and E_g vibrations, respectively (Bersani et al., 1999; Chamritski and Burns, 2005). Silica gel was also identified by SEM-EDS analysis (Figure V.5) in dissolving areas such as small fractures and etch pits. Micro-CT analysis showed the presence of two secondary phases (identified by their different contrast due to differences in X-ray attenuation), already identified in the same crystals using SEM-EDS. In Figure V.2e, the blue phase is amorphous silica and the green one is Na-phillipsite. It can be observed that precipitates were present inside the reacted crystals filling fractures that in some cases cross-cut the whole pyroxene. Image analysis of Micro-CT results showed 23 wt% augite replacement by 14.3 wt% Na-phillipsite and 8.7 wt% amorphous silica. These values do not agree with the mass difference for silicon calculated using Eq.(V.I):

$$\Delta m = m_{aug} - \left(m_{sol} + m_{phi}\right) \tag{V.1}$$

where m_{aug} is the molarity of Si from the reacted (dissolved) augite obtained from the Rietveld analyses, m_{sol} is the Si concentration in solution obtained by ICP-OES analyses and m_{phi} is the molarity of Si precipitated in the Na-phillipsite phase obtained by Rietveld analysis. Note that N-phillipsite is the only crystalline secondary silicate formed in these runs. The difference in concentration obtained, Δm, is interpreted here as the Si contained in the Si-bearing amorphous phases a deficit of Si in the solution was detected that should be present as a precipitate. It is suggested that the amorphous SiO_2 content obtained from Micro-CT analysis actually included calcite and amorphous silica due to the resolution constrains of the Micro-CT equipment. Mass balance calculations were performed to recalculate the values obtained by Micro-CT regarding the total amount of augite dissolved and the concentration of Si and Ca in solution, yielding 2.16 wt% SiO_2 and 2.61 wt% calcite. If it is normalized the phase contents obtained by Rietveld analysis to the amorphous silica and calcite determined by mass balance calculations, the corrected values for the quantitative analysis are 83.97 wt% augite, 9.86 wt% Na-phillipsite and 0.85 wt% hematite (Table V.1). Thus, it is assumed that due to the resolution constraints of Micro-CT equipment, the amounts of Na-phillipsite and $CaCO_3$ + SiO_2 were slightly overestimated.

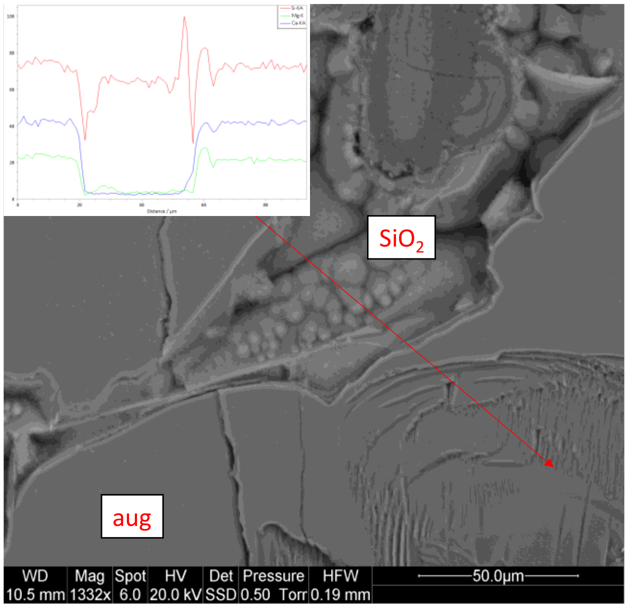

Figure V.5. SEM-EDS compositional profile showing silica gel (SiO2) and augite (aug) after 28 days of reaction in water.

In the case of diopside subjected to dissolution in water at pH 7.5, XRD and Rietveld analyses (Figure V.6 and V.2a) showed no major differences between unreacted and reacted samples, except for the presence of 1.23 wt% of Mg-Calcite (12 mol% Mg, Table V.2), also confirmed by SEM-EDS analyses (Figure V.7b-c). As mentioned above, calcite precipitation was caused by the presence of CO_2 in the head space of the reactor. µ-Raman analyses also confirmed the precipitation of this carbonate. In addition, SEM-EDX and XRD analyses confirmed the presence of hematite (0.4 wt%). Rietveld analyses showed a very limited replacement of diopside by secondary phases (< 2 wt%) and, in contrast with augite runs, no secondary crystalline silicates were detected. However, SEM-EDS analyses showed the presence of Ca- and Mg-free Si-rich precipitates in dissolution pits and on the surface of diopside, which it is interpreted as silica gel (Figure V.7d). Micro-CT analyses (Figure V.8) showed silica gel (2.7 wt%) after 28 days of reaction, but only on the surface of the starting material. As in the case of the augite run, mass balance calculations were performed to unravel the SiO_2 content. This analysis shows that the value obtained by Micro-CT analysis was overestimated, because the equipment could not differentiate between calcite and amorphous silica (identified by XRD and SEM-EDS, respectively) as they showed no detectable X-ray attenuation contrast. Rietveld calculations were normalized to the 1.7 wt% amorphous SiO_2 calculated by mass balance yielding 96.73 wt% diopside, and 1.23 wt% calcite (Table V.1). In contrast with augite runs, no pervasive fractures were identified by SEM or micro-CT analyses. Apparently, the formation of secondary crystalline silicate phases induces fracturing, but this is not the case for the precipitation of amorphous phases (see V.7 section).

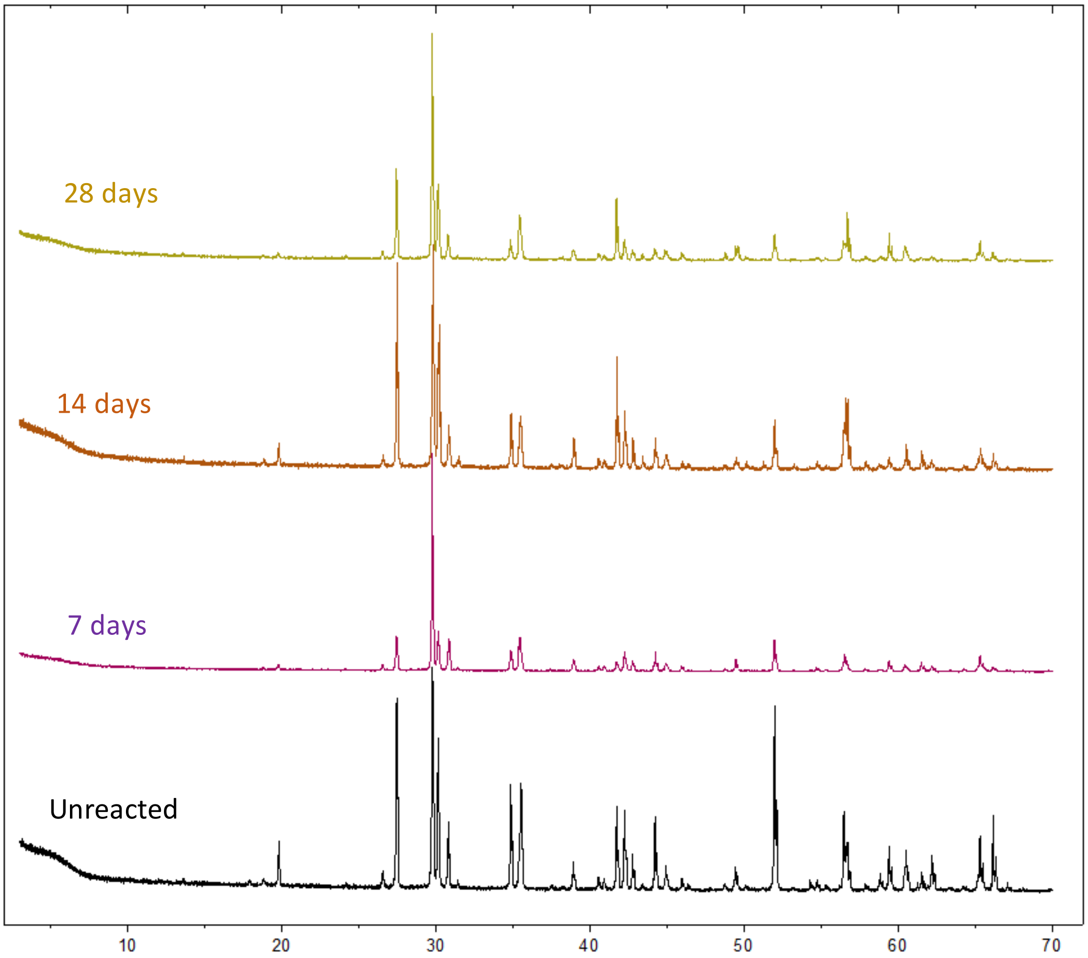

Figure V.6. XRD patterns of unreacted diopside and reacted in water during 7, 14 and 28 days.

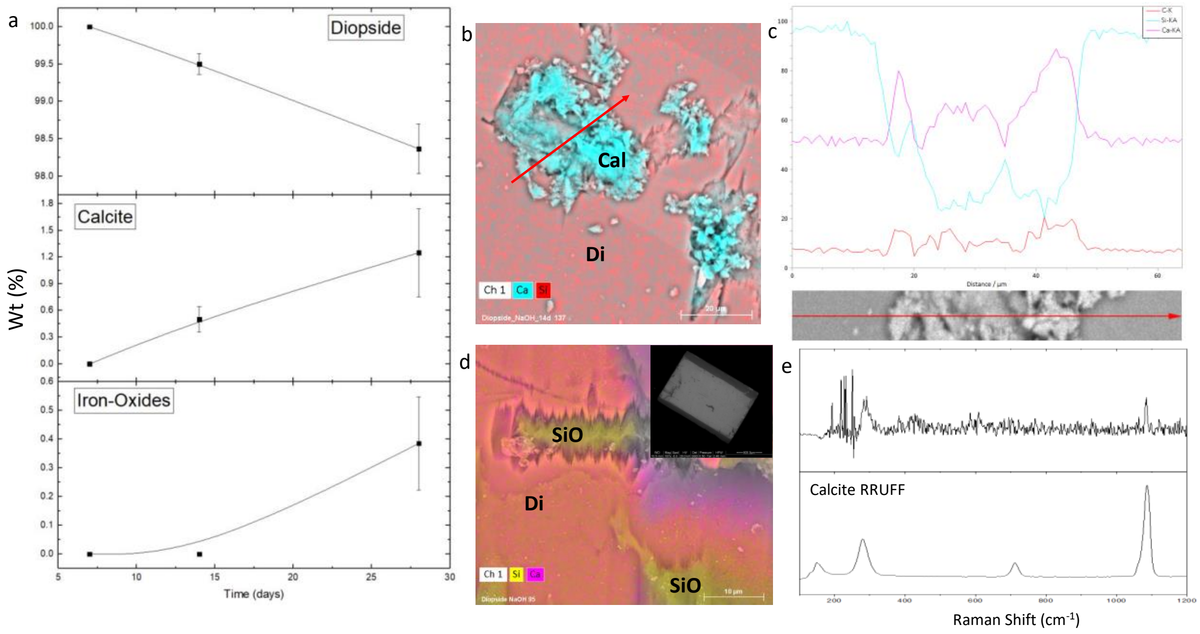

Figure V.7. Products of reaction between diopside and water: (a) Time evolution of the crystalline phases determined by XRD Rietveld analyses . (b) SEM-EDS compositional map showing calcite (cal) crystals in the dissolution pits of the diopside in 14 days run (di) material and the SEM-EDS line of the figure c. (c) SEM-EDS compositional line showing the evolution of Ca, Si and C along the line. (d) SEM-EDS compositional map showing the diopside (di) after 28 days of reaction showing a Si-bearing phase (SiO) inside the dissolution pits and in the surface of the starting material. (e) µ-Raman spectra of calcite crystal and calcite reference phase of RRUFF database.

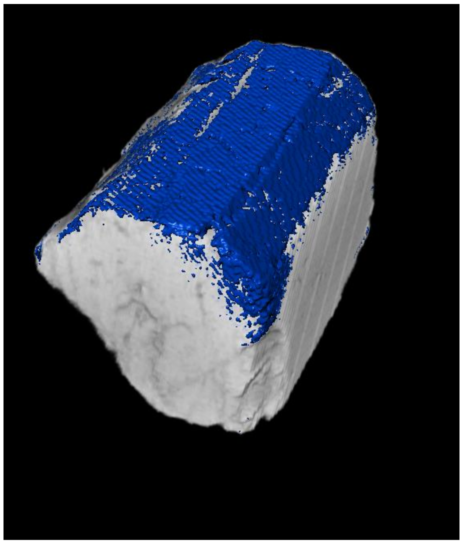

Figure V.8. Micro-CT analysis showing silica gel (blue) and diopside reacted in water for 28 days

V.3 Characterization of solids reacted in sodium bicarbonate solutions

XRD-Rietveld semiquantitative results (Figure V.9a and V.10) show that the reaction between augite and $NaHCO_3$ solution led to the formation of Na-phillipsite and calcite, as also occurred in the case of water. However, augite replacement was substantially higher (36.9 wt%) and secondary phases formation reached maximum values: 12.7 wt% Na-phillipsite (value very similar to water runs) and 22.3 wt% calcite. Importantly, the mass balance between Si in solution (Figure V.1c) and reacted augite from Rietveld analysis shows an excess of Si that should be incorporated into an additional secondary Si-bearing phase, which was not detected by XRD or SEM-EDS analyses. Based on the results of water runs (see above), it is suggested that such a missing Si was incorporated into amorphous silica. Rietveld analyses were normalized to the 2.1 wt% of newly-formed amorphous silica calculated from mass balance (Table V.1). Calcite formation was confirmed by µ-Raman analyses (Figure V.9d). SEM-EDS analyses (Figure inset V.9b and c) showed massive pervasive fracturing of the starting crystal and confirmed the presence of abundant Na-phillipsite and calcite precipitated within the fractures and on the surface of the starting material. Rhombohedral calcite crystals ~8 µm in size with surface-decorated iron-oxides were also identified. Micro-CT analyses (Figure V.9e) confirmed that the secondary phases precipitated within the fractures and the pores of the host augite crystal. Interestingly, Na-phillipsite precipitated directly in contact with the fracture/pore walls, filling the fractures inwards and fully covering the surface of the walls. In contrast, calcite crystals appeared on the surface of the pyroxene crystal and filling the cracks in contact with the Na-phillipsite (Figure V.11), evidencing a first precipitation of the zeolite and the subsequent formation of calcite. It should be noted that in this run the amount of newly-formed iron oxides reached the highest values of all experiments (2.01 wt%).

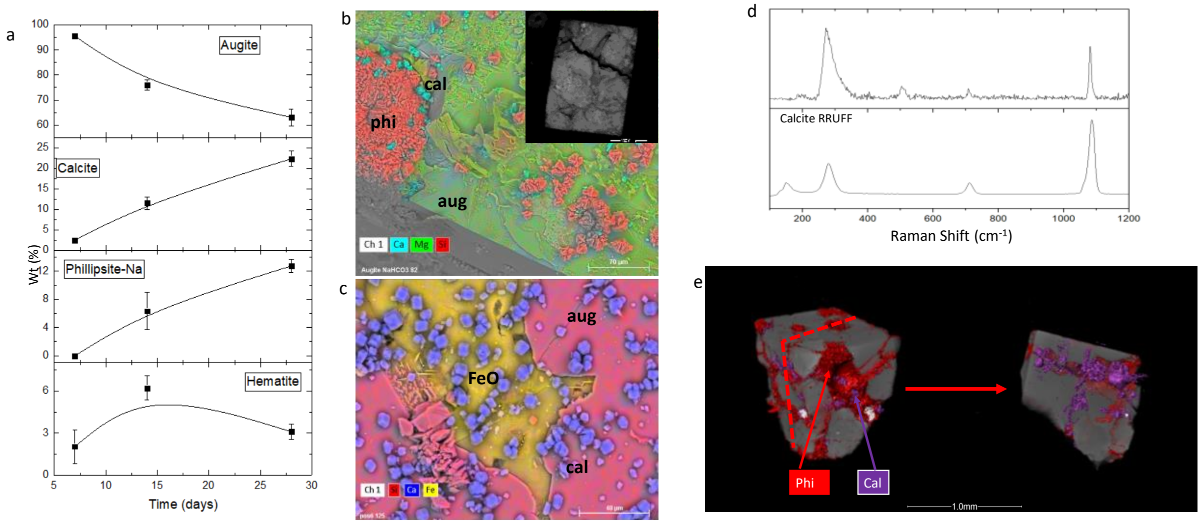

Figure V.9. Products of reaction between augite and NaHCO3 solution: (a) Time evolution of the crystalline phases determined by XRD Rietveld analyses (b) SEM image of the entire reacted crystal overlaid with EDS compositional map showing the augite (aug) crystal fractured after 28 days of reaction, inside the fractures, phillipsite (phi) and few crystals of calcite (cal). (c) SEM-EDS compositional map showing calcite (cal) crystals at the surface of the augite mineral (aug) and iron oxide (FeO) surfaces in dissolution areas. (d) µ-Raman spectra with Calcite reference phase of RRUFF database. (e) Micro-CT image showing in blue the 3D distribution of phillipsite (phi) in red and in purple the calcite (cal) in augite crystal after 28 days of reaction. Red dotted line of left image represents the virtual cut performed to observe the inside of the newly-formed filled fracture.

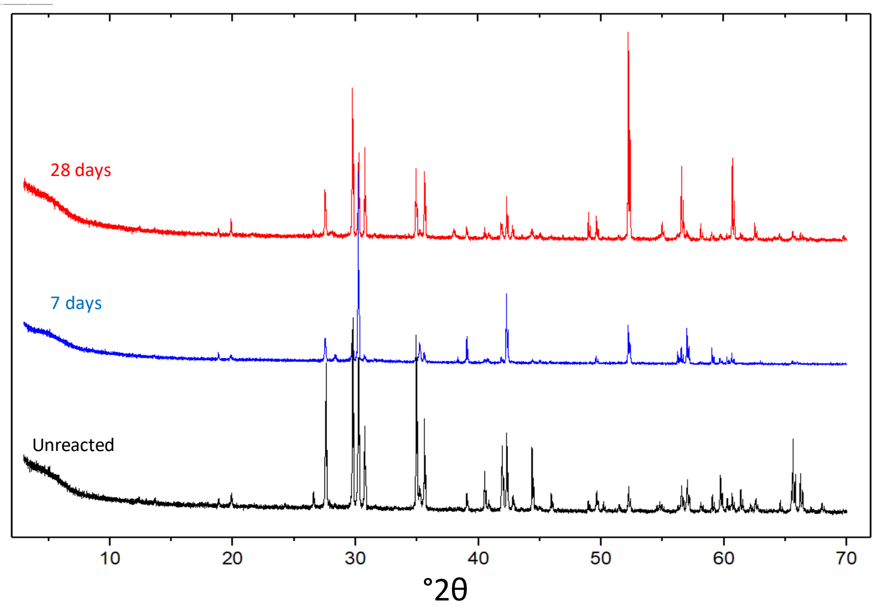

Figure V.10. XRD patterns of unreacted augite and reacted in NaHCO3 solution during 7, and 28 days

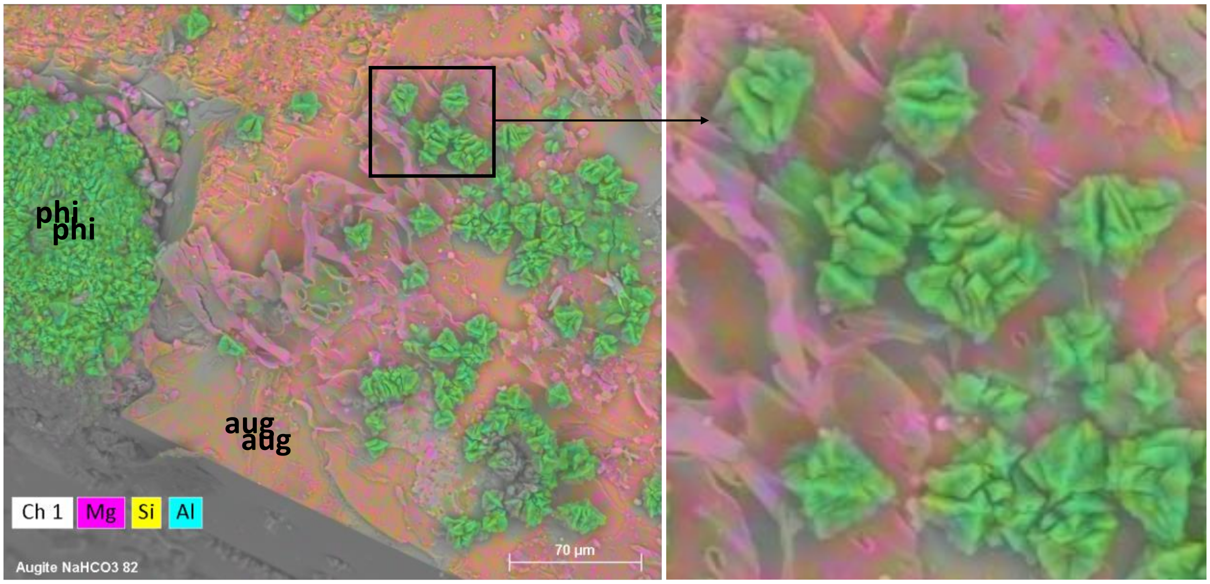

Figure V.11. SEM-EDS compositional map of Figure 4.b showing Mg (purple), Si (yellow) and Al (Blue). It can be observed that the augite (aug) crystal fractured after 28 days of reaction includes phillipsite (phi) in the fractures. Detailed image of the Na-phillipsite evidencing the typical zeolite morphology.

XRD-Rietveld analyses (Figure V.12 and V.13a) of diopside showed a much higher level of replacement (12.6 wt%) by newly-formed phases in $NaHCO_3$ solution than in water, but this value was significantly lower than that of augite reacted in bicarbonate solutions. Calcite was the most abundant secondary phase, showing a progressive increase up to 11.7 wt% over the whole spam of the experiment, whereas iron oxides were always under 1 wt%. Mass balance calculations showed a lack of precipitated Si. As in the previous case, this is interpreted as amorphous silica gel not detected by XRD. Quantitative Rietveld analysis results were normalized using the 1.27 wt% of amorphous SiO2 calculated form mass balance (Table V.1). Calcite precipitation was confirmed by µ-Raman (Figure V.13b) showing the characteristic bands at 286 cm^{-1}, 717 $cm^{-1,}$ and 1085 cm^{-1}, plus additional diopside bands, to due to the relatively high beam penetration depth. These inosilicate bands include: a band at 663 cm^{-1} corresponding to the $Si\text{-}O_{br}$ stretching, a band at 1012 cm^{-1} corresponding to $Si\text{-}O_{nbr}$ stretching and, in the lower frequency region, four bands at 206 cm^{-1}, 316 cm^{-1}, 350 cm^{-1} and 385 cm^{-1} corresponding to the Ca/Mg-O vibrations (Buzatu and Buzgar, 2010). Precipitation of calcite and iron oxides was also confirmed by SEM-EDS analyses (Figure V.13c and d). Rhombohedral calcite crystals were observed on the surface and within dissolution pits of the diopside substrate. EDS analyses of calcite crystals showed an important Mg content (Figure V.13c). From XRD analysis, the Mg content in calcite was determined to be 14.8 wt%. As in the pure water systems, and in contrast with augite runs, diopside crystals were not fractured (inset Figure V.13c). Due to the lack of fracturing, no secondary phases were detected in the interior of the diopside crystals by Micro-CT.

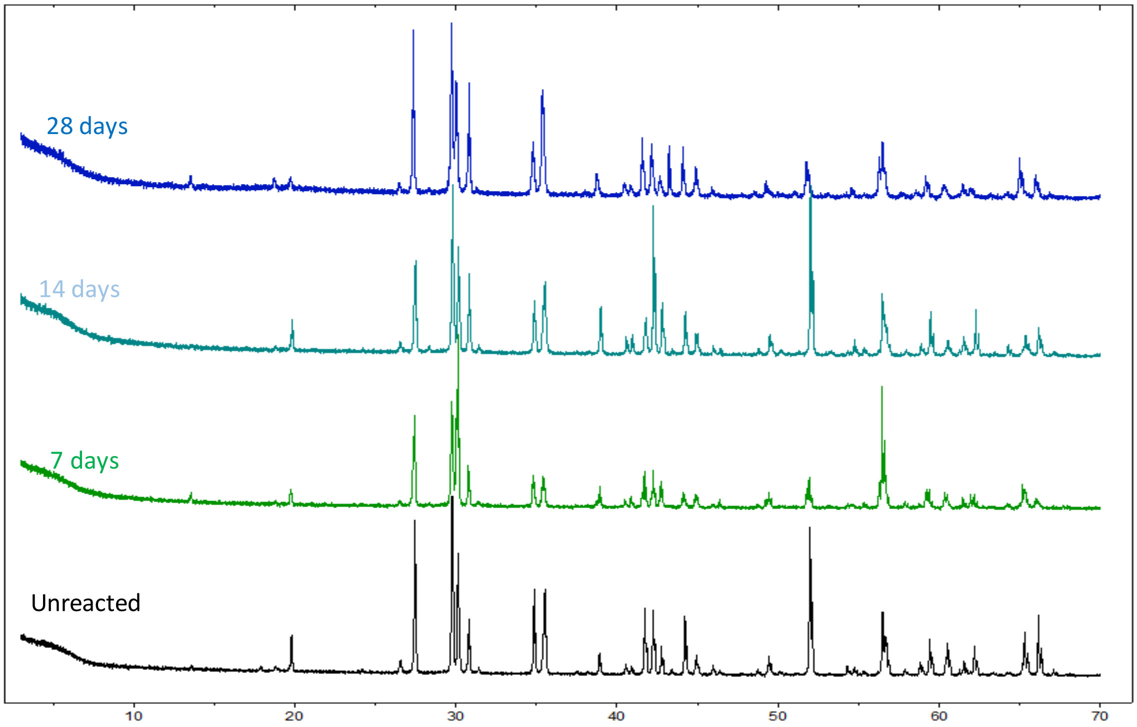

Figure V.12. XRD patterns of unreacted diopside and reacted $NaHCO_3$ solution during 7, and 28 days.

Table V.2. Mg content (mol%) in calcite after 28 days of reaction calculated following the procedure of Goldsmith et al. (1958)

Mg content in calcite (mol%)	NaOH	error	$NaHCO_3$	error	Na_2CO_3	error
Augite	8	2	15	3	12	2
Diopside	12	4	15	3	4	2

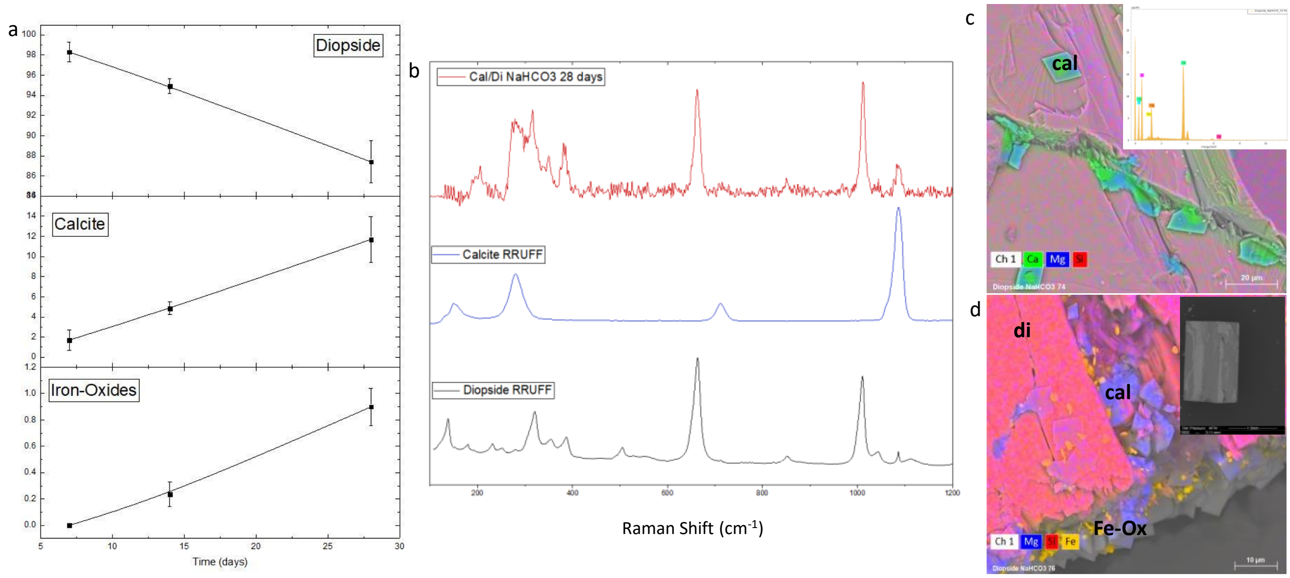

Figure V.13. Products of reaction between diopside and NaHCO3 solution: (a) Time evolution of the crystalline phases determined by XRD Rietveld analyses (b) µ-Raman spectra of calcite crystal in the 28 days run with Calcite and Diopside reference phases of RRUFF database. (c) SEM-EDS compositional map showing magnesium calcite crystals (cal) and diopside (di) after 28 days of reaction overlaid with EDS spectra of calcite (d) SEM-EDS compositional map showing calcite (cal) crystals inside the fractures of the diopside (di) and iron-oxide particles in the surface (Fe-Ox).

V.4 Characterization of solids reacted in sodium carbonate solutions

Although no major changes in augite reacted for 28 days, as compared with unreacted augite, were observed using XRD (Figure V.14a), the formation of Mg-calcite (12 mol% Mg), along with hematite, whose content increased almost linearly with time, was detected. Augite replacement in the Na_2CO_3 system was the lowest observed here (7.95 wt%). Mg-calcite reached 6.9 wt%, value in good agreement with Micro-CT analyses (7.7 wt%). Mg-calcite was principally present as rhombohedral crystals ~16 µm in size on the surface of the starting material and inside small surface cracks and dissolution pores, as shown by Micro-CT and SEM analyses (Figure V.14b and c). Fractures were not observed within reacted augite crystals (Figure V.14c). Furthermore, no Si-bearing secondary phases were identified.

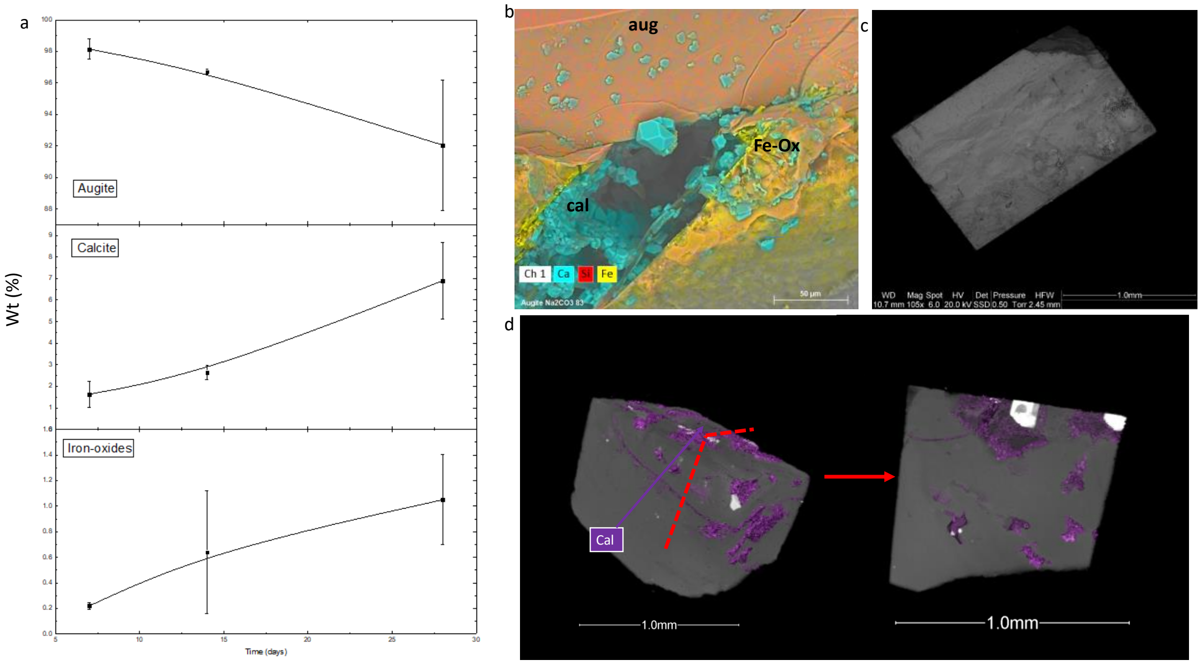

Figure V.14. Products of reaction between augite and Na_2CO_3 solution: (a) Time evolution of the crystalline phases determined by XRD Rietveld analyses (b) SEM-EDS compositional map of 28 adys reaction solids showing calcite (cal) crystals inside the fractures of the augite mineral (aug) and iron oxides (Fe-Ox) surrounding the fracture. (c) SEM image of the entire crystal after reaction (d) Micro-CT image showing the 3D distribution of calcite (purple) in augite crystal after 28 days of reaction. Red dotted line of left image represents the virtual cut performed to observe the inside of the crystal.

XRD results (Figures V.15a and b) showed minimal replacement of diopside (2.25 wt%) in Na_2CO_3 solution by low-magnesium calcite crystals (4 mol% Mg, the lowest value of all runs). SEM-EDS analysis of solids collected after 7 days of reaction (Figure V.16a) showed the presence of a gel-like Mg- and Si-rich surface precipitate with no Ca, in addition to rhombohedral crystals of calcium carbonate. Moreover, EDS analyses showed that the apparently amorphous Mg-silicate had a Mg/Si ratio of 0.72, in good agreement with mass balance calculations yielding a Mg/Si ratio of 0.63. It should be noted that Mg/Si ratio was calculated by mass balance as follows:

$$\Delta_{Mg}= m_{pyr} - \left(m_{sol} + m_{prec}\right) \tag{V.2}$$

where m_{pyr} is the molarity of Mg from the dissolved pyroxene obtained from the Rietveld analyses, m_{sol} is the Mg concentration in solution obtained by ICP-OES analyses and m_{prec} is the molarity of Mg precipitated in the Mg-containing phases obtained by Rietveld analysis. The difference in concentration obtained, Δm, is interpreted here as the Mg contained in the Mg/Si-bearing amorphous phases.

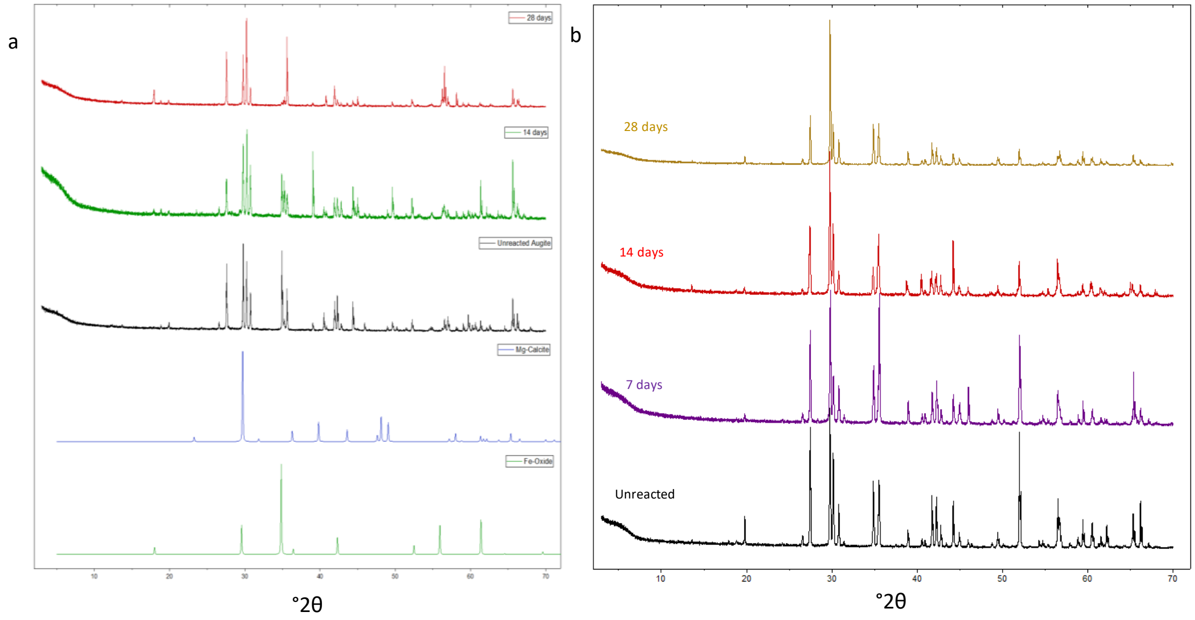

Figure V.15. XRD patterns in Na_2CO_3 solution during 7, 14 and 28 days of (a) unreacted and reacted augite (b) unreacted and reacted diopside.

Such values are in full agreement with the typical Mg/Si ratios observed for magnesium silicate hydrate (MSH) gels (0.6-0.9) (Brew and Glasser, 2005;; Lothenbach et al., 2015; Bernard et al., 2017). After 28 days of reaction (Figure V.16b and c), the MSH gel suffered a morphological transformation to a more condensed structure filling dissolution pits of diopside. Furthermore, calcite crystals were associated with MSH on the surface and within etch pits of the pyroxene. Micro-CT (Figure V.16d) analyses showed the distribution of MSH along the dissolution areas and the pores formed on the surface of diopside, but also in a few small cracks extending from the surface to the interior of the crystal (without cross-cutting the crystal). Micro-CT based calculation of MSH + calcite content yielded 9.7 wt% of both phases. If it is subtracted to this value the Rietveld value obtained for calcite, the MSH content should be 7.45 wt%. However, mass balance did not match these values, showing an excess of Si in the system. Refined calculation were performed considering the Si and Mg content in solution, yielding a MSH content of 5 wt%. Rietveld analyses were normalized to this value (Table V.1). It should be noted that calcite could not be differentiated from MSH using micro-CT due to analytical constraints.

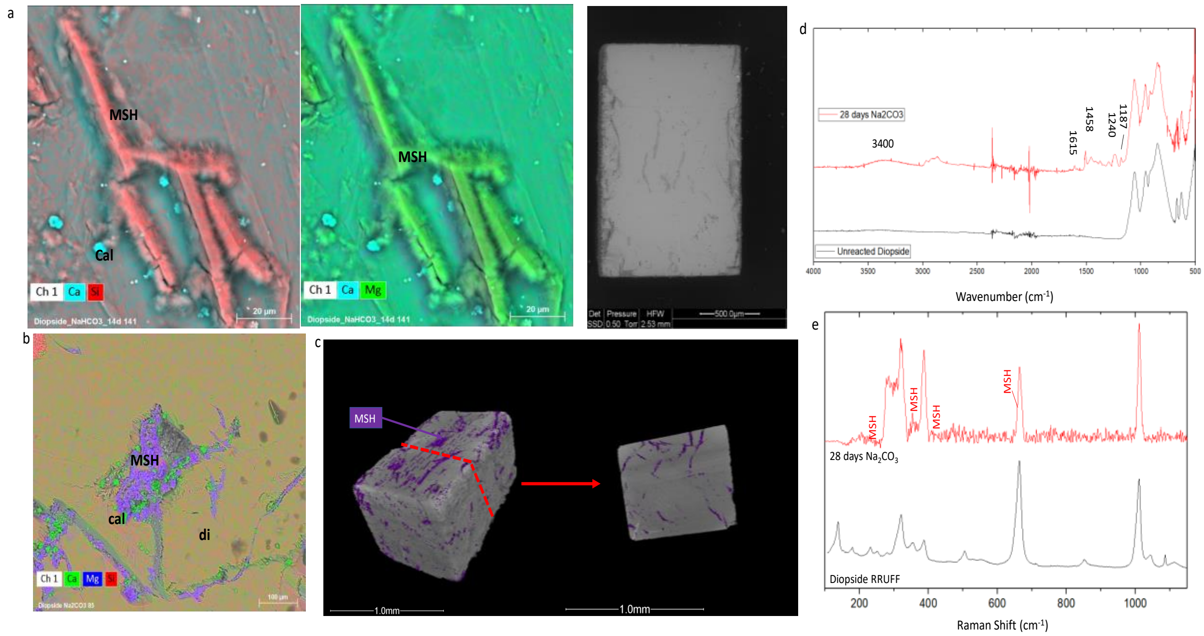

Figure V.16. Products of reaction between diopside and Na_2CO_3 solution: (a) SEM-EDS compositional map showing a proto magnesium silicate hydrate (MSH) and calcite particles (cal) in the surface of the diopside (di). (b) SEM-EDS compositional map showing the magnesium silicate hydrate (MSH) in the dissolution fractures of diopside (di) with calcite crystals (cal) and SEM image of the entire crystal (c) Micro-CT image showing the 3D distribution of MSH (red) and calcite (putple) in diopside crystal after 28 days of reaction. Red dotted line of left image represents the virtual cut performed to observe the inside of the crystal (c) FTIR spectra of the diopside reacted after 28 days in Na_2CO_3 solution and the unreacted diopside. (d) µ-Raman spectra of the diopside reacted after 28 days in Na_2CO_3 solution showing the bands corresponding to the MSH regarding Lothenbatch et al. (2015) and the pattern of diopside from RRUFF database.

MSH precipitation was confirmed by FTIR analyses (Figure V.16d) showing the broad v-OH stretching around 3400 cm^{-1} and the δ-OH bending at ~1615 cm^{-1} of water as well as a weak band at ~1240 cm^{-1} attributed to the Q_3 stretching vibration of Si-O bonds, a band at ~1180 corresponding to the v_3 vibration of the Si-O bond in fresh MSH gels, a band red-shifted from the typical v_3 Si-O band of CSH at 945 cm^{-1} (Ashraf and Olek, n.d.; D. R. M. Brew and Glasser, 2005; Lothenbach et al., 2015; Nied et al., 2016; Tonelli et al., 2016). The presence of a carbonate phase was also confirmed by the v_3 band at ~1458 cm^{-1} (Ashraf and Olek, n.d.; Gunasekaran et al., 2006).

It should be noted that calcite bands at 874 cm^{-1} and 713 cm^{-1} were not detected due to the overlapping of the broadband of ν_{as} Si-O-Si vibration of diopside (Omori, 1971; Mozgawa et al., 2004). To further corroborate the presence of MSH, µ-Raman analyses were performed (Figure V.16e). The bands of diopside were detected, as well as the bands corresponding to O-H-O vibrations at 219 cm^{-1}, O-Si-O bending at 354 cm^{-1} and Si-O-Si symmetrical bending at 450 cm^{-1} and 661 cm^{-1}, corresponding to MSH (Lothenbach et al., 2015; Nied et al., 2016; Bernard et al., 2017).

V.5 Quantitative comparison of carbonation extent

To better assess the carbonation extent of the different starting materials, values determined by Rietveld refinement (ξ_n^{RR}) were plotted as a function of mass balance values (ξ_n^{MB}) (Figure V.17):

$$\xi_n = (x_{Cal}/M_{cal})/(x_{py}/M_{py} + x_{cal}/M_{cal}) \qquad \text{(V.3)}$$

where x_{Cal} and x_{py} are the weight percent of calcite and pyroxene (diopside or augite) determined by Rietveld analysis or mass balance calculation, and M_{cal} and M_{py} are the molecular masses (g·mol^{-1}) of calcite and pyroxenes respectively, yielding dimensionless ξ_n.

Extents of carbonation determined by both methods are listed in Table V.1. The correlation coefficient of the linear regression of the corresponding data and the slope of the linear regression of both analyses were close to 1, showing that in both cases the ξ_n values obtained by Rietveld analysis are in perfect agreement with those obtained by mass balance analysis (Figure V.18). These results support, on the one hand, that Rietveld analysis is an accurate method for quantitative phase analysis, even in the case mineral phases present in very small amounts, and on the other hand, give extra reliability to the experimental work.

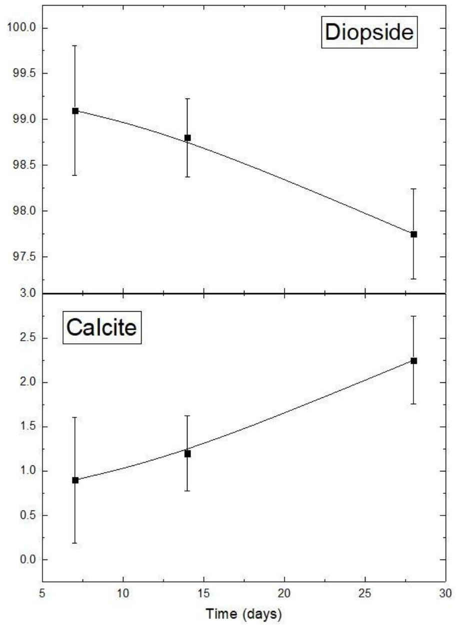

Figure V.17. Time evolution of crystalline phase content determined by XRD Rietveld analyses of unreacted diopside and reacted in Na_2CO_3 solution.

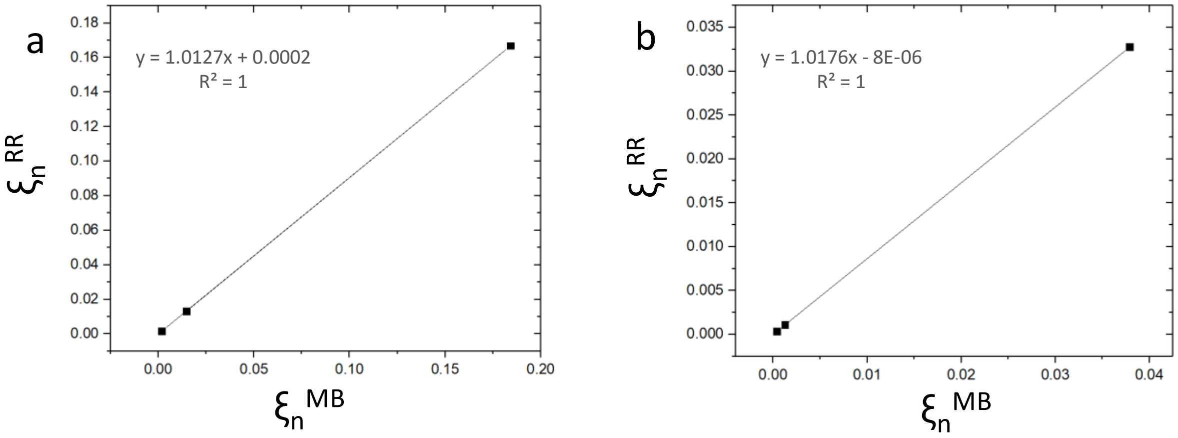

Figure V.18. Calibration plots of the two different quantitative methods used to determine extents of carbonation (Rietveld Method and Mass Balance). (a) Augite; (b) Diopside

V.6 Effect of pH and secondary phases precipitation during dissolution-carbonation

Dissolution kinetics of inosilicate minerals are negatively correlated with [H^+] (e.g., Schott et al., 1981; Drever, 1985; Dietzel, 2000; McAdam et al., 2008; Schott et al., 2012). Schott et al. 2003). Therefore, the concentration of released divalent metals susceptible to contribute to the carbonation reaction is expected to be higher at close-to-neutral than at alkaline pHs. Indeed, these results show that the replacement of both pyroxenes by secondary phases was strongly pH dependent. The amount of replaced reactant phase was maximum in sodium bicarbonate solution for both minerals studied here, reaching a ~38 wt% in augite and ~15 wt% in diopside. The next system to reach a higher replacement of the starting material should be the pure water run and the lowest replacement should take place in Na_2CO_3 solutions. This holds true for augite experiments, where 18.4 wt% replacement in water and 3.7 wt% in Na_2CO_3 solutions was observed. Unexpectedly, 7 wt% diopside was replaced in Na_2CO_3 systems and only 3.5 wt% in water. Thermodynamics is not able to explain this latter behavior, and kinetics factors (among others) should be taken into account (see below). Furthermore, these results demonstrate that DIC is necessary for the replacement reaction to progress to the maximum possible extent, in agreement with the previous work (Luis Monasterio-Guillot et al., 2019).

Calculation of Saturation Index (SI_{cal}) using PHREEQc (Figure V.19) show that the highest calcite supersaturation is reached for augite in $NaHCO_3$ runs. Due to the similar behavior of SI_{cal} for both pyroxenes, results for diopside SI modeling are not shown here. According to Morse and Bender (1990) low magnesium calcite (<10 mol%) presents a slight decrease in solubility product as compared with pure calcite. Thus, it can be expected a slight increase of the calculated SI_{cal} due to the Mg content, favoring Mg-calcite precipitation. Furthermore, the precipitation of calcium carbonate causes a pH decrease (Figure V.1) by proton release following the overall reaction (I.8) which would foster further pyroxene dissolution. Thus, the modeling is in good agreement with these experimental results showing that in $NaHCO_3$ runs calcite precipitation reached the highest yield as compared to the other systems (24.6 wt% in augite and 11.7 wt% in diopside). The highest Mg content in calcite was observed in $NaHCO_3$ runs, whereas in pure water a higher Mg content was observed in diopside than in augite runs. In turn, calcite formed after reaction of diopside in Na_2CO_3 solutions showed the lowest Mg content. It is suggested that at neutral-to-moderately alkaline pH (bicarbonate and water runs), the higher $[Ca^{2+}]/[CO_3^{2-}]$ ratio (closer to unity) as compared to higher pH runs (with higher $[CO_3^{2-}]$) in addition to the high SI_{cal} could enable faster calcite growth favoring Mg incorporation (Mavromatis et al., 2013). In addition, calcite precipitated in diopside runs with Na_2CO_3 solution must have a lower Mg content because Mg was also incorporated in MSH, a phase which according to SEM-EDX and µ-CT observations, preceded Mg-calcite.

In agreement with Gadikota et al. (2014), who showed that the addition of $NaHCO_3$ during ex situ CCS fostered the carbonation of Ca-Mg silicates due to its buffer effect, it is also observed enhanced silicate dissolution-carbonation in $NaHCO_3$ runs due to the relatively constant pH of the reaction ($7.5<pH<9$). This relatively constant pH enhances the dissolution of the pyroxenes as compared to a strongly-alkaline pH and, as a consequence, increases the amount of alkali-earth metal ions feed to the solution susceptible to react with CO_3^{2-} ions. This explain why it is obtained the highest levels of calcium carbonate precipitation in bicarbonate runs.

Regarding iron oxides precipitation, PHREEQc calculations (Figure V.19) show that under the whole pH range of these experiments, hematite was supersaturated. Therefore, precipitation of

Fe-oxides was expected right after Fe release following dissolution of the starting materials, in agreement with Schwertmann (1991). As in the case of Mg-calcite, precipitation of Fe-oxides should also favor the progress of the dissolution/carbonation according to the Le Chatelier's principle.

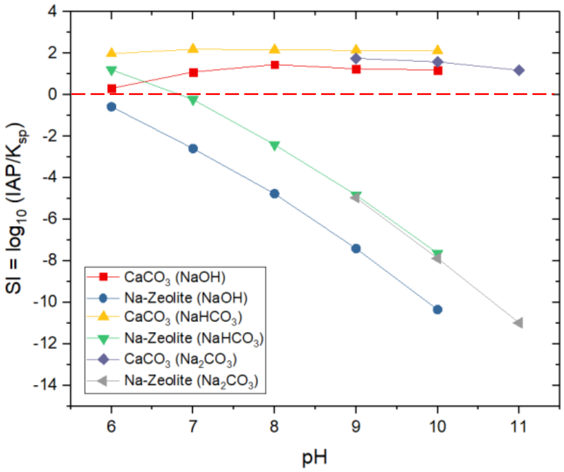

Figure V.19. PHREEQC simulations of saturation index evolution with pH of calcite and sodium zeolite during augite mineral replacement reaction at equilibrium. Red dotted line represent the equilibrium point

Regarding secondary silicate phases, amorphous silica, magnesium silicate hydrate (MSH) and Na-phillipsite precipitated in these experiments despite the theoretical outcome of Eq. (I.5), where the only secondary phase expected, in addition to calcite, was amorphous silica.

These analysis of the solutions chemistry evolution and SEM-EDS observations revealed that amorphous silica was precipitated after a moderate alkalinization in $NaHCO_3$ and water runs. SiO_{2am} was found within etch pits and as isolated precipitates on the surface of the pyroxene crystals. The formation of etch pits and their filing by amorphous silica evidences that a coupled dissolution-precipitation reaction at the mineral-fluid interface (ICDP) was at work here (Putnis, 2009; Ruiz-Agudo et al., 2012; Ruiz-Agudo et al., 2016). In the previous work (Monasterio-

Guillot et al. ongoing), it has been demonstrated that during weathering of these two clinopyroxenes under the same conditions studied here, amorphous silica was subsaturated with respect to the solution at $pH \geq 2$. The presence of this phase here, at $pH \geq 7.5$, strongly support an ICDP mechanism for amorphous silica precipitation following pyroxene weathering. According to previous works (Hellmann et al., 2003; Damien Daval et al., 2009a; Ruiz-Agudo et al., 2012; Ruiz-Agudo et al., 2014b; Ruiz-Agudo et al., 2016; Daval et al., 2017; Wild et al., 2019), replacement processes taking place at the mineral-fluid interface result in strong compositional gradients and important pH differences between the bulk solution and the mineral-fluid interface. Such gradients enable the precipitation via an ICDP mechanism of secondary phases, thermodynamically not possible in the bulk solution (Putnis, 2009), thus explaining the observed formation of amorphous silica (as well as the other two secondary silicates, as discussed below).

Under the highly alkaline pH of the Na_2CO_3 runs, it has been detected no amorphous silica precipitation. However, the highest Si concentration in solution was reached (Figure V.1). On the one hand, this result is consistent with the nearly exponential increase in silica solubility at $pH > 9$ (Fleming and Crerar, 1982; Béarat et al., 2006; Monasterio-Guillot et al., 2019), not favoring its precipitation. On the other hand, because pyroxene dissolution rates decrease with increasing pH (Schott et al., 2002), the Si release rate was substantially lower in highly alkaline systems than in moderately alkaline ones. This can led to a lower chemical gradient, enough to enable Si ions to diffuse from the mineral-fluid interface to the bulk solution until reaching equilibrium (i.e., undersaturation with respect to amorphous silica), thereby preventing amorphous silica precipitation (Ruiz-Agudo et al., 2012; Encarnación Ruiz-Agudo et al., 2016).

It should be noted that mass balance calculations showed a deficit of precipitated Mg in runs resulting in amorphous silica formation and where no Mg-bearing phases (other than Mg-calcite) were detected. Daval et al., (2013) have shown that during diopside dissolution, amorphous silica incorporated large amounts of Mg and/or Fe, suggesting an acceleration of SALs formation by this metal ions, as corroborated by several authors (King et al., 2010; Sissmann et al., 2013; Luis Monasterio-Guillot et al., 2019). This is a handicap for the effective carbonation of primary silicates because a fraction of Mg (and Fe^{2+}) will not be incorporated into the newly-formed carbonate phases. Thus, this effect cannot be ignored. However, SEM-EDS analyses do not show the presence of Mg or Fe in amorphous silica. Conversely, it is observed the incorporation of Mg in Na-phillipsite in augite runs at neutral-to-moderately alkaline pH, and in this case there will be no deficit in precipitated Mg. However, it cannot explain the Mg deficit in the case of augite reacted at high pH, or the case of diopside reacted at neutral-to-moderately alkaline pH. One possible explanation is an experimental error during analysis of Mg concentrations in solution.

Augite dissolution-carbonation at neutral-to-moderately alkaline pH, led to the precipitation of Na-phillipsite. Previous works have reported the precipitation of secondary Na-phillipsite during weathering of basic and ultrabasic rocks rich in aluminum-augite in pelagic environments (Glaccum and Boström, 1976; Hay and Sheppard, 2001; Etame et al., 2012; Ozpinar et al., 2013). To model the evolution of the Saturation Index of Na-phillipsite (SI_{phi}) at these experimental conditions, PHREEQc calculations were performed (Figure V.18). SI_{phi} values show that in $NaHCO_3$ solutions at pH<7, Na-phillipsite was supersaturated. Interestingly, the SI_{phi} was higher in $NaHCO_3$ solutions than in water at all pH values, which could explain why a higher amount of Na-phillipsite formed in the former run. However, values of $SI_{phi}<0$ (undersaturation) were obtained for all relevant pH values (i.e.,pH ≥7.5) in this studied systems. The latter indicates that it was not thermodynamically possible to precipitate this phase, contrary to these experimental observations. As in the case of the precipitation of $SiO_{2(am)}$ above discussed, if a sufficiently high

Na, Al and Si release rate is achieved, a high supersaturation will be reached at the mineral-fluid interface as to enable the heterogeneous precipitation of Na-phillipsite on the dissolving augite via an ICDP mechanism. In this respect, it is important to underline that a high solute concentration can be achieved within the constrained volume of etch pits formed during pyroxene dissolution (Plümper et al., 2012), and their pore surface will offer a large amounts of sites for heterogeneous nucleation (Scherer, 1999; Putnis, 2009; Emmanuel and Ague, 2011; Schiro et al., 2012; Ruiz-Agudo et al., 2014a). Altogether these combined effects would favor the observed precipitation of Na-phillipsite.

In the previous work (Luis Monasterio-Guillot et al., 2019) it is showed the formation of a secondary Ca+(Na/K)-bearing silicate (pectolite) during pseudowollastonite carbonation under equivalent conditions to those in this work. Other studies on pyroxenes and olivine carbonation demonstrated the formation of secondary crystalline Ca and Mg silicates (King et al., 2010; Sissmann et al., 2013), which fostered carbonation, as also shown here, but underlined that divalent metals incorporation into the secondary silicates was a handicap for an effective CCS (Monasterio-Guillot et al., 2019). In this case, the observed incorporation of small amounts of Mg in Na-phillipsite will also pose a handicap, yet very limited, for an effective carbonation of augite (Figure V.20 and Table V.3).

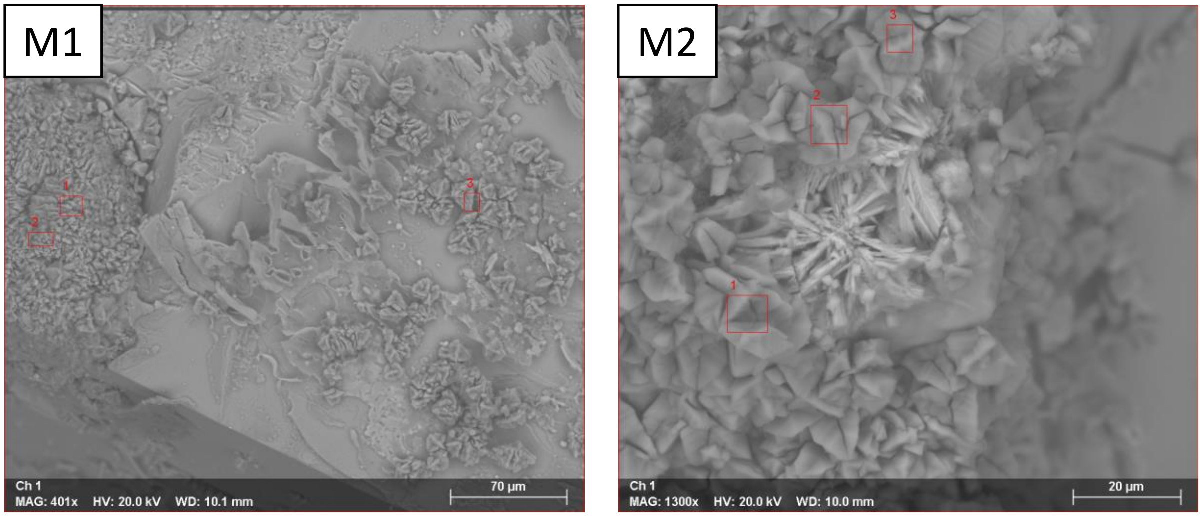

Figure V.20. SEM images of augite crystal surface after 28 days of reaction in $NaHCO_3$ solution. Two different zones (M1 and M2) are shown. The red squares correspond to the EDX analyses reported in table S4

Table V.3. EDS elemental composition (at %) of Na-phillipsite on the surface of the augite crystals after 28 days of reaction in NaHCO3 solution analyzed with SEM-EDS. Analysis # refer to numbered spots in the SEM image in **Figure V.20**. Note that O (and C) are excluded from the reported analysis composition (this is why the sum of at % is not 100%).

Analysis	Na	Mg	Al	Si
M1-1	6.92	0.00	7.44	10.97
M1-2	5.72	0.19	7.58	10.98
M1-3	7.44	0.72	8.14	11.08
M2-1	7.01	0.00	5.98	10.37
M2-2	8.85	0.03	7.64	10.72
M2-3	6.08	0.13	6.34	9.99
Average	7.00	0.18	7.19	10.68
Error	1.10	0.28	0.84	0.43

The amount of Na was double in Na_2CO_3 runs than in $NaHCO_3$ runs, and orders of magnitude higher than in water runs. However, no Na-aluminosilicates precipitated in the former runs. This is likely due to the low dissolution rates of pyroxenes under strongly-alkaline pH, preventing the build-up of sufficient supersaturation at the mineral-fluid interface as to enable Na-phillipsite precipitation despite the higher Na content. The lack of secondary crystalline silicates in Na_2CO_3 solutions during augite carbonation led to the lowest level of replacement and calcite yield. This emphasizes that the formation of secondary silicate phases is crucial to promote carbonation of primary silicates (Monaterio et al., 2019).

The lack of Na-phillipsite precipitation in diopside runs can be easily explained considering the absence of Al in the elemental composition of this mineral. However, other crystalline secondary Ca and/or Mg silicates could in theory be formed after diopside dissolution at neutral to moderately alkaline pH, as observed for instance after carbonation of olivine (King et al., 2010; Sissman et al., 2013; Daval et al.,2011) and wollastonite (Daval et al. 2009a, and b). However, in these systems, diopside shows a lower dissolution rate than augite, as demonstrated by ICP-OES analyses and the % replacement achieved after 28 days of reaction (Figure V.1 and Table V.1). Therefore, both the slow kinetics of Si release to the solution, and the limited amount of dissolution pores formed on diopside as to favor heterogeneous nucleation of secondary crystalline silicates, seem to have contributed to the reduced yield of secondary phases observed here at moderately alkaline pH..

The contrasting behavior of diopside as compared to augite in Na_2CO_3 solution is also exemplified by the formation of magnesium silicate hydrate (MSH) in the case of diopside runs. First, it is important to remark that, as indicated above, secondary Mg-bearing silicate phases could be interpreted as a handicap for effective CO_2 capture. However, Rietveld and mass balance analyses showed that carbonation yield of diopside during Na_2CO_3 experiments was double than that of water runs, in contrast to augite that reached similar carbonate yield in both runs (Table V.1). The formation of MSH after dissolution of a Mg-Ca-pyroxene is not totally unexpected under these experimental conditions, because in contrast to calcium silicate hydrate (CSH), which is stable at very highly alkaline pHs (≥12.4), MSH is stable at much lower pH values (pH ≈ 7.5) (Bernard et al., 2017). The formation of MSH has been previously reported during olivine carbonation at 170 ºC (Sissmann et al. 2013). However, the Mg/Si ratio reported by Sissman et al. (2013) was huge (Mg/Si = 3.72) as compared to these experimental result (Mg/Si ~ 0.7). It is suggested that this difference is due, on the one hand, to the molar concentration of Mg in the starting material (double in forsterite than in these pyroxenes), and on the other hand, to the higher dissolution rate of olivine as compared with diopside (Schott et al., 2012). Following Sissmann et al. (2013) and Lothenbach et al. (2015), PHREEQc calculations were performed using talc as a proxy to MSH, showing that such a Mg-rich silicate was supersaturated in the Na_2CO_3 solution and, therefore, precipitation was expected. In this respect, it is demonstrated that the precipitation of MSH during diopside carbonation can foster its dissolution leading to enhanced Ca release. Moreover, fracturing associated with MSH precipitation, could also contribute to expose fresh reactive surface, also favoring the progress of the dissolution-carbonation reaction (see below). These two effects help to explain why a higher amount of calcite was precipitated in this run as compared with the water run (i.e., effect of side reactions and reaction-driven fracturing). It is suggested that the absence of MSH formation in augite during Na_2CO_3 runs is due to the higher dissolution rate of this phase as compared with diopside, resulting in higher compositional gradients at the mineral interface that promoted the formation of Mg-calcite as a Mg sink, instead of a Mg-rich silicate phase. Note that SEM-EDX analysis demonstrates that MSH formation precedes calcite formation on the surface of diopside, showing that the kinetics of dissolution and carbonate precipitation in this system were sluggish.

To summarize, these results show that the formation of non-carbonate secondary phases (i.e., Na-phillipsite, hematite, MSH and amorphous silica), fostered the replacement of the starting material and its subsequent carbonation. Altogether, these experimental results demonstrate that the formation of secondary silicates (and oxides) exerted a key role due to the importance of side reactions on enhanced dissolution of primary silicates and on the subsequent effective carbonation.

V.7 Effect of reaction-driven fracturing

In all runs where Na-phillipsite precipitated, augite crystals showed massive pervasive fracturing (insets Figures V.2d and V.9b), whereas no such massive fracturing was observed in the rest of the reacted crystals, with the exception of diopside runs at high pH where some fracturing was observed associated with MSH crystallization. As mentioned above, Na-phillipsite precipitation started in the (wedge-like) etch pits or pre-existing cracks/pores of the host material, and continued by filling cracks generated by the crystallization of this phase. This reaction-driven fracturing is critical for the advancement of the carbonation process, resulting in the highest replacement and carbonate yields observed here. It is also expected to have an impact during GCS not just because Ca-Mg-Al pyroxenes are abundant in target rock-formation, but also because in such formations pore water is typically saline, showing high Na concentrations and neutral-to-moderately alkaline pHs (Matter et al., 2016), and plagioclase dissolution may act as an additional Al source, which may favor secondary Na-aluminosilicate formation. As shown by Correns (1949), due to the difference in chemical potential between ions in solution and in a solid phase, a pressure can be exerted by a solid crystallizing in a supersaturated solution, and such a crystallization pressure can be transmitted to confining surfaces such as the walls of pores or cracks. The crystallization pressure is defined by,

$$\Delta p = \frac{nRT}{V_m} \ln \frac{IAP}{k_{sp}}, \qquad \text{(V.3)}$$

where n is the number of ions forming the solid phase, IAP is the ion activity product, k_{sp} is the solubility product (IAP/k_{sp} is the supersaturation, β) and V_m is the crystal molar volume. Eq. (V.3) shows that Δp depends on supersaturation, which acts as a driving force for crystallization pressure generation (Schiro et al., 2012).

Δp can also be calculated using poroelasticity theory (Coussy, 2006),

$$\Delta p = \frac{3\mathrm{K}\varepsilon_\mathrm{f}}{\mathrm{b}\emptyset_\mathrm{e}}, \qquad \text{(V.4)}$$

where K is the bulk modulus of the (porous) material, ε_f is the linear strain, b is the Biot coefficient, and ϕ_e is the local volume fraction of crystallizing phase in the pores within the crystallization front. The local crystallization pressure can be related to the effective stress σ^*, by (Espinosa-Marzal et al., 2011):

$$\sigma^* \approx b\phi_e\Delta p = 3K\varepsilon_f. \qquad \text{(V.5)}$$

Failure due to crystallization pressure generation within a porous elastic material using an energy criterion will take place when the strain energy imposed by the growing crystals is bigger than the strain energy obtained during a uniaxial tensile strength test (Espinosa-Marzal et al., 2011), i.e., when $\sigma^* > \sigma_T$. One way to determine σ^*, once K is known, involves the calculation of Δp by experimentally measuring ε_f during crystallization of a solid phase within the pores of a material. Another possible way to determine σ^* involves the calculation of Δp using Eq. (7).

In these experiments, however, the supersaturation at which Na-phillipsite crystallized is unknown, so it cannot be calculated σ^* using the latter approach. Thus, it can be calculated σ^* based on poromechanics. A K value of 95.84 GPa for augite was calculated from the reported values of elastic modulus, E (143.76 GPa) (Alesandrov, 1964) and Poisson ratio, υ (0.25) (Ji et al., 2009) of this mineral and the formula (Landau and Lifshift, 1970),

$$K = \frac{E}{3(1-2\nu)}\,. \qquad \text{(V.6)}$$

It is determined ε_f using μ-CT and SEM images of reacted augite crystals showing pervasive cracks filled with Na-phillipsite as follows: based on published values of crack widths for crystalline rocks and plagioclase crystals (Kelemen and Hirth, 2012), a width of 100 nm was considered for the cracks initially formed following Na-phillipsite crystallization within etch pits (wedge effect) (Plümper et al., 2012; Lafay et al., 2018), now filled with Na-phillipsite and cross-cutting the reacted augite crystals. Their number was measured along a direction nearly normal to the cracks plane, which typically followed the [110] and [010] directions (i.e., the direction of the main cleavage planes in pyroxenes; {110} and {010}) (Deer et al., 1990). The sum of the width of each individual crack along such direction is Δl (i.e., the total length increase along a specific direction of the crystal due to crystallization damage). The total length of the crystal in a direction normal to the cracks plane was also measured, and to this value it is subtracted the width of the cracks filled with Na-phillipsite (as it is assumed that the widening of the cracks was due to further Na-phillipsite -and calcite, see below- growth after crystallization pressure-induced crack development), obtaining the value l. Finally, ε_f was calculated using the equation,

$$\varepsilon_f = \frac{\Delta l}{l-\Delta l} \qquad \text{(V.7)}$$

A ε_f value of 0.00092-0.00098 was obtained for the $NaHCO_3$ run, whereas a ε_f value of 0.00071-0.00093 was obtained for the water run. Using Eq. (V.5), σ^* values of 273±13 MPa and 244±32 MPa were obtained for the former and latter runs. These calculated σ^* values should be taken with caution, because there is significant uncertainty in the calculated ε_f values due to uncertainties regarding the exact width and number of cracks (near-simultaneously) formed during Na-phillipsite crystallization. σ^* values should thus be considered as an indication of the order of magnitude of the stresses generated during Na-phillipsite crystallization within augite. In any case, these analysis yields σ^* values very similar to those calculated for reaction-driven fracturing associated with olivine serpentinization (~300 MPa) (Kelemen and Hirth, 2012). The σ^* obtained here are necessarily larger than the tensile strength of augite crystals, otherwise no reaction-driven fracturing would have been observed. Note that while the theoretical maximum tensile strength for a crystal is ~E/10 (i.e., ~15 GPa for augite), the actual value is typically much lower because of the presence of flaws (Idrissi et al., 2016), explaining why fracturing of augite is observed under the calculated σ^* values. To the best of my knowledge, the tensile strength of augite has not been reported. However, a spalling fracture stress of 58 MPa (equivalent to tensile strength failure under high strain rates, which are expected in this system during Na-phillipsite crystallization at a high supersaturation, see below) has been reported for an augite-rich (65 %) peridotite (He et al., 1996). This stress can be considered as a lower bound for the stresses actually resulting in fracturing of these augite crystals upon Na-phillipsite crystallization.

A similar approach could be used to calculate the effective pressure and super saturation at the onset of MSH crystallization within diopside crystals, leading to its fracturing. In this case, however, the level of reaction-driven fracturing was more limited (i.e., no large, cross-cutting fractures were observed), but in any case, crystallization pressures larger than the tensile strengtyh of diopside had to be generated as to result in the observed fractures filled by MSH. The fact that no pervasive fractures were observed in any other experiments despite the precipitation of calcite and amorphous silica, demonstrates that the supersaturation at the onset of crystallization of these phases within preexisting cracks and newly-formed dissolution (wedge-like) etch pits was not high enough to generate an effective pressure higher than the tensile strength of the pyroxene crystals. Using Eq. (7), and the effective stress obtained here using poromechanics ($\sigma^* \geq 248$ Mpa), a supersaturation $\beta \geq 14$ for Na-phillipsite ($NaAlSi_3O_8 \cdot 3H_2O$, $n = 4$, and $V_m = 149.69$ cm^{3}mol^{-1}; data from Blanc et al., 2015) crystallization is obtained (at 423 K, and assuming that because the solid is initially non porous, the Biot coefficient is 1, and the filling of the dissolution pits is complete, as shown by SEM and micro-CT observations, so that $\phi = 1$). Such a high, yet reasonable β value, corresponding to a SI_{phi} of 1.15, underlines that the supersaturation that can be reached at the mineral-solution interface during dissolution processes via an ICDP mechanism can be significantly high, even when the bulk system is undersaturated to a particular phase, as shown here by PHREEQc modeling. If it is considered a lower bound for the crystallization pressure equal to the dynamic tensile strength of augite-rich peridotite (58 MPa), then a β value of 1.85 is calculated from Eq. (V.3), which also demonstrates that for fracture generation a significant supersaturation has to be generated at the mineral-solution interface in dissolution pits. As indicated abovem a similar calculation could be done for the case of diopside fracturing by MSH crystallization. However, the current lack of relevant thermodynamic parameters (e.g., V_m) prevented us from performing such calculations.

Large amounts of calcite were identified within fractures generated in the $NaHCO_3$ system during augite carbonation. It could thus be argued that calcite crystallization also contributed to fracture generation, as reported for newly-formed carbonates during primary silicate mineral carbonation (Kelemen et al., 2011; Kelemen and Hirth, 2012; Kelemen, P. B., Savage, H., & Hirth, 2013; Gadikota et al., 2014). However, due to the non-direct contact between calcite and the fracture walls observed in the Micro-CT analyses (Figure V.9e), it can be concluded that calcite did not generate the cracks but likely contributed to their widening.

Dissolution processes without crack development can create porosity and increase the reactive surface area (Lafay et al., 2018), but they do so to a very limited extent. Typically, precipitation of newly-formed phases during replacement reactions such as silicate carbonation reduces porosity and, therefore, can passivate the reaction by the decrease of reactive surface area (e.g. Emmanuel and Ague, 2011; Rodriguez-Navarro et al., 2015; Rodriguez-Navarro et al., 2016; Di Lorenzo and Prieto, 2017; Di Lorenzo et al., 2018).

These results demonstrate that reaction-driven fracturing due to crystallization pressure generation (Scherer, 1999; Emmanuel and Ague, 2011; Schiro et al., 2012) is critical for the advance of silicate dissolution and carbonate precipitation, because it increases the permeability of the substrate and the available reactive surface area (Kelemen et al., 2011; Kelemen and Hirth, 2012; Kelemen, P. B., Savage, H., & Hirth, 2013). In addition to the above mentioned mechanism, another reaction-driven fracturing mechanisms has been proposed. Jamtveit et al. (2000) explored the idea that fracture generation was caused by tensile stress generation due to solid volume decrease during mineral dissolution. However, this kind of process is ruled out here based on the absence of fracture generation during augite and diopside reactions in runs were no Na-phillipsite or MSH precipitated, but still dissolution occurred and a certain degree of replacement was obtained.

Altogether, it is proposed that fracture generation in augite was initiated by Na-phillipsite precipitation at the mineral-fluid interface (etch pits), at very high supersaturation, and under very fast crystallization kinetics, factors critical for the development of enough crystallization pressure as to generate fracturing (Derluyn et al., 2014). During augite dissolution, pores were generated in the matrix of the crystal. Due to the presence of Na and Al in the augite structure, plus the Na in the solution, in combination with the relatively high Si release rate at the pyroxene-solution interface, supersaturation with respect to Na-phillipsite occurred and (heterogeneous) precipitation was allowed. This event caused the generation of micro-fractures by crystallization pressure generation and, as a result, fresh fluid entered this micro-fractures, resulting in additional pyroxene dissolution of freshly exposed reactive surfaces and feeding the system with Al, Si (and Na) ions for additional precipitation of Na-phillipsite, crystallization pressure generation, and further fracturing via a positive feedback mechanism (Kelemen, P. B., Matter, J., Streit, E. E., Rudge, J. F., Curry, W. B., & Blusztajn, 2011; Kelemen et al., 2011; Kelemen, P. B., Savage, H., & Hirth, 2013) or "flow-loop" mechanism (O'Connor et al., 2005). This increase in permeability and fresh exposed area also fostered dissolution of the pyroxene and the release of Ca (and Mg) ions, causing a sufficiently high supersaturation in the pores/fractures as to enable calcium carbonate precipitation in very large amounts. This overall sequence of events has been previously modeled for the case of olivine serpentinization/carbonation by Kelemen et al. 2013 (Kelemen, P. B., Savage, H., & Hirth, 2013), and it has been pointed out that the positive feedback loop associated with reaction-driven fracturing offers a mechanism to explain why in nature very high fractions of serpentinization/carbonation are observed (Jamtveit et al., 2008; Iyer et al., 2008; Kelemen and Matter, 2008; Kelemen et al., 2011; Kelemen and Hirth, 2012; Macdonald and Fyfe, 1985; O'Hanley, 1992). The same rationale can be put forward to explain reaction-driven fracturing due to MSH crystallization in diopside, although in this case the effect is much more limited, as compared with Na-phillipsite crystallization in augite.

4.3. Origin of the differences in carbonation behaviour of diopside and augite

Despite their very similar chemical composition and structure, augite and diopside display a very different dissolution and carbonation behavior. In particular, a systematic higher extent of augite dissolution and carbonation was observed (Table V.1). Previous studies showed that augite has a higher dissolution rate than diopside over a whole range of pHs (McAdam et al., 2008; Van Pham et al., 2012; Schott et al., 2012). Furthermore, previous works on dissolution of iron-bearing pyroxenes (Siever and Woodford, 1979; Hoch et al., 1996) showed that they present a higher dissolution rate than non-iron-bearing pyroxenes due to the formation of highly insoluble Fe-oxides and hydroxides that shift the equilibrium to the product side. In particular, Hoch et al. (1996) showed that the higher dissolution rate of augite as compared with diopside was related to the oxidation of iron present in higher amounts in the former than in the latter clinopyroxene. The augite crystals include 2.3 mol% Fe, while diopside includes 1.7 mol% Fe. The higher Fe content in augite likely contributed to its faster dissolution according to the effect indicated above. Furthermore, it is suggested that the presence of Na and Al in augite contributed both to a faster release of divalent metals and silicate species to the solution and to the formation of secondary Na-aluminosilicates, thereby increasing the overall dissolution rate of this pyroxene (Berger et al., 1994; Berg and Banwart, 2000; Carroll and Knauss, 2005; Golubev et al., 2005). Overall, these results suggest that the presence of Al and the faster and ultimately higher release of Si, Fe, alkali, and alkaline-earth metals to the solution in the case of augite fostered, on the one hand, the shift of the dissolution-carbonation reaction to the products side and, on the other hand, the precipitation of secondary phases in etch pits and surface pores/cracks at a sufficiently high supersaturation as to generate crystallization pressure enough to result in massive fracturing and a significant increase in reactive surface area. These two effects created a strong positive dissolution-precipitation feedback-loop in the case of augite, which was not so strong in the case of diopside, thereby explaining the observed

Chapter VI. CO_2 sequestration with simultaneous zeolite production and toxic elements trapping by carbonation of Coal Fly Ash

Table VI. 1. Experiment codes, solution composition, initial and final pH, zeolitic content, carbonate content, Mg content in calcite and Carbonation Efficiency (CE) for each experimental run.

Code	Solutions	Initial pH	Final pH	Zeolitic content (wt%)	Carbonate content (wt%)	Mg content (mol%)	CE (%)
A1	MilliQ H_2O	9.26	9.8	0	1	0	0
N1	3.4M Na_2CO_3	11.63	10.77	60	4.9	1.19	79.26
N2	3.4M $NaHCO_3$	8.26	9.79	0	3.2	7.74	34.29
K1	3.4M K_2CO_3	12.02	11.35	33	3	1.36	44.96
K2	3.4M $KHCO_3$	8.2	9.32	0	2.6	2.43	33.88

IV.1 Chemistry and mineralogy of unreacted CFA

XRF analysis (Table VI.2) shows that Si, Al and Fe account for more that 80 wt% (expressed as oxides) of the CFA. Compositionally, this CFA can be classified as Class F, the most common and abundant type of CFA worldwide(Duxson and Provis, 2008). The relatively low CaO plus MgO content (5.43 wt%), which approaches the average alkaline-earth metal oxide content of CFA(Pan et al., 2012), poses a limit to the maximum net CO_2 capture capacity of this CFA. Several PTE are present in significantly high concentrations (e.g., Ba=1345 ppm; V=849; Cr=189; As=150 ppm), also on the same range of concentrations reported for other CFAs(Vassilev et al., 2003; Moreno et al., 2005). These results underline the potential toxicity of CFA leachates.

Table VI.2 Chemical composition of fresh coal fly ash by XRF analysis of major, minor and trace elements.

Major and Minor Elements (wt%)													
LOI*	MgO	Al_2O_3	SiO_2	K_2O	CaO	TiO_2	Fe_2O_3	Na_2O	V_2O_5	TiO_2	P_2O_5	SO_3	BaO
4.55	1.739	25.89	47.78	4.721	3.721	1.01	7.54	0.762	0.152	1.012	0.79	0.877	0.15

Trace Elements (ppm)												
Cr	Mn	Ni	Cu	Zn	Ga	As	Rb	Sr	Y	Zr	Os	Pb
189	496	254	171	260	44	150	245	398	37	175	16	147

*LOI: loss on ignition

XRD analysis (Figure 1) shows that this CFA is composed of a glass fraction (95±2 wt%), graphite (2.0±0.1 wt%), quartz (1.2±0.1 wt%), mullite (1±0.1 wt%), calcite (1±0.1 wt%) and traces of hematite (<1 wt%).

The presence of calcite in the unreacted fly ash is likely due to partial hydration of free CaO to $Ca(OH)_2$ and its subsequent carbonation to $CaCO_3$ during sample handling. Due to the low calcite content in this CFA, very low intensity (not easily visible) carbonate bands were detected in FTIR spectra (Figure VI.4b). FTIR analysis also shows high intensity bands at 1009 cm^{-1} and 650-720 cm^{-1}, corresponding to the asymmetric and symmetric vibration of T-O (T = Si or Al), respectively, and at 400-500 cm^{-1}, corresponding to T-O bending as well as combination modes of the aluminosilicate glass.(Farmer, 1974; Mozgawa et al., 2004).

FESEM observations show that the CFA is made up of spheres and cenospheres (and a few plerospheres) with size ≤ 20 μm (Figure VI.2).

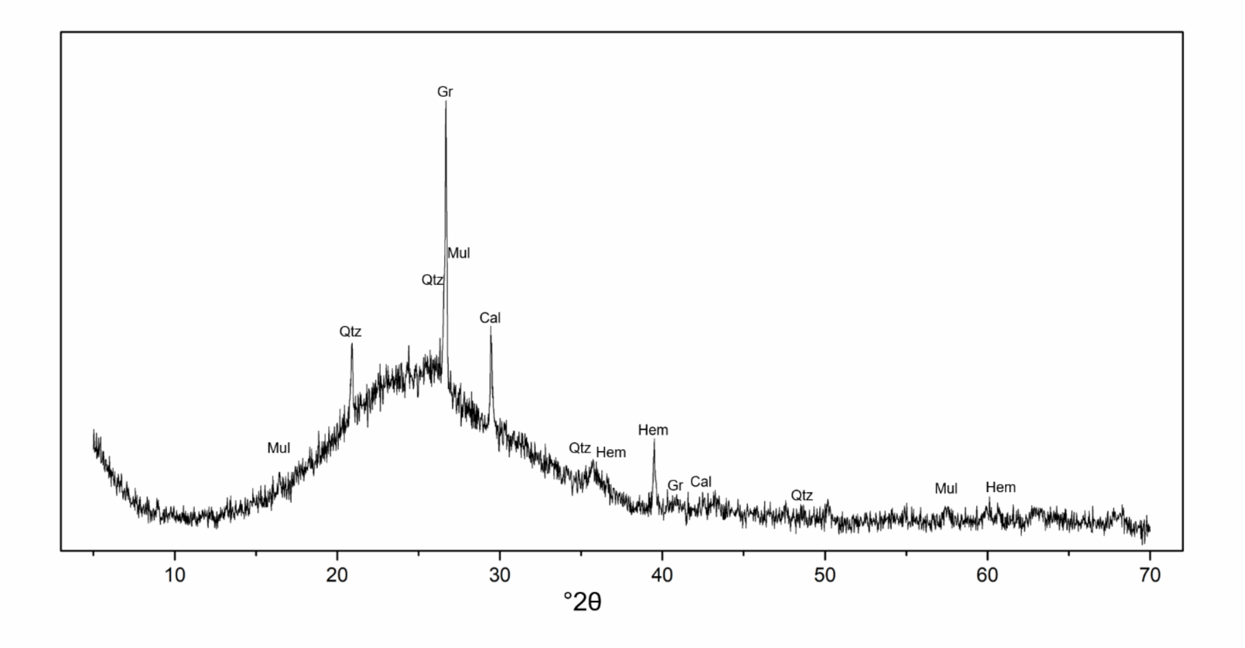

Figure VI.1. XRD pattern of unreacted CFA. (Qtz – Quartz; Mul – Mullite; Gr – Graphite; Cal – Calcite; Hem – Hematite).

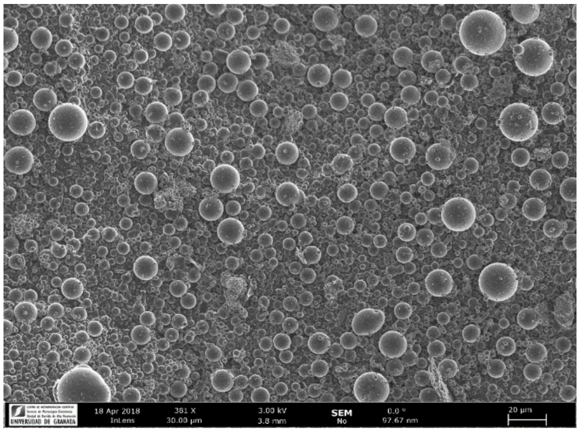

Figure VI.2. Representative FESEM image of the CFA from Compostilla coal-fired power plant made up of aluminosilicate spheres and cenospheres with size ≤ 20 μm.

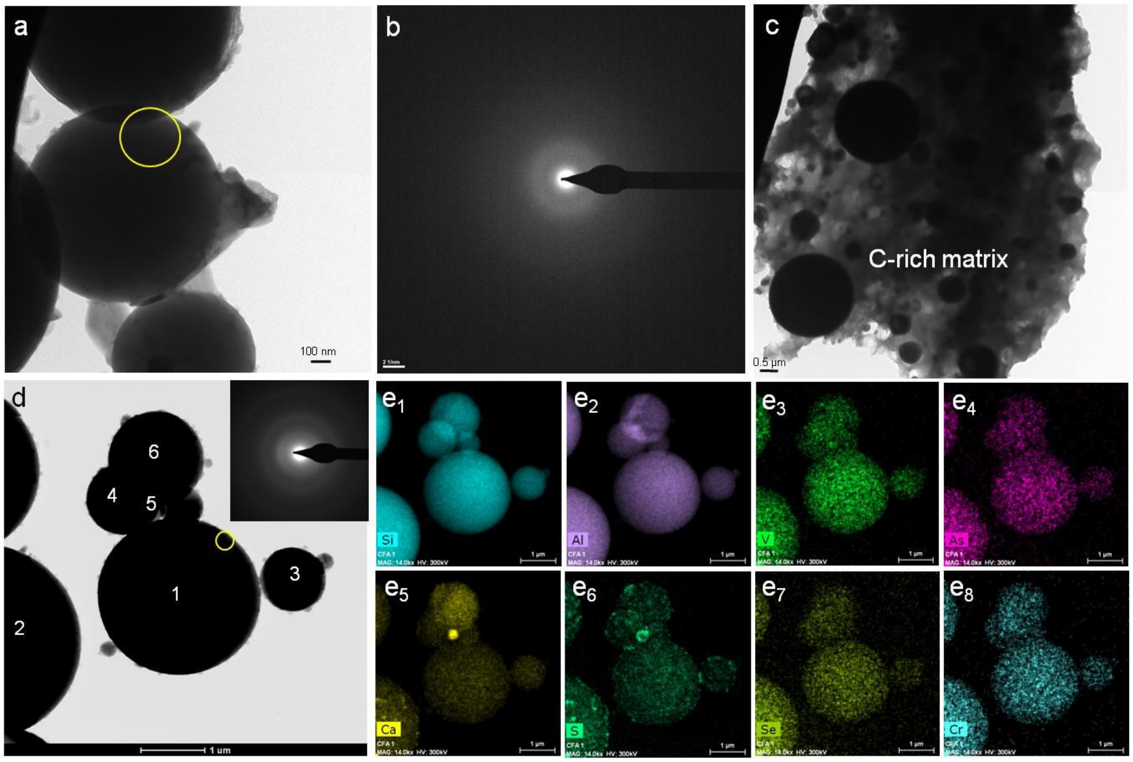

Figure VI.3. TEM-AEM analysis of unreacted CFA. (a) aggregate of aluminosilicate spheres; (b) their amorphous nature is demonstrated by the diffuse haloes in the SAED corresponding to the yellow circled area in (a); (c) Carbon matrix with embedded amorphous aluminosilicate spheres; (d) HAADF image of an aggregate of CFA spheres (SAED pattern, corresponding to the yellow circle area, in inset); (e_1-e_8) corresponding elemental maps of Si, Al, V, As, Ca, S, Se, and Cr. The numbers in the HAADF image in (d) correspond to the AEM point analyses reported in Table S3.

TEM-AEM analysis shows that this CFA is mainly composed of amorphous (see diffuse haloes in SAED patterns) micrometer-sized aluminosilicate glass spheres and scarce C-rich aggregates with embedded aluminosilicate spheres (Figure VI.3). AEM point analyses (Table S3) yield the following overall composition (wt%) for the spheres (N=6): 50.7±2.5 SiO_2, 32.7±1.8 Al_2O_3, 5.2±1.1 Fe_2O_3, 3.1±1.1 MgO, 2.6±2.5 CaO, 3.8±0.6 K_2O, 1.4±0.2 Na_2O, and 0.6±0.2 TiO_2, values very similar to those of the bulk CFA determined by XRF analysis (Table VI.3). This is not surprising considering that the glass phase accounts for nearly 95 wt% of CFA. AEM results also show that the amorphous spheres include ~70 % and ~100 % of the total CaO and MgO in the

CFA, respectively. This underlines that to achieve the highest possible CE, the glass phase has to be fully dissolved. EDS elemental maps show that the spheres include different PTE, and quantitative AEM point analyses (Table VI.4) yield the following average contents for selected PTE: V= 633 ppm, As= 416 ppm, Mn= 66 ppm; Cr= 16 ppm; Zn= 66 ppm, values consistent with XRF results.

Table VI.4. AEM elemental composition (at %) of CFA amorphous spheres analyzed with TEM-AEM. Analysis # refer to numbered spots in the HAADF image in Figure S1c. Note that O (and C) are excluded from the reported analysis composition (this is why the sum of at % is not 100%).

Analysis	Na	Mg	Al	Si	K	Ca	Fe	Cu*	Mo
1	0.71	1.59	12.27	16.90	2.43	0.18	3.41	0.39	0.09
2	0.76	1.15	13.53	16.58	2.65	0.43	3.10	0.43	0.21
3	0.65	2.32	11.23	17.11	2.00	0.49	2.42	0.32	0.13
4	0.55	0.68	13.64	16.78	2.29	0.38	2.54	0.32	0.02
5	0.84	1.28	12.05	15.26	1.70	5.10	2.49	0.48	0.00
6	0.85	1.10	11.79	19.35	2.38	1.25	1.72	0.39	0.10
Analysis	**Zr***	**Ti**	**V**	**As**	**Mn**	**Cr**		**S**	**Zn**
1	0.29	0.42	0.00	0.00	0.00	0.00		0.00	0.00
2	0.29	0.17	0.00	0.00	0.04	0.01		0.00	0.00
3	0.14	0.34	0.00	0.00	0.00	0.00		0.00	0.00
4	0.22	0.10	0.00	0.07	0.00	0.00		0.00	0.00
5	0.33	0.30	0.32	0.14	0.00	0.00		1.15	0.00
6	0.29	0.19	0.06	0.04	0.00	0.00		0.00	0.04

* Values for Cu and Zr appear to be systematically too high (>> 1000 ppm), possible due to inaccuracies during processing of EDS spectra (i.e., background subtraction).

The chemical and mineralogical composition determined for CFA is in very good agreement with that reported by Moreno et al.(Moreno et al., 2005) for CFA from the same source and, despite the reported variability,(Pan et al., 2012) is very similar to that of other Class F CFAs.(Thomas and Matthews, 1992; Lin and Hsi, 1995; Querol et al., 1997b; Querol et al., 1997a; Steenbruggen and Hollman, 1998; Inglezakis and Grigoropoulou, 2001; Murayama et al., 2002; Querol et al., 2002; Montes-Hernandez et al., 2009) Thus, these CFA are representative for Class F CFAs from several coal-fired power plants.

VI.2 Carbonation/zeolitization reaction.

XRD patterns of reacted CFA are shown in Figure VI.4a. Rietveld quantification shows that in Na_2CO_3 (N1) runs, a zeolite yield of ~60 wt% is obtained, which is substantial for hydrothermal CFA-derived zeolite synthesis (typical yields are in the range 20-65%).(Fernández-Pereira et al., 2002) Analcime (8 ± 2 wt%), Na-chabazite (17 ± 6 wt%), NaP1 zeolite (31 ± 9 wt%), and hydroxysodalite (4 ± 1 wt%) are identified, along with calcite (5 ± 1 wt%), hematite (<1 wt%), quartz (<1 wt%), mullite (<1 wt%) and glass (33 ± 9 wt%). In K_2CO_3 (K1) runs, the dissolution of the glass fraction and the subsequent precipitation of zeolites is more limited. The quantitative XRD results show the presence of K-zeolite (33 ± 9 wt%), calcite (3.4 ± 0.8 wt%), hematite (<1 wt%), quartz (<1 wt%), mullite (<1 wt%) and glass (61 ± 14 wt%). XRD analyses show no zeolites, nor any changes in terms of phase composition in N2, K2 and control (A1) runs, as compared with unreacted CFA.

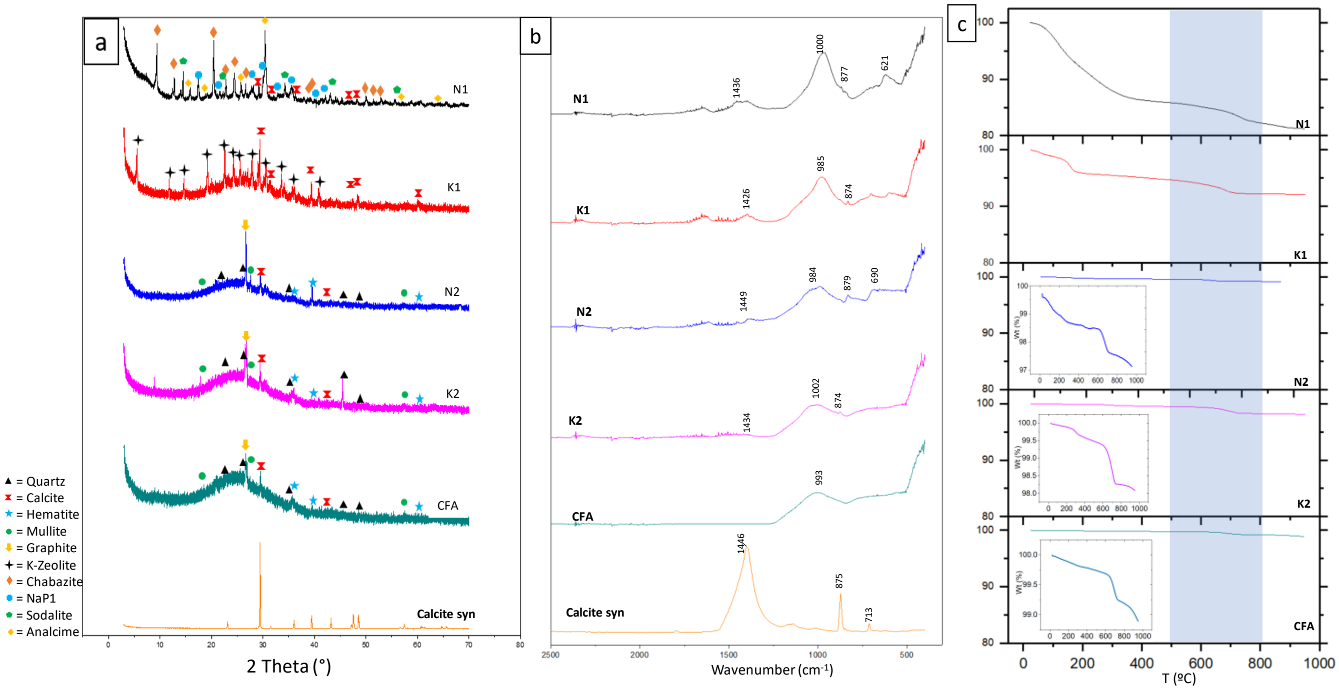

Figure VI.4. Unreacted CFA and products of its reaction in different carbonate solutions at 150ºC; Na_2CO_3 (N1), K_2CO_3 (K1), $NaHCO_3$ (N2), $KHCO_3$ (K2). (a) XRD patterns showing the Bragg peaks of the different crystalline phases; legend in inset; (b) FTIR spectra; and (c) TGA traces (insets show TGA traces with enlarged Y-axis). The shaded blue area represents the starting and the final T of carbonate decomposition (550-800 ºC).

FTIR spectra of samples K2, N2, K1 and N1 show well-defined bands at ~710 cm^{-1}, ~875 cm^{-1} and/or ~1440 cm^{-1} that confirm the new-formation of calcite (Fig. VI.4b). They also show the broad band at ~1000 cm^{-1} (T-O asymmetric stretching) of aluminosilicate phases. Bands at ~650-870 cm^{-1} corresponding to the T-O symmetric stretching, at ~442-503 cm^{-1} corresponding to the T-O bending, and at 550-575 cm^{-1} corresponding the double rings of analcime,(Sánchez-Hernández et al., 2016) sodalite, NaP1 zeolite and Na-chabazite,(Sánchez-Hernández et al., 2016) as well as K-zeolite,(Kosanovic et al., 1997) are observed in runs N1 and K1 respectively. Solids collected after runs N2 and K2 (bicarbonate runs) show similar T-O band as those described above. They also show the broad band at ~1000 cm-1 (T-O asymmetric stretching), and less intense (and poorly resolved) bands at ~650-870 cm-1 (T-O symmetric stretching) and the very intense, broad band at ~400-500 cm-1 corresponding to the T-O bending of aluminosilicate phases, consistent with the presence of unreacted CFA and newly-formed zeolites (in the case of runs N1 and K1) (confirmed by TEM-SAED analysis, see below).(Fahlke et al., 1987; Shigemoto et al., 1995; Morsli et al., 2007) No changes are detected in the FTIR spectra of the control run (A1) as compared with that of unreacted CFA. In combination with XRD, the FTIR results further demonstrate that a hydrothermal treatment with pure water leads to no mineral or structural changes to CFA.

TG-DSC analyses (Fig. VI.4c) show that the starting material and all products display a weight loss in the temperature range 550-800ºC, related to the thermal decomposition of calcium carbonate according to the reaction $CaCO_3 = CaO + CO_2$.(rodriguez-Navarro et al., 2009) However, it is observed that the starting *T* for the thermal decomposition of carbonates differ among runs, suggesting that either there are changes in calcite particle size (smaller size-fractions decomposing at lower *T* than larger size-fractions) and/or that Mg partially replaces Ca in the calcite phase, forming a (low) Mg-calcite, therefore lowering the starting decomposition temperature.(Demir et al., 2003; de Souza and Bragança, 2013) Note that XRD analyses show no (crystalline) magnesium carbonates. It is performed unit-cell refinement using Rielveld analysis to determine the Mg content in calcite using the method proposed by Goldsmith and Graff (1958)(Goldsmith et al., 1958) (results in Table VI.1). Calcite in unreacted CFA has no Mg. The highest Mg content in newly-formed calcite is observed in N2 runs, followed by K2, K1 and N1 runs. These results are in full agreement with TGA results and with the first derivate of the DSC analyses (Figure VI.5), showing a lower starting decomposition *T* for the Mg-calcites with the highest Mg content. It is suggested that at a moderately alkaline pH (bicarbonate runs), the higher

$[Ca^{2+}]/[CO_3^{2-}]$ ratio (closer to unity) as compared to higher pH runs (with higher $[CO_3^{2-}]$) could enable faster calcite growth favoring Mg incorporation.(Mavromatis et al., 2013)

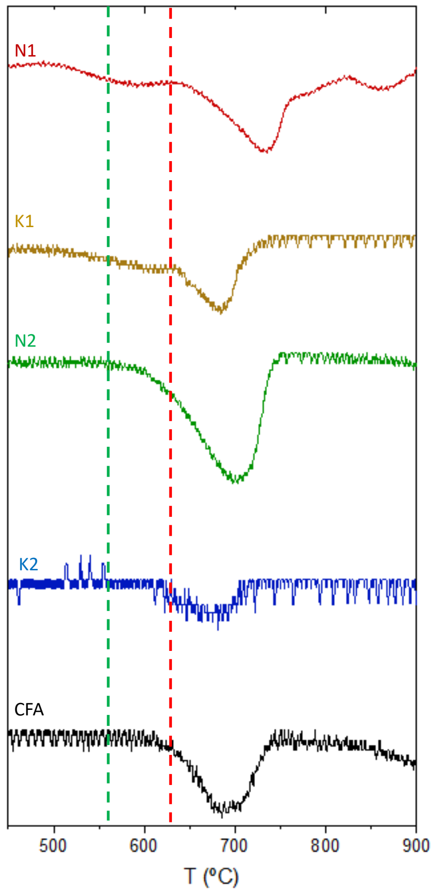

Figure VI.5. 1st derivate calculated from the TGA analyses showing the lowest initial temperature of the decomposition of carbonate phases (578 ºC) corresponding to N2 run (green dotted line) and the highest initial temperature (622 ºC) corresponding to unreacted CFA (red dotted line).

From the weight loss in the *T* range 550-850 °C, CE values of 34%, 34%, 45% and 79% are obtained for K2, N2, K1 and N1 runs, respectively. TGA analyses show an additional weight loss at 105-200ºC in N1, K1, N2 and K2 runs. In the case of N1 and K1 runs, this is likely due to loss of zeolitic water. Conversely, in runs N2 and K2, which lack crystalline zeolites, the weight loss is likely due to the decomposition of residual $NaHCO_3$ and $KHCO_3$ according to the reaction $2MHCO_3 = M_2CO_3 + CO_2 + H_2O$, where M is a monovalent cation (K or Na). However, it cannot be ruled out the possibility that this weight loss is due to dehydration of an amorphous zeolitic precursor. In any case, it should be noted that Na_2CO_3 and K_2CO_3 (if present as a residual) would undergo melting at 850ºC and 900ºC, respectively, therefore not interfering with the calcium carbonate decomposition, nor releasing any CO_2 at lower *T*.(L. Monasterio-Guillot et al., 2019) In all runs, including the control and unreacted CFA, the limited initial weight loss at $T < 550$ °C is likely due to dehydration of amorphous silica.(Luis Monasterio-Guillot et al., 2019) Note that such a weight loss overlaps with the weight loss associated with zeolitic water in runs where zeolites (and zeolitic precursors) are formed.

FESEM images show the presence of calcite (as indicated by XRD analysis) in all carbonation runs (Figure VI.6). Calcite appears as micrometer sized rhombohedral crystals attached to CFA spheres (Figure VI.6b and c). Reacted CFA spheres have irregular surfaces coated by newly formed precipitates (Figure VI.6b and c). It was, however, not possible to clearly differentiate by EDS microanalysis the composition of these precipitates from that of the unreacted spheres. According to Murayama et al.(Murayama et al., 2002) these coatings are most likely composed by new Si-Al phases formed after partial dissolution of the spheres and re-precipitation at the sphere-solution interface. Such newly-formed precipitates could act as a passivation layer on CFA particles, acting in a similar way as the amorphous silica-rich surface layers formed during weathering of primary silicate minerals.(Casey et al., 1989; Hellmann et al., 2003; Ruiz-Agudo et al., 2012; Encarnación Ruiz-Agudo et al., 2016) SEM-EDS analysis corroborates XRD analyses showing the presence of NaP1 (Figure VI.6d), Na-chabazite (hershelite) (Figure VI.6e), hydroxysodalite/cancrinite, and analcime (Fig. VI.6f) in N1 run, and K zeolite in K1 run (Figure VI.6g) (Querol et al., 1997b; Sánchez-Hernández et al., 2016)

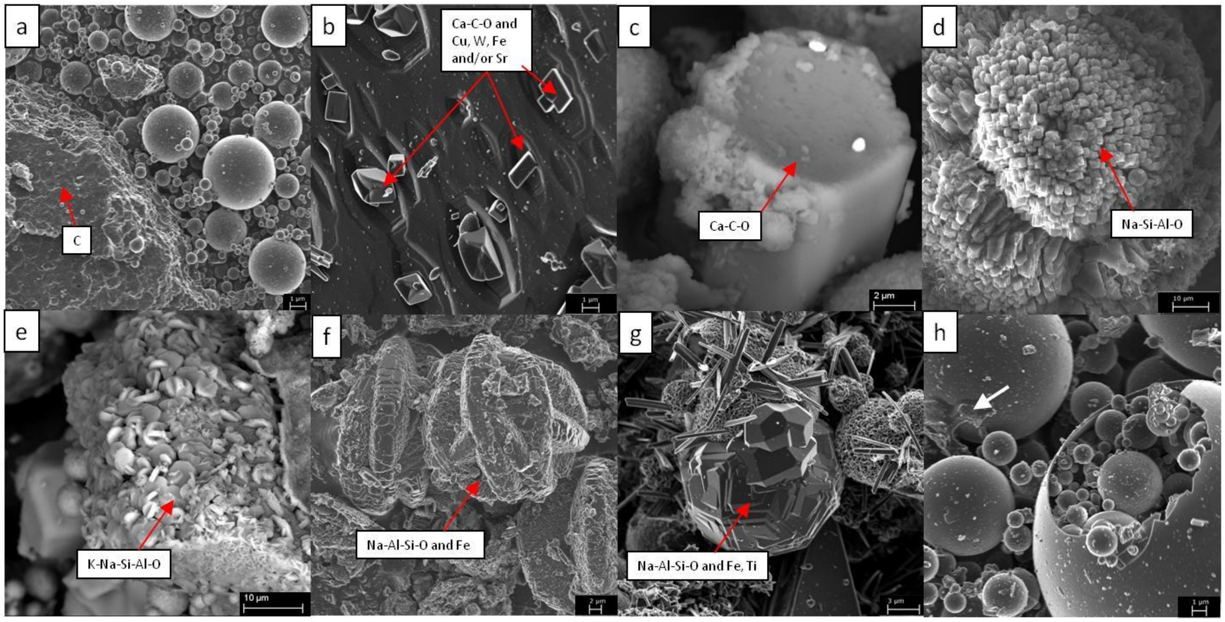

Figure VI.6. FESEM images of: (a) unreacted spheres of CFA and a graphite (C) particle; (b) calcite in N1; (c) calcite in K1; (d) NaP1 zeolite in N1; (e) K-zeolite in K1; (f) Na-chabazite (hershelite) in N1; (g) analcime in N1; and (h) large plerosphere (lower left) and solid spheres in run N2. The white arrow points to a shapeless deposit with features resembling an amorphous zeolitic precursor. The EDS elemental composition of the red-arrowed particles are shown in the insets.

SEM-EDS analysis also show that Sr, W and Ce are incorporated into the newly formed carbonates (Figure VI.7a and b), V is trapped in zeolite phases, and Cu is incorporated in both newly-formed phases (Figure VI.7c and d). Conversely, SEM-EDS analysis of carbonates formed in N2 and K2 experiments shows no trapping of PTE, although it is observed the presence of scattered shapeless coatings on some CFA spheres (Figure VI.6h), likely corresponding to an amorphous zeolitic precursor,(Shigemoto et al., 1995) as confirmed by TEM-SAED and AEM analyses (see below).

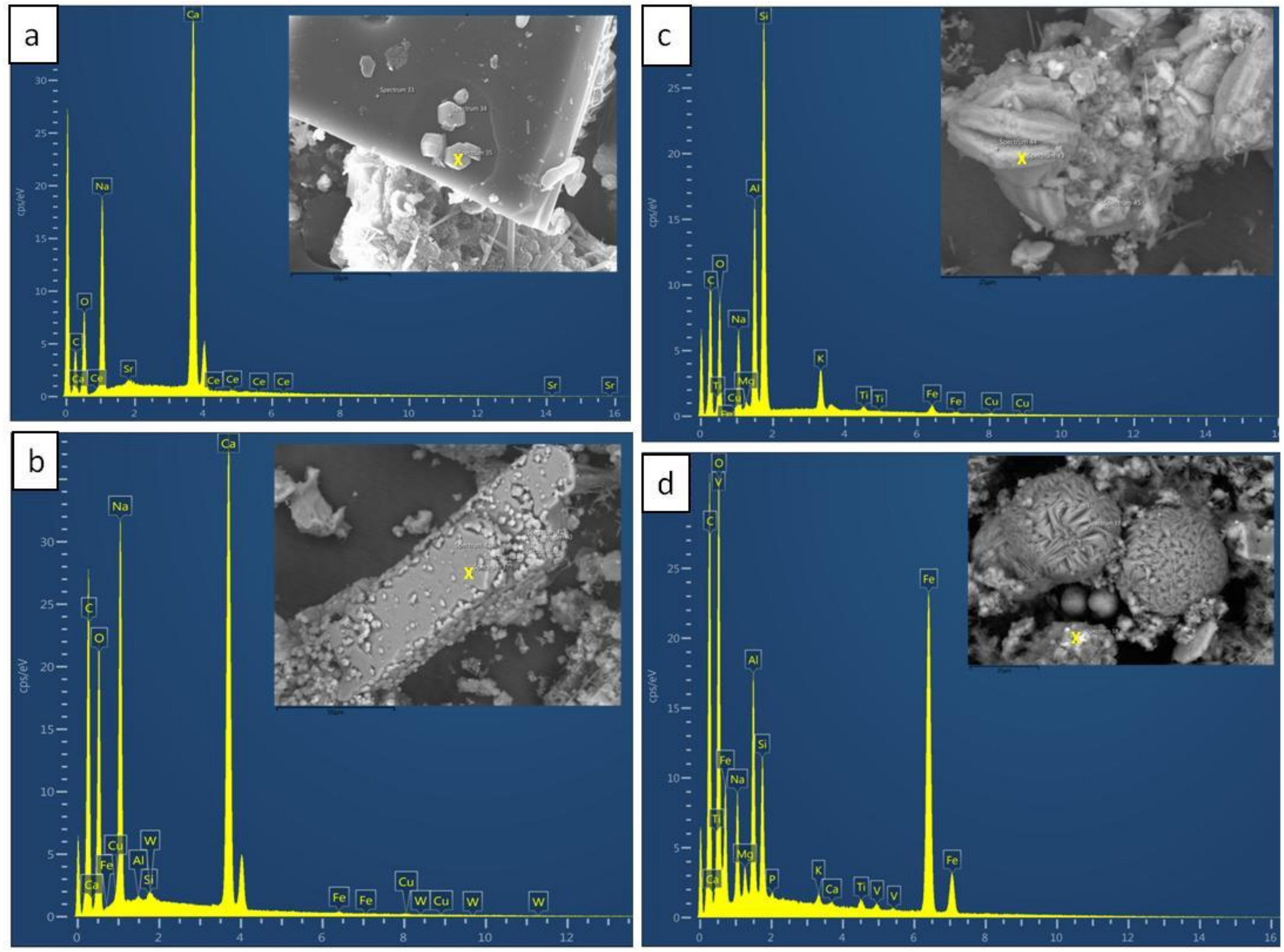

Figure VI.7. FESEM images and corresponding EDS spectra of calcite and zeolites in run N2 showing: trapping of Ce and Sr (a) and Cu and W (b) in calcite, and trapping of Cu (c) and V (d) in zeolites. The yellow × on SEM images mark the analyzed spots. Note that the high Na content in calcites (a and b) is due to contamination by residual Na_2CO_3, whereas the high Fe content in solids present in (d) is due to scattered nanospheres of Fe deposited on the zeolite.

Due to the background signal from the underlying spheres it could not be clearly determine using EDS microanalysis whether or not PTE are trapped in these latter precipitates. It is argued that the extensive dissolution of the glass particles in N1 and K1 runs favored the release and subsequent trapping of PTE into the newly formed carbonate and zeolite phases. No trapping of

PTE into the limited amount of newly formed crystalline phases (i.e., carbonates) in runs N2 and K2 is detected by SEM-EDS, likely due to the limited dissolution and PTE release from the glass phase Yet it is likely that the newly-formed amorphous zeolitic precursors formed in the bicarbonate runs also trapped PTE (see TEM-AEM results below).

TEM-AEM analysis of reacted CFA shows significant mineralogical and compositional changes in the case of run N1, i.e., the run with the highest carbonation and zeolitization level (Figure VI.8). Aggregates of newly formed poorly crystalline zeolitic nanophase with diffuse Debye rings in the SAED pattern and with d_{hkl} values consistent with a Na-chabazite (precursor) phase are observed (Figure VI.8a). In addition, well crystallized Na-chabazite crystals are identified by their SAED pattern (Figure VI.8b). HAADF images and corresponding EDS maps confirm the formation Na-zeolites, which include different PTE (Figure VI.8c and d). Quantitative AEM point analyses (Figure VI.8e and Table VI.5) demonstrate the presence of Na-chabazite with formula $Na_{3.4}K_{0.24}Mg_{0.28}Fe_{0.18}Al_6Si_{5.6}O_{24}\cdot 12H_2O$ (analysis 3 in Table S4), NaP1 with formula $Na_{6.32}K_{0.59}Mg_{2.69}Fe_{1.09}Al_{5.19}Si_{10}O_{32}\cdot 12H_2O$ (analysis 10 in Table S), and hydroxysodalite with formula $Na_{5.53}K_{0.14}Mg_{0.09}Fe_{0.24}Al_{4.71}Si_6O_{24}(OH)_2\cdot 2H_2O$ (analysis 6 in Table S4) plus a Na-poor aluminosilicate phase with a Si/Al ratio of 0.7 (analysis 12 in Table S4), consistent with the presence of an amorphous (gel) zeolitic precursor.(Catalfamo et al., 1993; Itani et al., 2009)The zeolitic phases include significant amounts of PTE: up to 500 ppm Zn, 300 ppm V, and 800 ppm Cu in NaP1; up to 1000 ppm Cu, and 200 ppm As in hydroxysodalite, and up to 600 ppm Cu, 500 ppm Mn, 500 ppm Zn, 3600 ppm Cr and 2400 ppm V in the amorphous zeolitic precursor (Table VI.5). Very similar results are observed in zeolitic products of run K1 (Figure VI.9, Table VI.7), where K zeolite with a representative formula $K_{2.34}Na_{0.62}Mg_{0.68}Ca_{0.11}Fe_{0.22}Al_{3.33}Si_9O_{24}\cdot 7H_2O$ (analysis #5, Table S5) is identified. The newly formed K zeolite includes significant amounts of

PTE: e.g., up to 424 ppm V, up to 631 Cr and up to 406 Mn. In the case of the bicarbonate runs, TEM-SAED reveals the presence of aggregates made up of amorphous nanoparticles ~20-50 nm in size attached to the CFA spheres (Figure VI.10).

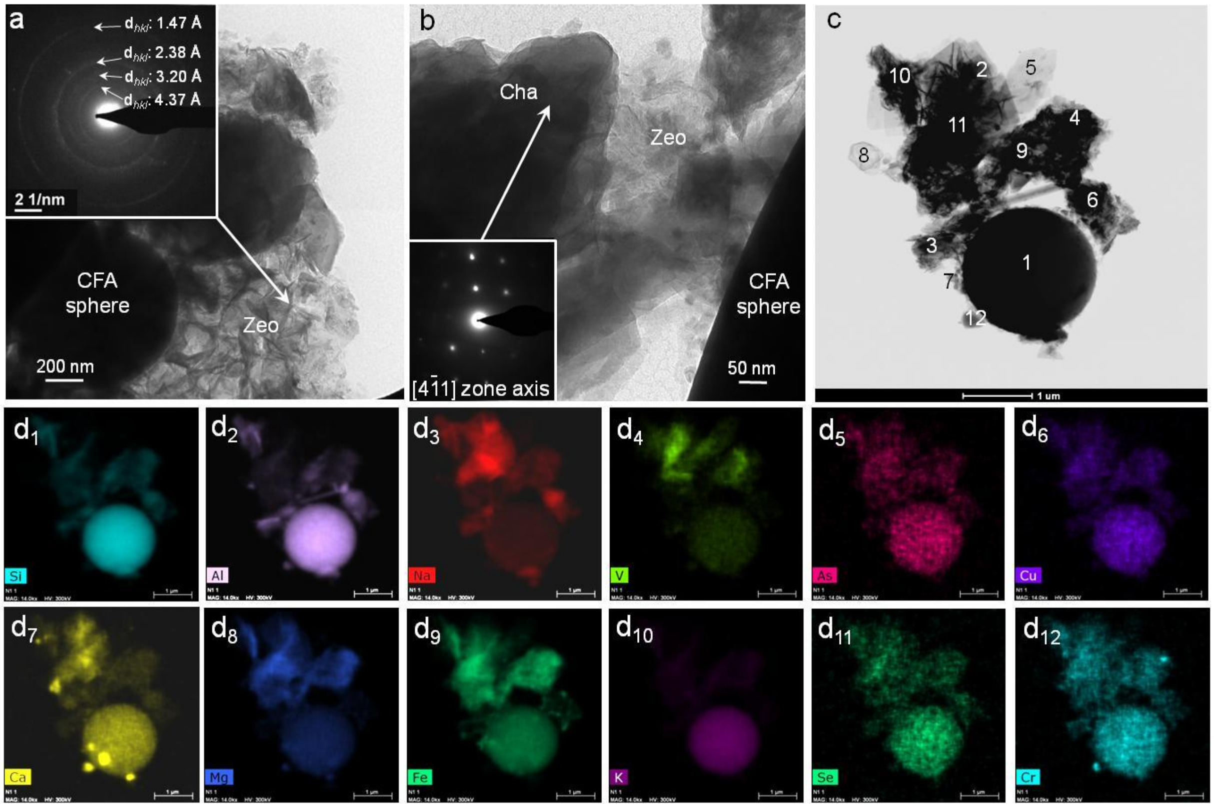

Figure VI.8. TEM-AEM analysis of reaction products of run N2. (a) Relict CFA sphere and newly formed zeolites (Zeo). The inset shows the SAED of the aggregate at the lower right. The diffuse Debye ring at the indicated d-spacing show the presence of a poorly crystlline precursor phase to Na-chabacite; (b) Large well-crystallized Na-chabazite (its [4-11] zone axis SAED pattern is shown in inset); (c) HAADF image of a sphere surrounded by newly-formed product phase. The numbers indicate AEM point analyses with composition reported in Table S4. (d1-d12) EDS elemental maps of the particles shown in (c).

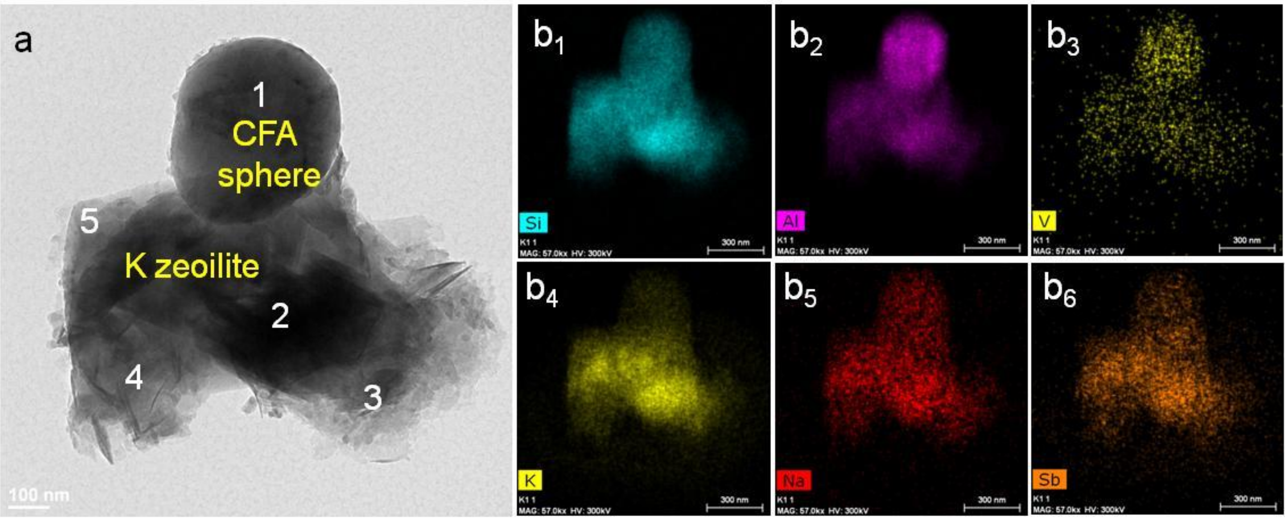

Figure VI.9. TEM-AEM analysis of reaction products of run K1. (a) Relict CFA sphere and newly formed K zeolite. The numbers indicate AEM point analyses with composition reported in Table S5; (b_1-b_6) EDS elemental maps of the particles shown in (a).

Table VI.5. AEM elemental composition (at %) of particles in CFA reacted in Na_2CO_3 solution (run N1). Analysis # refer to numbered spots in the HAADF image in Figure VI.8c. Note that O (and C) are excluded from the reported analysis composition (this is why the sum of at% is not 100%).

Element	Analysis #											
	1	2	3	4	5	6	7	8	9	10	11	12
Sodium	0.88	45.80	7.78	4.88	7.10	11.23	1.92	1.04	7.38	8.04	29.49	1.11
Magnesium	1.03	9.90	0.46	6.31	0.39	0.21	0.27		3.98	3.63	8.01	4.90
Aluminium	10.85	0.72	14.04	3.50	1.02	11.24	8.42		7.76	7.75	1.77	17.05
Silicon	20.27	3.97	13.65	13.50	2.26	14.89	1.82	1.66	16.70	15.54	6.99	11.48
Potassium	2.72	0.30	0.84	1.63		0.49			1.67	1.29	0.96	0.21
Calcium	0.20	1.11							0.05		1.20	4.56
Titanium	0.10	0.50	0.25	1.31	12.08	0.16			1.48	0.74	2.66	0.28
Iron	1.92	3.66	0.88	7.72	5.71	1.22	18.43		5.88	3.36	6.23	0.71
Copper	0.03					0.10			0.08	0.07	0.08	0.06
Molybdenum	0.03										0.01	
Manganese		0.50*									0.13	0.05
Zinc		0.21*							0.05		0.13*	0.05
Phosphorus		9.64										0.24
Arsenic						0.02						
Chromium							0.12					0.36*
Vanadium									0.03			0.24

* These values for Cu, Cr and Zr appear to be too high (>> 1000 ppm), possible due to inaccuracies during processing of EDS spectra (i.e., background subtraction). Blank cells indicate that this element was not quantified due the low concentration resulting in a very low signal/noise ratio in EDS spectra. Analysis 1 corresponds to an aluminosilicate sphere, with composition very similar to that of unreacted amorphous spheres reported in Table S3, but with a higher Na concentration likely due to incipient reaction with the Na_2CO_3 solution (formation of an amorphous zeolitic precursor). Analysis 2 corresponds to a (possible) Mg-Na phosphate phase, but the high Na content suggests contamination with Na salt. Analysis 3 corresponds to a Na-chabazite zeolite. Analysis 4 corresponds to NaP1 zeolite. Analysis 5 corresponds to Ti-Fe oxide (with Na contamination). Analysis 6 corresponds to hydroxysodalite. Analysis 7 corresponds to an Al-rich iron phase. Analysis 8 corresponds to a carbon particle. Analysis 9 and 10 corresponds to NaP1 zeolite. Analyses 11 and 12 are particularly complex, and seem to correspond to zeolites (or zeolite precursors) with an anomalously high Na concentration (salt contamination) in analysis 11 and with anomalously low Na and high Al concentration in analysis 12, likely corresponding to an amorphous (gel) pre-zeolitic phase.

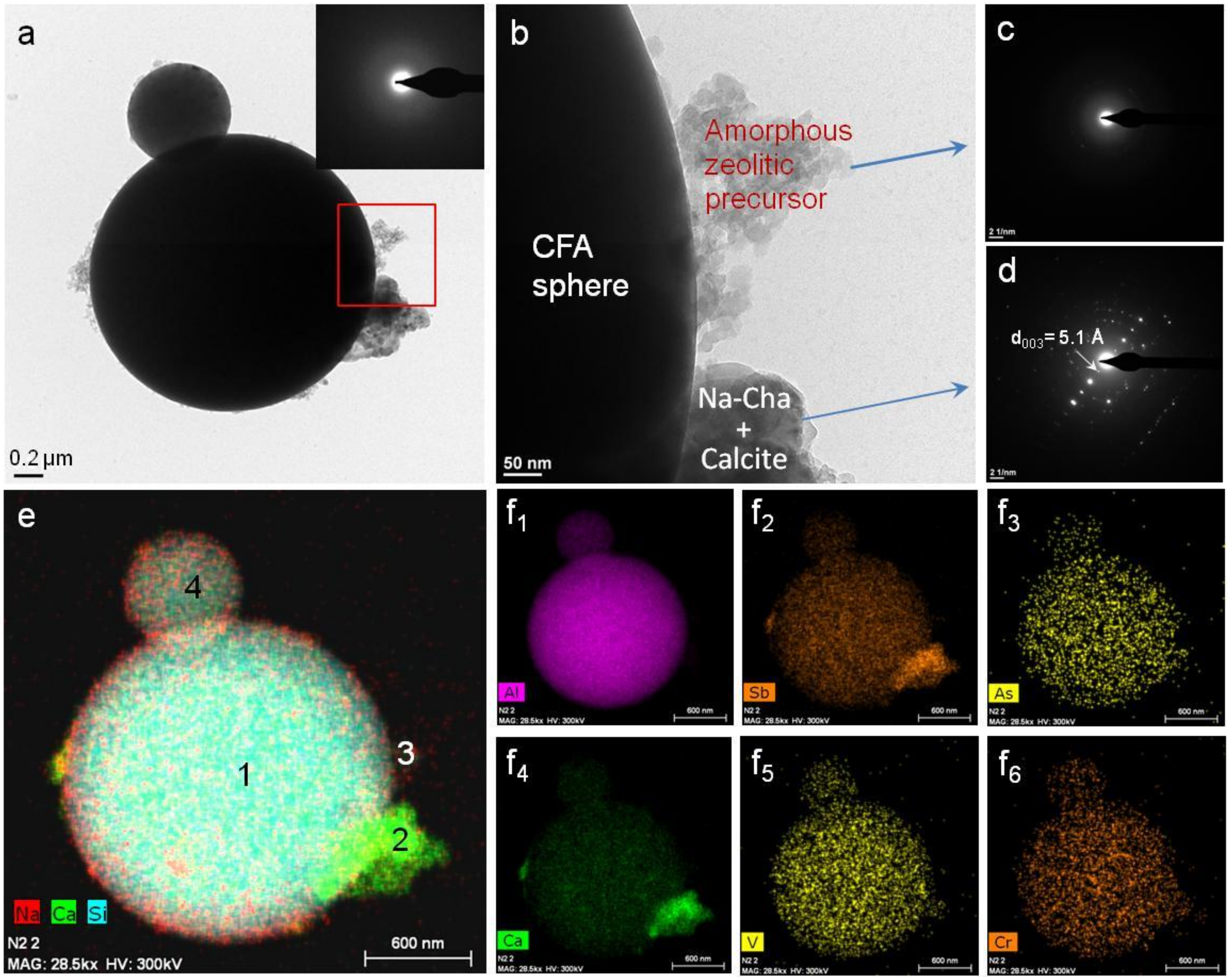

Figure VI.10. TEM-AEM analysis of reaction products of run N2. (a) CFA sphere (SAED in inset) and newly formed nanophases attached on its periphery; (b) Enlarged view of the red squared area in (a) showing a detail of the nanosized amorphous zeolitic precursor, as well an aggregate of newly formed calcite and Na-chabazite; (c) SAED patter of the amorphous zeolitic precursor in (b); (c) SAED pattern of the crystalline aggregate in (b) showing diffraction spot corresponding to the 003 Bragg reflections of Na-chabazite. Other spots correspond to non-oriented calcite crystals; (e) HAADF image of the particles in (a) showing with overlaped EDS maps for Na, Ca and Si; (f1-f2)

AEM analysis shows that in N2 runs they have a formula $Na_{3.56}K_{0.47}Ca_{0.74}Al_{5.97}Si_{10}O_{32}\cdot 12H_2O$ (analysis #3, Table VI.7), consistent with the formation of a (NaP1) zeolitic precursor. Similar nanosized amorphous zeolitic precursors have been observed previously.(Itani et al., 2009; Yan et al., 2015) Interestingly, EDS mapping and AEM point analyses of CFA spheres in this same run show Na-enrichment (up to 2 wt% Na_2O; analysis #2 in Table S6), which points to formation of zeolitic precursors blanketing the sphere. A relative high concentration of PTE such as Cu, V, and Mn is present in the reacted CFA spheres (Table VI.7). Altogether, these TEM-AEM results demonstrate that PTE originally present in CFA are preferentially incorporated into the newly-formed amorphous zeolitic precursor and zeolite phases.

Table VI.6. Elemental composition (at %) of particles in CFA reacted in K_2CO_3 solution (run K1). Analysis # refer to numbered spots in the TEM image in Figure VI.7a. Note that O (and C) are excluded from the reported analysis composition (this is why the sum of at% is not 100%).

	Analysis #				
Element	1	2	3	4	5
Silicon	20.69	22.17	18.92	20.19	21.83
Aluminium	21.85	8.99	7.43	7.32	7.77
Magnesium	1.53	0.43	3.95	3.42	1.32
Calcium	0.89	0.06	0.45	0.61	0.40
Iron	4.02	0.66	3.50	2.78	1.10
Potassium	3.90	8.43	8.08	6.88	7.89
Sodium	0.34				1.24
Titanium	0.37	0.14	0.33	0.43	0.13
Vanadium	0.20*	0.024	0.042	0.034	0.017
Chromium	0.38*		0.063	0.011	0.006
Manganese	0.07	0.027	0.04		0.034
Copper	0.15*	0.031	0.25*	0.11*	0.039

* These V, Cr and Cu concentration in these analyses appears to be excessively high, possible due to inaccuracies during processing of EDS spectra (i.e., background subtraction)

Table VI.7. Elemental composition (at %) of particles in CFA reacted in $NaHCO_3$ solution (run N2). Analysis # refer to numbered spots in the TEM image in Figure VI.9e. Note that O (and C) are excluded from the reported analysis composition (this is why the sum of at % is not 100%).

	Analysis #			
Element	1	2	3	4
Silicon	17.52	13.63	19.97	18.60
Aluminium	13.83	3.89	11.47	12.93
Magnesium	2.17	8.64		1.25
Calcium	0.15	11.31	2.13	0.40
Sodium	0.84	2.35	5.82	1.15
Potassium	2.18	0.22	1.31	2.26
Iron	2.46	2.79		2.37
Titanium	0.057	0.485		0.098
Copper	0.092	0.105		0.129
Vanadium	0.040*	0.168*		0.108*
Chromium	0.035	0.167		0.051
Manganese	0.050	0.023		
Phosphorus		0.337		

* These V, Cr and Cu concentration in these analyses appears to be excessively high, possible due to inaccuracies during processing of EDS spectra (i.e., background subtraction)

Finally, Brunauer-Emmett-Telller (BET) analysis(Thommes et al., 2015) shows that the unreacted CFA and the control A1 have a surface area of 1.1±0.1 m^2g^{-1}, whereas N1, K1, N2 and K2 have a surface area of 20.4±0.7 m^2g^{-1}, 4.3±0.1 m^2g^{-1}, 2.1±0.1 m^2g^{-1}, and 1.2±0.1 m^2g^{-1}, respectively. These results show that the formation of zeolites in N1 and K1 runs significantly increases the surface area, as expected for the presence of such microporous solids. They also show that the best absorbent product is achieved using Na_2CO_3 as alkaline activator. Interestingly, in the case of run N2, the surface area increases ~100% as compared with unreacted CFA. This is consistent with the formation of the amorphous zeolitic precursor detected with TEM, which reportedly are nanosized and have a relatively high surface area.(Morsli et al., 2007) Following zeolite formation in run K1 and, specially, in run N1, the isotherm of CFA changes from type II (typical of non-porous solids) to a combination of type II and type IV with H4 hysteresis loop typical of micro/mesoporous solids (Figure VI.11).(Thommes et al., 2015) The hysteresis loop is not that well defined in run N2, is nearly absent in run K1, and is completely absent in the unreacted CFA and control run A1. The latter further confirms that a zeolitic precursor is formed in the former runs, particularly in run N2.

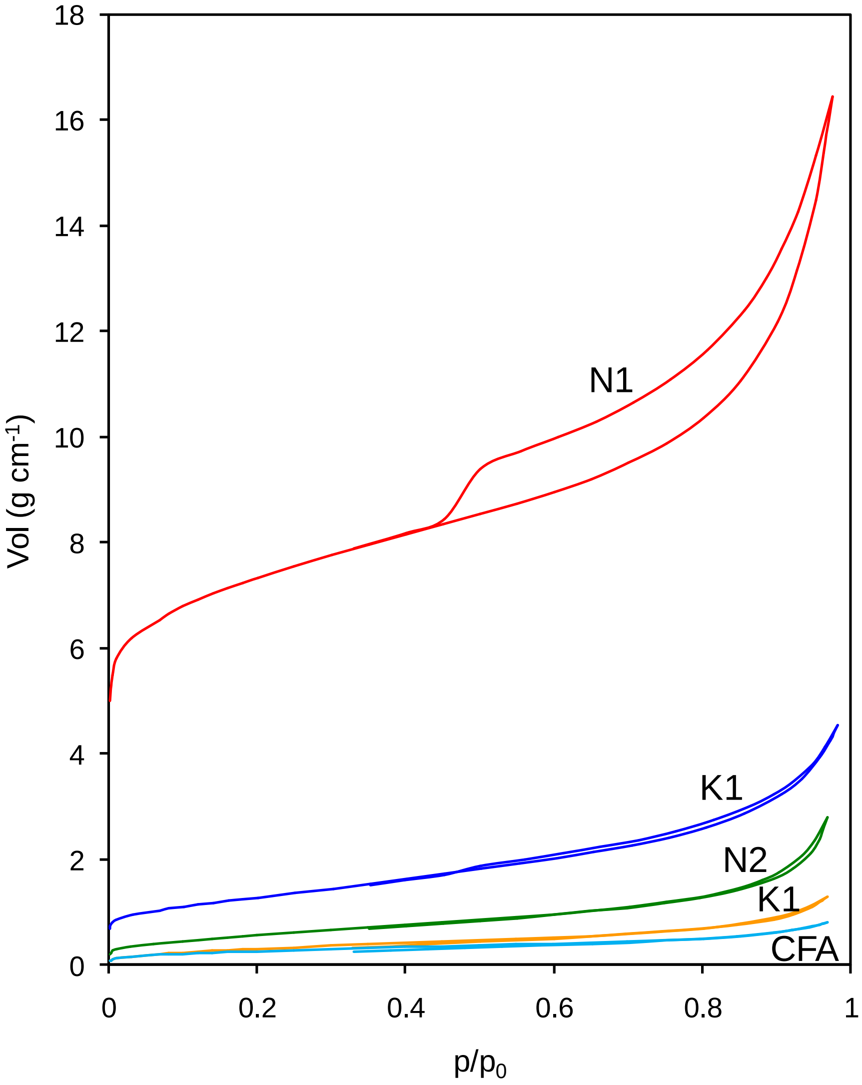

Figure VI.11. N_2 sorption isotherms of unreacted CFA and solids from carbonation runs N1, N2, K1 and K2.

VI.3 Factors affecting the progress of carbonation.

The higher carbonation reached in carbonate solutions (K1, N1) as compared to bicarbonate solutions (K2, N2) can be explained considering the much higher initial pH of the former solutions.(Parkhurst and Appelo, n.d.) CFA dissolution is significantly pH-dependent, increasing the dissolution rate with increasing pH(Shigemoto et al., 1993; Lin and Hsi, 1995; Querol et al., 1997b; Querol et al., 1997a; Steenbruggen and Hollman, 1998; Hollman et al., 1999; Murayama et al., 2002; Querol et al., 2002; Du Plessis et al., 2013). This is similar to the solubility trend of amorphous silica, which increases sharply for pH >9.0.(L. Monasterio-Guillot et al., 2019) Since Ca (and Mg) must be free in solution to be available for carbonation, an increase in pH should result in an increase in the amount of (Mg)calcite formed.(Rodríguez-Navarro et al., 2016) Moreover, at pH>10.3, the dominant C species in solution is CO_3^{2-} which is the species involved in the formation of carbonates, whereas at pH<10.3, HCO_3^- is the main aqueous C species, this limiting the extent of carbonation.

The lower CE of K1 run as compared with N1 run cannot be associated with a pH effect, because the initial (and final) pH of the former run was higher that the latter one (Table VI.1). The Ca concentration in solution (and also Si and Al, see Figure VI.12) was significantly higher in K_2CO_3 than in Na_2CO_3 experiments, although not much difference was observed in bicarbonate experiments. This fact shows that the presence of Na^+ ions enhances the formation of crystalline phases acting as “structure builders”, whereas K^+ ions hamper the precipitation of secondary phases, in agreement with Monasterio-Guillot et al(L. Monasterio-Guillot et al., 2019). Because Na^+ favours the precipitation of secondary crystalline phases (carbonates and zeolites), a more thorough dissolution of the amorphous Ca- and Mg-containing aluminosilicate spheres occurs, shifting the reaction towards the product side and fully explaining the contrasting results of N1 and K1 runs.

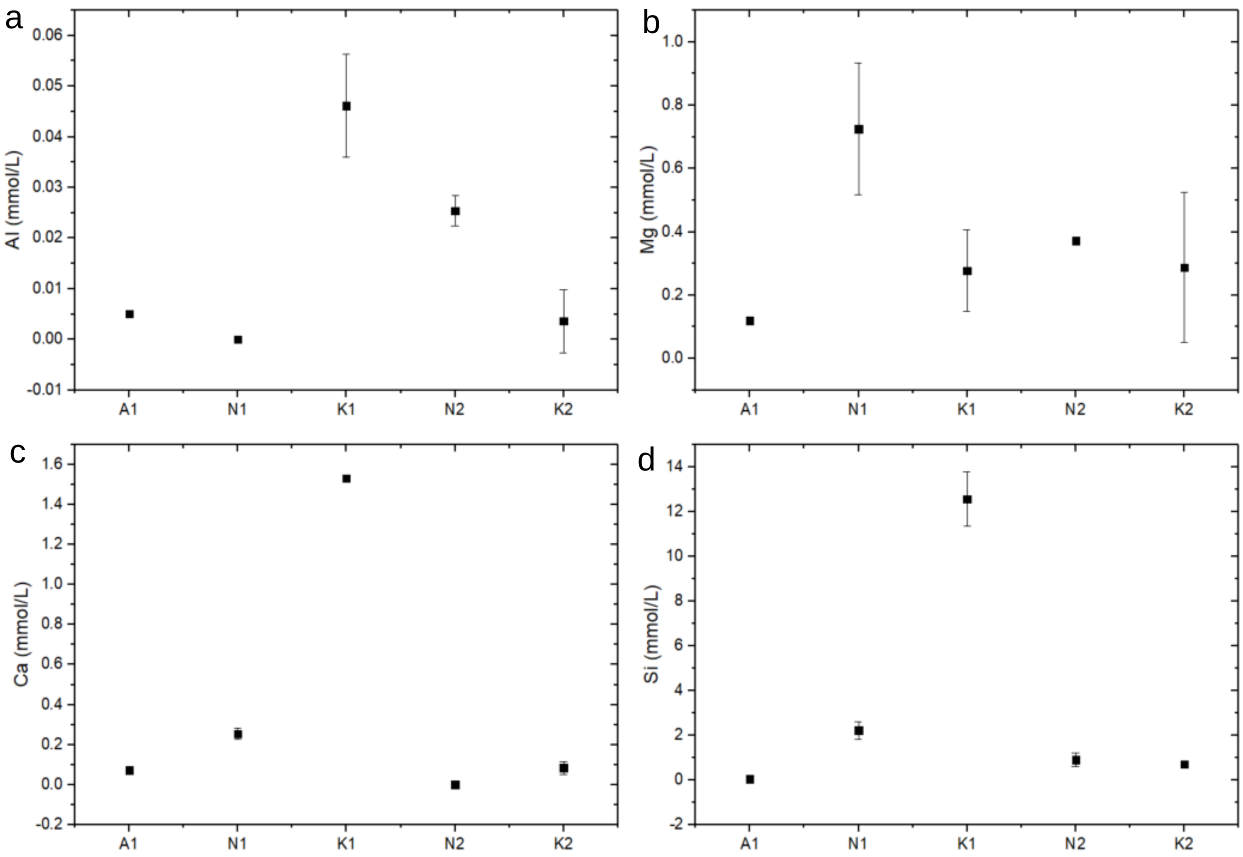

Figure VI.12. Results of ICP-OES analysis of the composition of solutions for the control (A1), Na_2CO_3 (N1), K_2CO_3 (K1), $NaHCO_3$ (N2) and $KHCO_3$ (K2) runs after reaction: (a) Aluminum, (b) Silicon, (c) Calcium and (d) Magnesium in solution

VI.4. Factors affecting zeolite formation.

These results show that: (i) a wider variety of zeolites are formed in the presence of Na^+ as compared to K^+, under otherwise similar experimental conditions, and (ii) higher zeolite yields are obtained with Na^+ as background ion, in agreement with Zeng et al.(Zeng et al., 2002) Crystalline zeolites were not detected in bicarbonate solutions, or in the controls with just water. Murayama et al.(Murayama et al., 2002) showed that the presence of high OH^- concentration in solution contributes to the release of Si and Al from CFA and, above 120ºC, allows the formation of an aluminosilicate gel, which is the precursor of zeolites. In this work, zeolites form due to a combination of the hydrothermal conditions (*T* >120ºC) and the alkaline pH (>10)(Shigemoto et al., 1993; Lin and Hsi, 1995; Querol et al., 1997b; Querol et al., 1997a; Steenbruggen and Hollman, 1998; Hollman et al., 1999; Moreno et al., 2001; Murayama et al., 2002; Querol et al., 2002; Du Plessis et al., 2013).

The release of Al and Si during dissolution of the CFA occurs in different stages, initially beginning with the dissolution of the glass, which is the most reactive phase, followed by quartz and mullite.(Querol et al., 2002) Commonly, high concentrations of NaOH or KOH (typically 1 to 5 M) under hydrothermal conditions (>120ºC) have been used to promote the dissolution of the glass fraction and the subsequent precipitation of zeolite-type phases.(Shigemoto et al., 1993; Lin and Hsi, 1995; Querol et al., 1997a; Steenbruggen and Hollman, 1998; Murayama et al., 2002; Zeng et al., 2002; Henry et al., 2004; Dwivedi and Jain, 2014) Interestingly, the high zeolite yield observed in the presence of Na^+ ions in run N1, which also yields the maximum amount of calcium carbonate, suggests that a synergistic action is at work during the precipitation of these phases. Apparently, higher levels of dissolution of the amorphous aluminosilicates in CFA are favored by the joint formation of both carbonates and zeolites, enabling a higher conversion of CFA into crystalline product phases. Remarkably, the high zeolite yield observed here is achieved at relatively mild *T* conditions with sodium carbonate solutions with lower $[OH]^-$ concentrations than typically used for zeolite synthesis via NaOH alkaline activation. Moreover, this route does not require alkali-fusion of CFA at high *T* (>500 °C), or the use of energy intensive microwave synthesis(Moreno et al., 2001), which is advantageous from an economic and environmental point of view.

VI.5Toxic elements leaching

Unreacted CFA shows a general higher release of PTE to the solution at both near-neutral and alkaline pHs as compared to reacted samples (Figure VI.13). This effect is most marked in runs N1 and K1, although solids from run N2 and K2 also show a significant reduction in PTE release. The release of As is pH-dependent for unreacted CFA, being higher at pH 6 than at pH 10. It has been reported that alkaline CFAs, like the one used here, show higher As release rates at high pH than at low pH, whereas the opposite is true for acidic CFA.(Izquierdo and Querol, 2012) Release of As from unreacted CFA is eight times higher than in reacted CFA. Such a huge difference is ascribed to its adsorption/entrapment into newly formed zeolites (or zeolite precursors in bicarbonate runs).

The behaviour of V and Sb (Figure S4c and f) is very similar to that of As(Spears and Martinez-Tarrazona, 2004), yet some subtle differences are observed. For instance, unreacted CFA present a higher Sb release at near neutral pH than at alkaline pH, whereas reacted samples show the opposite behaviour. This is likely due to the incorporation of this element in non-silicate phases (iron oxides) which prevent its release at acid-neutral pH, but is solubilized at alkaline pH.(Izquierdo and Querol, 2012) Regarding heavy metal ions such as Cu, Mo and Zn (as well as Sr, Mn and Ni) it is observed that their release rate is strongly pH-dependent (Fig. VI.13). At alkaline pH a systematic reduction in release rate occurs in reacted CFA as compared to unreacted CFA. This is consistent with the trapping of these metals both in carbonate and zeolitic phases as shown by TEM-AEM and SEM-EDS. In the case of Cu, this is likely due to its incorporation into zeolites as nanophase $Cu(OH)_2$ or CuO, as demonstrated by Terzano et al.(Terzano et al., 2005) In contrast, at pH 6 all these elements tend to be released at a higher rate in reacted than in unreacted CFA samples. A likely explanation for this behaviour is the release of such metals from their calcite host after the proton-promoted dissolution of the latter phase. Altogether, these results show that the precipitation of secondary phases plays a key role in the immobilization of PTE. These leaching results show that at alkaline conditions (i.e., the natural pH of this alkaline CFA), the PTE release of reacted samples including zeolitic precursors, zeolites and calcite, is significantly reduced as compared with raw CFA (i.e. As leaching in unreacted material (80 ppb) while in K2 run (1.9 ppb) in pH 6; V leaching in unreacted material 80 ppb, while in N2 run 30 ppb).

However, at mildly acidic conditions, release of some specific PTE trapped in newly formed carbonates might be an issue. Nonetheless, because after carbonation/zeolitization the pH of the CFA remains alkaline, such an acid-promoted PTE release will be unlikely if, for instance, the reacted CFA is disposed of in a pond or landfilled. Although CFA has been shown to be able to adsorb different acid gasses, including CO_2, and different PTE and organic pollutant, such an adsorption is known to be very poor.(Gupta et al., 2009) Transformation of CFA into carbonates and zeolites can overcome such limitations as it is shown here.

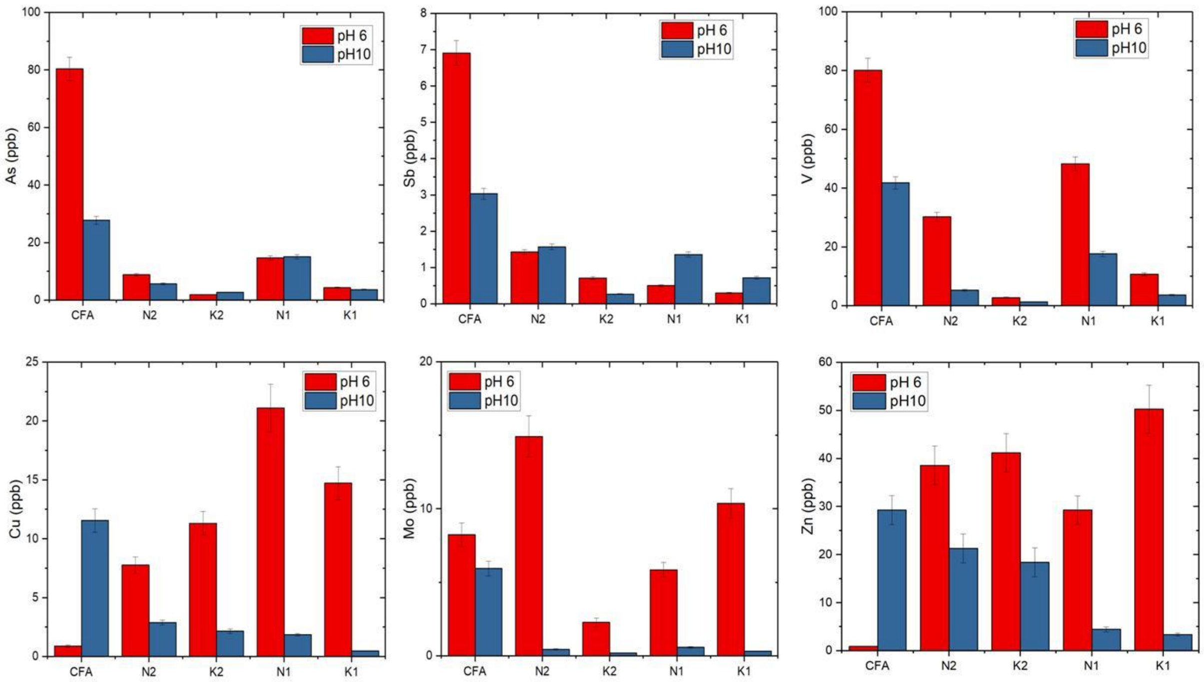

Figure VI.13. Results of leaching tests performed at pH 6 and pH 10. The total amount of selected elements (As, Sb, V, Cu, Mo, and Zn) leached from the unreacted CFA as well as of product from runs N2, K2, Ni and K1 is presented. The total amount was calculated by integrating the amount of element released at the predetermined sampling time intervals indicated in Materials and Methods.

Chapter VII. Conclusions

VII.I Hydrothermal reaction of pseudowollastonite with carbonate-bearing fluids: Implications for CO2 mineral sequestration (Chapter III)

A critical aspect highlighted by the results of these experiments is the dependence of substrate conversion rate and extent on the nature of the “background” alkali metal cations, which are not supposed to take part in the conversion of $CaSiO_3$ into $CaCO_3$.

The reason behind the observed difference in the kinetics and extent of the carbonation reaction is related to the formation of secondary silicate phases that can host the silicon ions released by psw dissolution. The formation of secondary silicates provides the system with an additional contribution to the free energy gradient that constitutes the thermodynamic driving force for the overall carbonation process. ICP-OES analysis of the final solutions showed that the aqueous silica concentrations were significantly higher in the $KHCO_3$ vs. $NaHCO_3$ and K_2CO_3 vs. Na_2CO_3 solutions, despite the corresponding similar starting pH.

The difficulty to accommodate the released Si forming K-bearing secondary silicate phases under these experimental carbonation conditions hampered the progress of psw reaction. According to the law of mass action, accumulation of Si ions in solution could be a possible cause for the observed limited (and even stoppage of) psw carbonation in the presence of K+ ions at highly alkaline pH.

Although these experiments with gaseous CO_2 demonstrated that the acidic conditions favor the dissolution of the substrate thus catalyzing psw carbonation, no significant kinetic effect of pH was observed in carbonation experiments performed under alkaline conditions using Na_2CO_3 (pH~13) and $NaHCO_3$ (pH~9), but the carbonate yield was however substantially lower in the case of the solution with the highest initial pH.

Conversely, a clear pH effect was observed in the case of K-containing carbonate solutions, with higher psw conversion and carbonate yield in the case of the lowest pH solution. These results underline that the carbonation of psw (and likely other primary alkaline earth metal silicates) is strongly dependent on pH and the specific background alkali metal ion. These results suggest that during carbonation of primary silicates in actual in situ CCS scenarios, where the presence of complex multicomponent CO_2-solutions with a range of dissolved alkali metal ions is expected, either supplied in the CO_2-brine, if sea water is used, or released after dissolution of silicate minerals in the host rock, dissolution of Ca^+ (and very likely, Mg and or Fe^{2+}) bearing silicates should be favored by inducing the precipitation of secondary silicate phases incorporating such alkali metal ions.

However, if monovalent cations in solution are not easily incorporated into secondary silicates (such as the case of K^+ in the studied system at the high pH) a significant reduction in the carbonation rate and yield could take place once the CO_2-rich plume reacts with the host silicate rock and experiences an increase in pH. Nonetheless, if the secondary silicates (crystalline and amorphous) incorporate Ca in their structure, as occurs in most of these experiments under alkaline conditions, the carbonation yield can be drastically reduced. Another remarkable change in behavior between the experiments with carbonate and bicarbonate salts was the transient formation of aragonite in the latter, related to the presence of high silica concentrations in solution at mild alkaline conditions due to the higher psw solubility and the fact that at $T > 50$ °C, aragonite preferentially forms at $pH<10$ while calcite does at $pH > 10$. Also, it is observed no polymorphic transformation (from β-$CaSiO_3$ to α-$CaSiO_3$) during the dissolution experiments, whereas parawollastonite formed in the experiments with Na_2CO_3 and $NaHCO_3$. This demonstrated that this latter polymorphic transformation could only proceed through a dissolution-precipitation process, at least in time scale of these experiments.

Finally, the experimental study of psw reactivity presented here in the different scenarios considered provides relevant information to be considered for the optimization of the conditions for geological carbon sequestration using a technology based on silicate conversion and for the geochemical modeling of the fate of CO_2 injected during in situ CCS. In particular, this study underlines the importance of a careful evaluation of the chemistry of aqueous fluids in contact with substrate rocks during in situ silicate carbonation projects. Moreover, these results show that geochemical modeling of the fate of injected CO_2 during in situ CCS should consider the formation of secondary silicate phases, the role of background electrolytes, and the reduction in carbonate yield associated with the precipitation of divalent metal-silicates (crystalline and amorphous).

This study also sheds light on the phase evolution taking place during the setting and hardening of a novel class of low Ca/Si cements with reduced carbon footprint based on $CaSiO_3$ that hardens via carbonation and could be applied for the sealing of CO_2 injection wells during geological carbon sequestration.

VII.II Kinetics and mechanisms of the acidic weathering of pyroxenes (Chapter IV)

The results of this study show how under the far-from-equilibrium conditions prevailing in these experiments, pyroxene dissolution results in extensive etch pit formation, where cracks can initiate and propagate by stress corrosion. Fracture formation is essential to this weathering process, as it facilitates the transport of fluids within an otherwise impermeable material and increases the fluxes of Ca and Mg released to the solution.

In contrast to other faster-dissolving silicate minerals, such as wollastonite, the formation of an amorphous Si-rich phase takes place mostly in highly localized areas of the mineral surface; mostly within deep etch pits and cracks. Although in pyroxenes dissolution is commonly surface-controlled, in these areas there is a low fluid renewal, and thus the reaction will be more likely controlled by transport of ionic species. This allows the build up of high Si-concentrations within these areas, and thus supersaturation with respect to amorphous silica can be reached locally resulting in precipitation.

The faster reaction rate of augite compared to diopside, most likely due to its higher iron, sodium and aluminum content, results in a greater amount of amorphous silica formation during augite dissolution, but also in a higher Ca and Mg release to the solution, feeding the system with alkali-earth metals, susceptible to enhance the carbonate yield in the presence of a Dissolved Inorganic Carbon source.

Unlike augite, in the case of diopside this amorphous Si-rich phase incorporates significant amounts of Mg, so that the precipitate could be regarded as a MSH precursor. This is an indirect indication of the high pH conditions (>7) reached at the diopside surface during dissolution, quite different to those measured in the bulk. This is an experimental evidence demonstrating that the transformations occurred in these systems could only be achieved by an ICDP mechanism. Furthermore, it should be mentioned that the use of diopside-bearing rocks in geological CO_2 storage, could prevent the Mg incorporated in this phase to be available for its precipitation as carbonates, acting as a handicap for an effective GCS strategy.

Altogether, these results highlight relevant information to use in the modeling of GCS strategies to enhance the use of silicate-carbonation. Particularly, this study shed light on the relevance of the silicate mineral composition (Fe and Na content) on the subsequent yield CO_2 mineralization, as it was demonstrated in Chapter V.

VII.III Physical-chemical control on carbonation of calcium-magnesium pyroxenes: Effect of reaction-driven fracturing

The implications of the results obtained during this work are manifold. A critical aspect highlighted by these results is the important role of secondary phases precipitation on the advancement of the reactions, not contemplated in the conversion of pyroxenes into carbonates. The formation of secondary iron oxides and crystalline and amorphous secondary silicates provides a free energy contribution to the system, allowing the progress of the carbonation reaction. The high amounts of secondary phases observed in augite experiments with DIC in solution enhanced the progress of the reaction as compared with pure water, while in diopside systems, the small amount of secondary phases hampered this progress. These results show that the presence of DIC in the system is crucial for the progress of the reaction, acting as a generator of secondary phases that contribute to shift the reaction towards the product side, but the effectiveness of this process is strongly dependent of the specific crystal-chemistry of the pyroxenes.

Also, it is shown the formation of secondary phases filling dissolution pits and fractures whose precipitation was, in theory, thermodynamically not possible in these systems. This demonstrates that these latter transformations could only be achieved by an ICDP mechanism.

Another important outcome of this work was the effect of pH in the systems' evolution. The advancement of the reaction was strongly pH-dependent, showing higher dissolution rates in moderately-alkaline than in strongly-alkaline pH systems. This effect has a direct impact on the formation of secondary phases, fostering their precipitation in large amounts in the former case and hampering the progress of the reaction in the latter.

Experimental results also demonstrate that the in-pore crystallization of secondary crystalline phases (Na-phillipsite and, to a lesser extent MSH) is responsible of the fracture generation during dissolution-carbonation processes. It shows that in contrast to acidic conditions, at moderately-alkaline and alkaline pHs, the reaction-driven fracturing derives from crystallization pressure, and not by cracks associated with mineral dissolution.

Finally, it has been experimentally demonstrated that the amount of Al, Fe (and Na) ions in the pyroxenes has a strong effect during dissolution-carbonation processes, explaining why augite, which includes a higher Fe, Na, and Al content than diopside, shows the highest dissolution rate and the highest conversion and carbonate yield.

Altogether, these results provide relevant information to be considered for the enhancement of the GCS using silicate carbonation strategies. In particular, this study shed light on the importance of the silicate mineral composition of target rock formations during in situ CCS, showing the importance of alkali metal (Na) secondary aluminosilicate crystallization on reaction-driven fracture development, providing flow channels and fresh reactive surface areas to improve the carbonation reaction.

VII.IV CO_2 mineral trapping by carbonation of Fly Ash from coal combustion power plant (Chapter VI)

It has been demonstrate that 1 ton of CFA can contribute to the sequestration of 45 kg of CO_2, a value that is much higher than those reported for other CFA, even with higher CaO (and MgO) content (Ukwattage et al., 2015; Sun et al., 2012; He et al., 2013; Dananjayan et al., 2016). Still, this capacity is relatively small if compared with other alkaline waste materials such as steel slag, cement kiln dust, municipal solid waste incinerator (MSWI) ash or air pollution control (APC) residues where values of net CO_2 mineral sequestration up to 290 kg of CO_2/ton of alkaline waste have been reported (Pan et al., 2012). However, considering the amount of CFA produced annually worldwide, and the amount already landfilled, CFA carbonation can effectively contribute to the reduction of the C footprint of the coal-firing sector.

Also shown in this works is that the background alkaline metal ion plays a key role in the carbonation and zeolitization efficiency. The “structure builder” role of Na^+, led to 60 wt% conversion of CFA into zeolites, also reaching the highest CE of all runs (79.26 %). To my knowledge, these values are among the highest ones obtained for zeolite conversion and carbonation efficiency using CFA (Lin et al., 1995; Querol et al., 2002; Sanchez-Hernandez et al. 2016; Hollman et al., 1999). In contrast, with K^+ as background electrolyte, only a 30% zeolitic yield and about half the CE of the N1 run were achieved. These results demonstrate that the use of a sodium alkaline solution for CO_2 mineral capture and zeolite production is the best choice.

Finally, what is more important is that CFA carbonation/zeolitization makes less hazardous these wastes for their disposal of in ponds or landfills, while simultaneously increasing their value as a result of the formation of reaction byproducts (carbonates and zeolites) with a potential commercial use in several applications, with promising capacities to immobilize PTE from wastewaters, or for flue gas treatment and separation of different greenhouse gases (e.g., CO_2, NH_4). Ultimately, this study opens a new pathway on the combined carbonation and zeolitisation of CFA under hydrothermal conditions to add an extra value to these wastes to form reusable materials and, also, to avoid the hazardous consequences due to the leaching of potentially toxic elements.

VII.V General Conclusions and future developments

As discussed in the section I.6 of this Thesis, five specific objectives were raised.

The first objective was to disclose **the effect of background electrolytes** during GCS strategies via silicate carbonation. It has been demonstrated that monovalent cations have a strong effect on the carbonation reaction under hydrothermal conditions. Na^+ ions acted as “structure builders” units for the precipitation of newly-formed secondary phases (e.g. pectolite, Na-phyllipsite, CSH, analcime, chabazite and NaP1) observed in Chapters III, V and VI.

Conversely, K^+ ions hampers the carbonation and formation of secondary silicate phases due to the absence of an effective sink for this alkali-metal and therefore, yielding a lower carbonation of the primary silicates. Regarding the carbonation of wastes materials (CFA), K^+ was, however, a builder of K-silicate phases. Despite the limited formation of secondary K-bearing silicates, lower positive effect during dissolution-carbonation reactions was observed as compared to Na^+. It is demonstrated that the presence of both background electrolytes strongly influences the CCS strategies and must be taken into account for modelling CO_2 mineral sequestration mechanisms.

The second objective of this Thesis was to unravel the **effect of the pH during carbonation reactions of primary silicates.** It has been demonstrated that pH strongly influences the dissolution reaction, and subsequently the carbonation reaction. Higher carbonate yield content in all systems studied here, were achieved under neutral-to moderately alkaline conditions following the addition of alkali metal bearing carbonates, and under starting acid pH during direct injection of CO_2 systems (Chapter III and V). Thus, pH of the injection brines and pH of the pore-water in host-rocks must be carefully studied to reach the highest efficiency of carbonation during in situ GCS strategies. Furthermore, during dissolution processes of primary silicates, pH is the strongest factor that controls the reaction. Hence, it is important to carefully chose the optimal pH of reaction fluids during ex situ CCS strategies such as the pH-swing method, or during in situ GCS.

The third objective of this Thesis was is to determine **the effect of secondary phases formation during carbonation reactions of primary silicates.** It has been demonstrated that secondary phases precipitation, in addition to carbonate phases (i.e. pectolite, Na-phillipsite, chabazite, NaP1) strongly controls the carbonation reaction. Side reactions are key factors for the development of an efficient primary silicate carbonation. Furthermore, it has been experimentally proved that the crystallization of crystalline silicates (Na-phillipsite, chapter V) could exert very high crystallization pressure as to exceed the tensile strength of individual silicate minerals, and by extension, host rocks, during mineral carbonation and, therefore, cause fracturing, increasing the reactive surface of the primary silicates and enhancing the reaction. However, the presence of secondary amorphous silica (Chapter IV) could prevent the complete reaction of the primary silicates by a passivation effect, and therefore, acting as a strong handicap for GCS strategies.

The fourth objective was to gain some insight on **the actual mechanisms of pyroxene dissolution and SALs formation at low pH and the effect of the hydrodynamic conditions**. It has been demonstrated that the hydrodynamic conditions are key factors for the precipitation of SALs that passivate silicate mineral carbonation. It has been demonstrated that a strong knowledge of the aqueous system during GCS is absolutely necessary to avoid as much as possible the passivation of these reactions.

Finally, the last objective of this work was to **disclose the key features of CFA carbonation under mild hydrothermal conditions using alkaline (bi)carbonate solutions, combined with the formation of zeolites and the effective capture of PTE present in CFA.** It has been proved that a better understanding on the mechanisms that regulate CFA wastes dissolution and therefore, the feeding to the solution of ions susceptible to be carbonated is mandatory to reach high yield of CO_2 trapped as carbonate phases in these materials. Furthermore, the formation of secondary crystalline silicates as zeolites is relevant on the one hand, to achieve a higher carbonation reaction exerted by side reactions, and on the other hand, to trap PTE in their structure and avoid their release to soils and waters.

Future perspectives of this Thesis

Subsequently to this work, it should be interesting to apply the gained knowledge to other primary silicate minerals and wastes materials, to disclose some new features and new fields of study (i.e. the behaviour of other Ca-rich wastes on carbonation reaction)

Furthermore, experiments at other pH and T ranges than those studied here must be explored to disclose the behaviour of these reactions under economically feasible conditions, relevant for industrial CCS strategies.

In addition, the activation of primary silicates and industrial wates would be developed to understand the behaviour and the possible enhancement of this reactions.

Finally, the effect of catalysts such as MOFs, silicase and carbonic anhydrase would be explored during dissolution and carbonation of the materials used in this Thesis, as a biomimetic approach for enhanced silicate dissolution and carbonation at mild conditions.

References

Alexander, G. B., Heston, W. M., & Iler, R. K. (1954). The solubility of amorphous silica in water. The Journal of Physical Chemistry, 58(6), 453-455.

Álvarez-Ayuso E., García-Sánchez A. and Querol X. (2003) Purification of metal electroplating waste waters using zeolites. *Water Res.* **37**, 4855–4862.

Anon American Coal Ash Association's. *https://www.acaa-usa.org/*.

Anon European Coal Combustion Products Association e.V. *http://www.ecoba.com/*.

Archer D. (2008) Carbon cycle: Checking the thermostat. *Nat. Geosci.* **1**, 289.

Ashraf W. and Olek J. (2016) Carbonation behavior of hydraulic and non-hydraulic calcium silicates: potential of utilizing low-lime calcium silicates in cement-based materials. *J. Mater. Sci.* **51**, 6173–6191.

Ashraf, W., Olek, J., & Tian, N. (2016). Multiscale characterization of carbonated wollastonite paste and application of homogenization schemes to predict its effective elastic modulus. Cement and Concrete Composites, 72, 284-298.

Ashraf, W., Olek, J., & Jain, J. (2017). Microscopic features of non-hydraulic calcium silicate cement paste and mortar. Cement and Concrete Research, 100, 361-372.

Ashraf, W., & Olek, J. (2018). Elucidating the accelerated carbonation products of calcium silicates using multi-technique approach. Journal of CO2 Utilization, 23, 61-74.

Atakan V. Sahu S. Quinn S. Hu X. DeCristofaro N. (2014) CO2 matters - advances in a new class of cement. Zement Kalk Gips, 3, 60-63.

Atkinson B. K. (1984) Subcritical crack growth in geological materials. *J. Geophys. Res. Solid Earth* **89**, 4077–4114.

Atkinson B. K. (1982) Subcritical crack propagation in rocks: theory, experimental results and applications. *J. Struct. Geol.* **4**, 41–56.

Aza D. and Aza D. (2000) Morphological and structural study of pseudowollastonite implants in bone. *J. Microsc.* **197**, 60–67.

Bachu S. (2002) Sequestration of CO2 in geological media in response to climate change: road map for site selection using the transform of the geological space into the CO2 phase space. *Energy Convers. Manag.* **43**, 87–1029].

Back M., Kuehn M., Stanjek H. and Peiffer S. (2008) Reactivity of alkaline lignite fly ashes towards CO2 in water. *Environ. Sci. Technol.* **42**, 4520–4526.

Bailey, A., & Reesman A. L. (1971) A survey study of the kinetics of wollastonite dissolution in H 2 O-CO 2 and buffered systems at 25 degrees C. American Journal of Science, 271(5), 464-472.

Banfield J. F., Ferruzzi G. G., Casey W. H. and Westrich H. R. (1995) HRTEM study comparing naturally and experimentally weathered pyroxenoids. *Geochim. Cosmochim. Acta* **59**, 19–31.

Bauer M., Gassen N., Stanjek H. and Peiffer S. (2011) Carbonation of lignite fly ash at ambient T and P in a semi-dry reaction system for CO2 sequestration. *Appl. geochemistry* **26**, 1502–

1512.

Béarat H., McKelvy M. J., Chizmeshya A. V. G., Gormley D., Nunez R., Carpenter R. W., Squires K. and Wolf G. H. (2006) Carbon sequestration via aqueous olivine mineral carbonation: role of passivating layer formation. *Environ. Sci. Technol.* **40**, 4802–4808.

Berg A. and Banwart S. A. (2000) Carbon dioxide mediated dissolution of Ca-feldspar: implications for silicate weathering. *Chem. Geol.* **163**, 25–42.

Berger G., Claparols C., Guy C. and Daux V. (1994) Dissolution rate of a basalt glass in silica-rich solutions: implications for long-term alteration. *Geochim. Cosmochim. Acta* **58**, 4875–4886.

Bernard E., Lothenbach B., Chlique C., Wyrzykowski M., Dauzeres A., Pochard I. and Cau-Dit-Coumes C. (2019) Characterization of magnesium silicate hydrate (MSH). *Cem. Concr. Res.* **116**, 309–330.

Bernard E., Lothenbach B., Le Goff F., Pochard I. and Dauzères A. (2017) Effect of magnesium on calcium silicate hydrate (CSH). *Cem. Concr. Res.* **97**, 61–72.

Berner, R.A.; Lasaga, A.; Garrels, R.M. (1983) The carbonate-silicate geochemical cycle and its effect on atmospheric carbon dioxide over the past 100 million years. Am. J. Sci., 283, 641-683.

Berner R. A. (2006) GEOCARBSULF: a combined model for Phanerozoic atmospheric O2 and CO2. *Geochim. Cosmochim. Acta* **70**, 5653–5664.

Berner R. A. (2003) The long-term carbon cycle, fossil fuels and atmospheric composition. *Nature* **426**, 323.

Berner R. A. (1992) Weathering, plants, and the long-term carbon cycle. *Geochim. Cosmochim.*

Acta **56**, 3225–3231.

Berner R. A. and Caldeira K. (1997) The need for mass balance and feedback in the geochemical carbon cycle. *Geology* **25**, 955–956.

Berner R. A., Sjöberg E. L., Velbel M. A. and Krom M. D. (1980) Dissolution of pyroxenes and amphiboles during weathering. *Science (80-.).* **207**, 1205–1206.

Bhatt A., Priyadarshini S., Mohanakrishnan A. A., Abri A., Sattler M. and Techapaphawit S. (2019) Physical, chemical, and geotechnical properties of coal fly ash: A global review. *Case Stud. Constr. Mater.* **11**, e00263.

Biagioni, C., Merlino, S., & Bonaccorsi, E. (2015). The tobermorite supergroup: a new nomenclature. Mineralogical Magazine, 79(2), 485-495.

Blanc P., Vieillard P., Gailhanou H., Gaboreau S., Gaucher E., Fialips C. I., Madé B. and Giffaut E. (2015) A generalized model for predicting the thermodynamic properties of clay minerals. *Am. J. Sci.* **315**, 734–780.

Blissett R. S. and Rowson N. A. (2012) A review of the multi-component utilisation of coal fly ash. *Fuel* **97**, 1–23.

Boot-Handford M. E., Abanades J. C., Anthony E. J., Blunt M. J., Brandani S., Mac Dowell N., Fernández J. R., Ferrari M.-C., Gross R. and Hallett J. P. (2014) Carbon capture and storage update. *Energy Environ. Sci.* **7**, 130–189.

Boyd P. G., Chidambaram A., García-Díez E., Ireland C. P., Daff T. D., Bounds R., Gładysiak A., Schouwink P., Moosavi S. M. and Maroto-Valer M. M. (2019) Data-driven design of metal–organic frameworks for wet flue gas CO 2 capture. *Nature* **576**, 253–256.

Brady P. V and Carroll S. A. (1994) LETTER Direct effects of CO2 and temperature on silicate weathering: Possible implications for climate control. *Geochim. Cosmochim. Acta* **58**, 1853–1856.

Brandt J. E., Simonin M., Di Giulio R. T. and Bernhardt E. S. (2019) Beyond selenium: coal combustion residuals lead to multielement enrichment in receiving lake food webs. *Environ. Sci. Technol.* **53**, 4119–4127.

Brantley S. L. (2008) Kinetics of mineral dissolution. In *Kinetics of water-rock interaction* Springer. pp. 151–210.

Brunauer, S., Kantro, D. L., & Weise, C. H. (1956). The surface energies of amorphous silica and hydrous amorphous silica. Canadian Journal of Chemistry, 34(10), 1483-1496.

Bukowski, J.M. and Berger, R.L. (1979) Reactivity and strength development of CO2 activated non-hydraulic calcium silicates, Cem. Concr. Res. 9 57–68.

Carroll S. A. and Knauss K. G. (2005) Dependence of labradorite dissolution kinetics on CO2 (aq), Al (aq), and temperature. *Chem. Geol.* **217**, 213–225.

Casey W. H. (1990) Leaching of minerals and glass surface during dissolution. *Miner. interface geochemistry*, 397–426.

Casey W. H., Westrich H. R. and Arnold G. W. (1988) Surface chemistry of labradorite feldspar reacted with aqueous solutions at pH = 2, 3, and 12. *Geochim. Cosmochim. Acta* **52**, 2795–2807.

Casey W. H., Westrich H. R., Massis T., Banfield J. F. and Arnold G. W. (1989) The surface of labradorite feldspar after acid hydrolysis. *Chem. Geol.* **78**, 205–218.

Catalano J. G., Huhmann B. L., Luo Y., Mitnick E. H., Slavney A. and Giammar D. E. (2012) Metal release and speciation changes during wet aging of coal fly ashes. *Environ. Sci. Technol.* **46**, 11804–11812.

Catalfamo P., Corigliano F., Primerano P. and Di Pasquale S. (1993) Study of the pre-crystallization stage of hydrothermally treated amorphous aluminosilicates through the composition of the aqueous phase. *J. Chem. Soc. Faraday Trans.* **89**, 171–175.

Chang E. E., Chen C. H., Chen Y. H., Pan S. Y. and Chiang P. C. (2011) Performance evaluation for carbonation of steel-making slags in a slurry reactor. *J. Hazard. Mater.* **186**, 558–564. Available at: http://dx.doi.org/10.1016/j.jhazmat.2010.11.038.

Chen, H. F., Song, S. R., Lo, H. J., Li, L. J., Fang, J. N., Chen, Y. L., Lin, I. C., Liu, Y. J., Liu, C. M., & Kuo, L. W. (2005). Dissolution of Na2O·CaO·nSiO2 glasses in Na2CO3 solution for long-term and short-term experiments. Journal of non-crystalline solids, 351(16-17), 1417-1425.

Chinnam, R. K., Bernardo, E., Will J. & Boccaccini A. R. (2015) Processing of porous glass ceramics from highly crystallisable industrial wastes, Advances in Applied Ceramics, 114:sup1, S11-S16.

Chizmeshya, A. V. G., McKelvy M. J., Squires, K., Carpenter, R. W. & Béarat, H. (2008) A novel approach to mineral carbonation: Enhancing carbonation while avoiding mineral pretreatment process cost. US Department of Energy Final Report 924162 (Arizona State Univ., Arizona).

Cole D. R. and Oelkers E. H. (2008) *Carbon Dioxide Sequestration.*,

Crowley T. J. and Berner R. A. (2001) CO2 and climate change. *Science (80-.).* **292**, 870–872.

Dauzeres A., Achiedo G., Nied D., Bernard E., Alahrache S. and Lothenbach B. (2016)

Magnesium perturbation in low-pH concretes placed in clayey environment—solid characterizations and modeling. *Cem. Concr. Res.* **79**, 137–150.

Daval D., Bernard S., Rémusat L., Wild B., Guyot F., Micha J. S., Rieutord F., Magnin V. and Fernandez-Martinez A. (2017) Dynamics of altered surface layer formation on dissolving silicates. *Geochim. Cosmochim. Acta* **209**, 51–69.

Daval D., Hellmann R., Corvisier J., Tisserand D., Martinez I. and Guyot F. (2010) Dissolution kinetics of diopside as a function of solution saturation state: Macroscopic measurements and implications for modeling of geological storage of CO2. *Geochim. Cosmochim. Acta* **74**, 2615–2633.

Daval D., Hellmann R., Saldi G. D., Wirth R. and Knauss K. G. (2013) Linking nm-scale measurements of the anisotropy of silicate surface reactivity to macroscopic dissolution rate laws: New insights based on diopside. *Geochim. Cosmochim. Acta* **107**, 121–134.

Daval D., Martinez I., Corvisier J., Findling N., Goffe B. and Guyot F. (2009a) Carbonation of Ca-bearing silicates, the case of wollastonite: Experimental investigations and kinetic modeling. *Chem. Geol.* **265**, 63–78.

Daval D., Martinez I., Corvisier J. J., Findling N. N., Goffé B., Guyot F. F., Goffe B. and Guyot F. F. (2009b) Carbonation of Ca-bearing silicates, the case of wollastonite: Experimental investigations and kinetic modeling. *Chem. Geol.* **262**, 262–277.

Daval D., Martinez I., Guigner J. M., Hellmann R., Corvisier J., Findling N., Dominici C., Goffé B., Guyot F., Goffe B. and Guyot F. (2009c) Mechanism of wollastonite carbonation deduced from micro- To nanometer length scale observations. *Am. Mineral.* **94**, 1707–1726.

Daval D., Sissmann O., Menguy N., Saldi G. D., Guyot F., Martinez I., Corvisier J., Garcia B., Machouk I., Knauss K. G. and Hellmann R. (2011) Influence of amorphous silica layer formation on the dissolution rate of olivine at 90°C and elevated pCO2. *Chem. Geol.* **284**, 193–209.

De Aza, P. N., Luklinska, Z. B., Martinez, A., Anseau, M. R., Guitian, F., & De Aza, S. (2000). Morphological and structural study of pseudowollastonite implants in bone. Journal of Microscopy(UK), 197(1), 60-67.

Deer W. A., Howie R. A. and Zussman J. (1997) Rock-forming minerals: single-chain silicates, Volume 2A. In Geological Society of London.

Demir F., Dönmez B., Okur H. and Sevim F. (2003) Calcination kinetic of magnesite from thermogravimetric data. *Chem. Eng. Res. Des.* **81**, 618–622.

Dietzel M. (2000) Dissolution of silicates and the stability of polysilicic acid. *Geochim. Cosmochim. Acta* **64**, 3275–3281.

Dixit S. and Carroll S. A. (2007) Effect of solution saturation state and temperature on diopside dissolution. *Geochem. Trans.* **8**, 1–14.

Di Lorenzo, F., & Prieto, M. (2017). Dissolution–Recrystallization of (Mg, Fe) CO3 during Hydrothermal Cycles: FeII/FeIII Conundrums in the Carbonation of Ferromagnesian Minerals. Crystal Growth & Design, 17(8), 4170-4182.

Di Lorenzo, F., Ruiz-Agudo, C., Ibañez-Velasco, A., Gil-San Millán, R., Navarro, J. A. R., Ruiz-Agudo, E., & Rodriguez-Navarro, C. (2018). The Carbonation of Wollastonite: A Model Reaction to Test Natural and Biomimetic Catalysts for Enhanced CO2 Sequestration.

Minerals, 8(5), 209

Dove P. M. and Han N. (2007) Kinetics of mineral dissolution and growth as reciprocal microscopic surface processes across chemical driving force. In *AIP Conference Proceedings* American Institute of Physics. pp. 215–234.

Dove P. M., Han N., Wallace A. F. and De Yoreo J. J. (2008) Kinetics of amorphous silica dissolution and the paradox of the silica polymorphs. *Proc. Natl. Acad. Sci.* **105**, 9903–9908.

Drever J. I. (1985) *The Chemistry of Weathering*., Springer Netherlands.

Drever J. I. and Stillings L. L. (1997) The role of organic acids in mineral weathering. *Colloids Surfaces A Physicochem. Eng. Asp.* **120**, 167–181.

Duxson P. and Provis J. L. (2008) Designing precursors for geopolymer cements. *J. Am. Ceram. Soc.* **91**, 3864–3869.

Duxson, P., Provis, J. L., Lukey, G. C., Van Deventer, J. S. J., Separovic, F., & Gan, Z. H. (2006). 39K NMR of free potassium in geopolymers. Industrial & Engineering Chemistry Research, 45(26), 9208-9210.

Duxson, P., Fernández-Jiménez, A., Provis, J. L., Lukey, G. C., Palomo, A., & van Deventer, J. S. (2007). Geopolymer technology: the current state of the art. Journal of Materials Science, 42(9), 2917-2933.

Dwivedi A. and Jain M. K. (2014) Fly ash – waste management and overview : A Review. *Recent Res. Sci. Technol.* **6**, 30–35.

Ecke H. (2003) Sequestration of metals in carbonated municipal solid waste incineration

(MSWI) fly ash. *Waste Manag.* **23**, 631–640.

Eikeland, E., Blichfeld, A. B., Tyrsted, C., Jensen, A., & Iversen, B. B. (2015). Optimized carbonation of magnesium silicate mineral for CO2 storage. ACS applied materials & interfaces, 7(9), 5258-5264.

Emmanuel S. and Ague J. J. (2011) Impact of nano-size weathering products on the dissolution rates of primary minerals. *Chem. Geol.* **282**, 11–18. Available at:

Etame J., Suh C. E., Gerard M. and Bilong P. (2012) Phillipsite formation in nephelinitic rocks in response to hydrothermal alteration at Mount Etinde, Cameroon. *Geochemistry* **72**, 31–37.

Evangelos Georgakopoulos (Cranfield University, UK), Rafael M. Santos (Sheridan Institute of Technology, Brampton, Ontario, Canada), Yi Wai Chiang (University of Guelph, Ontario, Canada), Vasilije Manovic (Cranfield University U. (2016) Influence of process parameters on carbonation rate and conversion of steelmaking slags – Introduction of the 'carbonation weathering rate.' *Greenh. Gases Sci. Technol.* **6**, 470–491.

Fahlke B., Starke P., Seefeld V., Wieker W. and Wendlandt K.-P. (1987) On the intermediates in zeolite Y synthesis. *Zeolites* **7**, 209–213.

Farmer V. C. (1974) Orthosilicates, Pyrosilicates, and other Finite-chain Silicates. In *The Infrared Spectra of Minerals* (ed. V. C. Farmer). Mineralogical Society of Great Britain and Ireland

Fahey, J. J. (1962). Saline Minerals of the Green River Formation. Geological Survey Professional Paper 405, US Government Printing Office, Washington.

Falkowski, P.; Scholes, R.J.; Boyle, E.E.A.; Canadell, J.; Canfield, D.; Elser, J.: Gruber, N.; Hibbard, K.; Högberg, P.; Linder, S.; Mackenzie, F.T.; Moore III, B.; Pedersen, T.; Rosenthal, Y.; Seltzinger, S.; Smetacek, V.; Steffen, W. (2000) The global carbon cycle: A test of our knowledge of Earth as a system. Science, 290, 291–296.

Farnam, Y., Villani, C., Washington, T., Spence, M., Jain, J., & Weiss, W. J. (2016). Performance of carbonated calcium silicate based cement pastes and mortars exposed to NaCl and MgCl2 deicing salt. Construction and Building Materials, 111, 63-71.

Fernández-Pereira C., Galiano Y. L., Rodríguez-Piñero M. A., Vale J. and Querol X. (2002) Utilisation of zeolitised coal fly ash as immobilising agent of a metallurgical waste. *J. Chem. Technol. Biotechnol. Int. Res. Process. Environ. Clean Technol.* **77**, 305–310.

Fernández Bertos M., Simons S. J. R., Hills C. D. and Carey P. J. (2004) A review of accelerated carbonation technology in the treatment of cement-based materials and sequestration of CO 2. *J. Hazard. Mater.* **112**, 193–205.

Farnam, Y., Villani, C., Washington, T., Spence, M., Jain, J., & Weiss, W. J. (2016). Performance of carbonated calcium silicate based cement pastes and mortars exposed to NaCl and MgCl2 deicing salt. Construction and Building Materials, 111, 63-71.

Ferruzzi, G. G. (1993). The character and rates of dissolution of pyroxenes and pyroxenoids. MS, University of California, Davis.

Fleming B. A. and Crerar D. A. (1982) Silicic acid ionization and calculation of silica solubility at elevated temperature and pH application to geothermal fluid processing and reinjection. *Geothermics* **11**, 15–29.

Fleury B., Godon N., Ayral A. and Gin S. (2013) SON68 glass dissolution driven by magnesium silicate precipitation. *J. Nucl. Mater.* **442**, 17–28.

Foster G. L., Royer D. L. and Lunt D. J. (2017) Future climate forcing potentially without precedent in the last 420 million years. *Nat. Commun.* **8**, 14845.

Frings P. J. (2019) Palaeoweathering: how do weathering rates vary with climate? *Elem. An Int. Mag. Mineral. Geochemistry, Petrol.* **15**, 259–265.

Frings P. J. and Buss H. L. (2019) The Central Role of Weathering in the Geosciences. *Elem. An Int. Mag. Mineral. Geochemistry, Petrol.* **15**, 229–234.

Friedlingstein, P., Andrew, R. M., Rogelj, J., Peters, G. P., Canadell, J. G., Knutti, R., Luderer, G., Raupach, M. R., Schaeffer, M., van Vuure,, D. P. & Le Quéré, C. (2014). Persistent growth of CO 2 emissions and implications for reaching climate targets. Nature Geoscience, 7(10), 709.

Gadikota G. and Alissa Park A. (2015) Accelerated Carbonation of Ca-and Mg-Bearing Minerals and Industrial Wastes Using CO 2 8 CHAPTER OUTLINE. *Carbon Dioxide Util.*, 115–127

Gadikota G., Matter J., Peter Kelemen bc and Alissa Park A. (2014) Chemical and morphological changes during olivine carbonation for CO 2 storage in the presence of NaCl and NaHCO 3. *Phys. Chem. Chem. Phys* **16**, 4679.

Gerdemann SJ, O'Connor WK, Dahlin DC, Penner LR, Rush H (2007) Ex situ aqueous mineral carbonation. Environ Sci Technol 41:2587–2593.

Gislason S. R., Oelkers E. H., Eiriksdottir E. S., Kardjilov M. I., Gisladottir G., Sigfusson B., Snorrason A., Elefsen S., Hardardottir J. and Torssander P. (2009) Direct evidence of the feedback between climate and weathering. *Earth Planet. Sci. Lett.* **277**, 213–222.

Glaccum R. and Boström K. (1976) (Na, K)-phillipsite: Its stability conditions and geochemical role in the deep sea. *Mar. Geol.* **21**, 47–58.

Goldsmith J. R., Graf D. L., Chodos A. A., Joensuu O. I. and McVicker L. D. (1958) Relation between lattice constants and composition of Ca-Mg carbonates. *Am. Mineral. J. Earth Planet. Mater.* **43**, 84–101.

Golubev S. V, Pokrovsky O. S. and Schott J. (2005) Experimental determination of the effect of dissolved CO2 on the dissolution kinetics of Mg and Ca silicates at 25 C. *Chem. Geol.* **217**, 227–238.

Green E. and Luttge A. (2006) Incongruent dissolution of wollastonite measured with vertical scanning interferometry. *Am. Mineral.* **91**, 430–434.

Greenberg, S. A. (1956). The chemisorption of calcium hydroxide by silica. The Journal of Physical Chemistry, 60(3), 325-330.

Gupta V. K., Carrott P. J. M., Ribeiro Carrott M. M. L. and Suhas (2009) Low-cost adsorbents: growing approach to wastewater treatment—a review. *Crit. Rev. Environ. Sci. Technol.* **39**, 783–842.

Hammer, V. M., Libowitzky, E., & Rossman, G. R. (1998). Single-crystal IR spectroscopy of very strong hydrogen bonds in pectolite, NaCa2 [Si3O8 (OH)], and serandite, NaMn2 [Si3O8 (OH)]. American Mineralogist, 83(5-6), 569-576.

Hamilton V. E. (2000) Thermal infrared emission spectroscopy of the pyroxene mineral series. *J. Geophys. Res. E Planets* **105**, 9701–9716.

Harkness J. S., Sulkin B. and Vengosh A. (2016) Evidence for coal ash ponds leaking in the southeastern United States. *Environ. Sci. Technol.* **50**, 6583–6592.

Hay R. L. and Sheppard R. A. (2001) Occurrence of zeolites in sedimentary rocks: An overview. *Rev. Mineral. geochemistry* **45**, 217–234.

Hellmann R., Daval D. and Wirth R. (2013) Formation of Amorphous Silica Surface Layers by Dissolution-Reprecipitaton During Chemical Weathering: Implications for CO2 Uptake. *Procedia Earth Planet. Sci.* **7**, 346–349.

Hellmann R., Penisson J. M., Hervig R. L., Thomassin J. H. and Abrioux M. F. (2003) An EFTEM/HRTEM high-resolution study of the near surface of labradorite feldspar altered at acid pH: Evidence for interfacial dissolution-reprecipitation. *Phys. Chem. Miner.* **30**, 192–197.

Hellmann R., Wirth R., Daval D., Barnes J. P., Penisson J. M., Tisserand D., Epicier T., Florin B. and Hervig R. L. (2012) Unifying natural and laboratory chemical weathering with interfacial dissolution-reprecipitation: A study based on the nanometer-scale chemistry of fluid-silicate interfaces. *Chem. Geol.* **294–295**, 203–216..

Henry J., Towler M. R., Stanton K. T., Querol X. and Moreno N. (2004) Characterisation of the glass fraction of a selection of European coal fly ashes. *J. Chem. Technol. Biotechnol.* **79**, 540–546.

Hewlett, P. (2003). Lea's chemistry of cement and concrete (4th edt.). Elsevier, Amsterdam.

Hilley G. E. and Porder S. (2008) A framework for predicting global silicate weathering and CO2 drawdown rates over geologic time-scales. *Proc. Natl. Acad. Sci.* **105**, 16855–16859.

Hoch A. R., Reddy M. M. and Drever J. I. (1996) The effect of iron content and dissolved O2 on dissolution rates of clinopyroxene at pH 5.8 and 25 C: preliminary results. *Chem. Geol.* **132**, 151–156.

Höller H. and Wirsching U. (1985) Zeolite formation from fly ash. *Fortschritte der Mineral.* **63**, 21–43.

Hollman G. G., Steenbruggen G. and Janssen-Jurkovičová M. (1999) Two-step process for the synthesis of zeolites from coal fly ash. *Fuel* **78**, 1225–1230.

Huijgen W. J. J. and Comans R. N. J. (2005) Carbon Dioxide Sequestratation By Mineral Carbonation Literature Review Update 2003-2004.

Huijgen W. J. J., Witkamp G. J. and Comans R. N. J. (2006) Mechanisms of aqueous wollastonite carbonation as a possible CO2 sequestration process. *Chem. Eng. Sci.* **61**, 4242–4251.

Iijima A. (1988) Diagenetic transformations of minerals as exemplified by zeolites and silica minerals-a Japanese view. In *Developments in sedimentology* Elsevier. pp. 147–211.

Inglezakis V. J. and Grigoropoulou H. P. (2001) Applicability of simplified models for the estimation of ion exchange diffusion coefficients in zeolites. *J. Colloid Interface Sci.* **234**, 434–441.

Ingrin J. (1993) TEM imaging of polytypism in pseudowollastonite. *Phys. Chem. Miner.* **20**, 56–62.

IPCC (2014) *Climate Change 2014: Synthesis Report. Fifth Assesment Report of the Intergovernmental Panel on Climate Change.*,

Itani L., Liu Y., Zhang W., Bozhilov K. N., Delmotte L. and Valtchev V. (2009) Investigation of the physicochemical changes preceding zeolite nucleation in a sodium-rich aluminosilicate gel. *J. Am. Chem. Soc.* **131**, 10127–10139.

IYER K., JAMTVEIT B., MATHIESEN J., MALTHESORENSSEN A. and FEDER J. (2008) Reaction-assisted hierarchical fracturing during serpentinization. *Earth Planet. Sci. Lett.* **267**, 503–516.

Iyer S. D., Sudhakar M. and Das P. (2007) Composition and genesis of zeolitic claystones from the Central Indian Ocean Basin. *Acta Geol. Sin. Ed.* **81**, 756–770.

Izquierdo M. and Querol X. (2012) Leaching behaviour of elements from coal combustion fly ash: An overview. *Int. J. Coal Geol.* **94**, 54–66.

Jagniecki, E. A., Jenkins, D. M., Lowenstein, T. K., & Carroll, A. R. (2013). Experimental study of shortite (Na2Ca2(CO3)3) formation and application to the burial history of the Wilkins Peak Member, Green River Basin, Wyoming, USA. Geochimica et Cosmochimica Acta, 115, 31-45.

Jamtveit B., Austrheim H. and Malthe-Sørenssen A. (2000) Accelerated hydration of the Earth's deep crust induced by stress perturbations. *Nature* **408**, 75–78.

JAMTVEIT B., MALTHESORENSSEN A. and KOSTENKO O. (2008) Reaction enhanced permeability during retrogressive metamorphism. *Earth Planet. Sci. Lett.* **267**, 620–627.

Jamtveit Bjørn, Putnis Christine V. M.-S. A. (2008) Reaction induced fracturing during replacement processes. *Contrib. to Mineral. Petrol.* **157**, 127–133.

Jha B. and Singh D. N. (2016) *Fly Ash Zeolites: Innovations, applications and directions*.,

Ji L., Yu H., Wang X., Grigore M., French D., Gözükara Y. M., Yu J. and Zeng M. (2017) CO2sequestration by direct mineralisation using fly ash from Chinese Shenfu coal. *Fuel*

Process. Technol. **156**, 429–437.

Ji L., Yu H., Yu B., Zhang R., French D., Grigore M., Wang X., Chen Z. and Zhao S. (2018) Insights into Carbonation Kinetics of Fly Ash from Victorian Lignite for CO 2 Sequestration.

Jones M. R., McCarthy A. and Booth A. P. P. G. (2006) Characteristics of the ultrafine component of fly ash. *Fuel* **85**, 2250–2259.

Johnson, D. R., & Robb, W. A. (1973). Gaylussite: thermal properties by simultaneous thermal analysis. American Mineralogist, 58(7-8), 778-784.

Jun, Y. S., Giammar, D. E., & Werth, C. J. (2013). Impacts of Geochemical Reactions on Geologic Carbon Sequestration. Environmental Science and Technology, 47, 3-8.

Kagi, H., Nagai, T., Loveday, J. S., Wada, C., & Parise, J. B. (2003). Pressure-induced phase transformation of kalicinite (KHCO3) at 2.8 GPa and local structural changes around hydrogen atoms. American Mineralogist, 88(10), 1446-1451.

Karlsson C., Zanghellini E., Swenson J., Roling B., Bowron D. T. and Börjesson L. (2005) Structure of mixed alkali/alkaline-earth silicate glasses from neutron diffraction and vibrational spectroscopy. *Phys. Rev. B* **72**, 64206.

Kasting J. F. (2019) The Goldilocks planet? How silicate weathering maintains Earth "just right." *Elem. An Int. Mag. Mineral. Geochemistry, Petrol.* **15**, 235–240.

Kelemen, P. B., Matter, J., Streit, E. E., Rudge, J. F., Curry, W. B., & Blusztajn J. (2011) Rates and Mechanisms of Mineral Carbonation in Peridotite: Natural Processes and Recipes for Enhanced, in situ CO2 Capture and Storage. *Annu. Rev. Earth Planet. Sci.* **39**, 545–576.

Kelemen, P. B., Savage, H., & Hirth G. (2013) Reaction-Driven Cracking During Mineral Hydration, Carbonation and Oxidation. In *Poromechanics V: Proceedings of the Fifth Biot Conference on Poromechanics* pp. 823–826.

Kelemen P. B. and Hirth G. (2012) Reaction-driven cracking during retrograde metamorphism: Olivine hydration and carbonation. *Earth Planet. Sci. Lett.* **345**–**348**, 81–89.

Kelemen P. B., Matter J., Streit E. E., Rudge J. F., Curry W. B. and Blusztajn J. (2011) Rates and Mechanisms of Mineral Carbonation in Peridotite: Natural Processes and Recipes for Enhanced, in situ CO 2 Capture and Storage. *Annu. Rev. Earth Planet. Sci* **39**, 545–76.

Kellermeier, M., Cölfen, H., & Gebauer, D. (2013). Investigating the early stages of mineral precipitation by potentiometric titration and analytical ultracentrifugation. In Methods in enzymology (Vol. 532, pp. 45-69). Academic Press.

Kellermeier, M., Glaab, F., Klein, R., Melero-García, E., Kunz, W., & García-Ruiz, J. M. (2013). The effect of silica on polymorphic precipitation of calcium carbonate: an on-line energy-dispersive X-ray diffraction (EDXRD) study. Nanoscale, 5(15), 7054-7065.

King H. E., Plümper O. and Putnis A. (2010) Effect of secondary phase formation on the carbonation of olivine. *Environ. Sci. Technol.* **44**, 6503–6509.

King H. E., Satoh H., Tsukamoto K. and Putnis A. (2014) Surface-specific measurements of olivine dissolution by phase-shift interferometry. *Am. Mineral.* **99**, 377–386.

Knauss K. G., Nguyen S. N. and Weed H. C. (1993) Diopside dissolution kinetics as a function of pH, C02, temperature, and time. *Geochim. d Cosmochim. Acta* **57**, 285–294.

Kosanovic C., Subotic B., Smit I., Cizmek A., Stubicar M. and Tonejc A. (1997) Study of structural transformations in potassium-exchanged zeolite A induced by thermal and mechanochemical treatments. *J. Mater. Sci.* **32**, 73–78.

Lackner K. S. (2011) A Guide to CO 2 Sequestration. **1677**.

Lackner K. S. (2009) Capture of carbon dioxide from ambient air. *Eur. Phys. J. Spec. Top.* **176**, 93–106.

Lackner K. S. (2002) Carbonate chemistry for sequestering fossil carbon. *Annu. Rev. Energy Environ.* **27**, 193–232.

Lackner K. S., Wendt C. H., Butt D. P., Joyce E. L. and Sharp D. H. (1995) Carbon dioxide disposal in carbonate minerals. *Energy* **20**, 1153–1170.

Lafay R., Montes-Hernandez G., Renard F. and Vonlanthen P. (2018) Intracrystalline reaction-induced cracking in olivine evidenced by hydration and carbonation experiments. *Minerals* **8**, 412.

Lasaga A. C. (1995) Fundamental approaches in describing mineral dissolution and precipitation rates. *Chem. Weather. rates Silic. Miner.*, 23–86.

Lee K.-M. and Jo Y.-M. (2010) Synthesis of zeolite from waste fly ash for adsorption of CO 2. *J. Mater. Cycles Waste Manag.* **12**, 212–219.

Leemann, A., Le Saout, G., Winnefeld, F., Rentsch, D., & Lothenbach, B. (2011). Alkali–silica reaction: the influence of calcium on silica dissolution and the formation of reaction products. Journal of the American Ceramic Society, 94(4), 1243-1249.

Leung D. Y. C., Caramanna G. and Maroto-Valer M. M. (2014) An overview of current status of carbon dioxide capture and storage technologies. *Renew. Sustain. Energy Rev.* **39**, 426–443.

Lin C. F. and Hsi H. C. (1995) Resource Recoveiy of Waste Fly Ash: Synthesis of Zeolite-like Materials. *Environ. Sci. Technol.* **29**, 1109–1117.

Di Lorenzo F. and Prieto M. (2017) Dissolution–Recrystallization of (Mg,Fe)CO $_3$ during Hydrothermal Cycles: Fe ^{II} /Fe ^{III} Conundrums in the Carbonation of Ferromagnesian Minerals. *Cryst. Growth Des.* **17**, 4170–4182.

Di Lorenzo F., Ruiz-Agudo C., Ibañez-Velasco A., Gil-San Millán R., Navarro J., Ruiz-Agudo E. and Rodriguez-Navarro C. (2018) The Carbonation of Wollastonite: A Model Reaction to Test Natural and Biomimetic Catalysts for Enhanced CO2 Sequestration. *Minerals* **8**, 209.

Lüttge A., Arvidson R. S. and Fischer C. (2013) A stochastic treatment of crystal dissolution kinetics. *Elements* **9**, 183–188.

Makreski, P., Jovanovski, G., Gajović, A., Biljan, T., Angelovski, D., & Jaćimović, R. (2006). Minerals from Macedonia. XVI. Vibrational spectra of some common appearing pyroxenes and pyroxenoids. Journal of Molecular Structure, 788(1-3), 102-114.

Marini L. (2006) *Geological sequestration of carbon dioxide: thermodynamics, kinetics, and reaction path modeling*., Elsevier.

Matter J. M. and Kelemen P. B. (2009) Permanent storage of carbon dioxide in geological reservoirs by mineral carbonation. *Nat. Geosci.* **2**, 837–841.

Matter J. M., Stute M., Snæbjörnsdottir S. Ó., Oelkers E. H., Gislason S. R., Aradottir E. S., Sigfusson B., Gunnarsson I., Sigurdardottir H. and Gunnlaugsson E. (2016) Rapid carbon mineralization for permanent disposal of anthropogenic carbon dioxide emissions. *Science*

(80-.). **352**, 1312–1314.

Mavromatis V., Gautier Q., Bosc O. and Schott J. (2013) Kinetics of Mg partition and Mg stable isotope fractionation during its incorporation in calcite. *Geochim. Cosmochim. Acta* **114**, 188–203.

McAdam A. C., Zolotov M. Y., Sharp T. G. and Leshin L. A. (2008) Preferential low-pH dissolution of pyroxene in plagioclase–pyroxene mixtures: Implications for martian surface materials. *Icarus* **196**, 90–96.

McGrail B. P., Schaef H. T., Ho A. M., Chien Y. J., Dooley J. J. and Davidson C. L. (2006) Potential for carbon dioxide sequestration in flood basalts. *J. Geophys. Res. Solid Earth* **111**, 1–13.

McConnell, J. D. (1954). The hydrated calcium silicates riversideite, tobermorite, and plombierite. Mineralogical Magazine, 30(224), 293-305.

Merrill, R. C. (1947). Chemistry of the soluble silicates. Journal of Chemical Education, 24(6), 262-269.

Miller, Q.R.S.; Thompson, C. J.; Loring, J.S.; Windisch, C.F.; Bowden, M.E.; Hoyt, D.W.; Hu, J.Z.; Arey, B.W.; Rosso, K.M.; Schaef, H.T. Insights into silicate carbonation processes in water-bearing supercritical CO2 fluids. Int. J. Greenhouse Gas Contr. 2013, 15, 104-118.

Monasterio-Guillot L., Di Lorenzo F., Ruiz-Agudo E. and Rodriguez-Navarro C. (2019) Reaction of pseudowollastonite with carbonate-bearing fluids: Implications for CO<inf>2</inf> mineral sequestration. *Chem. Geol.* **524**.

Monasterio-Guillot Luis, Di Lorenzo F., Ruiz-Agudo E. and Rodriguez-Navarro C. (2019)

Reaction of pseudowollastonite with carbonate-bearing fluids: Implications for CO2 mineral sequestration. *Chem. Geol.* **524**, 158–173.

Montes-Hernandez G., Pérez-López R., Renard F., Nieto J. M. and Charlet L. (2009) Mineral sequestration of CO2 by aqueous carbonation of coal combustion fly-ash. *J. Hazard. Mater.* **161**, 1347–1354.

Moreno N., Querol X., Andrés J. M., Stanton K., Towler M., Nugteren H., Janssen-Jurkovicová M. and Jones R. (2005) Physico-chemical characteristics of European pulverized coal combustion fly ashes. *Fuel* **84**, 1351–1363.

Moreno N., Querol X., Ayora C., Pereira C. F. and Janssen-Jurkovicová M. (2001) Utilization of zeolites synthesized from coal fly ash for the purification of acid mine waters. *Environ. Sci. Technol.* **35**, 3526–3534.

Morimoto, N. (1988). Nomenclature of pyroxenes. Mineralogy and Petrology, 39(1), 55-76.

Morse J. W. and Bender M. L. (1990) Partition coefficients in calcite: Examination of factors influencing the validity of experimental results and their application to natural systems. *Chem. Geol.* **82**, 265–277.

Morsli A., Driole M.-F., Cacciaguerra T., Arletti R., Chiche B., Hamidi F., Bengueddach A., Quignard F. and Di Renzo F. (2007) Microporosity of the amorphous aluminosilicate precursors of zeolites: The case of the gels of synthesis of mordenite. *Microporous mesoporous Mater.* **104**, 209–216.

Min, Y.; Li, Q.; Voltolini, M.; Kneafsey, T.; Jun, Y.S. Wollastonite carbonation in water-bearing supercritical CO2: Effects of particle size. Environ. Sci. Technol. 2017, 51, 13044-13053.

Min, Y., & Jun, Y. S. (2018). Wollastonite carbonation in water-bearing supercritical CO2: Effects of water saturation conditions, temperature, and pressure. Chemical Geology, 483, 239-246.

Morey, G. W. (1917). The ternary system H2O-K2SiO3-SiO2. Journal of the American Chemical Society, 39(6), 1173-1229.

Mozgawa Wlodzimierz, Mozgawa W, Handke M. and Jastrze W. (2004) Vibrational spectra of aluminosilicate structural clusters Synthesis and structural studies of zeolite membranes on geopolimeric supports View project Vibrational spectra of aluminosilicate structural clusters. *Artic. J. Mol. Struct.*.

Müntener O. (2010) Serpentine and serpentinization: A link between planet formation and life. *Geology* **38**, 959–960.

Murayama N., Yamamoto H. and Shibata J. (2002) Mechanism of zeolite synthesis from coal fly ash by alkali hydrothermal reaction. *Int. J. Miner. Process.* **64**, 1–17.

Nyambura M. G., Mugera G. W., Felicia L. and Gathura N. P. *Carbonation of brine impacted fractionated coal fly ash: Implications for CO 2 sequestration*.,

O'Connor W. K., Dahlin D. C., Rush G. E., Gerdemann S. J., Penner L. R. and Nilsen D. N. (2005) Aqueous Mineral Carbonation. *Doe/Arc-Tr-04-002*, 1–99.

Oelkers E. H., Gislason S. R. and Matter J. (2008) Mineral Carbonation of CO2. *Elements* **4**, 333–337

Omori K. (1971) Analysis of the Infrared Absortion Spectrum of Diopside. *Am. Mineral.* **56**.

Ozpinar Y., Semiz B. and Schroeder P. A. (2013) Zeolites in mafic pyroclastic rocks from the Sandikli-Afyonkarahisar region, Turkey. *Clays Clay Miner.* **61**, 177–192.

Pacala S. and Socolow R. (2004) Stabilization wedges: Solving the climate problem for the next 50 years with current technologies. *Science (80-.).* **305**, 968–972.

Pan S. Y., Chang E. E. and Chiang P. C. (2012) CO2capture by accelerated carbonation of alkaline wastes: A review on its principles and applications. *Aerosol Air Qual. Res.* **12**, 770–791.

Park A. H. A. and Fan L. S. (2004) CO2 mineral sequestration: Physically activated dissolution of serpentine and pH swing process. *Chem. Eng. Sci.* **59**, 5241–5247.

Parkhurst D. L. and Appelo C. A. J. *USER'S GUIDE TO PHREEQC (VERSION 2)-A COMPUTER PROGRAM FOR SPECIATION, BATCH-REACTION, ONE-DIMENSIONAL TRANSPORT, AND INVERSE GEOCHEMICAL CALCULATIONS*.,

Paradiso, P., Santos, R. L., Horta, R. B., Lopes, J. N. C., Ferreira, P. J., & Colaço, R. (2018). Formation of nanocrystalline tobermorite in calcium silicate binders with low C/S ratio. Acta Materialia, 152, 7-15.

Peuble S., Godard M., Luquot L., Andreani M., Martinez I. and Gouze P. (2015) CO2 geological storage in olivine rich basaltic aquifers: New insights from reactive-percolation experiments. *Appl. Geochemistry*.

Van Pham T. H., Aagaard P. and Hellevang H. (2012) On the potential for CO 2 mineral storage in continental flood basalts–PHREEQC batch-and 1D diffusion–reaction simulations. *Geochem. Trans.* **13**, 5.

Du Plessis P. W., Ojumu T. V. and Petrik L. F. (2013) Waste minimization protocols for the process of synthesizing zeolites from South African coal fly ash. *Materials (Basel).* **6**, 1688–1703.

Plümper O., Røyne A., Magrasó A. and Jamtveit B. (2012) The interface-scale mechanism of reaction-induced fracturing during serpentinization. *Geology* **40**, 1103–1106.

Pokrovsky O. S. and Schott J. (2000) Kinetics and mechanism of forsterite dissolution at 25°C and pH from 1 to 12. *Geochim. Cosmochim. Acta* **64**, 3313–3325.

Pokrovsky O. S., Shirokova L. S., Benezeth P., Schott J. and Golubev S. V (2009) Effect of Organic Ligands and Heterotrophic Bacteria on Wollastonite Dissolution Kinetics. *Am. J. Sci.* **309**, 731–772.

Plattenberger, D. A., Ling, F. T., Tao, Z., Peters, C. A., & Clarens, A. F. (2018). Calcium Silicate Crystal Structure Impacts Reactivity with CO2 and Precipitate Chemistry. Environmental Science & Technology Letters, 5(9), 558-563.

Plattenberger, D., Ling, F. T., Peters, C. A., & Clarens, A. F. (2019). Targeted Permeability Control in the Subsurface Via Calcium Silicate Carbonation. Environmental science & technology.

Power, I. M.; Harrison, A.L.; Dipple, G.M.; Wilson, S.A.; Kelemen, P.B.; Hitch, M.; Southam, G. Carbon mineralization: from natural analogues to engineered systems. Rev. Miner. Geochem. 2013, 77, 305-360.

Prentice I. C., Farquhar G. D., Fasham M. J. R., Goulden M. L., Heimann M., Jaramillo V. J., Kheshgi H. S., LeQuéré C., Scholes R. J. and Wallace D. W. R. (2001) The carbon cycle and atmospheric carbon dioxide. In Cambridge University Press.

Putnis a. (2014) Why Mineral Interfaces Matter. *Science (80-.).* **343**, 1441–1442.

Putnis A. (2009) Mineral replacement reactions. *Rev. Mineral. geochemistry* **70**, 87–124.

Putnis A. and Putnis C. V. (2007) The mechanism of reequilibration of solids in the presence of a fluid phase. *J. Solid State Chem.* **180**, 1783–1786.

Querol X., Alastuey A., López-Soler A., Plana F., Andrés J. M., Juan R., Ferrer P. and Ruiz C. R. (1997a) A fast method for recycling fly ash: Microwave-assisted zeolite synthesis. *Environ. Sci. Technol.* **31**, 2527–2533.

Querol X., Moreno N., Umaa J. C., Alastuey A., Hernández E., López-Soler A. and Plana F. (2002) Synthesis of zeolites from coal fly ash: an overview. *Int. J. Coal Geol.* **47**, 413–423.

Querol X., Plana F., Alastuey A. and Lbpez-Soler A. (1997b) Synthesis of Na-zeolites from fly ash. *Fuel* **76**, 236100188–3.

Qian, B., Li, X., & Shen, X. (2016). Preparation and accelerated carbonation of low temperature sintered clinker with low Ca/Si ratio. Journal of Cleaner Production, 120, 249-259.

Richet P., Mysen B. O. and Ingrin J. (1998) High-temperature X-ray diffraction and Raman spectroscopy of diopside and pseudowollastonite. *Phys. Chem. Miner.* **25**, 401–414.

Richet P, Mysen B., Ingrin J., Richet Pascal and Mysen B. O. (1998) *O R I G I N A L P A P E R High-temperature X-ray diffraction and Raman spectroscopy of diopside and pseudowollastonite.*, Springer-Verlag

Rietveld, H. (1969). A profile refinement method for nuclear and magnetic structures. Journal of applied Crystallography, 2(2), 65-71.

Rodriguez-Navarro C., Burgos Cara A., Elert K., Putnis C. V. and Ruiz-Agudo E. (2016) Direct Nanoscale Imaging Reveals the Growth of Calcite Crystals via Amorphous Nanoparticles. *Cryst. Growth Des.* **16**, 1850–1860.

Rodriguez-Navarro C., Kudlacz K., Cizer O. and Ruiz-Agudo E. (2015) Formation of amorphous calcium carbonate and its transformation into mesostructured calcite. *CrystEngComm* **17**, 58–72.

Rodriguez-Navarro C., ruiz-agudo eNCarNaCioN, luque aNa, rodriguez-Navarro alejaNdro B. and ortega-Huertas M. (2009) Thermal decomposition of calcite: Mechanisms of formation and textural evolution of CaO nanocrystals. *Am. Mineral.* **94**, 578–593.

Rodríguez-Navarro C., Ruiz-Agudo E., Harris J. and Wolf S. E. (2016) Nonclassical crystallization in vivo et in vitro (II): Nanogranular features in biomimetic minerals disclose a general colloid-mediated crystal growth mechanism.

Roosz C., Grangeon S., Blanc P., Montouillout V., Lothenbach B., Henocq P., Giffaut E., Vieillard P. and Gaboreau S. (2015) Crystal structure of magnesium silicate hydrates (MSH): The relation with 2: 1 Mg–Si phyllosilicates. *Cem. Concr. Res.* **73**, 228–237.

Røyne A., Jamtveit B., Mathiesen J. and Malthe-Sørenssen A. (2008) Controls on rock weathering rates by reaction-induced hierarchical fracturing. *Earth Planet. Sci. Lett.* **275**, 364–369.

Ruhl L., Vengosh A., Dwyer G. S., Hsu-Kim H. and Deonarine A. (2010) Environmental impacts of the coal ash spill in Kingston, Tennessee: an 18-month survey. *Environ. Sci. Technol.* **44**, 9272–9278.

Ruiz-Agudo Encarnacion,´ Lvarez-Lloret P. A., Ibañ Ez-Velasco A. and Ortega-Huertas M. (2016) Crystallographic Control in the Replacement of Calcite by Calcium Sulfates. Available at: https://pubs.acs.org/doi/10.1021/acs.cgd.6b00522. [Accessed July 2, 2019].

Ruiz-Agudo Encarnación, King H. E., Patiño-López L. D., Putnis C. V, Geisler T., Rodriguez-Navarro C. and Putnis A. (2016) Control of silicate weathering by interface-coupled dissolution-precipitation processes at the mineral-solution interface. *Geol.* **44**, 1–4.

Ruiz-Agudo E., Putnis C. and Rodriguez-Navarro C. (2017) Reactions between minerals and aqueous solutions. In MINERALOGICAL SOCIETY GREAT BRITAIN & IRELAND.

Ruiz-Agudo E., Putnis C. V. and Putnis A. (2014a) Coupled dissolution and precipitation at mineral-fluid interfaces. *Chem. Geol.*

Ruiz-Agudo E., Putnis C. V. and Putnis A. (2014b) Coupled dissolution and precipitation at mineral–fluid interfaces. *Chem. Geol.* **383**, 132–146.

Ruiz-Agudo E., Putnis C. V., Rodriguez-Navarro C. and Putnis A. (2012) Mechanism of leached layer formation during chemical weathering of silicate minerals. *Geology* **40**, 947–950.

Sáez Del Bosque I. F. F., Martínez-Ramírez S. and Blanco-Varela M. T. T. (2014) FTIR study of the effect of temperature and nanosilica on the nano structure of C-S-H gel formed by hydrating tricalcium silicate. *Constr. Build. Mater.* **52**, 314–323.

Sánchez-Hernández R., López-Delgado A., Padilla I., Galindo R. and López-Andrés S. (2016) One-step synthesis of NaP1, SOD and ANA from a hazardous aluminum solid waste. *Microporous Mesoporous Mater.* **226**, 267–277.

Sanna A., Uibu M., Caramanna G., Kuusik R. and Maroto-Valer M. M. (2014) A review of mineral carbonation technologies to sequester CO2. *Chem. Soc. Rev.* **43**, 8049–8080.

Scherer G. W. (1999) Crystallization in pores. *Cem. Concr. Res.* **29**, 1347–1358.

Schiro M., Ruiz-Agudo E. and Rodriguez-Navarro C. (2012) Damage mechanisms of porous materials due to in-pore salt crystallization. *Phys. Rev. Lett.* **109**, 265503.

Schott J. and Berner R. A. (1985) Dissolution mechanisms of pyroxenes and olivines during weathering. In *The chemistry of weathering* Springer. pp. 35–53.

Schott J., Berner R. A. and Sjöberg E. L. (1981) Mechanism of pyroxene and amphibole weathering-I. Experimental studies of iron-free minerals. *Geochim. Cosmochim. Acta* **45**, 2123–2135.

Schott J. and Oelkers E. H. (1995) Dissolution and crystallization rates of silicate minerals as a function of chemical affinity. *Pure Appl. Chem.* **67**, 903–910.

Schott J., Pokrovsky O. S., Spalla O., Devreux F., Gloter A. and Mielczarski J. A. (2012) Formation, growth and transformation of leached layers during silicate minerals dissolution: The example of wollastonite. *Geochim. Cosmochim. Acta* **98**, 259–281.

Schweinsberg, H., & Liebau, F. (1972). Darstellung und kristallographische Daten von K2Si2O5, KHSi2O5I und K2Si4O9. Zeitschrift für anorganische und allgemeine Chemie, 387(2), 241-251.

Schwertmann U. (1991) Solubility and dissolution of iron oxides. *Plant Soil* **130**, 1–25.

Seifritz W. (1990) CO2 disposal by means of silicates. Nature. *Nature* **345**, 486. Available at: https://www-nature-com.gaelnomade-1.grenet.fr/articles/345486b0.pdf [Accessed November 26, 2018].

Seryotkin Y. V, Sokol E. V and Kokh S. N. (2012) Natural pseudowollastonite: crystal structure, associated minerals, and geological context. *Lithos* **134**, 75–90.

Shackleton N. J. (2000) The 100,000-year ice-age cycle identified and found to lag temperature, carbon dioxide, and orbital eccentricity. *Science (80-.).* **289**, 1897–1902.

Sheng, H., Lv, L., Liang, B., Li, C., Yuan, B., Ye, L., Yue, H., Liu, C., Wang, Y., Zhu, J. & Xie, H. (2015). Aqueous carbonation of the potassium-depleted residue from potassium feldspar–CaCl 2 calcination for CO 2 fixation. Environmental Earth Sciences, 73(11), 6871-6879.

Shigemoto N., Hayashi H. and Miyaura K. (1993) Selective formation of Na-X zeolite from coal fly ash by fusion with sodium hydroxide prior to hydrothermal reaction. *J. Mater. Sci.* **28**, 4781–4786.

Shigemoto N., Sugiyama S., Hayashi H. and Miyaura K. (1995) Characterization of Na-X, Na-A, and coal fly ash zeolites and their amorphous precursors by IR, MAS NMR and XPS. *J. Mater. Sci.* **30**, 5777–5783.

Siegel D. I. and Pfannkuch H.-O. (1984) Silicate mineral dissolution at pH 4 and near standard temperature and pressure. *Geochim. Cosmochim. Acta* **48**, 197–201.

Siever R. and Woodford N. (1979) Dissolution kinetics and the weathering of mafic minerals. *Geochim. Cosmochim. Acta* **43**, 717–724.

Simon Emmanuel J. J. A. (2009) Modeling the impact of nano-pores on mineralization in sedimentary rocks. *WATER Resour. Res.* **45**.

Simonsen M. E., Sønderby C., Li Z. and Søgaard E. G. (2009) XPS and FT-IR investigation of silicate polymers. *J. Mater. Sci.* **44**, 2079–2088.

Singer A. and Berkgaut V. (1995) Cation exchange properties of hydrothermally treated coal fly ash. *Environ. Sci. Technol.* **29**, 1748–1753.

Singh B. and Gilkes R. J. (1993) Weathering of spodumene to smectite in a lateritic environment. *Clays Clay Miner.* **41**, 624–630.

Siriwardane R. V., Shen M. S., Fisher E. P. and Losch J. (2005) Adsorption of CO2on zeolites at moderate temperatures. *Energy and Fuels* **19**, 1153–1159.

Sissmann O., Daval D., Brunet F., Guyot F., Verlaguet A., Pinquier Y., Findling N. and Martinez I. (2013) The deleterious effect of secondary phases on olivine carbonation yield: Insight from time-resolved aqueous-fluid sampling and FIB-TEM characterization. *Chem. Geol.* **357**, 186–202.

Sjöberg, S. (1996). Silica in aqueous environments. Journal of Non-Crystalline Solids, 196, 51-57.

Snæbjörnsdóttir S. Ó., Sigfússon B., Marieni C., Goldberg D., Gislason S. R. and Oelkers E. H. (2020) Carbon dioxide storage through mineral carbonation. *Nat. Rev. Earth Environ.*, 1–13.

de Souza F. and Bragança S. R. (2013) Thermogravimetric analysis of limestones with different contents of MgO and microstructural characterization in oxy-combustion. *Thermochim. Acta* **561**, 19–25.

Spears D. A. and Martinez-Tarrazona M. R. (2004) Trace elements in combustion residues from a UK power station. *Fuel* **83**, 2265–2270.

Steenbruggen G. and Hollman G. G. (1998) The synthesis of zeolites from fly ash and the properties of the zeolite products. *J. Geochemical Explor.* **62**, 305–309.

Stockmann G., Wolff-Boenisch D., Gislason S. R. and Oelkers E. H. (2008) Dissolution of diopside and basaltic glass: the effect of carbonate coating. *Mineral. Mag.* **72**, 135–139.

Stumm W. (1987) *Aquatic surface chemistry: Chemical processes at the particle-water* *interface*., John Wiley & Sons.

Sumida K., Rogow D. L., Mason J. A., McDonald T. M., Bloch E. D., Herm Z. R., Bae T.-H. and Long J. R. (2011) Carbon dioxide capture in metal–organic frameworks. *Chem. Rev.* **112**, 724–781.

Sun Y., Parikh V. and Zhang L. (2012) Sequestration of carbon dioxide by indirect mineralization using Victorian brown coal fly ash. *J. Hazard. Mater.* **209**–**210**, 458–466.

Suzuki, Y., Nakata, M., & Komuro, K. (2013) Carbonation of pectolite under hydrothermal condition: an experiment with sodium carbonate and bicarbonate solution. Shigen-Chishitsu 63, 1-6.

Svensson, K., Neumann, A., Menezes, F. F., Lempp, C., & Pöllmann, H. (2018). The Conversion of Wollastonite to CaCO3 Considering Its Use for CCS Application as Cementitious Material. Applied Sciences, 8(2), 304.

Sverdrup H. U. (1990) *The kinetics of base cation release due to chemical weathering*., Krieger Publishing Company.

Tai C. Y., Chen W. R. and Shih S. M. (2006) Factors affecting wollastonite carbonation under CO2supercritical conditions. *AIChE J.* **52**, 292–299.

Tamilselvi Dananjayan R. R., Kandasamy P. and Andimuthu R. (2016) Direct mineral carbonation of coal fly ash for CO2sequestration. *J. Clean. Prod.*

Taylor, H. F. W. (1959). The dehydration of tobermorite. Clays and Clay Minerals, 6, 101-109.

Taylor, J. R., & Dinsdale, A. T. (1990): Thermodynamic and phase diagram data for the CaO-SiO2 system. Calphad, 14(1), 71-88.

Teng H. H., Fenter P., Cheng L. and Sturchio N. C. (2001) Resolving orthoclase dissolution processes with atomic force microscopy and X-ray reflectivity. *Geochim. Cosmochim. Acta* **65**, 3459–3474.

Terzano R., Spagnuolo M., Medici L., Vekemans B., Vincze L., Janssens K. and Ruggiero P. (2005) Copper stabilization by zeolite synthesis in polluted soils treated with coal fly ash. *Environ. Sci. Technol.* **39**, 6280–6287.

Thiery M., Villain G., Dangla P. and Platret G. (2007) Investigation of the carbonation front shape on cementitious materials: Effects of the chemical kinetics.

Thomas M. D. A. and Matthews J. D. (1992) Carbonation of fly ash concrete. *Mag. Concr. Res.* **44**, 217–228.

Thommes M., Kaneko K., Neimark A. V, Olivier J. P., Rodriguez-Reinoso F., Rouquerol J. and Sing K. S. W. (2015) Physisorption of gases, with special reference to the evaluation of surface area and pore size distribution (IUPAC Technical Report). *Pure Appl. Chem.* **87**, 1051–1069.

Tisserand D. and Hellmann R. (2008) Bridging the’gap’between laboratory dissolution and natural chemical weathering.

United Nations Framework Convention on Climate Change (2015) *Report of the conference of the Parties on its twenty- first session, held in Paris from 30 November to 13 December 2015.*,

Urey H. C. (1952) The planets: their origin and development. , 245.

Vassilev S. V, Menendez R., Alvarez D., Diaz-Somoano M. and Martinez-Tarazona M. R.

(2003) Phase-mineral and chemical composition of coal fly ashes as a basis for their multicomponent utilization. 1. Characterization of feed coals and fly ashes☆. *Fuel* **82**, 1793–1811.

Vicente-Rodríguez M. A., Suarez M., Bañares-Muñoz M. A. and Lopez-Gonzalez J. D. D. (1996) Comparative FT-IR study of the removal of octahedral cations and structural modifications during acid treatment of several silicates. *Spectrochim. Acta - Part A Mol. Spectrosc.* **52**, 1685–1694.

Walker J. C. G., Hays P. B. and Kasting J. F. (1981) A negative feedback mechanism for the long-term stabilization of Earth's surface temperature. *J. Geophys. Res. Ocean.* **86**, 9776–9782.

Wang L., Jin Y. and Nie Y. (2010) Investigation of accelerated and natural carbonation of MSWI fly ash with a high content of Ca. *J. Hazard. Mater.* **174**, 334–343.

Wang, F., & Giammar, D. E. (2012). Forsterite dissolution in saline water at elevated temperature and high CO2 pressure. Environmental science & technology, 47(1), 168-173.

Wee J. H. (2013) A review on carbon dioxide capture and storage technology using coal fly ash. *Appl. Energy* **106**, 143–151.

De Weerdt K. and Justnes H. (2015) The effect of sea water on the phase assemblage of hydrated cement paste. *Cem. Concr. Compos.* **55**, 215–222.

Weldes, H. H., & Lange, K. R. (1969). Properties of soluble silicates. Industrial & Engineering Chemistry, 61(4), 29-44.

Weissbart E. J. and Rimstidt J. D. (2000) Wollastonite: Incongruent dissolution and leached layer formation. *Geochim. Cosmochim. Acta* **64**, 4007–4016.

White A. F. and Yee A. (1985) Aqueous oxidation-reduction kinetics associated with coupled electron-cation transfer from iron-containing silicates at 25 C. *Geochim. Cosmochim. Acta* **49**, 1263–1275.

Wild B., Daval D., Guyot F., Knauss K. G., Pollet-Villard M. and Imfeld G. (2016) pH-dependent control of feldspar dissolution rate by altered surface layers. *Chem. Geol.* **442**, 148–159.

Wild B., Daval D., Micha J.-S., Bourg I. C., White C. E. and Fernandez-Martinez A. (2019) Physical Properties of Interfacial Layers Developed on Weathered Silicates: A Case Study Based on Labradorite Feldspar. *J. Phys. Chem. C.*

Whitfield, P.S.; Mitchell, L.D. (2009) In situ laboratory X-ray powder diffraction study of wollastonite carbonation using a high-pressure stage. Appl. Geochem., 24, 1635-1639.

Wolff-Boenisch, D. (2011). On the buffer capacity of CO2-charged seawater used for carbonation and subsequent mineral sequestration. Energy Procedia, 4, 3738-3745.

Wojdyr M. (2010) Fityk: a general-purpose peak fitting program. *J. Appl. Crystallogr.* **43**, 1126–1128.

Wu, J. C. S., Sheen, J. D., Chen, S. Y., & Fan, Y. C. (2001). Feasibility of CO2 fixation via artificial rock weathering. Industrial & engineering chemistry research, 40(18), 3902-3905.

Yamanaka T. and Mori H. (1981) The structure and polytypes of α-CaSiO3 (pseudowollastonite). *Acta Crystallogr. Sect. B Struct. Crystallogr. Cryst. Chem.* **37**, 1010–1017.

Yan F., Jiang J., Li K., Tian S., Zhao M. and Chen X. (2015) Performance of Coal Fly Ash Stabilized, CaO-based Sorbents under Different Carbonation−Calcination Conditions.

Yanagisawa Y. (2001) A new CO2disposal process via artificial weathering of calcium silicate accelerated by acetic acid. *Energy* **26**, 341–354.

Yang H. and Prewitt C. T. (1999) On the crystal structure of pseudowollastonite (CaSiO3). *Am. Mineral.* **84**, 929–932.

Yang X., Roonasi P. and Holmgren A. (2008) A study of sodium silicate in aqueous solution and sorbed by synthetic magnetite using in situ ATR-FTIR spectroscopy. *J. Colloid Interface Sci.* **328**, 41–47.

Yang X., Roonasi P., Jolsterå R. and Holmgren A. (2009) Kinetics of silicate sorption on magnetite and maghemite: An in situ ATR-FTIR study. *Colloids Surfaces A Physicochem. Eng. Asp.* **343**, 24–29.

Yang Y., Colman B. P., Bernhardt E. S. and Hochella M. F. (2015) Importance of a nanoscience approach in the understanding of major aqueous contamination scenarios: case study from a recent coal ash spill. *Environ. Sci. Technol.* **49**, 3375–3382.

Yu, P., Kirkpatrick, R.J. (1999) Thermal dehydration of tobermorite and jennite. Concrete Sci. Eng. 1, 185-191.

Zakaznova-Herzog V. P., Nesbitt H. W., Bancroft G. M. and Tse J. S. (2008) Characterization of leached layers on olivine and pyroxenes using high-resolution XPS and density functional calculations. *Geochim. Cosmochim. Acta* **72**, 69–86.

Zeebe R. E. and Caldeira K. (2008) Close mass balance of long-term carbon fluxes from ice-core

CO 2 and ocean chemistry records. *Nat. Geosci.* **1**, 312.

Zeng R., Umana J. C., Querol X., Lopez-Soler A., Plana F. and Zhuang X. (2002) Zeolite synthesis from a high Si-Al fly ash from East China. *J. Chem. Technol. Biotechnol.* **77**, 267–273.

Zhao, H.; Park, Y.; Lee, D.H.; Park, A.H.A. (2013) Tuning the dissolution kinetics of wollastonite via chelating agents for CO2 sequestration with integrated synthesis of precipitated calcium carbonates. Phys. Chem. Chem. Phys., 15, 15185-15192

Zhang L. and Lüttge A. (2009) Theoretical approach to evaluating plagioclase dissolution mechanisms. *Geochim. Cosmochim. Acta* **73**, 2832–2849.

Zhang S. and Depaolo D. J. (2017) Rates of CO 2 Mineralization in Geological Carbon Storage.

Zholobenko V. L., Holmes S. M., Cundy C. S. and Dwyer J. (1997) Synthesis of MCM-41 materials: an in situ FTIR study. *Microporous Mater.* **11**, 83–86.